The Physics of the High-Temperature Superconducting Dynamo and No-Insulation Coils

by

Ratu Craig Te Ahurangi Mataira-Cole

A thesis
Submitted to the Victoria University of Wellington
in partial fulfilment of the requirements for the degree of
Doctor of Philosophy

31st of March 2022

Abstract

High-T_c superconducting (HTS) dynamos are a fascinating topic as practical engineering research preceded fundamental understanding, a lead then maintained for at least a decade. These devices, counter to expectation, produce a dc voltage where 'textbook' electromagnetism would predict a zero dc component. Simply by replacing a normal conducting stator in a standard dynamo with HTS conductor a dc — auto-rectifying — effect is created. This thesis reports my work in uncovering and codifying the underlying mechanism that gives rise to this effect — namely the broken symmetry that is usually present with Ohm's law. An explanation of the dc voltage then leads to an explanation of the internal resistivity of such devices, which in turn allows more efficient dynamos to be designed, and modelled. The underlying logic of the HTS dynamo mechanism is also sufficiently strong to predict a complimentary electromagnetic device, a semiconducting dynamo, which remains to be experimentally verified.

Ultimately, such HTS dynamos could be used to energise powerful HTS magnets. The modelling techniques developed in this thesis also provide insight into the operational behaviour of no-insulation coils (NI coils). Such coils are extremely robust to mechanical, thermal, and electrical stresses and faults. A simple model of such coils is presented that captures their essential physics with enough fidelity to predict shielding and magnetisation currents inherent with HTS conductors and turn-to-turn current flow. These two technologies represent key topics for the future of high field HTS magnet technologies and their supporting systems.

Thesis Supervisor: Dr. Chris W. Bumby
Title: Chief Scientist, Robinson Research Institute.
Principle Investigator, MacDiarmid Institute.

Thesis Supervisor: Prof. Rod A. Badcock
Title: Deputy Director, Chief Engineer, Robinson Research Institute.

Acknowledgements

For me, doing a PhD was a chance to live out the stories of my heroes, men and woman who, through their hard work, were able to make huge strides and leaps of understanding. I think all physicists try to imagine what being Einstein must have been like. Like many mythological characters, these heroes have multiple feats, each deserving of a place in history. In a world where opportunities to make great leaps is shrinking, and the chasms to be leapt are growing wider and deeper, I am most grateful for the opportunity to tackle my own physical mysteries. To the men who revived the HTS dynamo, defended it and kept the research alive, I thank you. For a decade this device resisted understanding, yet you persisted experimentally knowing that the device and its physics were special and worthy of understanding.

Life doesn't pause when you do a PhD, and I am grateful that mine has continued as well. I have found my partner Tahlia, strengthened my relationship with my Father Michael, and I've been able to spend time with my Mother Ngareta in Western Australia. My friendships have blossomed and the opportunity to travel planted the seeds of many more. Three and a half years is a long time, and in that time my both my Father and Mother have fought and won their own battles with cancer; to their respective spouses, Corinne and David I thank you from the bottom of my heart, arohanui.

To my Mother, thank you for setting me on this path. You, while never exerting pressure or being remotely forceful, painted a picture of the world where this was entirely inevitable. You saw, in me, a little physicist when I was only a boy and nothing has ever meant more to me. To my Father, your support has provided the essential backbone to enable me to pursue this PhD. I am immensely privileged to be your son, and I suspect people don't actually tell you that you are indeed inspirational, even if a little grumpy.

To all those who have worked in these labs beside me over these past years, thank you. Olly, thank you for your work on these dynamos before I had my chance. Jianzhao, it was a pleasure to work with you while we could, you were the role model

that I couldn't quite replicate! Dr. Maximilian Fisser, you showed that standing up for your own self-worth, in a system that is often exploitative, is not just possible, but also dignified. It is a frame of mind I hope that I have spread to the PhD students that follow me.

To my supervisors, Rod Badcock, Chris Bumby and Mark Ainslie, thank you for taking me on. Rod, thanks for taking a chance on me all those years ago. You have been a constant example and role model for how science and engineering research can be justified, your salesmanship and gumption have enabled me to work on problems that would otherwise never be investigated. Mark, you gave all you time and techniques to some young lads from NZ, they were the gifts that Gus and I could build a career on. And Chris, you are the consummate scientist, thank you for engaging and giving me a real discussion when I was just a summer student asking questions about the dynamos. The scientific culture and attitude that you cultivate is exemplary, exploratory, demanding, and still welcoming.

To my friends, thank you for sharing the ride. Gabe, you were for a long time a cornerstone of my sanity and mental health. Gus, you are a comrade as we have battled away from our little corner of the world. Alex, thank you for letting me dance a little in Einstein's world, it is a life I wish I could have had. And James, I suspect, that I will always owe you a lot more than you ever owe me, try not to forget it.

And to my beautiful, sweet, forgiving, and kind Tahlia, who has now born the brunt of dealing with a stressed, over stretched, burned out, and despondent me, thank you. I rely on you to have a inexhaustible lust for life.

List of publications

During the tenure of this PhD, I have presented, authored, or co-authored the following works.

- E. F. Talantsev and **R. C. Mataira**. Polar projections for big data analysis in applied superconductivity. *AIP Advances*, 8(7):075213, 2018.

- **Ratu C. Mataira**, Mark D. Ainslie, Rod A. Badcock, Chris W.Bumby. Simulation of flux-pinning effects on high-T_c superconducting dynamos, *presented at AMN9*, 02/2019.

- Y. Liu, M. Fisser, J. Fang, Z. Jiang, **R. Mataira**, and R. A. Badcock. Feasibility study of fiber bragg grating sensor for quench detection of high temperature superconductors. *IEEE Transactions on Applied Superconductivity*, 29(5):1–6, Aug 2019.

- **R. C. Mataira**, M. D. Ainslie, R. A. Badcock, and C. W. Bumby. Origin of the dc output voltage from a high-T_c superconducting dynamo. *Appl. Phys. Lett.*, 114(16):162601, 2019.

- Evgueni F. Talantsev, **Ratu C. Mataira**, and Wayne P. Crump. Classifying superconductivity in Moiré graphene superlattices. *arXiv*, page arXiv:1902.07410, Feb 2019.

- E F Talantsev and **R C Mataira**. Classifying superconductivity in ThH-ThD superhydrides/superdeuterides. *Materials Research Express*, 7(1):016003, jan 2020.

- **R. Mataira**, M. D. Ainslie, R. Badcock, and C. W. Bumby. Modeling of stator versus magnet width effects in high-T_c superconducting dynamos. *IEEE Transactions on Applied Superconductivity*, 30(4):5204406, 2020.

- Kent Hamilton, **Ratu Mataira**, Jianzhao Geng, Chris Bumby, Dale Carnegie, and Rod Badcock. Practical estimation of HTS dynamo losses. *IEEE Transactions on Applied Superconductivity*, 30(4):9037084, 2020.

- **R C Mataira**, M D Ainslie, R A Badcock, and C W Bumby. Finite-element modelling of no-insulation HTS coils using rotated anisotropic resistivity. *Superconductor Science and Technology*, 33(8):08LT01, jun 2020.

- **Ratu Mataira**, Mark Ainslie, Andres Pantoja, Rod Badcock, and Chris Bumby. Mechanism of the high-T_c superconducting dynamo: Models and experiment. *Phys. Rev. Applied*, 14:024012, Aug 2020.

- Mark Ainslie, Francesco Grilli, Loïc Quéval, Enric Pardo, Fernando Perez-Mendez, **Ratu Mataira**, Antonio Morandi, Asef Ghabeli, Chris Bumby, and Roberto Brambilla. A new benchmark problem for electromagnetic modelling of superconductors: the high-T_c superconducting dynamo. *Superconductor Science and Technology*, 33(10):105009, sep 2020.

- Yanchao Liu, **Ratu Mataira**, Rod Badcock, Zhenan Jiang, and Jin Fang. Application of epoxy-bonded fbg temperature sensors for high-temperature superconductor-coated conductor quench detection. *IEEE Transactions on Applied Superconductivity*, 31(2):9250587, 2021.

- Mark D. Ainslie, Loïc Quéval, **Ratu C. Mataira**, and Chris W. Bumby. Modelling the frequency dependence of the open-circuit voltage of a high-T_c superconducting dynamo. *IEEE Transactions on Applied Superconductivity*, 31(5):9350153, 2021.

- **Ratu Mataira**, Mark D. Ainslie, Rod Badcock, and Chris W. Bumby. Modelling parallel-connected, no-insulation high-T_c superconducting magnets. *IEEE*

Transactions on Applied Superconductivity, 31(5):1–5, 2021.

- E. F. Talantsev and **R. C. Mataira**. Cooper pair trajectories in superconducting slab at self-field conditions. *Modern Physics Letters B*, 35(13):2150226, 2021.

- J M Brooks, M D Ainslie, **R Mataira**, R Badcock, and C W Bumby. Below 1 μv cm-1: determining the geometrically-saturated critical transport current of a superconducting tape. *Superconductor Science and Technology*, 34(8):085004, jun 2021.

- Asef Ghabeli, Mark Ainslie, Enric Pardo, Loïc Quéval, and **Ratu Mataira**. Modeling the charging process of a coil by an HTS dynamo-type flux pump. *Superconductor Science and Technology*, 34(8):084002, jul 2021.

Contents

List of Figures

Chapter 1

Introduction

Superconductivity has always been looked at as a potential source of technological revolution and breakthrough. Ever since the first measurements were made [1], the extrapolation to more powerful magnets and more powerful machines was natural. Fast forward more than 100 years and some of the promise has been made real, Magnetic Resonance Imaging (MRI), research, industrial, and clinical accelerators make tangible contributions to the world that could not be done in any other way. A superconducting machine could run at higher current densities (A/m^2), reducing size, while also increasing magnetic field. These compact machines, operating at higher fields can apply more torque between their stator and rotor windings. Such a machine would also forgo iron, having sufficiently high field to saturate Iron, reducing the weight and inertia of the machine leading to an increase in operating frequency. Both an increase in torque and an increase in frequency lead to an increase in power, for a given size and mass of machine, i.e. higher power density. Despite this, superconducting motor and generators, have been slower to the mark, struggling to find a niche where they can out perform their normal conducting (copper) counterparts and achieve feats otherwise unattainable.

The first generation of useful superconductors, known as the low temperature superconductors (LTS), found use in DC magnets, and research AC magnets. However, the use of LTS materials in superconducting motor-generators was precluded by efficiency concerns. The necessity to operate such machines at 4 K, which incurs a

cooling penalty of 300 watt/watt of heat dissipated at 4K, meant that any AC losses incurred in the machines would result in machines more complicated, less reliable, and with dubious efficiency advantages. The advent of high temperature superconductors (HTS) has revived speculation that these problems could be overcome. Higher operating temperatures give more forgiving cooling penalties, ie 15-30 watt/watt dissipated at 77 K, and more reliable cryogenic systems, leading to viable economics.

However, HTS technologies come with their own difficulties. The hard to manufacture ceramic superconductors are insulating at room temperature, reducing conductor stability. Furthermore, where LTS were often simple alloys that could be easily jointed, the complex crystal structure of the HTS materials resisted making true superconducting joints. Without such joints, the ultimate promise of these materials, persistent electromagnets, seems out of reach.

Finally, climate change, and our response as a civilisation to it, has made it clear that our economy must be decarbonised. This provides a deep technical challenge to most aspects of the modern world. Our workhorse materials, plastic and steel, are both deeply reliant on fossil fuels. And while electric cars are making improvements in cost and range, moving 1-4 people remains significantly easier than moving heavy freight or many people 20-200.

This thesis chronicles my journey through understanding and contributing to two of the major breakthroughs in high temperature superconductivity in the last decade. These two breakthroughs were published within 6 months of each other, and neither with much immediate prestige, being published in the journal *IEEE Transactions on Applied Superconductivity*. Since then, both papers have spawned a flurry of work. The first, published by Hahn et. al. in December 2010, *HTS Pancake Coils Without Turn-to-Turn Insulation* [2] has amassed 429[1] citations to date. Hahn's proposal no-insulation coils (NI coils) dramatically improve the stability and viability of HTS coils for application.

The second breakthrough, *Flux Pump for HTS Magnets* [3] by Hoffmann et. al., was published 6 months later in June 2011, revitalised investigation in the use of

[1] as of January 2022

superconducting flux pumps, potentially alleviating the need for copper current leads or persistent joints. Both pieces of work have seen considerable advancement over the last decade, and pushed the integrated systems performance of high temperature superconducting machines into the realm of application.

These two somewhat unrelated breakthroughs share an underlying challenge. The use of HTS tape, which are essentially long 2D conductive sheets, permit the existence of spontaneous and persistent circulating currents. These currents can exist independently of, or interact with net transport currents that one may inject into the superconductor for a given purpose. In the case of a magnet, a coil of HTS tape is energised with an operating current I_{op} but the existence of shielding currents can affect field quality and cause unexpected Lorentz forces, damaging high field coils [4].

In the case of the HTS dynamo, it will be shown here that these shielding currents give rise to a dc voltage across the HTS dynamo stator, and their interaction with transport currents leads to internal resistance in such devices. Understanding these two phenomena, with sufficient clarity to achieve experimental verification requires advanced numerical modelling. This thesis largely describes my work in expanding existing techniques to successfully model the complicated circulating currents in superconductors.

1.1 Research questions

The two breakthroughs that motivate this thesis have largely independent literature, where the development of one has not depended on the other. This is of course a scientific and technical boon, as interrelated complexity can cause difficulty. However, even as the two subjects enjoy separability in isolated publications, there is a clear pressure to consider both when looking at the future of integrated HTS magnet systems.

My work, in this thesis, has been concerned with answering questions across several levels of the technology that would allow for advanced HTS systems and machines. I have concentrated my focus on those issues that have seemed recalcitrant to the level

of physical understanding expected of deployable, scalable technologies. These two technologies, the HTS NI coils and HTS dynamos, are both promising and yet both exhibit barriers to their understanding. For the NI coil the problem is relatively simple in that the ability to numerically model — and therefore design — these magnets has lagged the modelling techniques available for insulated superconducting magnets of similar performance. This lag is fundamentally a result of geometric complexity intrinsic to the NI coil concept, and this thesis presents progress in managing that extra complexity. In the case of the HTS dynamo, the problem is deeper. Ultimately, an operating mechanism is required to make useful predictions of HTS dynamo performance. To establish that understanding, numerical models of the HTS dynamo need to be established and validated. As such, this thesis explores if progress can be made in modelling these devices; if the models of the HTS dynamo elucidate a mechanism; and finally, if the mechanism proves useful in predicting improved performance. These questions can be captured as such:

1. Can existing finite element modelling techniques be expanded/improved to capture the novel and necessary superconducting physics of the HTS NI coils and HTS dynamos?

2. What insights can a quantitatively predictive finite element model of the HTS dynamo yield?

3. Does understanding of the HTS dynamo mechanism present options for optimising their design and ultimate utility?

This thesis will address these questions, and provide a basis on which future advancement can be built.

1.2 Thesis outline

The aim of my PhD, when I first set out, was to develop a predictive theory for the operation of the HTS dynamos proposed by Hoffmann. I am very proud to say that

we have achieved that and more. Not only has a theory been developed which is predictive of existing results, but it also predicts new results, and has made a clear pathway for more efficient dynamos to be designed.

My efforts to understand the no-insulation coils were a natural consequence of our success in implementing H-formulation models at Robinson and the ongoing work we have on such coils. While coming after my first results with the dynamos, the NI coil models will be introduced first so that H-formulation methods can, themselves, be introduced in a simpler setting. After the H-formulation has been introduced in the context of the NI coil, we will introduce the model of the HTS dynamo and the conclusions drawn from it. The bulk of this thesis comprises results that have flowed from the HTS dynamo model.

I am very proud to say that much of the work contained here has been very successful, and has already been widely cited. As such, a full view of the literature of the HTS dynamos is not possible, without, at some point, introducing the work presented in chapters 4-8. Hence the literature review is split into two parts, one at the beginning that will bring you up to the sate-of-the-art at the start of this PhD. A second, post-thesis review is also includes later that contextualises my work in the expanded literature that has sprung up around it.

The chapters, hereafter, appear as:

Chapter 2 introduces the literature up to 2019, including a streamlined introduction to superconductivity, the development of the no-insulation coils, a review of the flux pumps, an introduction to the phenomenology of the HTS dynamos, and an exposition of the H-formulation numerical method.

Chapter 3 serves as a reference for methods used that are commonly non-obvious in implementing the models or experiments. It does not include aspects of the methods that are critical for understanding the results presented in each chapter, which are instead presented in each chapter respectively.

Chapter 4 uses the H-formulation approach to create a geometrically simplified model of the HTS No-insulation coils. This model highlights the strength of H-formulation methods for solving highly nonlinear problems in superconductivity.

In **Chapter 5**, an H-formulation model for the HTS dynamo is introduced, which shows how the dc voltage is generated. It is concluded that only the non-linear resistivity of HTS materials is necessary to generate the effect.

Chapter 6 applies this model of the HTS dynamo to the broad set of operational parameters that have been explored in experiment. Beyond electrical characterisation, magnetic field observations are also used to validate and compare the calculated current distributions from the finite element model. And finally, model behaviour gives a phenomenological understanding of the internal resistance of the dynamo.

Chapter 7 extends the model of the HTS dynamo to include wider (>12 mm) stators. These wide stators are found to have higher open circuit voltages, as well as lower internal resistances.

Chapter 8 tests the original notion that nonlinearity of resistivity is the proper explanation. A hypothetical semiconducting dynamo is presented. A-formulation modelling is used to explore some basic properties.

Chapter 9 contextualises the work presented and its impact on literature. A brief review of the literature that has sprung up around the work in this thesis is presented, and together they inform a set of interesting future work.

Finally, **Chapter 10** summarises the results presented, draws together their implications and impacts, before concluding with some suggestions for future work.

Chapter 2

Review of preexisting literature

Foreword

The following is an overview of the existing literature that contextualises this work, up to when I started my PhD in 2018, and is by no means exhaustive. Chapter 9 will complete the overall literature review by including work that has been built upon material presented in this thesis. Theses are unique in having extremely different audiences, markers, researchers, grad students etc. but this literature review is targeted at a new graduate student who is looking to understand HTS dynamos or NI coils. This review therefore covers a minimal amount of theory, aimed at a graduate level, required to motivate the following chapters. Any figures reproduced are done so under the principle of fair use.

2.1 Superconductivity

A strong introduction to the physics of superconductivity can be found in [7]. Here we will quickly identify the key aspects of superconductivity that differentiate it from normal conductivity or perfect conductivity. Broadly speaking, superconductors can conduct dc currents with zero resistance, somewhat like perfect conductors. Unlike perfect conductors, superconductors display two extra behaviours; one, they will spontaneously expel magnetic flux (Meissner effect); and two, there is a maximum

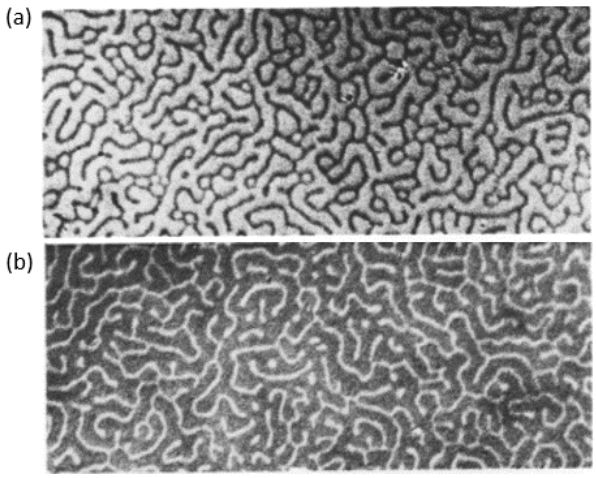

Figure 2-1: Magneto optical images of superconducting lead in an applied field less than B_c, (a) increasing field to 348 Gs, (b) decreasing field to 101 Gs. The geometry of the sheet means that shielding currents concentrate the field locally above $B_c = 500$ Gs, suppressing the superconductivity in the regions shown in white. Reproduced from Huebener [5].

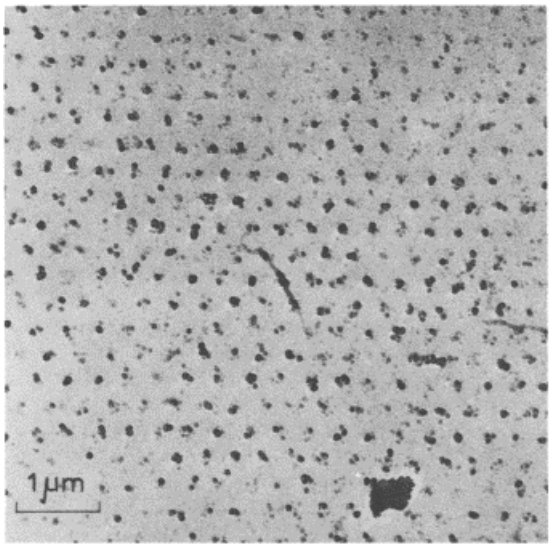

Figure 2-2: Vortex structure as revealed by magnetic particle distribution on indium-doped lead at 1.1 K. Given the applied field at the lattice spacing, this validates the result in eq. 2.1. [6]

magnetic field and current that the conductor can sustain (B_c, J_c) before reverting to the normal conducting state. These two behaviours give rise to two types of superconductor "type-I" and "type-II".

Type-I superconductors will generate spontaneous currents to exclude magnetic flux, however these shielding currents may serve to increase the local current density elsewhere in the material. In a type-I conductor this results in some regions going normal and others maintaining their superconductivity. This behaviour is analogous to the mixing of immiscible fluids such as oil and water, and produces similar patterns, see fig. 2-1. This effect occurs over arbitrary length scales, and renders these materials largely impractical, as the normal zones are resistive. At 4 K, the cooling penalty, the ratio of the work needed by the refrigerator to the heat extracted is equal to 300. Hence even a normal zone with the conductivity of copper would imply disadvantageous losses.

On the other hand, type-II materials enable applied magnetic flux to enter the bulk of the material. Type-II materials have a negative surface energy density between the normal and superconducting domains. This negative energy is akin to the effect of adding detergent to a mixture of oil and water, the detergent preferring to maximise the area between the two compounds, reduces the volume of any given domain towards zero. For type-II superconductor this surface energy has the effect of 'dissolving' applied magnetic fields[1] in the bulk until quantum mechanics places a limit on the smallest amount of flux possible, the flux quanta:

$$\Phi_0 = \frac{h}{2e}. \tag{2.1}$$

From the perspective of this text, type-II HTS material is only differentiated from normal conductors by their macroscopic behaviours. While literature stresses the role of quantized flux as the core source of physics in HTS materials, here, we will never consider length scales shorter than the separation of two vortices. Beyond this scale,

[1]This argument would seem to, for type-II materials very close to their upper critical field B_{cII}, imply that superconducting domains would instead dissolve into the normal phase. However, the surface energy of such an "inverse-vortex", with a superconducting core, would always be positive as the circulating current would always die off as fast as the order parameter $|\psi|^2$.

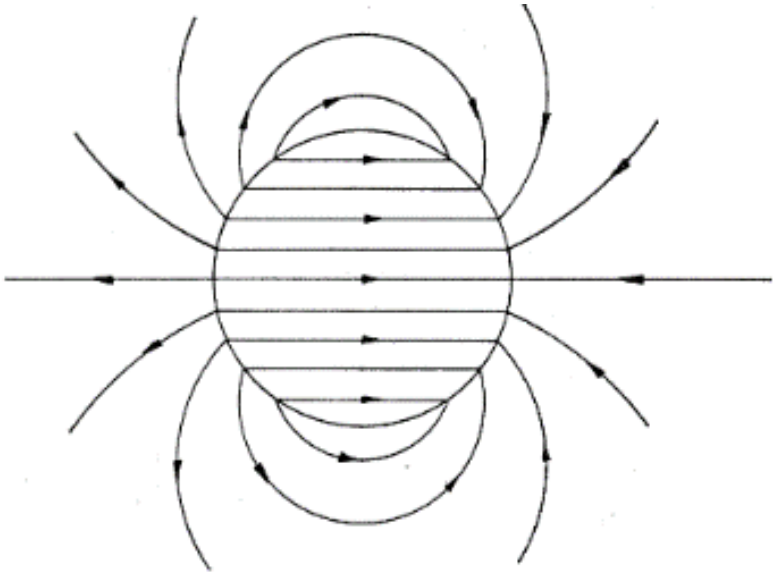

Figure 2-3: Solution for the gradient of the scalar potential surrounding a vortex moving up the page. When added with the time derivative of the A-vector the electric field in the superconducting phase is indeed zero. Reproduced from Bardeen [9].

we will not see any effects from the vortices that can not be governed by continuum approximations.

2.1.1 Quantitative superconductivity

Most practical superconductors are type-II [8], as the dissolved vortices allow many geometries of conductor that would otherwise lead to large dead zones where $B > B_c$. However the existence of the vortices, provides a raft of issues of their own. Primarily they provide a sub critical ($B < B_{cII}$) mechanism for loss in type-II conductors.

Essentially, as described fully by Bardeen [10], the flow of current in a superconductor applies a force to the vortices[2]. Macroscopically this can be thought of as a Lorentz force, between the applied, non-quantised, magnetic field B and the current flowing in the conductor. In steady state, we can set the net force on a vortex (or a charge carrier) to zero, so that:

$$\vec{E} = -\vec{v} \times \vec{B} \tag{2.2}$$

[2]Sadly it is not the purpose of this Thesis to question the notion of applying a force to a "line of flux".

where $\vec{v}$ is the average relative velocity of the charge carriers and the vortices. Predominantly the relative velocity is transverse to the current[3] and so a resistive electric field is established in the material, without eliminating the superconducting state. Fig. 2-3 reproduced from [9] depicts the scalar potential gradient in and around a vortex as it moves up the page. As suggested more loosely by Kim [11], the electric field associated with the vortex motion does not interfere with the superconducting state as it is microscopically isolated to the current flows within the normal cores of the vortices.

The prevailing orthodox view has remained static since the work of Bardeen, Kim and others [12–14], that vortex motion is the indisputable source of loss in type-II conductors. And that the only reason any loss-less current is possible is due to a phenomena known as "flux pinning", where by a secondary static force F_p is available in the material to counteract the Lorentz force $\vec{F} = \vec{v} \times \vec{B}$.[4]

Flux pinning is typically attributed to inhomogenities in the lattice of the superconductor. These inhomogenities can provide static energy barriers to flux motion by affecting the electromagnetic energy density gradient or by affecting the local condensation energy associated with the superconducting state itself. Typically defects that cause pinning can be considered by their dimensionality to be either: 0D point defects, 1D columnar (or spiral) defects, and 2D planar defects.

Fig. 2-4, reproduced from [15], shows measured $J_c(B, \theta)$ values for two different YBCO coated conductor tapes [16]. Here we see the effect of added point, 1D, defects in the lattice, which reduce anisotropy, but at the expense of peak in-field performance. Understanding how superconductors perform in-field, and how pinning affects that performance is a critical step for building practical devices, such as magnets, from these materials.

The different dimensionalities of defects lead to significant anisotropy in the loss-less current densities vs applied magnetic field angle θ. In the case of Yttrium Barium Copper Oxide (YBCO), naturally present CuO planes give the material excellent

[3]The parallel component of the velocity gives rise to a small, non-dissipative Hall effect.

[4]Now the vortices are stationary, so the velocity is dominated by the charge carrier velocity.

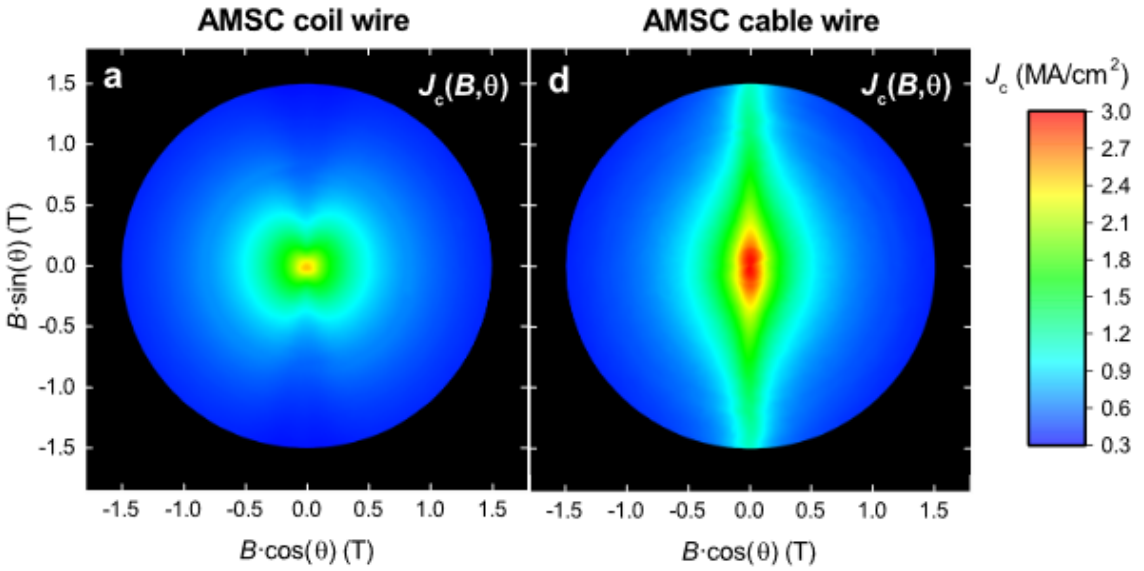

Figure 2-4: Polar projections of the critical current density J_c as a function of applied field magnitude and angle. (a) Point pinning additives improve the isotropy of the YBCO. (b) As grown YBCO films show strong anisotropy due to effective pinning in 2D CuO planes. Reproduced from [15].

pinning performance in fields that are parallel to these CuO planes, and parallel to the plane of common 'coated-conductor' tapes. However, when the applied field is perpendicular to these planes, they provide no pinning potential and the loss-less current is significantly reduced.

As the performance of these materials is determined by bulk inhomognieties, measurements of flux flow phenomena in practical samples are aggregate measurements of the flow of vortices through large numbers of varied grain boundaries and other defects. As such, the onset of flux flow is not immediate in type-II materials, and instead follows a percolation theory [17, 18]. As flux flow requires flux to traverse the width of the conductor, the motion of vortices follows networks of defects where this flow is easier. Furthermore, different networks, located anywhere between two given voltage taps, will have different depinning currents. Hence some small amount of loss may occur at much lower currents, before the majority of flux flow paths form. It has been shown that this macroscopic behaviour can be captured as a power law

resistivity [18]:

$$E = E_0 \left(\frac{|J|}{J_c(B, \theta)} \right)^n . \tag{2.3}$$

Here E_0 is some threshold electric field, typically taken as $E_0 = 1\mu\text{V/cm}$, which defines J_c as a practical analogue to the loss-less current density. n is the aptly named 'n-value' which for typical HTS materials exhibit a value between 15 and 40.

Equation 2.3 captures all the superconducting physics required to build the models presented in this thesis.

2.2 Superconducting magnets

Ever since the discovery of superconductivity it has been seen as an opportunity to surpass the magnetic fields achieved by Bitter [19] (10 T in 1933). The current record for a dc magnetic field is held by Hahn *et al* for a composite LTS-HTS superconducting magnet with a center field of 45 T [4], achieved in 2019. The primary limitation in resistive magnets is simply heating. There are two ways to deal with this heat, either by pulsing the magnet [20] to limit net heat generation or by using dc bitter magnets [19]. Superconductors offer a way of avoiding the heating issue by having much lower, or zero, resistivity. However, superconducting materials come with several material properties that add different challenges when designing and operating a magnet.

LTS magnets are typically made from wires of simple pure metal or bi metal alloys,. This means that they maintain the convenient properties of metals when in the normal state. The most prevalent of these materials Niobium and Niobium Titanium [8], can be formed into closed superconducting loops. By winding these materials into large coils, and then closing them, they can carry persistent supercurrents for as long as the magnet is kept cold. This is the basis of every MRI magnet in use today.

The same is not true of HTS materials, which are made from complicated, non-stochometric mixtures of various materials, such as the cuperate perovskites [21, 22], or iron pnictide [23]. Their more complicated chemistry has made the development of

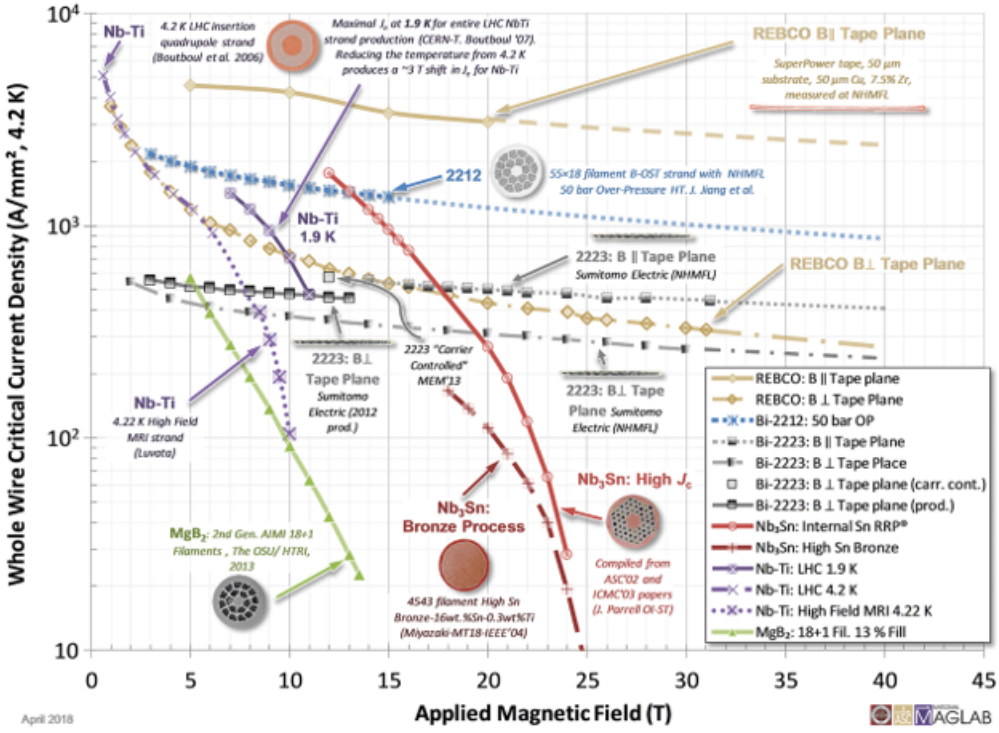

Figure 2-5: Engineering critical current densities of various superconducting wires vs applied magnetic field, perpendicular and parallel. Collated by the National High Field Magnet laboratory [27].

superconducting joints extremely difficult[5]. For this reason, all practical HTS magnets have included resistive joints and must be operated in a driven mode using an external power supply. Despite this disadvantage, the HTS materials are considered the future of magnet development [8, 25, 26], due to their much higher critical fields, see fig. 2-5. Hence we must contend with the practical difficulties of designing, building, and operating magnets comprised of these materials.

So far, HTS magnets have conventionally been driven using external power supplies connected to the magnet using resistive current leads. This technique inevitably introduces heat leaks into the cryogenic system. As the Wiedemann–Franz law describes, excellent electrical conductors are also excellent conductors of heat. This has placed a considerable design limitation on all superconducting magnets to date, as it forces designers to avoid higher currents, and hence design coils of significantly higher

[5]Recent work has resulted in superconducting joints in the lab [24], but these have not yet been implemented in a practical magnet design.

inductance. The current leads typically cause at least 30% of the cryogenic heat load in an HTS magnet [28, ch. 3].

To exacerbate the problem, HTS materials are also prone to the phenomenon of localised quench, where small sections of an HTS magnet will transition into the normal state, and resistively dissipate the stored energy in the magnet. These quench events are typically destructive and magnet designers must find ways to avoid, protect against, and survive these events. A promising way of avoiding this issue is to move away from high-inductance low-current magnets toward high-current low-inductance equivalents.

2.2.1 No-insulation coils

One pathway to making robust HTS coils is to wind them without including any insulation between each turn (NI coils). Such NI coils were first proposed by Hahn [2], and have many useful properties [4, 29–31] and applications [4, 32–39]. Figure 2-6 depicts the NI coil that holds the current world record for DC field strength [4]. Omitting insulation between the turns of the coil provides both current and heat with alternative pathways to flow through the coil's structure. In the case of current flow this is particularly valuable, as localised faults in the HTS winding can be bypassed, with current instead flowing into and through adjacent turns. This avoids the potentially destructive quench events that commonly threaten insulated (INS) HTS coils [34, 35, 40]. From a macroscopic viewpoint, the extra turn-to-turn current paths can be considered as a resistance in parallel with the inductance of the coil. This parallel resistance corresponds to the current flow through one turn of the coil to the next, bypassing the inductive spiral path. However, the introduction of these extra degrees of freedom to the current flow poses challenges when attempting to model and understand the current and field distribution within an NI coil.

Previous experiments and modelling [41–49] have shown that current flow, and the associated electric and magnetic fields are more complicated than that captured by a simple equivalent-circuit model. However, a full resolution model of such NI coils is practically difficult to implement due to the high aspect ratio of the superconductor

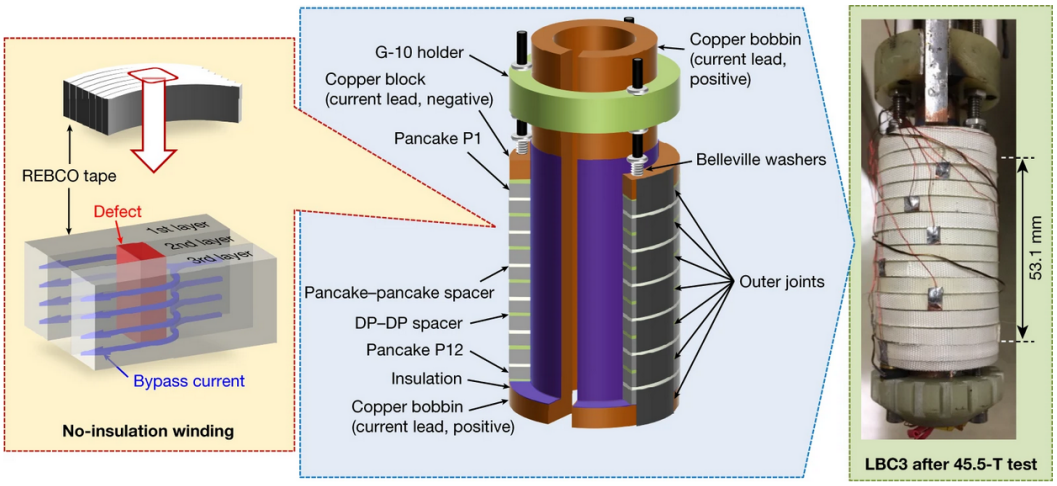

Figure 2-6: Left, principle of the no-insulation technique. Centre, construction design of Little Big Coil (LBC) (not to scale). Right, Photograph of LBC. Owing to the no-insulation technique, any dissipative region is bypassed by current transfer to adjacent turns. Because of this vital 'current-sharing' feature, electrical burn-out — often observed in 'insulated' high-field HTS coils — was not observed after the 45.5 T quench, even at the extremely high conductor current density of 1,420 A mm^{-2}. Reproduced from [4].

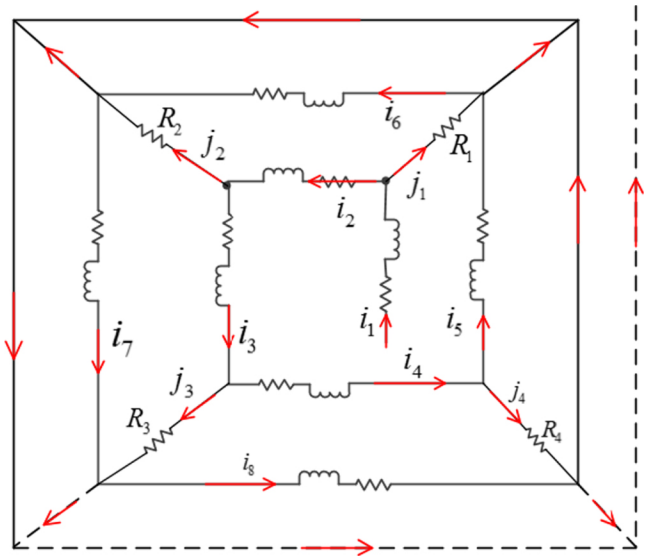

Figure 2-7: The schematic illustration of the equivalent circuit grid (ECG) model for a Superpower (SP) NI coil, $n_\theta = 4$. Reproduced from [41].

and the need to consider the currents flowing normal to the conductor's surface. While progress has been made using circuit grid models (CGM) [41, 50–53], pictured in fig. 2-7, these models lose axial fidelity and cannot simulate the associated shielding currents, or the associated stress [54], within the HTS windings [49, 55–57].

2.3 LTS flux pumps

The desire to avoid current leads and move to 'high-current-designed' magnets started within the LTS community [58]. LTS flux pumps were the first alternative technology to current leads, operating on the principle that dc currents can be induced directly in the LTS circuit. In fact many of the exact arguments made for the HTS flux pumps are taken directly from this era. An excerpt from S.L. Wipf [58]:

> *Why do we need to plead the case for flux pumps? Why does one who favours them find himself in the role of a salesman or on the defensive?... It may be fear of the disadvantages which have perhaps not been spelled out too clearly...*

Ultimately, LTS flux pumps fell out of favour when the use of persistent joints and detachable current leads for ramping LTS magnets became the norm. Regardless, it is worth outlining the operation of the LTS flux pumps, mention some key designs, and identify the aspects which lead to their disuse.

2.3.1 Mechanism

The mechanism of the LTS pumps was a matter of some debate, although the LTS systems were physically simpler, lacking a mixed state that is commonly found in the type-II conductors. Using concepts from London and Little-Parks, one can state that closed superconducting loops, which lack electrical resistance, must conserve the amount of magnetic flux that they enclose. The LTS flux pumps are considered to circumvent this conservation in the case of multiply connected bodies, where flux penetrating one part of the body can be wound into other parts of the body by

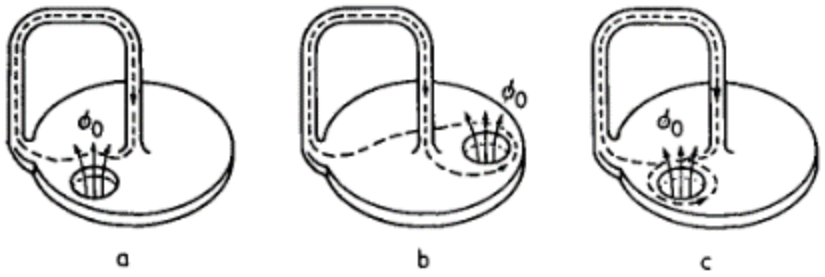

Figure 1. Schematic description of pumping action by a superconducting dynamo of the homopolar type. The circular plate with the zone containing the operative flux φ_0 stands for the actual dynamo, the loop for the circuit or coil to be energized. The manipulation with the dashed contour of integration is performed by moving around the flux-containing zone and is shown in three subsequent stages

Figure 2-8: Reproduced from Suchtelen [59] with original caption.

movement of a 'normal spot' of high local magnetic field, see fig. 2-8. In this way, as the normal spot repeatedly transverses some other closed loop in the material, the other loop picks up a corresponding amount of flux, such that the original contour integral can be kept constant. This concept of pumping flux into the circuit is the source of the name flux pump.

2.3.2 Rectifiers

Given the afore described mechanism any device which induces a dc current to flow in a superconducting circuit is referred to as a 'flux pump'. However, this thesis is focused solely on 'superconducting dynamos', which captures a specific geometry and construction. In this view, two kinds of devices can be separated, the dynamos vs the rectifiers. The superconducting rectifiers work in exactly the same way as a classical rectifier, where-by an applied *emf* is rectified using a variable resistivity. Superconducting rectifiers only differ in that the varying resistivity needs to be created in a bridge that can be periodically returned to the superconducting state.

Several rectifiers are possible, in fact any topology of classical rectifier can be recreated in the superconducting case. Of more interest is how the switching effects are created. One obvious method is to use an applied magnetic field to push the con-

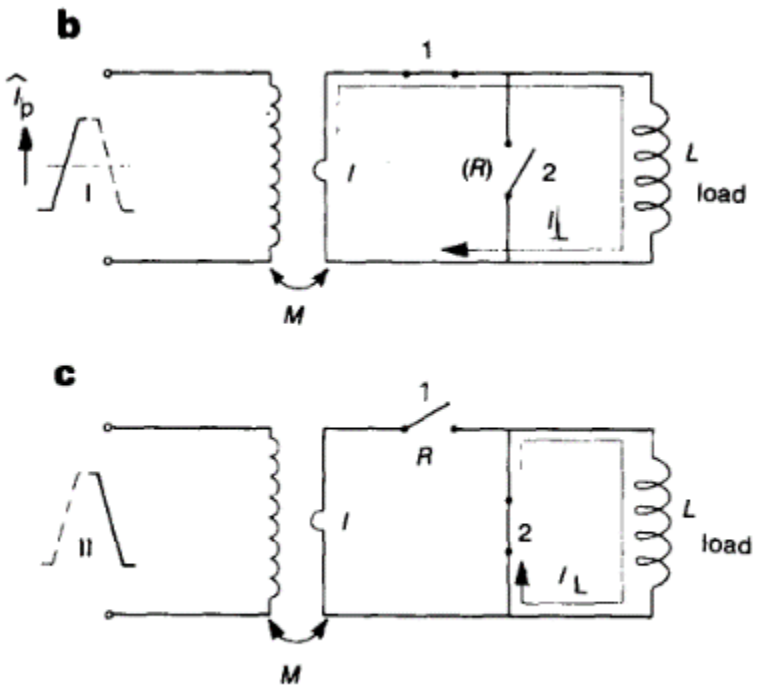

Fig. 16 a — Normal conducting half wave rectifier; b — Superconducting rectifier, pump half cycle; c — Reset half cycle

Figure 2-9: A schematic of the full cycle operation of an LTS Rectifier. Reproduced from Klundert [62], sub figure (a) omitted.

ductor above B_c, destroying the superconducting state. Similar methods use applied ac fields, or even thermal methods to suppress the superconductivity [60, 61]. In any case these devices work on the principle that flux can be introduced into a secondary loop, and then passed into the load loop as the bridge resistance is increased, see fig. 2-9. Another, more interesting, method for switching the resistivity of a superconducting bridge is to drive it past its critical current I_c. By using an asymmetric wave form applied to the secondary, the induced secondary current can be made to have a high magnitude peak during one half of the cycle. This high peak can drive currents in excess of the critical current in the bridge, hence reintroducing the asymmetric resistance between the positive and negative parts of the cycle. During the second part of the cycle, the induced currents are all lower than the critical current, and so the previously introduced flux remains trapped in the load loop. [62]

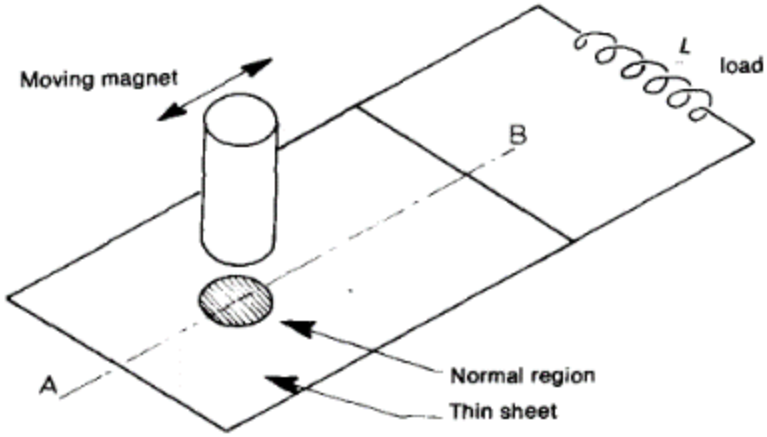

Figure 2-10: An LTS dynamo type flux pump, where the applied field creates a normal spot by which flux is dragged into the superconducting loop. Reproduced from Klundert [62]

2.3.3 Dynamos

This thesis concentrates on the superconducting dynamos, where the motion of flux through a superconductor is driven mechanically. Several geometries and topologies of pump are possible [62–64]. Following the flux pumping argument, the easiest device to understand would be the simple foil dynamo, where a thin foil of superconductor is used as a stator to some applied magnetic field. This applied field can be made sufficient to drive the conductor normal in a localised spot under the magnet, as in fig. 2-10. However, unlike fig. 2-8, the flux is then dragged directly into the superconducting load loop.

It is at this point where thinking about flux pumping becomes problematic. As flux motion serves as a simple heuristic model for the behaviour of the device that can lead to some strange conclusions. As an example, consider that the flux that penetrated the simple dynamo stator is from a permanent magnet, and is now localised in the load loop, and the magnet must now be removed so that the cycle can be continued, which path should the removal of the magnet take? An answer is that the flux that is introduced into the circuit cannot be the flux from the permanent magnet itself, as the magnet does not 'lose' flux during the process. It is more reasonable to instead consider that new flux is created that links the load loop, one polarity through the

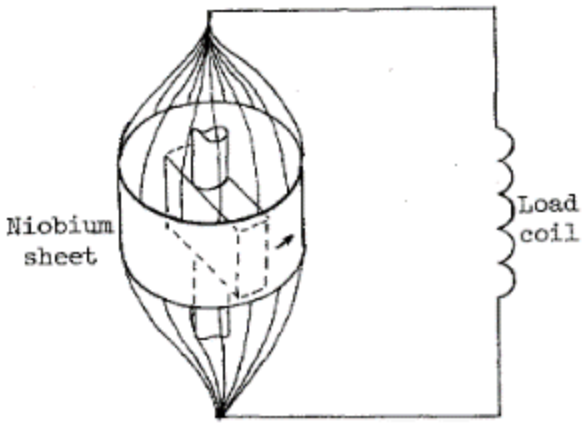

Figure 2-11: A Barrel type pump as depicted by Mawardi [65].

loop and the opposite polarity through the loop's geometric compliment.

A third dynamo topology of interest here is the Barrel/Drum design, where the stator sheet is wrapped into a cylinder, and the normal spot swept around its circumference, fig. 2-11. Here, like in fig. 2-8, flux never explicitly enters or leaves the load loop of the device. Instead we must rely on the same arguments as used by [59, 63] that the flux is "wound" into the load loop.

2.3.4 Comments on mechanism

Giaever once ended a paper with a cautionary note when referring to flux motion: '*We must use extreme caution when we try and develop this and similar physical pictures...*' [66]. However, this caution has fallen away as the view of flux motion has become orthodox. Rather than suggest that this orthodoxy is wrong, like Giaever, it is simply important to remember that it is Maxwell's equations that should ultimately be inspected for the behaviour of these devices.

As an example, consider the device of Volger and Suchtelen, in fig. 2-8, and likewise fig. 2-11, we must ask where the generated flux in the load loop has come from. Strictly speaking this has a simple answer, it comes from the induced currents in that loop. But then, given that the superconducting state is not broken in the load loop, how has the reverse-polarity of this newly generated flux exited the load loop?

The above argument may seem esoteric, however a very similar argument can be made in the case of the rectifiers. As described in the reviews [62, 64] the half wave rectifiers require a reset portion of each cycle whereby applied flux is allowed to leave/enter the secondary loop, see fig. 2-9 (c). This shows that over the course of the ramping of the load current/field, that flux is given some path from one side of the load loop to the other, which is not proposed situation in Van Suchtelen et. al. [59]. We could then imagine that the case in [59], must actually include some period akin to a flux reset cycle in fig. 2-9, potentially caused by the interaction of the induced eddy current around the normal zone interacting with the induced current to provide a path for the newly generated flux to exit the load loop.

2.4 HTS dynamos

High-T_c superconducting dynamos complicate matters as no 'normal spot' can be created by applying practically achievable magnetic fields, as B_{cII} of YBCO is > 200 T. The explanations from Suchtelen [59] become less tractable given the complications of the mixed state. However, for a long time the orthodox view remained the same, that flux could be introduced to the circuit by 'pumping' Abrikosov vortices into the load loop. Essentially, a model that had proven tractable in one case, was still being used to physically describe behaviour in another. The development of the HTS dynamos has taken a primarily experimental pathway, with flux transfer used as a explanatory tool rather than as a predictive phenomenology [67,68]. Here I introduce previous experimental work on the HTS flux pumps that capture their behaviour and present some of the prior attempts to explain them.

2.4.1 The simple dynamos

The first simple HTS dynamo, depicted in fig. 2-12, was demonstrated by Hoffmann [3], which was followed by Coombs [69] in 2014. The simple dynamos use single tapes of commercially available YBCO wire as the dynamo stator. Such wires are typically 12 mm wide. These devices showed that HTS coils could be excited to full current

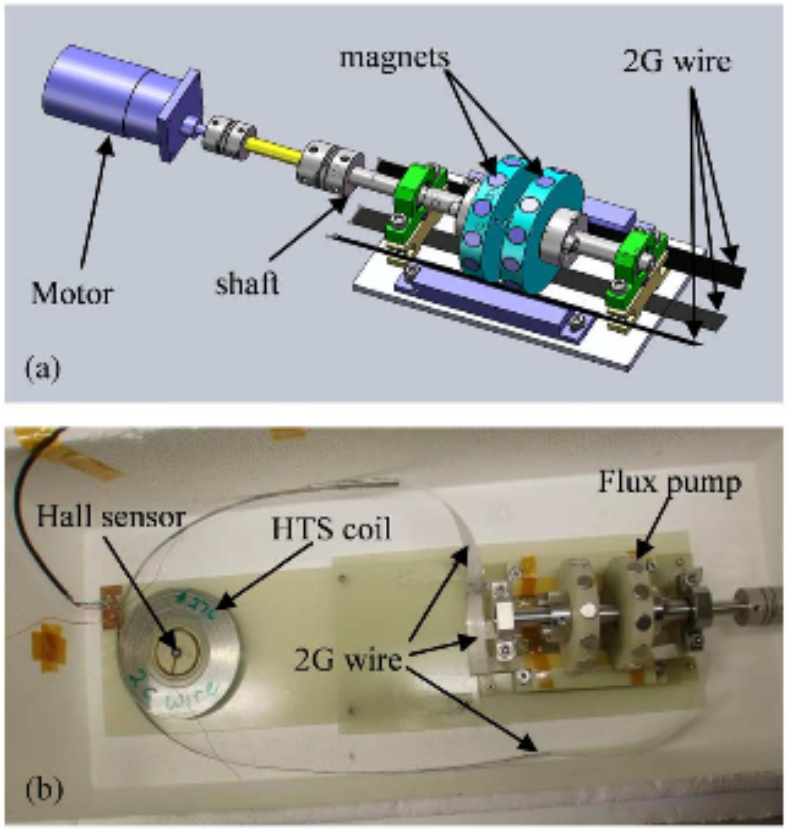

Figure 2-12: (a) Flux pump unit with motor. Cylindrical magnets are mounted on discs which rotate over strips of 2G wire. The magnets motion is perpendicular to the length of the wire. (b) Flux pump and superconducting circuit in a styro-foam box. During operation the entire setup is immersed in liquid nitrogen. Reproduced from Hoffmann [3].

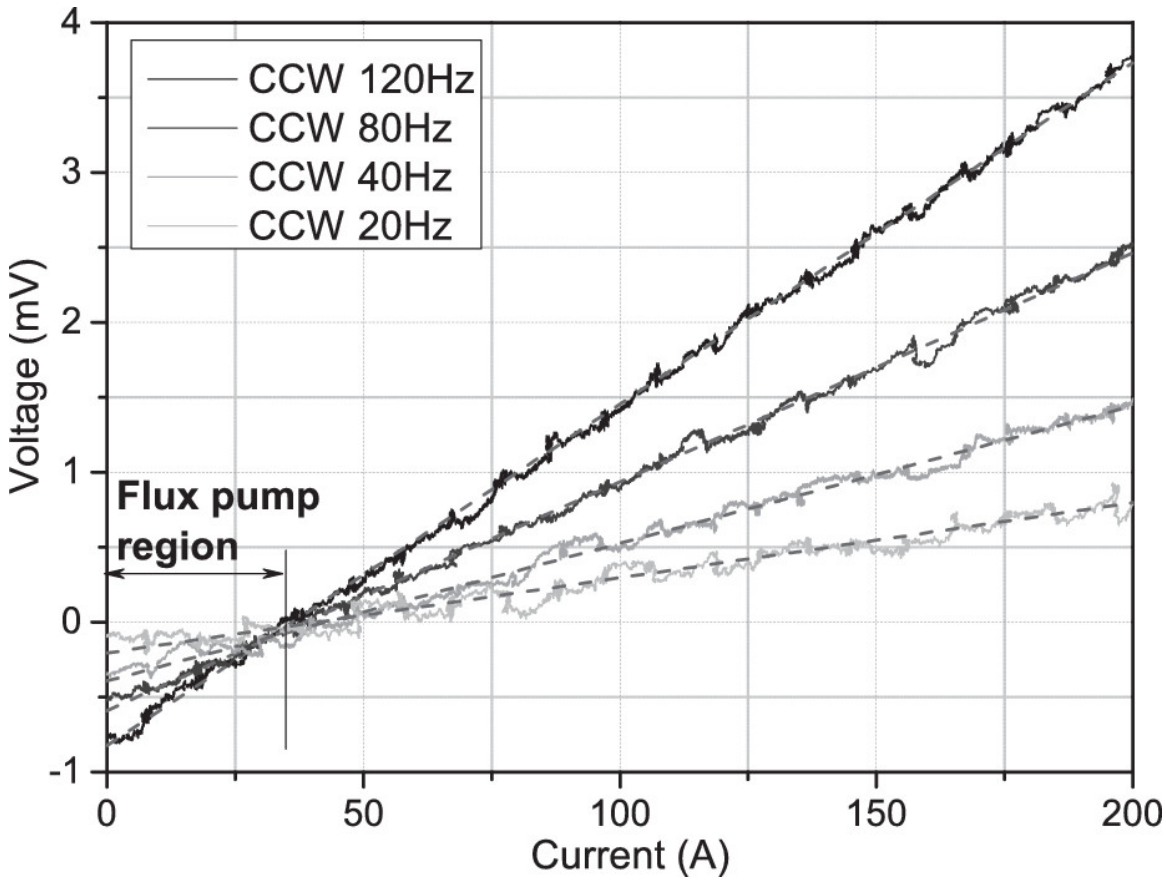

Figure 2-13: V-I curves from counter clockwise rotating magnets together with linear fitting curves. For each field frequency, all curves start with a negative open circuit voltage. The curves cross together at $V = 0$, $I = 35$ A. From $I = 0$ to $I = 35$ A, it is actually working as a flux pump. $I = 35$ A is therefore the maximum current the device can output in a flux pump. Reproduced from [70]

without using a normal spot. From the current vs time curves of coil charging, the I-V characteristic of the device could be extracted, showing that the dynamos exhibit a linear internal resistance, best shown in fig. 2-13 [70].

To understand this internal resistance, Jiang [71] proposed a model based on dynamic resistance [72], where hysteric magnetisation interacts with the dc transport current. As the process is hysteretic the dynamic resistance is proportional to frequency. Despite the success of this study, in a following study [73] on the effect of the flux gap on the dynamic resistance, Jiang notes that while the dynamic resistance effect matches the observed internal resistance, the origin of the open circuit voltage still remained unclear.

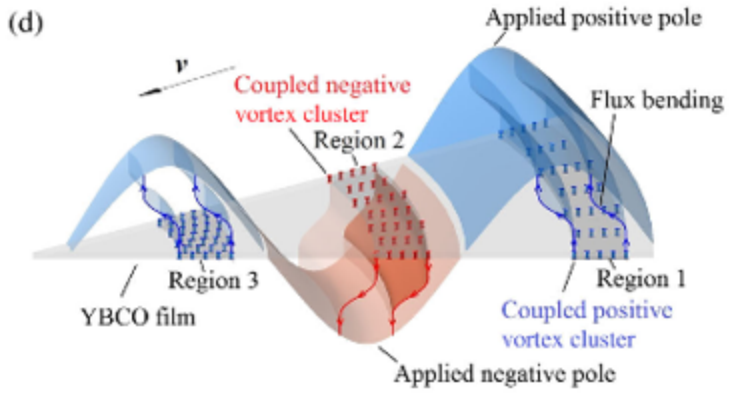

Figure 2-14: fig. 2 (d) reproduced from Wang [67], depicting the proposed 'Macroscopic flux coupling' mechanism for a radially travelling cylindrical magnetic wave.

A further confusion related to the language of flux pumping was the idea that the load coil was in some way part of the physical process of pumping. To dispel this, Bumby [74] operated an HTS dynamo in open circuit, measuring the generated voltages. Bumby found that even in open circuit, the HTS dynamo generates a dc voltage, which would indeed ramp a coil if connected. This was considered anomalous as the topology of the HTS dynamo should preclude a dc component to the *emf*. This work further showed that the open circuit voltage was linearly proportional to frequency f, and sensitive to the flux gap g between the magnet and stator.

The next step in characterising the device was to replace the coils with a power supply so that the full I-V characteristic could be mapped [70], fig. 2-13. This work quickly confirmed that the internal resistance is linear over the range of operation where $I < I_c$, stating that in the sub critical regime that the voltage is due to the interaction of shielding currents and the transport current, but once the current is higher than I_c the behaviour is dominated by the flux flow characteristic of the wire, becoming frequency independent (not shown in fig. 2-13).

2.4.2 Magnetic coupling

At this point, two points of view have formed, one that HTS dynamos should be viewed as general voltage-current sources, and another that flux transfer is still the

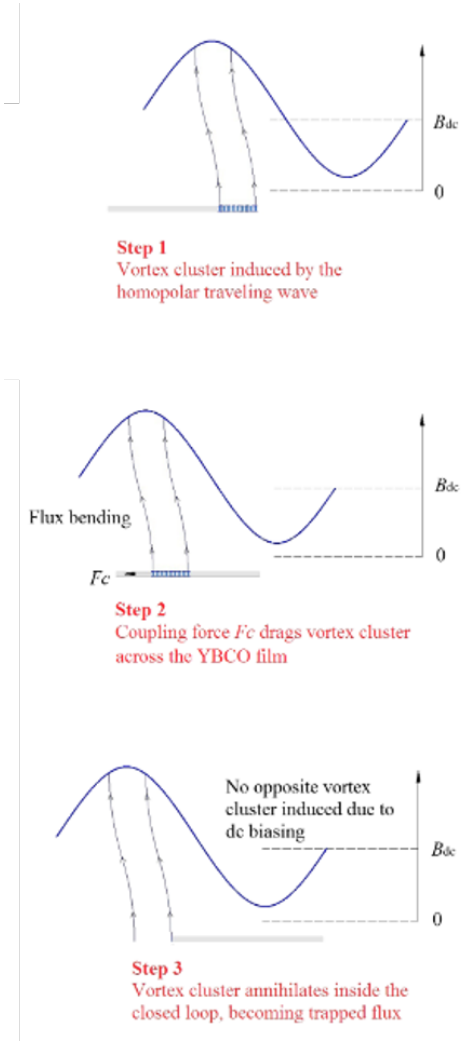

Figure 2-15: fig. 4 (a')-(b') reproduced from Wang [67], Showing the proposed role of a dc bias field to the motion of 'coupled' vortices.

best way to understand these devices. In an attempt to capture the transfer of magnetic flux Wang [75] constructed a circularly symmetric travelling wave pump in order to magnetise HTS wafers. Using this device, Wang claims to detect [76] the magnetic field traversing through the superconducting wafer, using hall probes. As a set of observations these works are reasonable, however the geometry makes them distinct from the dynamo case where, by rotational symmetry, no notion of azimuthal voltage is defined, let alone generated.

Of more concern, is Wang's 2018 paper [67] which claims a new phenomenon of macroscopic flux coupling, depicted in fig. 2-14, akin to the microscopic form described by Giaever [77] and Clem [78]. This paper highlights the serious dangers, ironically already pointed out by Giaever, of using flux flow phenomenology too heavily. Fig. 2-15 shows that when the principle of 'macroscopic coupling' is combined with a dc bias field, the oscillating field drives vortices in a single direction, and no corresponding antivortices on the other half of the cycle. Wang's work includes finite element simulations in the H-formulation. It is claimed that these simulations agree with the experimental data presented as well as the phenomenology offered in fig. 2-15. However, the simulations use a constant value for J_c and therefore the simulations themselves can only be dependent on the time derivative of B and not its dc value. As we will explore next, H-formulation does not encode or imply any new physics, such as flux coupling. Fortunately, as of this writing, this point of view has not gained any widespread traction.

2.4.3 The anomalous dc voltage

Finally, the point of view that would ultimately prevail was hypothesised by Bumby [74] and proposed that the non-linear resistivity of the HTS material gave rise to an auto-rectification effect as over-critical currents circulated in the HTS tape. It is clear throughout the literature that the point of contention is the generation of a dc voltage. Bumby points out that because the dynamics of the device are linear with rotational frequency, the data permits normalisation by frequency, fig. 2-16 (a). Furthermore, the dynamics of the device can be captured in *emf* free waveforms —

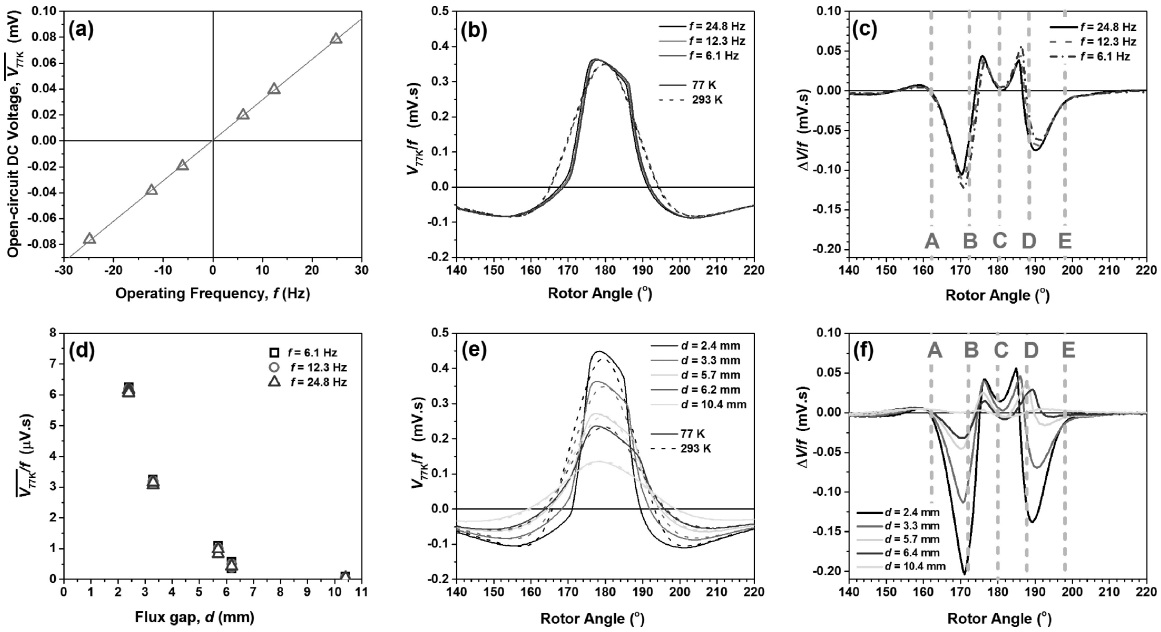

Figure 2-16: (a) Measured open-circuit DC voltage, $\overline{V_{77K}}$ as a function of operating frequency (negative frequency indicates reverse motion of rotor). (b) Frequency-normalised output voltage, V_{77K}/f, versus rotor angle, θ, obtained at three different operating frequencies at a flux gap, $d = 3.3$ mm. (c) Frequency-normalised voltage difference, $\Delta V/f$, versus rotor angle, θ, for three different operating frequencies at a flux gap $d = 3.3$ mm. (d) Frequency-normalised DC voltage, $\overline{V_{77K}}/f$, obtained at different values of flux gap d at three different frequencies (in both forwards and reverse direction). (e) Frequency-normalised output voltage, V_{77K}/f, for different flux gaps at $f = 12.3$ Hz. (f) Frequency-normalised voltage difference, $\Delta V/f$ versus rotor angle, θ, at five different flux gaps at $f = 12.3$Hz. Reproduced from [74].

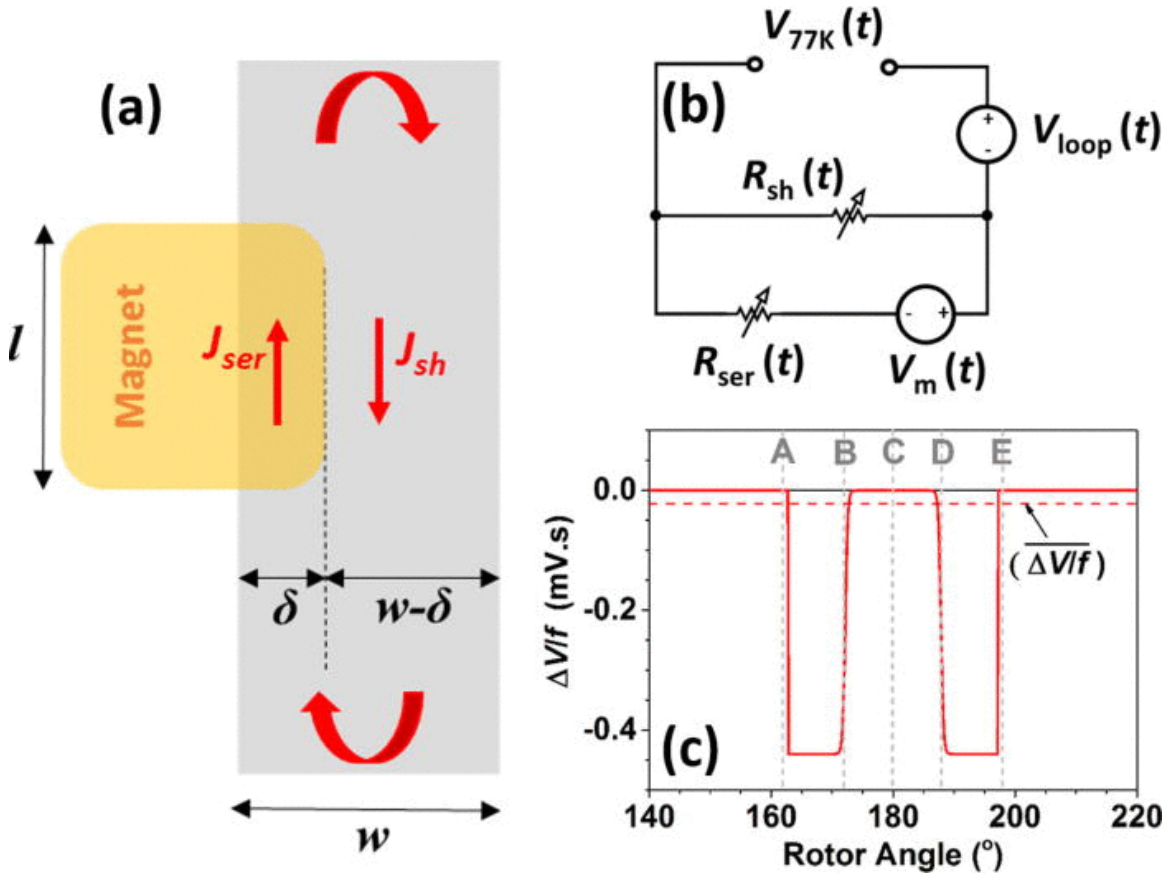

Figure 2-17: "(a) Schematic diagram illustrating circulating eddy currents in the HTS coated conductor wire as the rotor magnet passes over the stator. (b) Equivalent circuit which describes the effect of shunt leakage current path due to the circulating current. (c) Plot of Equation (7) for an idealized 10 mm × 10 mm square magnet operating at a flux gap of 1.5 mm, with $B_\perp = 0.2$ T and $n = 23$. Reproduced from [74].

fig. 2-16 (b-c), (d-f) — which show that the generative portion of the cycle occurs as the magnet enters (positions A → B) and exits (positions D → E) the tape.

Bumby proposed a simple model to capture the dynamics of local eddy currents in the HTS tape, as they are induced by the transit of the magnet. This model, shown in fig. 2-17, posits that the dc voltage occurs according [74, (7)]:

$$\begin{aligned}\Delta V &= V_{77\mathrm{K}}(t) - V_{300\mathrm{K}}(t) \\ &\approx V_{77\mathrm{K}}(t) - [V_{\mathrm{loop}}(t) - V_{\mathrm{m}}(t)] = \frac{-V_{\mathrm{m}}}{1 + \frac{R_{\mathrm{sh}}(t)}{R_{ser}(t)}} \approx \frac{V_{\mathrm{m}}(\theta)}{1 + \left(\frac{\delta(\theta)}{w - \delta(\theta)}\right)^n},\end{aligned} \tag{2.4}$$

Where, ΔV is the difference between the voltages measured in the superconducting, $V_{77\mathrm{K}}$, and normal, $V_{300\mathrm{K}}$, states; and the remaining parameters are drawn from fig. 2-17. The changing resistivity, R_{sh} and R_{ser}, experienced by the eddy currents flowing in the direction along the tape is caused by the changing size of the eddy current paths δ.

The most notable issue with the model proposed by Bumby is that it seeks to show that the non-linearity of the resistivity n drives the emergence of the dc component, fig. 2-17 (c). However, eq. 2.4 implies that the dc value of this wave form is independent of n-value[6]:

$$\partial_n V_{\mathrm{dc}} = \partial_n \int_0^{360} \frac{V_{\mathrm{m}}(\theta)}{1 + \left(\frac{\delta(\theta)}{w - \delta(\theta)}\right)^n} d\theta \approx 0. \tag{2.5}$$

This would imply that a copper stator should also exhibit a dc voltage, which is obviously not the case. This leaves two options as to why the formula given in [74, (7)] has a dc component: one, the wave form simply inherits a dc bias from approximations in the form of V_{m}; or two, it is unreasonable to assume that the eddy currents are constrained to the proposed paths over the range of n-values. In either case, the need for an explicit numerical model is clear.

2.5 H-formulation finite element modelling

While excellent experimental progress has been made for both NI coils and HTS flux pumps, the inadequacies in existing modelling capabilities call for a clearer theoretical frameworks to understand each device. For both NI coils and HTS dynamos, there are underlying questions about both the validity and clarity of proposed circuit models. Specifically for the dynamos, the phenomenology of flux transfer fails to translate into calculable predictions. However, for both devices, Maxwell's laws should always provide a complete classical framework in which to build qualitative understanding. While the particulars of defining each problem with respect to Maxwell's laws will be

[6]This is a somewhat surprising and specific property of this type of function.

described in the appropriate chapters, the issue of solving the equations themselves is not trivial. Where undergraduate courses focus on teaching the qualitative behaviours of these laws by exploring analytical solutions to simple problems, the majority of interesting problems do not submit to simple analytical expression. Hence, numerical methods are necessary.

The following is an exposition of the formal steps necessary to justify the use of the so called "H-formulation". However, as H-formulation solvers are available commercially, we will omit details of the explict implementation.

2.5.1 Numerical modelling

Several methods exist for numerically solving Maxwell's equations, which in the context of superconductivity are summarised well by Campbell [79]. Of the available techniques, I will focus on Finite element modelling (FEM), which solves Maxwell's equations in their differential form. All methods of numerical modelling face the same underlying challenge, to convert from continuous functions and fields, defined over the real numbers $\mathbb{R}^{3+1}$, to some discrete set of numbers $\mathbb{S}^{3+1}$, where $S = x_1, x_2, ...x_n$, that can actually be represented in computer memory. In the case of FEM, "weak formulation" is used to change how the notion of solution is defined, and reduce the problem to a set like $\mathbb{S}$.

Weak formulation

From an abstract point of view, the first problem with defining solutions to a system of partial differential equations (PDE) is that the solutions are themselves abstract functions that map one space of objects to another. While we may represent a given function by plotting, this is not the function itself, only a representation. The formal way to deal with this issues is to recognise that the functions are abstractly vectors in a Banach space (complete normed vector space) U. That is:

$$\mathbf{A}u = f, \tag{2.6}$$

where $u \in U$, $\mathbf{A} : U \to U'$, U' is the duel of U, and $f \in U'$. From here we can define the notion that u is a solution of eq. 2.6 if $\mathbf{A}u$, as a function, acts in the same way as f (equality between functions). This test of the solution can be defined by seeing how the functions act with respect to an inner product, as so:

$$\langle \mathbf{A}u, v \rangle = \langle f, v \rangle \quad \text{for} \quad \forall v \in U, \tag{2.7}$$

where $\langle \cdot, \cdot \rangle$ is the inner product between U and U'. As the result of an inner product is some scalar value, we may raise the notion equality between the scalars in eq. 2.7 to define the equality in eq. 2.6. Although we maybe able to construct some proof that eq. 2.7 is true for some simple problems, we are faced with harder problems where this is still not possible, and we can not test our solution u against the infinite number of available $v \in U$.

To truncate the process of evaluating a statement such as eq. 2.7, the weak formulation is simply a truncation of the test vectors v that we use to run the test such that:

$$\mathbf{A}u = f \quad \text{iff} \quad \langle \mathbf{A}u, v \rangle = \langle f, v \rangle \quad \text{for} \quad \forall v \in U_{\mathrm{t}}, \tag{2.8}$$

where U_{t} is a finite subset of U. Thus the problem is solved, and we can test potential solutions u against a finite number of vectors/functions v. Of course, we must chose the test functions such that we believe the solution is representative of the original question.

Formulation

Weak formulation aside, to solve a given set of PDEs we may still have choices in how to pose the problem. The most familiar of these kinds of choices is the choice to use potentials to express the solutions, such as $\vec{A}$ and V which is commonly called A-formulation. For H-formulation [80, 81] we wish to express the solutions of our abstract problem u as being the functions of the auxiliary field $\vec{H}$. Other than our

geometry, the problem is then defined by our constitutive relationship:

$$\vec{E} = \rho(\vec{J})\vec{J}, \tag{2.9}$$

and Maxwell's laws. Of these, the two laws that we will consider are Faraday's law:

$$\nabla \times \vec{E} = \mu_0 \partial_t(\vec{H}), \tag{2.10}$$

and Ampere's law for slow fields:

$$\nabla \times \vec{H} = \vec{J}. \tag{2.11}$$

In H-formulation eq. 2.11 is essentially taken to define our notion of $\vec{J}$. In this sense, the sub-problem of solving eq. 2.11 is solved in what would be called, the "strong formulation". This choice allows us to combine eqs. 2.9, 2.10, and 2.11:

$$\nabla \times (\rho(\nabla \times \vec{H})\nabla \times \vec{H}) - \mu_0 \partial_t \vec{H} = 0, \tag{2.12}$$

which finally expresses our problem as some operator acting on our solution $\vec{H}$, where again, equality is defined by the weak formulation of the problem. Note that the position of the $-\mu_0 \partial_t \vec{H}$ term depends on how time discretisation should be handled.

Linearisation

Even with the problem posed in weak formulation, it still cannot be solved by a simple computer due to the nonlinearity in $\rho(J)$. Essentially, we must also transform eq. 2.12 into a linear equation that can be solved using the techniques of linear algebra. This is done using Newton's method, which treats eq. 2.9 iteratively:

$$\vec{E_i} = \rho(\vec{J}_{i-1})\vec{J_i}, \tag{2.13}$$

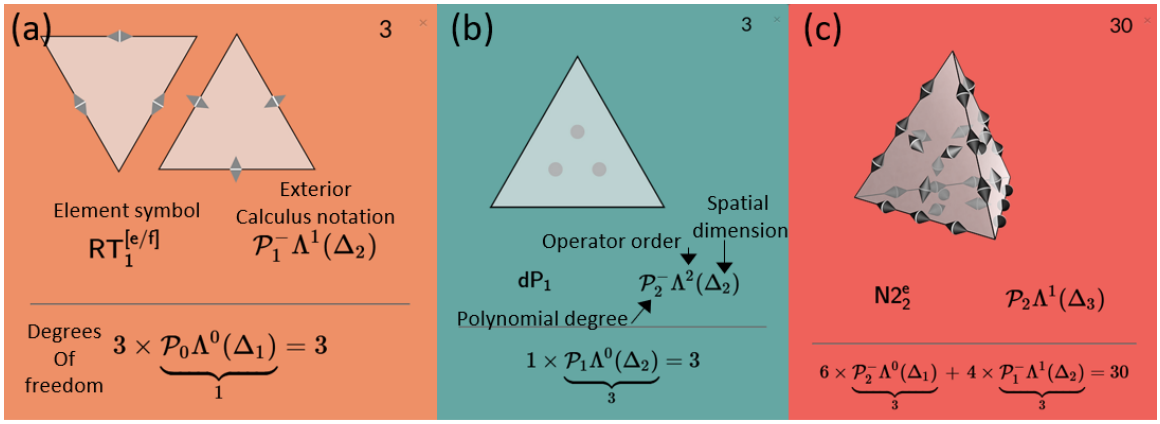

Figure 2-18: Depiction of various finite elements reproduced from Arnold [82].(a) Lagrange elements in two dimensions, H-formulation assigns the tangential variables to the tangential component of the Auxiliary field $\vec{H}$. (b) a 2$^{\text{nd}}$ order (quadratic) 2D element discretising the 2$^{\text{nd}}$ order derivative operator (the Laplacian ∇^2), typically the default in A-formulation. (c) Example of a second order curl element in 3D, appropriate for H-formulation, showing the large increase in degrees of freedom per element.

Where i is the iteration of the non-linear solver. For any given iteration, the whole problem, eq. 2.12, now appears linear. We then allow the solver to iterate until:

$$\nabla \times \vec{H}_i - \nabla \times \vec{H}_{i-1} < \epsilon, \tag{2.14}$$

where ϵ is some small numerical tolerance.

Finite elements

With the notion of weak formulation defined, and the problem posed as a linear operator acting on a solution vector, we may chose the particular set of test functions used. Some examples of finite elements which discretise the spatial domain of the problem are given in fig. 2-18. A full mathematical picture of the finite elements as a topic of their own can be found in [82]. These finite elements define the polynomial test functions, v, of degree r, that make up our test space U_{t}, and approximate the behaviour of the solution over a given element. To increase the resolution of the model we may chose smaller, and therefore more, elements; or we may increase the order of the polynomial functions. For commercial H-formulation solvers the discretisation of

the time domain is handled dynamically, but in principle this could be encoded into the finite element process itself.

It can be shown that the constructions so far enable the transformation of our problem into the domain of linear algebra. In this context, the operator A takes the form of a matrix and our solution a simple vector. Finally, the problem has been reduced to solving the system of linear equations:

$$\mathbf{A}u(t_i) = u(t_{i-1}), \tag{2.15}$$

where, A is our operator expressed as a matrix, and $u(t_i)$ the solution being solved for, and $u(t_{i-1})$ is the previous time step.

Finally, $u(t_i)$ can be found by inverting the operator A:

$$u(t_i) = \mathbf{A^{-1}}u(t_{i-1}), \tag{2.16}$$

and hence the solution can be found by a computer which is capable of inverting the operator. As A is a linear operator, expressible as a matrix, the solver can operate by inverting the matrix to find the appropriate A^{-1}. Hence the problem can now be solved by a computer!

2.5.2 Why H-formulation

As discussed previously, superconducting material is best described in FEM by the power law eq. 2.3, which is well justified by Elliot [83] and Morandi [84]. Unfortunately, the more conventional A-formulation has very poor convergence properties when using eq. 2.3. In A-formulation, the current is defined as a function of the electric field, which requires a definition of a conductivity σ, however eq. 2.3 would give an infinite conductivity for very low currents. More importantly, small variations of under-critical current $J < J_c$ result in huge, but meaningless variations of the conductivity. The advantage of the H-formulation is that the electric field is defined with respect to the current, and hence it uses resistivities. These issues are explored

very well in [85], including the situation where both formulations must be used at the same time.

Other than the fact that H-formulation should work, there is a very large literature of its successful application to problems in HTS machines modelling. Overall, the H-formulation has been used in studying topics such as: ac loss [86], dynamic resistance [87], pulse magnetisation of bulks [88], demagnetisation of bulks [89], magnetic levitation [90], and many more. A modern review of such H-formulation applications can be found in [91]. Hence, its use here is well justified.

Chapter 3

Methods

Foreword

This chapter covers some of the basic methods for how modelling and experimental work presented in this thesis was undertaken. However, aspects of the methods that are specific to each chapter's implementation, or are key to physical understanding of that chapter will be presented in those chapters respectively. Hence, the content here, while potentially necessary to recreate the results, is not critical or informative to understanding those results. This chapter is targeted at someone just starting their PhD in applied superconductivity. If you think you find value here, please continue, however, nothing in this chapter will be required to understand the results to be presented in the chapters to come. To that end, the rest of the thesis will maintain a style that does not expect knowledge from this chapter.

3.1 Subtle aspects of modelling

3.1.1 Weak constraints and contributions

Learning to use software like COMSOL Multiphysics is largely an exercises in intuition as a physicist or engineer. Most aspects are presented by the software in a way that represents the physics involved rather than the mathematics or machinery of the

underlying model. However, one example where this falls down is the notion of a weak constraint, which are presented in their pure mathematical form. This is because the whole physics interface is, in fact, an example of weak constraints and contributions that have been specified in such a way as to represent an aspect of the physics, for example Faraday's law.

The weak constraints interface is a means to define non-standard physics. This is often necessary where we want to drive a model using an external rule, without worrying about why that rule is appropriate in reality. It is also the case when we would like to 'play a trick' that would represent the necessary aspects of a system in a way so simple that it could not be physically realised. The models in this thesis use these concepts repeatedly, but the specifics will be covered in this chapter imminently, see secs. 3.1.6 and 3.1.4.

So what is a weak constraint? If we think of our model in terms of a Lagrangian, a weak constraint or contribution is a contribution to that Lagrangian that we can simply add. The term 'weak' refers to the addition of these contributions at the level of the weak formulation, see sec. 2.5.1. Where we keep in mind that the whole Lagrangian is solved in the weak formulation with respect to the function basis provided by the finite elements.

As a modeller, one issue that made me feel uneasy about these 'weak contributions' was the notion that I already had a model, with fully defined physics that had a solution; in what way was I free to just add extra contributions? We often think about models in reference to their geometric boundary conditions, where an aspect of the solution is defined externally. In some sense, weak contributions are the same, except that they can also be applied to the interior aspects of the solution. And indeed, by adding them, we are expanding the physics from the one that we started with. Physical models are typically riddled with such choices, some are given explict names, and some are not, and many come in the form of constitutive relationships. The simplest example in electromagnetism of a weak contribution that is not actually defined by Maxwell's laws is the addition of Ohm's law. Ohm's law is an additional statement that there should be an electric field aligned with and proportional to a

given current density and has the immediate interpretation that the current is doing physical work. We are taught that this work is thermal, the currents discharge energy converting it to heat. But heat is not a concept in electromagnetism itself, and hence ohm's law should be seen as an extension. In a resistor electrons are subject to an additional force:

$$F_{\text{electron}} = F_{\text{Lorentz}} + F_{\text{Drude}} = 0, \tag{3.1}$$

where F_{Lorentz} is the force predicted by Lorentz, F_{Drude} is the force due to stochastic/quantum scattering, and the equation must sum to zero for electrons flowing evenly.

Ohm's law is obviously so pervasive as to be given explicit status in the modelling of electromagnetic systems. However, while pervasive, it is not special, and the need to make other similar physical couplings or extensions is almost always necessary for interesting problems. Another example, would be a model of a dc rotor spinning in the moving field generated by a stator in a electric motor/generator. Ultimately, the rotor experiences a torque as it rotates, and so must be doing or receiving work. Again, this work is mechanical and not an explicit feature of Maxwell's electromagnetism by itself, thereby requiring additional physics.

Figure 3-1 illustrates that while a given Lagrangian may have global extrema over some functional space, the solution to the constrained problem can be seen as the projection of that Lagrangian onto the hypersurface (a curve in fig. 3-1) defined by that constraint. In physics speak, adding 'weak' contributions or constraints extends the physics by adding more requirements on the solutions defined by the original Lagrangian. And as modellers and engineers we have the right to do so in order to represent the systems that we are interested in.

3.1.2 Non-standard axisymmetric H-formulation

Chapter 4 introduces a novel axisymmetric model of the NI coil. The specific innovation of using rotated anisotropic resistivities will be explained in that chapter. However, one subtlety, that is completely physical but entirely non-standard, is that

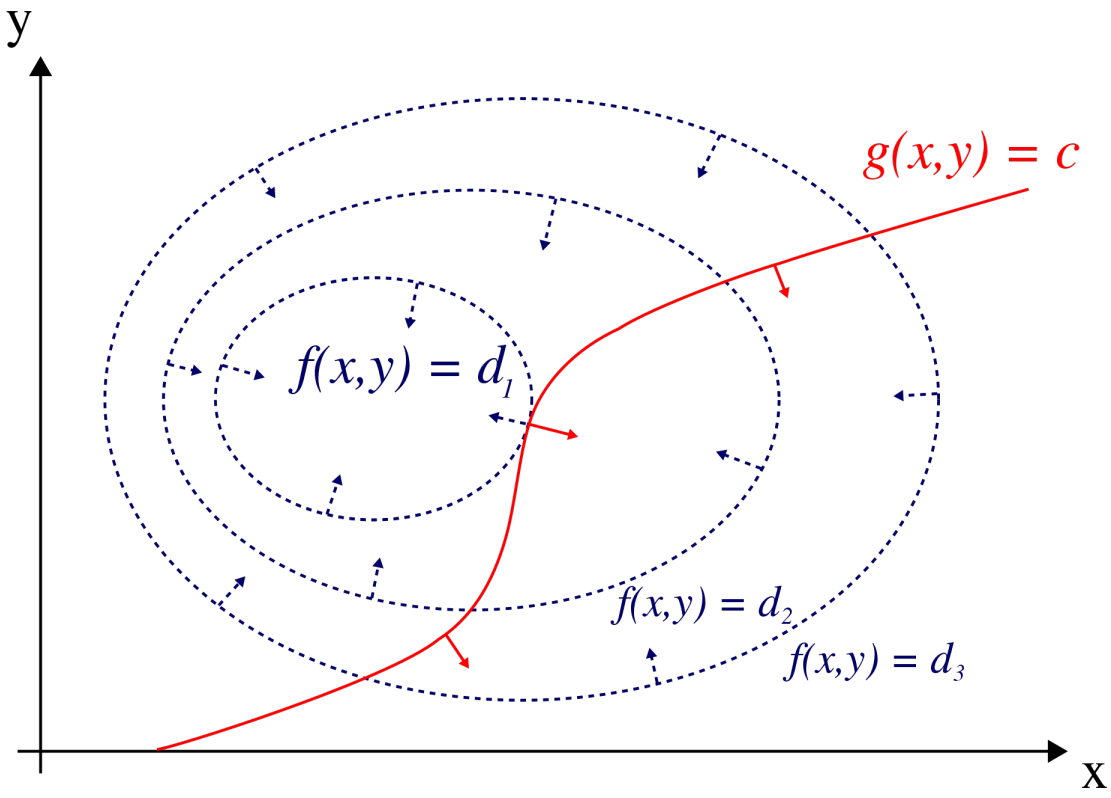

Figure 3-1: A function $f(x, y)$ may have a clear maxima some where within level set $f(x, y) = d_1$, however, the real problem may be defined by the projection of $f(x, y)$ onto the constraint $g(x, y) = d$, where the constrained maxima falls on the tangent between $f(x, y) = d_1$ and $g(x, y) = d$. In analogy, $f(x, y)$ may be Maxwell's laws, and $g(x, y) = d$ may be Ohm's law or similar.

the axisymmetric model solves for all 3 of the components of $\vec{H}$. Typical axisymmetric models of magnets, superconducting or otherwise, are only concerned with the in-plane magnetic field H_{r} and H_{z} and the current that creates it J_{ϕ}. However, to capture the turn-to-turn currents in the NI coil, we want to capture those currents that flow in-plane, J_{r} and J_{z}, and hence we need to solve for the 3$^{\mathrm{rd}}$ component of the magnetic field H_{ϕ}.

Modelling this extra component, H_{ϕ}, is not an obvious choice, in part because what is normal practice is often confused with what is required or implied by the symmetry itself. And hence, to justify modelling H_{ϕ} we can examine the rules of axisymmetry from first principles. Axisymmetry is captured in the simple statement:

$$\partial_{\phi} = 0, \tag{3.2}$$

that all functions/fields/quantities that make up a solution must have zero ϕ derivatives. Hence functions should take the form:

$$F(r, z, \phi) \Rightarrow F(r, z). \tag{3.3}$$

This is a very different requirement to:

$$H_{\phi} = 0, \tag{3.4}$$

which is normal practice in axisymmetric modelling, but not required by said symmetry. Indeed, the normal practice is only the result of modellers, correctly, reducing their models to the functions of interest to them.

Figure 3-2 shows a cross section of the NI Coil model to be presented in ch. 4, where the coil and power supply are shown connected by normal conducting current bus. Figure 3-2 illustrates the above points by showing how H_{ϕ} is restricted to the region between the current leads running from the top and bottom of the coil. The contours of constant $H_{\phi} \times r$ give the lines of current flow, which can be seen passing through the magnet and the current leads. Note that the magnitude of the H_{ϕ} is

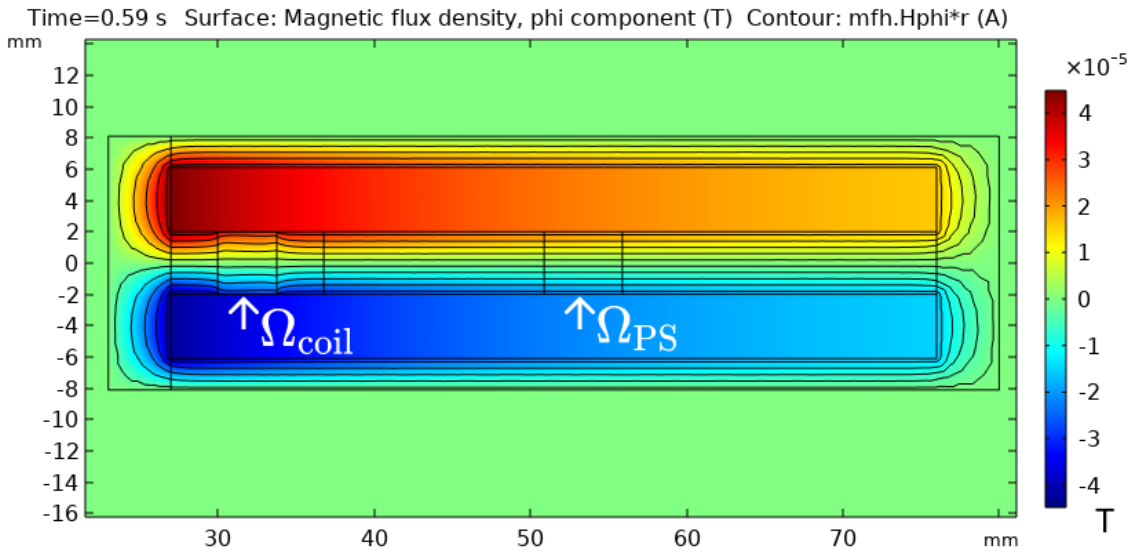

Figure 3-2: Intensity of the modelled H_ϕ component of the magnetic field. Contours depict radial and axial current flow through the normal conducting current bus. Cross sectional domain of the coil and power supply identified as Ω_{coil} and Ω_{PS} respectively.

minute, as the current leads can be thought of as a single turns toroidal field coil operating at I_{op}. Finally, fig. 3-2 shows the next subtlety, that where currents flow in-plane, they must circulate, $\nabla \cdot \vec{J} = 0$, and hence the model requires the current leads pictured.

3.1.3 A large and absurd current bus

While the current leads in fig. 3-2 look like simple domains in the 2D view of the model, they represent a very strange physical object. Figure 3-3 presents a revolved 3D view of the model where the current leads seen as large two large annuli. Such a current bus would be completely impractical in the real world but is the natural consequence of the axisymmetry and the need for current leads.

There are probably different ways of handling the current recirculation for the NI coil model. Some colleagues have instead had the current return in the air domain. In some sense, the choice of how to recirculate the current is to the taste of the modeller, and should be argued in context. Here, the use of such current leads ensures that the current can be returned in a similar way as would happen in experiment (through

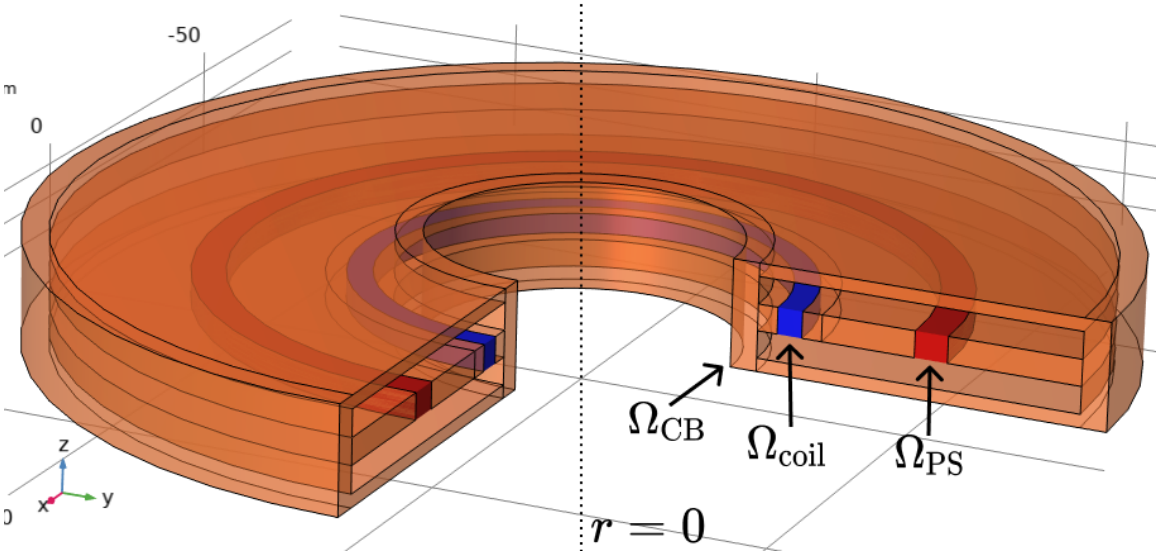

Figure 3-3: Revolved view of current carrying parts of the NI coil model. Copper shaded region, Ω_{CB}, is the current bus that connects the coil, Ωcoil, to the power supply, Ω_{PS}.

current leads) and that the process would not imply large electric field anywhere in the model. These judgements are not authoritative, and are simply examples of what I was worried about at the time. Several options were tried at the time, but optimising this aspect of the model is a perfect example of missing the point. Hence, we have these very large current rings. I suggest to the reader that you return the current in what ever way you see fit, and that you can justify to yourself and colleagues.

3.1.4 Modelling a current source

Another odd aspect to the NI coil model is the necessity to have a current source in the modelling domain. The aforementioned current leads form a circuit between the coil and the current source that serves as the electrical source. This additional domain is another example of how we need weak contributions to express the physics of a given system. Electromagnetism by itself does not define a natural notion of power source. Every battery ever put in a circuit diagram is an example of extending Maxwell's equations beyond simple electromagnetism.

Just as resistors are an extension, justified by noting that electrons do work in the form of heat, a current supply is simply a region where some additional mechanism

does work on the electrons. In the case of a battery it is the chemical potential that provides a force to move the electrons against the reversed electric field:

$$q\vec{E} = q\nabla\mu, \tag{3.5}$$

where $\nabla\mu$ is the gradient of the chemical potential of the electrons. Taking $\nabla\mu$ as given would define an idealized voltage source.

Rather than model a battery, an idealized current source is more appropriate. For this, COMSOL provides a node for adding an 'external' current density that obeys the equation in H-formulation:

$$\vec{E} = \rho\nabla \times \vec{H} \Rightarrow \vec{E} = \rho(\nabla \times \vec{H} - \vec{J}_e), \tag{3.6}$$

Where $\vec{J}_e$ is external defined where as $\nabla \times \vec{H}$ is solved for. One consequence of this implementation is that there are in fact 2 distinct currents that flow in the domain, $\vec{J} = \nabla \times \vec{H}$ and $\vec{J}_e$. This system is easier to understand in circuit context as:

$$V_{\text{source}} = R_{\text{int}}(I_{\text{op}} - I_{\text{ext}}) = Z_{\text{Load}}I_{\text{op}} = V_{\text{load}}, \tag{3.7}$$

where V_{source} and V_{load} are the source and load voltages, R_{int} is the internal resistance, I_{op} and I_{ext} are the operational and external currents respectively, and Z_{Load} is the load impedance. To implement an ideal current source we want $I_{\text{op}} = I_{\text{ext}}$, which is realised in the limit:

$$I_{\text{op}} \sim I_{\text{ext}} \quad \text{as} \quad \frac{\mathrm{R_{int}}}{\mathrm{Z_{load}}} \to \infty. \tag{3.8}$$

Hence, the resistivity in eq. 3.6 must be as large as possible:

$$\rho \to \rho_{\text{ins}}. \tag{3.9}$$

3.1.5 Insulation in H-formulation

Equation 3.9 introduces another subtlety in H-formulation, in that we cannot set the conductivity $\sigma = 0$.[1] We are then forced to chose a resistivity for the insulating parts of our models that is sufficiently high to be "effectively infinite". While the choice of insulator resistivity involves a trade-off it is unlikely to be an expensive or critical one. Essentially, the higher resistivity that is chosen, the closer we push the numerical solver to the singularity around $\sigma = 0$, where small variations in the solved current, $\nabla \times \vec{H}$, lead to huge variations in the electric field. The closer the model runs to this singularity, the shorter each time-step needs to be to converge the model. However, all we need to do is have ρ_{ins} be sufficiently high to suppress the spurious current densities flowing through said insulator. A rule of thumb is to chose $\rho_{\text{ins}} = 1\ \Omega \cdot \text{m}$, and then adjust for model speed or accuracy.

The insulator resistivity is not a huge issue in the upcoming models of this thesis, but it does put an upper limit on the voltages that can be handled in an H-formulation model. For example, a machine that actually requires some form of turn-to-turn insulation, i.e. a motor/generator stator would be difficult model in pure H-formulation due to the low resistivity of ρ_{int}. However, in such cases a mixed formulation is usually possible such as H-A or T-A.

3.1.6 Simulating a moving magnet

To solve the issue of a moving magnetic field in the H-formulation, as found in the HTS dynamo problem, I proposed a "current shell" method that represents the magnet Ω_M, see fig. 3-5, as a current density on the boundary of the rotor domain $\partial\Omega_{\text{R}}$, fig. 3-4. This is done by calculating the shielding currents J_s on $\partial\Omega_{\text{R}}$ that would completely contain the field from the magnet. The opposite shielding currents are then applied using a weak condition to the boundary $\partial\Omega_{\text{R}}$ in the full problem:

$$\nabla \times \vec{H} = -J_{\text{s}}(\theta_{\text{R}}(t)) \text{ on } \partial\Omega_{\text{R}} \tag{3.10}$$

[1] Superinsulators do in fact exist [92]. materials where $\sigma = 0$ in the same way that Superconductors exhibit $\rho = 0$.

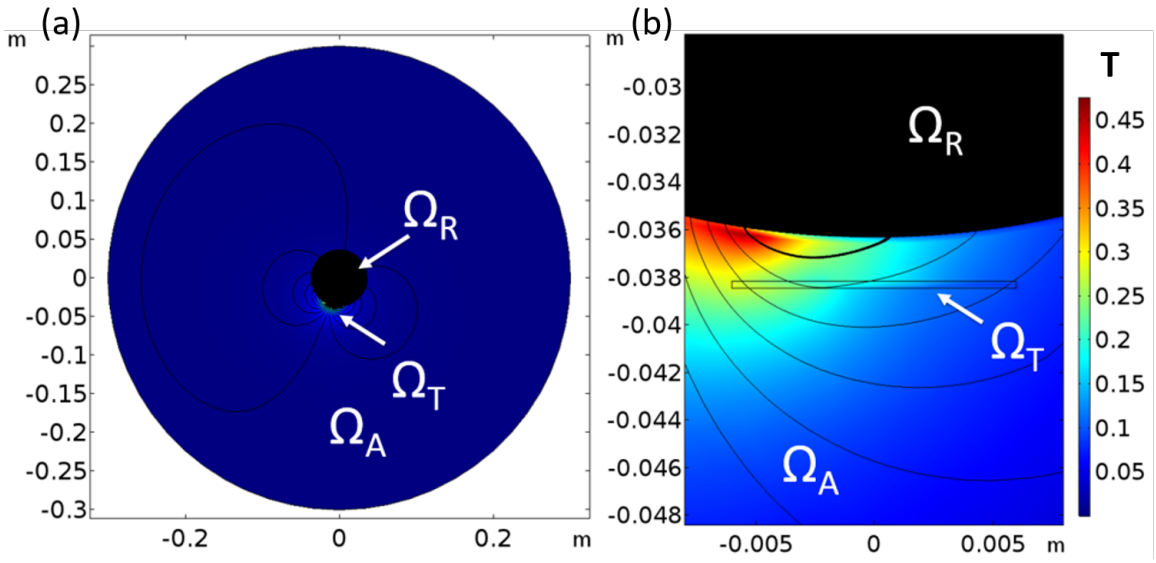

Figure 3-4: Snapshot of the numerical model at position **A** including the magnitude of the magnetic field $\vec{B}$. The field in domain Ω_R lies outside the defined boundary conditions and hence is not shown.(a) The total modelling domain, showing the rotor domain Ω_R, the air domain Ω_A, and the HTS domain Ω_T. (b) A magnified view of the superconducting tape domain, Ω_T.

where J_s is the shielding current density as a function of rotor angle. This reproduces the magnetic field in the domains outside of the rotor domain Ω_R. Critically this technique also allows the induced fields to pass into the rotor domain unimpeded by a Dirichlet boundary. If a bare Dirichlet boundary had been used to model the rotor field, by superposition that same boundary would have appeared as a perfect conductor to any induced currents and fields in the superconducting stator, something that is clearly not physical. Consequently the field in Ω_R, although modelled, is not physical, and is omitted from subsequent figures depicting the magnetic field in the dynamo.

3.2 Aspects of HTS dynamo experiments

It is natural when presenting experimental results that many extraneous details are omitted in service of clarity. While this drives the literature forward, it begins to build barriers-to-entry for others who wish to contribute to a topic. The following are a

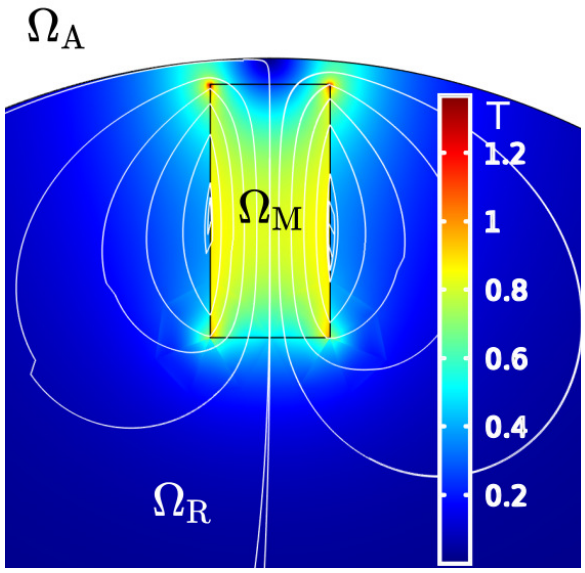

Figure 3-5: Shell current calculation model, showing the static solution for the magnetic field constrained to the rotor domain.

series of experimental considerations when building and characterising HTS dynamos. Experiments presented in this thesis were collected by others in the Robinson group, however, my own experience in improving experimental techniques, or navigating their flaws, are presented here. In theme for this chapter, these issues should not affect your understanding of such devices, but may well save you a lot of hardship in trying to replicate them. Further, some of these points can be translated to good experimental practice in many other systems.

3.2.1 Motors, loads, and overly complex control

The HTS dynamo is a simple concept that only requires a rotating magnetic field applied to an HTS stator. Practically however, the source of rotation can be a serious experimental concern. Some thought is necessary to characterise what kind of motion that we want. Just as an electrical source has its own internal impedance and control logic, so does a source of mechanical rotation. For HTS dynamos, we essentially want a motor that runs at constant speed, and can achieve that speed over a wide range of load conditions. In one case, we will operate the motor at room temperature, where the load will be dominated by the inertia of the rotor itself. However, once we cool

the experiment in a bath of nitrogen the dominant rotational load is provided by friction with the liquid nitrogen coolant.

It is very common in experimental systems to dramatically over design/specify components that are necessary, but are not under direct study themselves. This practice is not intrinsically bad, but can cause issues if not properly considered. In the case of an electric motor to drive the shaft of an HTS dynamo, two aspects of the original motor were over specified: one, the motor power; and two, the motor control algorithm. In this case, the motor power was approximately 10 times greater than required and did not cause issues. However, the motor control was significantly more complex than necessary, and had been designed for a completely different and extreme application.

The original motor was a 400W Omron R88M-K40030-S2 servo motor with feedback controller[2] and motor driver. This motor was chosen with the logic that such a servo motor would deliver excellent speed accuracy using simple PID control, adjusting to the wide range of load conditions expected. However the motor's control scheme was actually significantly more complex, which lead to highly unpredictable behaviour. Figure 3-6 depicts the simplest control mode for the Omron motor, including more than 21 separate control parameters, which could not be reduced to a simple PID like system.

Why did more advanced control not lead to better outcomes and system flexibility? Essentially, the Omron motor was not designed/or-marketed as a mechanical power deliver system, as needed for the HTS dynamo. Rather, the Omron R88M-K40030-S2 is an excellent linear motion driver used for repeatable process automation. That is to say the Omron's advanced control schemes are all designed to provided fast, accurate, precise, repeatable, and efficient motion where a single motion cycle includes predictable loads that can be tuned against. To pay this Omron servo its due respect, coupled with the correct high quality ball screw linear stage, the Omron R88M-K40030-S2 can achieve linear positional repeatability less than 1 μm. All of which is to say, the Omron R88M-K40030-S2 is not the appropriate motor to drive an HTS

[2]A slightly redundant statement as 'servo' refers to a motor that has feedback control.

6-2-4 Block Diagram for Speed Control Mode

The following block diagram is for speed control using an R88D-KN□□□-ECT-series Servo Drive.

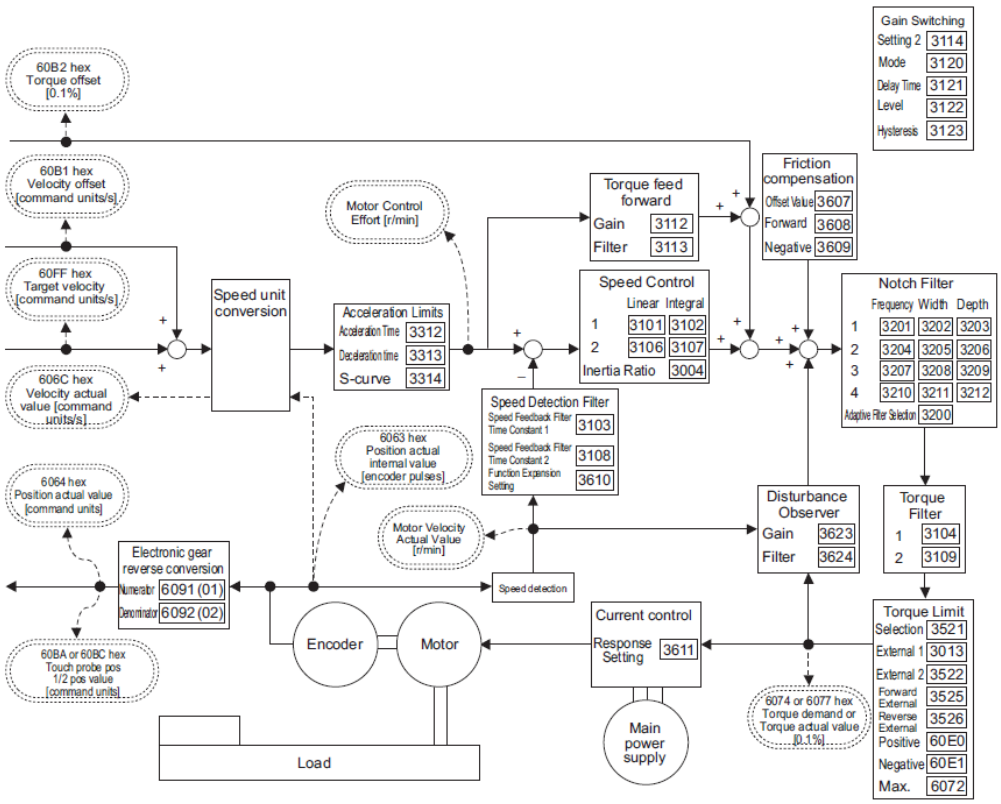

Note 1 Numbers within parentheses are sub-index numbers.

2 Numbers within boxes are hexadecimal index numbers.

3 The electronic gear function is not supported for unit version 2.0. For the Servo Drives with unit version 2.0, set the electronic gear ratio to 1.1.

Figure 3-6: Velocity control scheme for the Omron R88M-K series servo drives. Overly complicated for mechanical power transfer in an experimental setting. [93]

dynamo experiment.

Current dynamo experiments at Robinson Research Institute are now driven by a 700 W Maxon synchronous dc motor with simple PID speed control. A separate optical interrupt on the shaft is used to detect rotations and calculate speed, and speed control is scaled in software based on measured speed under different load conditions.

3.2.2 Cryogenic rotational power transfer

HTS dynamos are useful because they allow power to be transfered from a room temperature environment, into the cryogenic HTS circuit, with minimal heat leak. Even in experimental dynamos this is useful as it means that the motor can sit at room temperature, running reliably, and deliver power via a shaft that extends into the cold envelope. Designing rotor shafts is a basic and fundamental skill for mechanical engineers, but the added complexity of working in a cryogenic environment deserves extra attention. Some of the issues caused by cryogenics include: Shaft sensors unable to operate, shaft couplings loosening, and bearings slipping or crushing.

The first issue is that for a submerged cryogenic experiment, it may not be possible to install reliable sensors to monitor shaft behaviour. This can affect feedback control of the motor, timing issues for data collection, or even basic triggering for data acquisition. While not impossible to solve, many issues can make such shaft sensors unreliable costing time and invalidating data sets.

Data published by Bumby et.al. [74], and analysed in ch. 5 was captured using a dynamo that did not have such a shaft position sensor. Instead, peak detection of *emf* pick up was used to center each data set against rotor angle. While acceptable at the time, it became clear that higher resolution data would require a more robust angular position datum, that was acquired separately from the signal under study.

Optimally, we want to deploy a shaft position sensor as close to the rotor as possible, while remaining outside of the liquid nitrogen. Ideally, there will be no shaft couplings between the sensor and the rotor, except perhaps the coupling between the rotor and shaft themselves. Such joints or displacements will introduce backlash

or a load dependant position error. Like many engineering choices, some trade off is necessary, but can often be satisfactory if trade-offs are kept bellow justifiable margins.

The system that is currently utilised in the Robinson group relies on an optical interrupter plate that rotates through a LED-photodiode pair. This circuit, while not in nitrogen, is still subject to extremely cold vapour, and accidental mechanical stresses. Overall the sensor system, while integral to capturing high quality data, is one of the single largest contributors to experiment failure and data set rejection. A new more robust system should be developed, with special care paid to durability and ease of use (accident prevention).

Extreme cold does not just affect electronics, mechanical systems are also subject to issues. Any pairing of dissimilar materials can exhibit differing length contractions when cooled cryogenically, leading to stress, failure, fatigue, over tightening, or even paradoxical loosening of mechanical mates. For instance, one failure mode for the optical interrupt was caused by fasteners loosening, such that the mechanical connection between the shaft and interrupt disk changed from a clamping action provided by the set screw to a locking action of the set screw in the key hole. This mechanical change meant that a backlash was introduced between the shaft and the recorded position.

Loosening was also present in connections that were not directly exposed to liquid cryogen. Whether by conductive or convective cooling, the bottom-most shaft coupling, see fig. 3-7, would experience cooling and warming cycles from one experiment to the next. This aluminium coupling would tighten onto the steel rotor shaft due to the differential expansion of the two materials, only to loosen upon warming. The loosened lower shaft coupling, combined with the inappropriate servo control scheme of the Omron R88M-K40030-S2, see sec. 3.2.1, resulted in a dramatic shaft failure, where by the lack of torque transfer through the coupling, caused the Omron servo controller to unnecessarily jog the shaft backward and forward at a high rate. This jogging, which may have been superimposed on the targeted net rotation, caused the coupling to loosen further, and for the whole system to vibrate dangerously. Fortu-

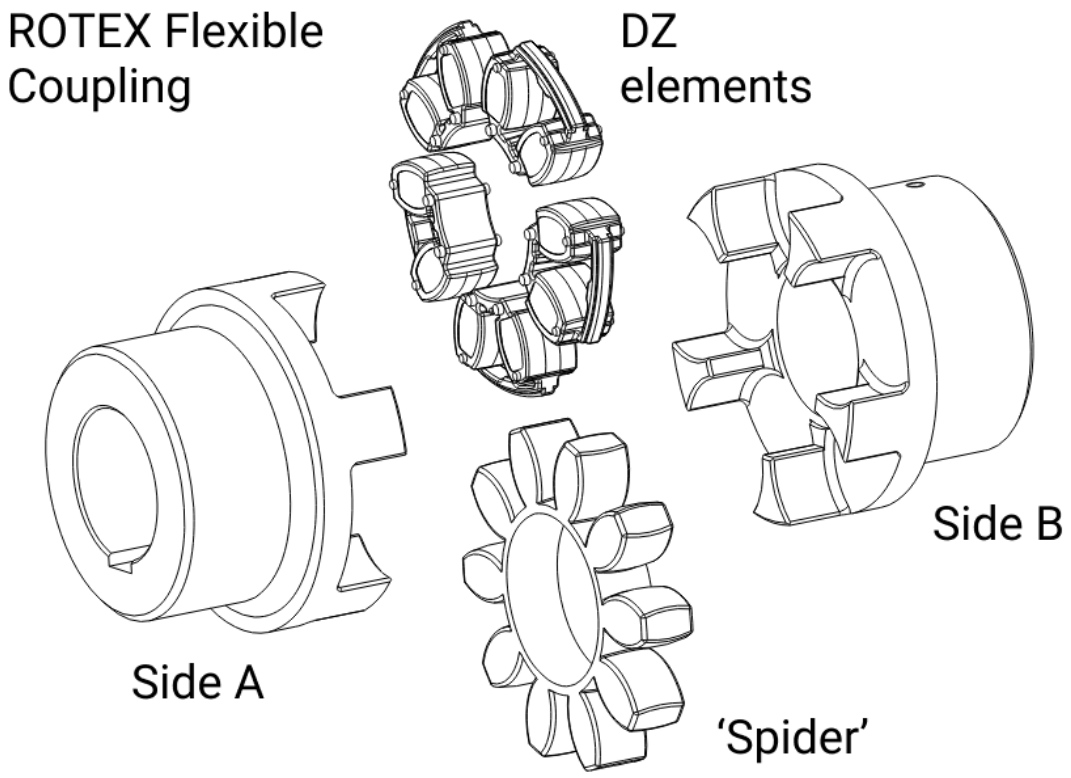

Figure 3-7: ROTEX 3 part flexible shaft coupling designed to take up small axial and angular misalignment. Improvement in a cryogenic context could easily be made by matching the material of each side of the coupling to the shaft being mated.

nately, this event happened at room temperature, under close supervision on the lab bench, during attempts to tune the Omron's control settings. The emergency stop was pressed, and the event firmly precipitated the move away from the Omron servo motor system.

Even simple systems, such as a motor, shaft, and rotor can have complex failure modes when operated in research environments. Section 3.2.1 covered changes to the motor to avoid the situation, but the loosening effect caused in the shaft coupling has only be addressed by procedural adaption, where by couplings are checked for tightness each run. This compromise is less than ideal for two important reasons. One, apparatus themselves should embody the lessons needed for them to function predictably, rather than rely on ad-hoc human procedures to insure their proper operation. Two, an experiment operator is right, by default, in not wanting to tamper with an experiment, run-to-run, where data sets are expected to be directly compared. These two issues express a high likelihood that such mistakes will be repeated until the apparatus itself is upgraded against this failure mode. Ironically, the simple 3 part flexible coupling used suggest an ideal solution, where by each side of the coupling is fashioned from the material onto which it is expected to clamp. This combined with appropriate choices of fasteners, will eliminate the issue, and improve experimental reliability and safety.

3.2.3 Simultaneous vs multiplexed data acquisition

Recording multiple signals at 'the same time' is a non trivial issue when designing an experiment. While there are many other branches of advanced physics where such issues are much more serious, The HTS dynamo results are affected by how measurement timing is handled. The major issue being the definition of what it means to say two values were sampled at 'the same time'.

Modern experimental physics is possible thanks to the ubiquity, resolution, and speed of voltage measurement technology. Almost all other quantities of interest to a modern Physicist or Engineer are converted by a 'sensor' into an electrical voltage or current, indeed this may even be a suitable definition of 'sensor' in modern usage.

Analogue voltages, which we would see on the needle of a voltmeter, are now digitised by Analogue-to-Digital Converters (ADCs), and then processed using modern digital technologies. Unfortunately, end-to-end, this process cannot be ignored when designing an experiment and, as always, many trade-offs exist.

In the case of the dynamo, the need to capture multiple signals at once necessitates the use of a multi-channel DAQ card. However, the cost of any given channel is dominated by the ADC, and hence cheaper multi-channel cards instead use multiplexers to link many acquisition channels to a single, shared ADC sequentially. On the surface level, this trade-off appears simply be one of time resolution, i.e. is the time that sequential readings take, τ_{sequ}, acceptable when considering the experimental definition of 'simultaneous' $\tau_{\text{sequ}} < \tau_{\text{simu}}$. However, the real issue is that multiplexing is not a perfect process and other artefacts can be introduced.

All of the HTS dynamo data published to date by the Robinson group was collected using a multiplexed NI9008 DAQ with sequential channel reads for multiple inputs. A feature of this data, that was never focused on, was a simple asymmetry in the measured dc voltage between clockwise and anticlockwise rotation of the HTS dynamo rotor. This apparent asymmetry was to form the focus of the later part of this thesis, but proved to be too difficult to conclude clearly[3]. When the original work was conceived, to investigate the rotational asymmetry of the HTS dynamo, the apparent size of the asymmetry was as high as a 15% difference between the two voltages, which certainly warranted an investigation.

Given the number of other mechanical symmetries that could be defined for any given real HTS dynamo, a complicated experimental set up was conceived, that I will not describe in detail here. However, a systematic investigation of the asymmetry revealed that the mechanical symmetries of the apparatus could not be matched to the different measured asymmetries. Eventually, it was discovered that the majority of the measured asymmetry was caused by cross-talk between the different channels as they were multiplexed to the DAQ's single ADC. In particular, the higher voltage

[3]To any current postgraduates reading this, not everything needs to make it into your thesis, and some things may never see the light of day, this is one of the major risks we take when we do research. It isn't even necessarily failure just a part of the process.

range of one of the input channels meant that even small residual charges in the Multiplexer/ADC bled into the much smaller signals of the HTS dynamo output.

The multiplexer cross-talk issue was incredibly difficult to discover for many reasons common in research programs. As research scientists and engineers we don't just come together to collaborate all at the same time, just like a multiplexer connects signals in sequence, a research program will often have several people working on a project sequentially, over short and long time periods. This is truly a form of collaboration as different people add, adapt, expand, and maintain not just apparatus, but data sets, know-how, hypothesis, speculations, wisdom, and all the other factors that form a body research. For instance, it is extremely common that the different skill sets needed for a project will be bought on sequentially. In the case of the data acquisition system, it was designed, conceived, run, and evolved, by the experimentalists before me, Drs. Chris Bumby, Rodney Badcock, Zhenan Jiang, Olly Pantoja, and Mr. Kent Hamilton. My contribution in this chain, was to target an apparent phenomenon, that required a sensitivity and attention to detail that finally rooted out a measurement issue that, while it existed, had not yet caused any issues in producing the findings previously desired.

The HTS dynamo asymmetry problem is concerned with a small effect on the dc voltage, about $\sim 5\%$, which is is itself a small effect on the total measured *emf*, again about $\sim 5\%$. In attempting to quantify the effect in a systematic way, I managed to greatly improve the quality of data coming from a Robinson group HTS dynamo. You will not see the results of that work in this thesis. Ultimately, that effort was embarked upon thinking we could stretch an existing system to measure an effect of a given size. However, in light that the real effect (bar other measurement issues) is at least $3\times$ smaller than initially expected, a fresh experimental effort, formulated and designed from scratch is warranted.

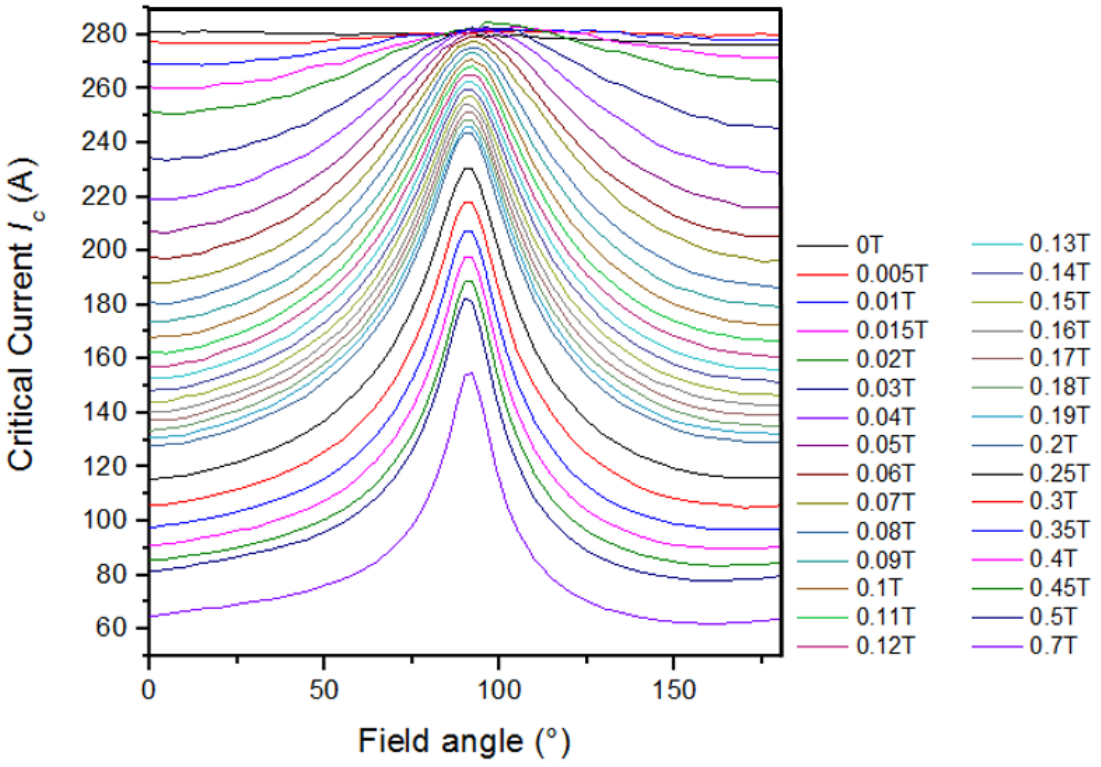

Figure 3-8: Experimental $I_c(B,\theta)$ data used in the H-formulation model. Data was measured at 77.5 K in magnetic fields up to 0.7 T from a short sample of Superpower SF12050CF wire. The $J_c(B,\theta)$ data is corrected for self-field using the technique presented in [94] and input into the model using a two-variable, direct interpolation [87]. Experimental data courtesy of Dr Stuart Wimbush.

3.3 Critical current to critical current density: $I_c(B,\theta) \rightarrow J_c(B,\theta)$

A recurring feature of the work presented in the following chapters is the necessity to model different types of REBCO tape. What makes one tape different to another is not a major concern of this work. Rather we want to represent the behaviour of the tape faithfully to aid comparison between models and experiment. It is therefore fortunate that this work was undertaken at Robinson Research Institute where a full $I_c(B,\theta)$ characterisation system is available, see [95]. Some of the data presented is available via the public HTS database, however some data sets are not, and were either held internally or measured specifically for this work. Overall, 3 types of superconductor are used in the subsequent models.

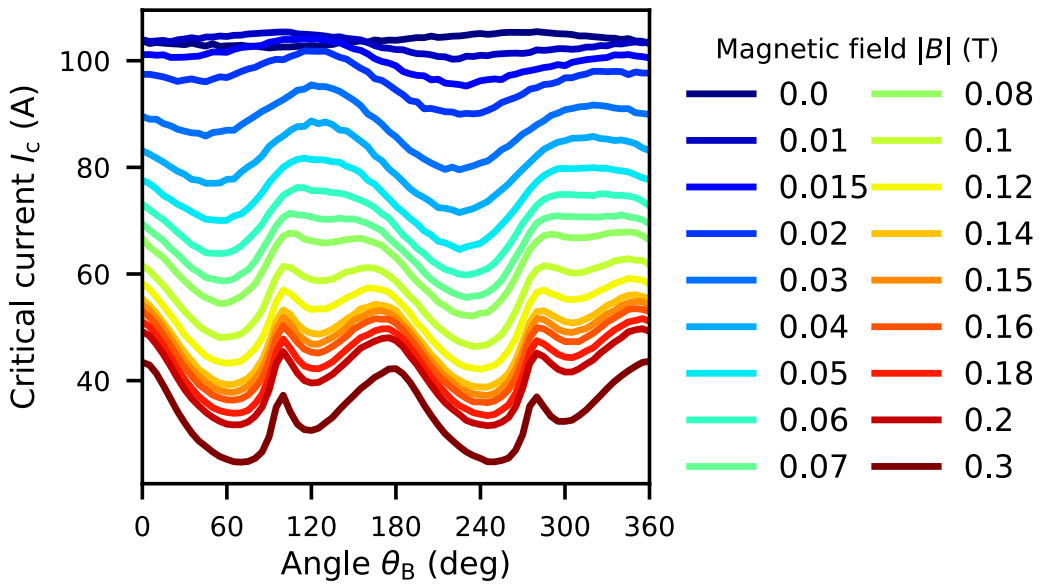

Figure 3-9: Measured, in-field $I_c(B,\theta)$ performance of 4 mm wide SuperPower SCS4050 AP superconductor at 77 K, I_c which is scaled to a 12 mm width as used in dynamo experiments.

Figure 3-8 shows the measured $I_c(B,\theta)$ for the first REBCO tape, SF12050CF, made by Superpower and used in original experiments presented in [74]. Like all 3 data sets, this data was collected using the technique and instruments described in [95], where θ is the angle of the applied field with respect to normal of the tape surface. The data in fig. 3-8 is used in ch. 5 to model the HTS dynamo. However, in order to do this the some assumptions are necessary to shift from measured $I_c(B,\theta)$ data to $J_c(B,\theta)$ to be used in the model.

For the SP SF12050CF it is assumed that wire behaviour is symmetric, by reflection along 0^o of applied field. This extends the data from the 180^o behaviour measured to the full 360^o necessary for the model. The next issue is how the self-field of the current carrying tape would suppress the measured value of I_c for a given local $J_c(B(x),\theta(x),x)$ behaviour. For this data set the inverse problem is solved by following the method of Zermeño et al. [94]. Zermeño's method solves the forward problem by modelling the $I_c(B,\theta)$ measurement process using a $J_c(B,\theta)$ function that is uniform across the width of the tape. Multiple models are run and the input $J_c(B,\theta)$ is modified until the modelled $I_c(B,\theta)$ matches the input experimental data. This

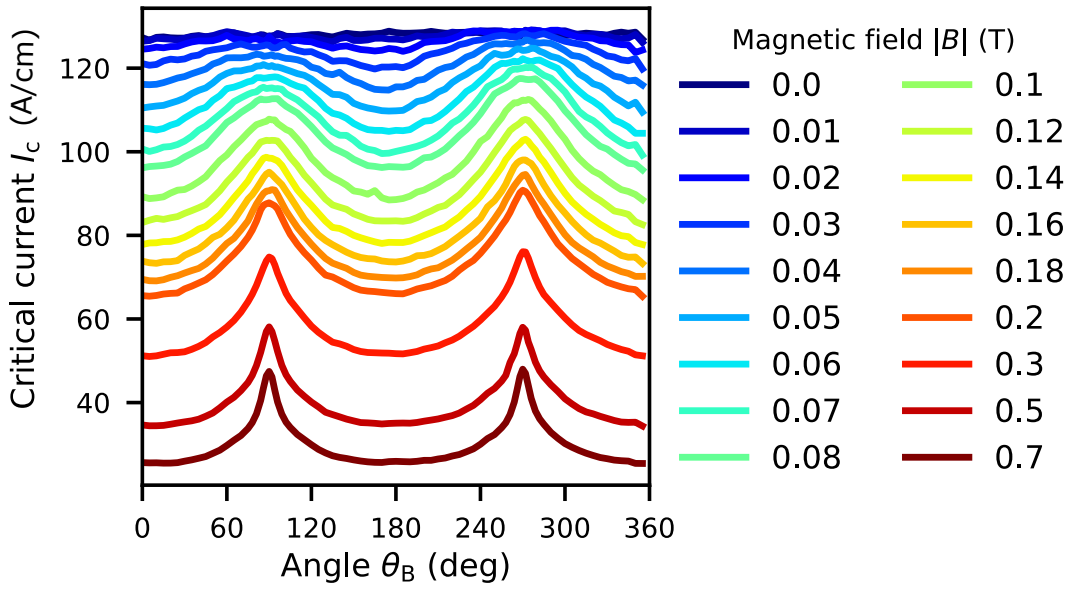

Figure 3-10: Measured, in-field $I_c(B, \theta)$ performance of 46 mm wide AMSC cable formulation superconductor at 83 K.

procedure then gives the $J_c(B, \theta)$ function that best matched.

The next $I_c(B, \theta)$ data set, shown in fig. 3-9 is for Superpower SCS4050AP tape, where AP stands for "Advanced Pinning". This tape has the same formulation, although a narrower width, as tape used in HTS dynamo experiments presented in [96]. This data is used in ch. 6 so that models best match [96] allowing for the most direct comparison. Other than being a different REBCO tape, the eventual $J_c(B, \theta)$ function differs from the first data set it two ways. Firstly, the $I_c(B, \theta)$ behaviour has been characterised for the full 360^o of rotation, meaning no assumption of symmetry is needed. Secondly, the utility of the Zermeño et al. was questioned, and ultimately a simpler scheme was chosen, defined simply as:

$$J_c(B, \theta) = \frac{I_c(B, \theta)}{wd}, \tag{3.11}$$

Where w is the width of the measured section of HTS tape and d is the thickness of the modelled HTS tape. As we will see in ch. 6, this simpler choice still reproduces the desired HTS dynamo physics with close agreement to experiment.

Lastly, ch. 7 investigates wider stators in much that same way as experiments

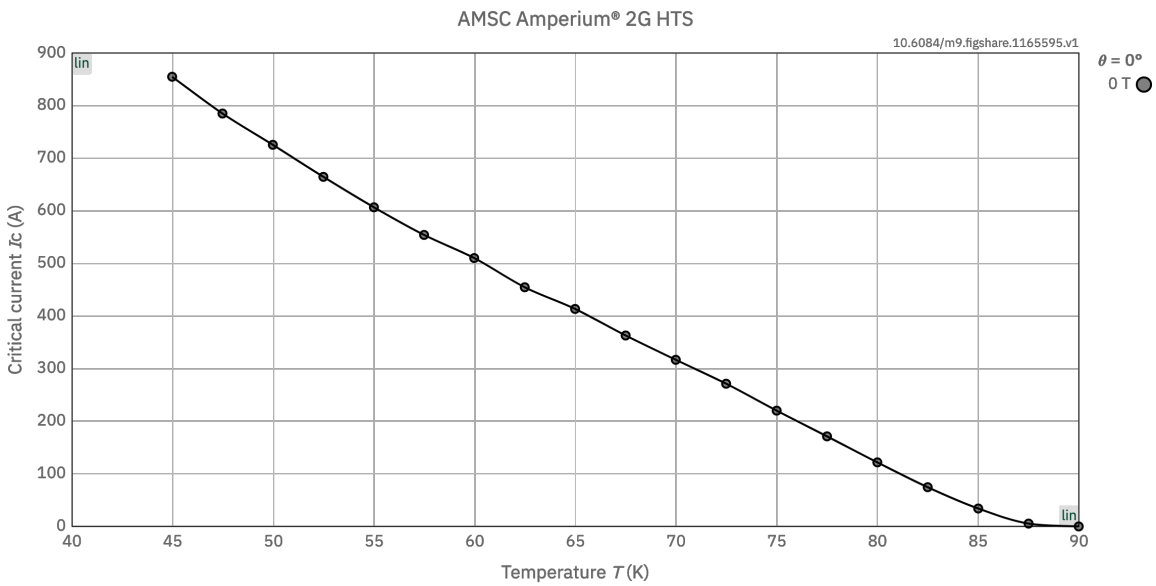

Figure 3-11: Critical current density I_c of AMSC Amperium© REBCO tape as a function of temperature. Retrieved from HTS wire database [95].

published in [97]. Figure 3-10 presents critical current per unit width for 46 mm wide AMSC 'cable formulation Amperium©' superconductor at 83 K. Again, 360 degrees of data are measured so no symmetries need be assumed to generate a $J_c(B, \theta)$ function. Again, eq. 3.11 is used to convert $I_c(B, \theta) \rightarrow J_c(B, \theta)$. Finally, the full data set used includes temperature dependence $I_c(B, \theta, T)$, with two main temperatures considered 83 K, as shown in fig. 3-10, and at 53 K. For models in ch. 7 the $J_c(B, \theta)$ at 77 K is is interpolated from the 83 K and 53 K data. This interpolation can be safely justified by inspecting fig. 3-11.

Chapter 4

Modelling no-insulation HTS coils

Foreword

The following chapter describes the application of H-formulation modelling to the problem of the NI coil, covered in sec. 2.2.1. Here, H-formulation is introduced in a relatively simple setting, where results require only straight forward analysis but still carry rich aspects of HTS physics. This chapter will therefore serve as a practical introduction to H-formulation modelling, and the kinds of results and analysis that are possible. This chapter is largely formed from material published in: Finite-element modelling of no-insulation HTS coils using rotated anisotropic resistivity *Supercond. Sci. Technol.* 33 08LT01 [98]. The model described here was then also extended in: Modelling Parallel-Connected, No-Insulation High-T_c Superconducting Magnets, *IEEE Trans. Appl. Supercond.*, vol. 31, no. 5, , Aug. 2021, Art no. 4602205 [99], which examines the effect of connecting the coils of a magnet in parallel. While [99] was motivated by my work on the use of HTS flux pumps as high current power supplies, it is omitted from this thesis for brevity.

4.1 Introduction

An insulated coil, operating below the break-down voltage of the insulation, can be analysed using very simple approximations. Firstly, that the conductivity of the

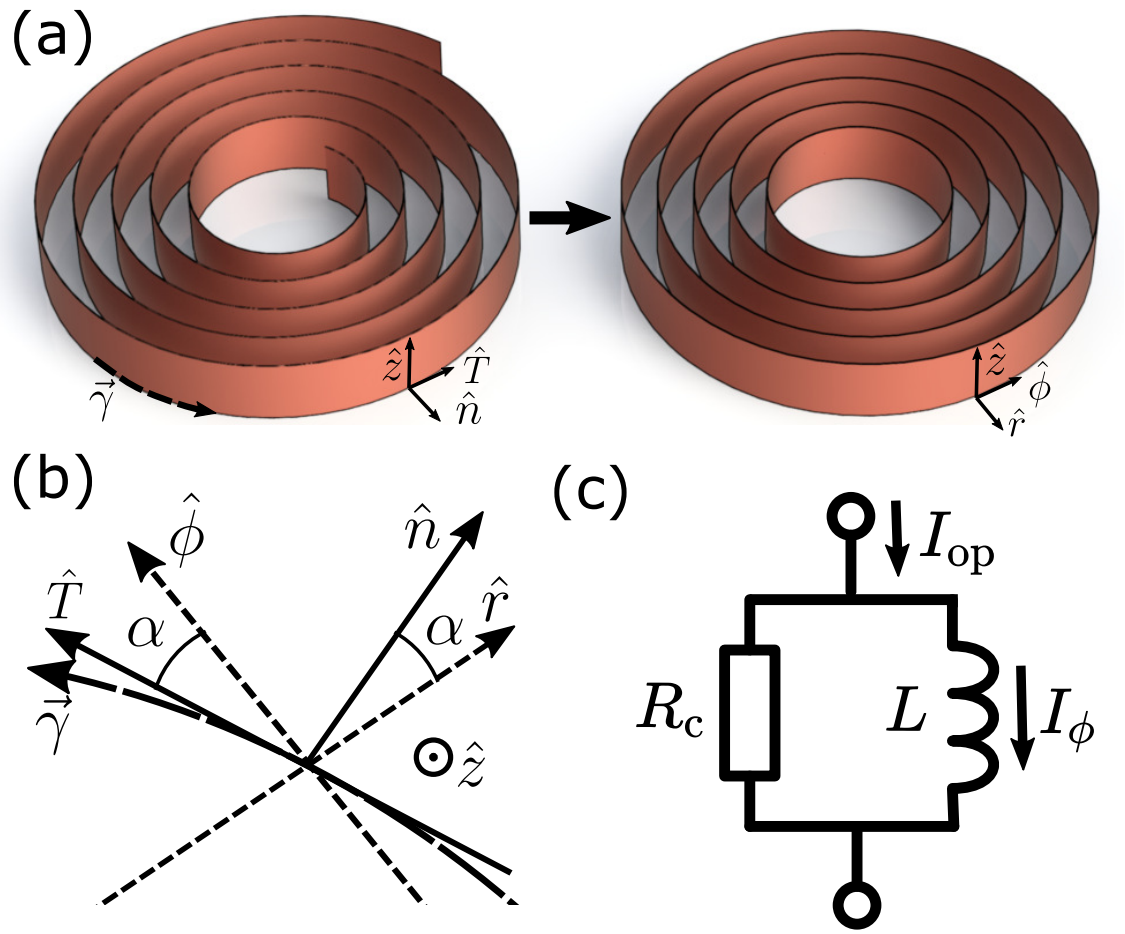

Figure 4-1: (a) Illustration of the spiral winding of an HTS pancake coil, exaggerating the pitch and spacing of the turns (left), as well as the traditional concentric approximation used to enforce axial symmetry in INS coils (right). (b) A comparison of the locally defined normal-tangential unit vectors, $\hat{n}$ and $\hat{T}$, for the spiral winding vs the cylindrical unit vectors $\hat{r}$ and $\hat{\phi}$, which differ by a small angle α. (c) Lumped circuit model of the NI coil.

insulation is essentially zero, and therefore the current in each turn is essentially the same turn-to-turn. If the coil is also normal-conducting, FE models built in A-formulation can be used to great success. However, coils without insulation (NI Coils, reviewed in sec. 2.2.1), and made from HTS tapes, fail every one of the above approximations. To cover the superconductivity of the HTS material, H-formulation can be used instead, and avoids the singularities involved in having near-infinite and variable conductivity. Even so, the other approximations that are typically available to magnet modellers must also be reconsidered in more detail.

The goal of any modeller is to model everything that matters, and ignore everything else. For the NI coil we wish to capture the electromagnetic behaviour and consequences of allowing turn-to-turn current flow, as well as the peculiar dynamics caused by the HTS material and its geometry. In this chapter I propose, derive and validate a 2D, axially symmetric FE model of an NI (or partially insulated) coil that captures all the inherent electromagnetic properties of these coils, including axial vs radial current flow and critical current $J_c(B, \theta)$ suppression, and also reproduces well-known charging and discharging characteristics. The model has been validated against previously reported experimental discharge measurements.

The FE model also delivers results that are consistent with the expected equivalent-circuit behaviour. However, by modelling the NI coil in 2D, we gain axial and radial fidelity. Although circuit grid models (CGM) give radial fidelity, the addition of axial fidelity captures the magnetisation behaviour typically seen in HTS tapes. Similar magnetisation effects have been explored extensively, including in H-formulation [91], and have been captured for the case of insulated HTS coils. The question to be answered here is "can these magnetisation effects be modelled in the case where turn-to-turn currents exist, and what interplay do they have?"

4.1.1 Chapter overview

First, sec. 4.2 outlines the underlying modelling techniques including conductor homogenisation. Section 4.2.1 introduces the specific framework for defining tensoral and anisotropic resistivity, which is followed by a discussion of the overall constitutive behaviour in sec. 4.2.2. The final aspect of the model, implementing current control, is then defined in sec. 4.2.3.

With the model defined, sec. 4.3 compares center-field decay results with experimental data from Wang et.al. [100]. This validates the model. Further results are extracted by inspection in sec. 4.4, which includes: the evolution of average currents (sec. 4.4.1); current distributions vs radial position (sec. 4.4.2); as well as snap shots of current densities and associated magnetic field aberrations (sec. 4.4.3). The model results are then briefly expanded in sec. 4.5 by driving the current well over

the critical current. Finally, results are summarised in sec. 4.6.

4.2 Model derivation

A critical technique used to simplify the modelling of insulated (INS) coils is the 'homogenisation' of conductors [101–104]. Homogenisation describes the aggregation of detailed microscopic properties of the conductor and coil architecture, into bulk properties that can be used to represent the homogenised system at larger length scales. This enables the essential physics of a macroscopic system to be described while ignoring extraneous detail, and hence reduces computational cost. The key insight carried forward in this chapter is that homogenisation can be combined with the notion that an NI coil is nearly axially symmetric.

In INS coils, model homogenisation is normally justified by approximating each turn of the coil to be concentric and azimuthal (see fig. 4-1(a) right). This is possible because the spiral current through the windings is always equal to the operational current $I_{\mathrm{T}} = I_{\mathrm{op}}$. However this constraint does not hold for an NI coil where radial currents may also flow. Instead, homogenisation can be used to approximate the 3D spiral geometry of an HTS pancake coil — reducing the problem to 2D — while still encoding the notion of being spirally wound. We are left with a bulk property that can be treated computationally with axial symmetry.

4.2.1 Anisotropic resistivity

Rather than assume that each turn of the NI coil is azimuthal, we shall instead homogenise the resistivity of each portion of a turn across its thickness. This process can be performed in coordinates local to each part of the HTS winding. Shown in fig. 4-1, such coordinates are defined by the unit vectors: the surface normal to the HTS side of the tape $\hat{n}$, the tangent to the spiral of the tape $\hat{T}$, and the axial direction $\hat{z}$. In this coordinate system the anisotropic resistivity of the tape is easily understood in the tensor form:

$$\vec{E}' = \boldsymbol{\rho}'\vec{J}' = \begin{bmatrix} \rho_{\mathrm{n}} & 0 & 0 \\ 0 & \rho_{\mathrm{sc}} & 0 \\ 0 & 0 & \rho_{\mathrm{z}} \end{bmatrix}_{\hat{n},\hat{T},\hat{z}} \vec{J}', \tag{4.1}$$

where $\vec{E}'$ is the electric field, $\vec{J}'$ is the current density, and $\boldsymbol{\rho}'$ is the resistivity tensor containing: the turn-to-turn resistivity ρ_{n}, the resistivity of the superconductor ρ_{sc}, and the axial resistivity ρ_{z}. Note that $'$ denotes the local coordinate system which is always oriented tangential to the conductor.

At any given point in the global cylindrical coordinate system, r, ϕ, z, the local tangential coordinates are simply small rotations from the cylindrical system, given by the rotation matrix:

$$g = \begin{bmatrix} \cos(\alpha) & -\sin(\alpha) & 0 \\ \sin(\alpha) & \cos(\alpha) & 0 \\ 0 & & 1 \end{bmatrix}, \tag{4.2}$$

where α is the small angle of deviation between the orientation of the spiral winding and the azimuthal direction. This angle is given geometrically by:

$$\alpha = \pm\tan^{-1}(\frac{d}{2\pi r}) \sim \pm\frac{d}{2\pi r} \qquad \text{as} \quad \frac{\mathrm{d}}{\mathrm{r}} \to 0, \tag{4.3}$$

where d is the thickness of the turn and the $\pm$ accounts for the winding direction of the coil[1].

The resistivity tensor can be rotated from the tangential system, where it is easily understood, into the global cylindrical coordinate system where it can be expressed in an axially symmetric finite element model:

$$\vec{E} = g\vec{E}' = g\boldsymbol{\rho}'g^{-1}\vec{J}, \tag{4.4}$$

[1]In the original paper, [98], the $\tan^{-1}$ in equation eq. 4.3, was given as $\sin^{-1}$. This error was later corrected by Dr. Sriharsha Venuturumilli. Although the equation gives the same result in the limit.

where $\vec{E}$ and $\vec{J}$ are the electric field and current density in the global coordinates. Substituting equations (1) and (2) into (4), we then obtain the axially-symmetric resistivity tensor in the global coordinates as:

$$\boldsymbol{\rho}_{\mathbf{coil}} = g\boldsymbol{\rho}'g^{-1} = \begin{bmatrix} \rho_{\mathrm{rr}} & \rho_{\mathrm{r}\phi} & 0 \\ \rho_{\phi\mathrm{r}} & \rho_{\phi\phi} & 0 \\ 0 & 0 & \rho_{\mathrm{z}} \end{bmatrix}_{\hat{r},\hat{\phi},\hat{z}}, \tag{4.5}$$

where the components are:

$$\rho_{\mathrm{rr}} = \rho_{\mathrm{n}} \cos^2(\alpha) + \rho_{\mathrm{sc}} \sin^2(\alpha), \tag{4.6}$$

$$\rho_{\mathrm{r}\phi} = \rho_{\phi\mathrm{r}} = \frac{1}{2}(-\rho_{\mathrm{n}} + \rho_{\mathrm{sc}}) \sin(2\alpha), \tag{4.7}$$

$$\rho_{\phi\phi} = \rho_{\mathrm{sc}} \cos^2(\alpha) + \rho_{\mathrm{n}} \sin^2(\alpha). \tag{4.8}$$

As $\boldsymbol{\rho}_{\mathbf{coil}}$ is now expressed in the cylindrical coordinate system, we can explicitly associate a resistivity with every point of our model. The off-diagonal terms, $\rho_{\mathrm{r}\phi}$ and $\rho_{\phi\mathrm{r}}$, describe the desired coupling between the radial and azimuthal currents. In principle, with appropriate choices of ρ_{n}, ρ_{sc}, and ρ_{z}, the full range of coil behaviour can be successfully modelled, from no-insulation ($\rho_{\mathrm{n}} \to 0$), to fully insulated ($\rho_{\mathrm{n}} \to \infty$).

4.2.2 Constitutive behaviour

Recalling the E-J power law, eq. 2.3, to capture the non-linear behaviour of the HTS material, we simply set the resistivity of the superconductor to be:

$$\rho_{\mathrm{sc}} = \frac{E_0}{J_{\mathrm{c}}(B,\theta)^n} |\vec{J}'_{\parallel}|^{n-1}, \tag{4.9}$$

where E_0 is the threshold field used to define J_c (conventionally $E_0 = 1\ \mu\mathrm{V/cm}$), n is the flux creep exponent, $\vec{J}'_{\parallel}$ is the in-plane current density of the HTS tape. $J_{\mathrm{c}}(B,\theta)$ is the homogenised engineering critical current density of the tape, expressed as a

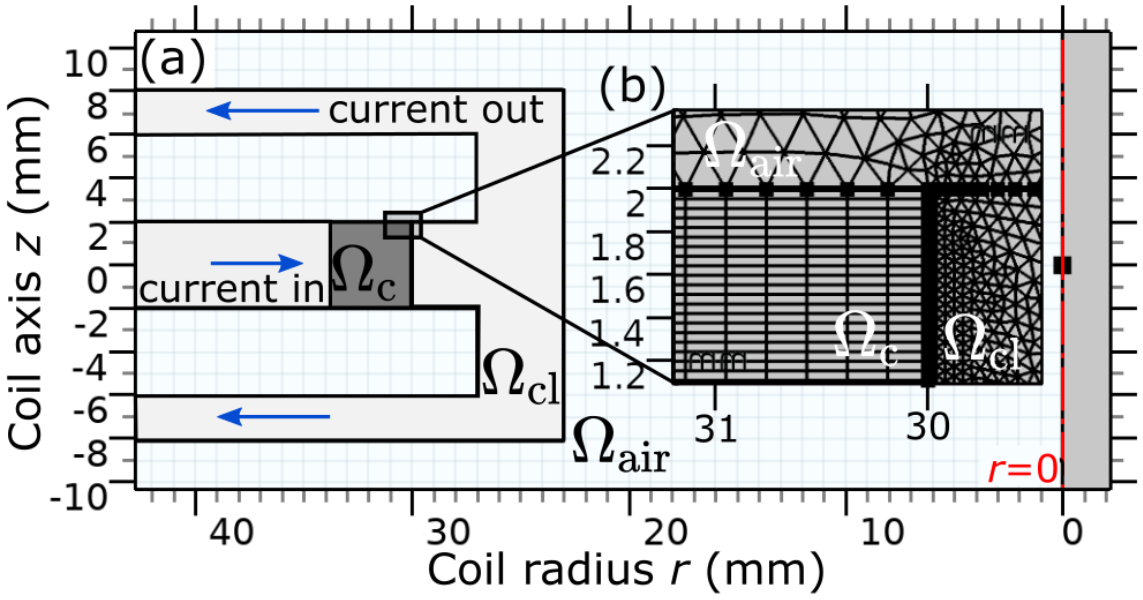

Figure 4-2: Geometry of the 60 turn coil model. (a) The coil itself is labelled Ω_c (dark grey), current leads Ω_{cl} (light grey) leading to and from the current source (not shown), and air Ω_A (blue grid). (b) Magnified view of the coil domain corner showing the rectangular and triangular finite element meshs used to achieve high resolution in the air-superconductor interface.

function of the local magnetic field magnitude B and field angle θ to the tape. In this case $J_c(B,\theta)$ is given by:

$$J_c(B,\theta) = \frac{I_c(B,\theta)}{wd}, \tag{4.10}$$

where $I_c(B,\theta)$ is the measured [95] critical current performance of the conductor, w and d are the width and thickness of the tape respectively. Any minor perturbations due to self-field generated in the I_c measurements are ignored [94]. For simplicity the axial resistivity ρ_z is also assumed to be equal to ρ_{sc}. Finally, for ρ_n we simply assume that the contact resistance is evenly distributed over the contact area. We then allocate the contact resistivity R_{ct} (with units $\Omega \cdot m^2$) as a bulk value ρ_n:

$$\rho_n = \frac{R_{ct}}{d}. \tag{4.11}$$

4.2.3 Current control

Unlike the traditional approach, the total current in the coil is not explicitly constrained, rather an artificial current lead is defined to connect the coil to a current source, see fig. 4-2 . This effectively applies a constraint only on the net radial current $I_{\mathrm{r}} = 2\pi r \int_{-w/2}^{-w/2} J_{\mathrm{r}} dz = I_{\mathrm{op}}$. The operating current I_{op} is transfered to the coil through a normal-conducting bus simulated as copper with a resistivity $\rho_{\mathrm{cu}} = 1.67 \times 10^{-8}$ Ωm.

The above approach produces a model that can be executed in the H-formulation. To do this, the model was built in COMSOL Multiphysics, version 5.4. The execution in H-formulation is justified for the reasons discussed in ch. 2.5, i.e. it handles the non-linearity and low magnitudes of the resistivities effectively. However, the underlying geometric arguments outlined above, regarding the anisotropic resistivities, do not need to be limited to the H-formulation method, and should be applicable more generally.

4.3 Model validation

This finite element (FE) model was validated against three experimental data sets collected by Wang et al. [100] from a pancake coil with varying number of total turns, N. These authors initially performed sudden-discharge measurements on a 60 turn dry-wound pancake coil, before reducing the turn number to make a 40 turn coil on which the measurements were repeated. The process of turn removal was then repeated once more to create a 20 turn coil on which measurements were also repeated. The reported experiments employed a constant winding tension throughout, in an attempt to maintain a constant contact resistivity R_{ct} within the coils. Wang et al. analysed their sudden-discharge results using an equivalent (or lumped) circuit model, see fig. 4-1(c), and their geometric interpretation of the turn-to-turn resistance [100]:

$$R_{\mathrm{c}} = \sum_{i=1}^{N} R_i = \sum_{i=1}^{N} \frac{R_{\mathrm{ct}}}{2\pi r_{\mathrm{i}} w}, \tag{4.12}$$

Parameter	N20	N40	N60
Inner radius R_{in} (mm)	30.0	30.0	30.0
Outer radius R_{out} (mm)	31.25	32.5	38.8
Turns N	20	40	60

Table 4.1: Key coil design parameters as reported by Wang et al. The dimensions of the tape used for all coils were width $w = 4.0$ mm and thickness $d = 63$ μm. [100] .

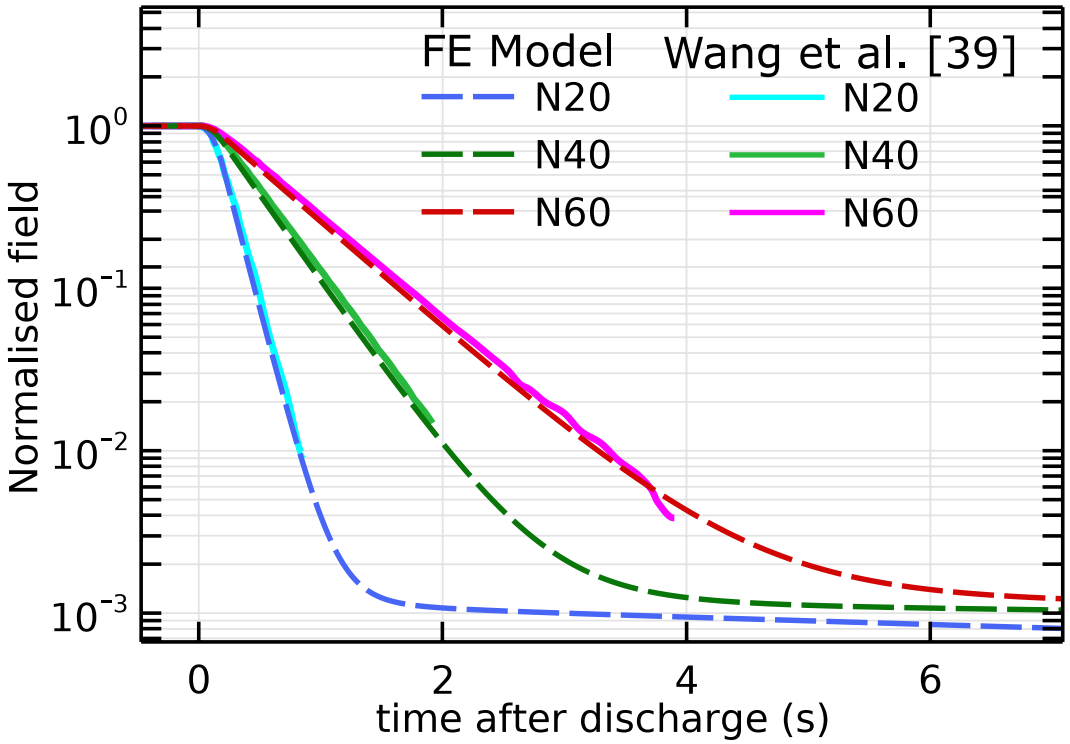

Figure 4-3: Comparison of experimental decay data for all three coils from Wang et al. [100] with the 2D axially symmetric model presented here.

where, R_{i} is the resistance between the i^{th} turn and the next and r_{i} is the radius of the i^{th} turn itself.

Table 4.1 shows the geometric parameters for each of the experimental coils, which have also been modelled in 2D axial cross-section. Figure 4-2 shows the model geometry used to deliver current to and from the coil. The critical current $I_{\text{c}}(B, \theta)$ for the model is taken from measured data of a SuperPower Inc. Advanced Pinning tape [95, 105], similar to that used by Wang et al.

Experimentally, the azimuthal current cannot be measured directly, so the central field B_{m}, measured by a Hall probe, is reported as an analogue. Figure 4-3 shows

the experimental sudden discharge measurements for each coil, normalised to $B_0 = B_{\mathrm{m}}|_{t=t_{\mathrm{d}}}$, where t_{d} is the discharge time. The experimental curves (solid) show a slight rounding at the onset of the decay, which may correspond to a finite switching time $\tau_{\mathrm{s}} \approx 200$ ms in the experiment (although this is not commented on in [100]).

The decay time constant of each coil is determined from the gradient of the straight-line sections of each curve shown in fig. 4-3, using :

$$\tau = \frac{t_0 - t_1}{\ln\left(\frac{B_{\mathrm{m}}(t_1)}{B_{\mathrm{m}}(t_0)}\right)}, \tag{4.13}$$

where t_0 is taken to be 300 ms (to ensure it is more than than the switching time τ_{s}). To match the data over the whole decay we take $t_1 = t(B_{\mathrm{m}}/B_0 = 2\%)$, to ensure confidence in the fidelity of the data extracted from [100]. Then, the characteristic resistance R_{c} can be calculated from $\tau = L/R_{\mathrm{c}}$. Hence, values for ρ_{n} in the model are obtained from eq. 4.12 and eq. 4.7. Note that the original paper by Wang. et. al. simply uses:

$$\tau = t(y/y_0 = 1/e), \tag{4.14}$$

as its definition of the time constants, which is likely inadequate given the finite switch opening time apparent in the data.

Running the FE model gives the 3 dashed curves in fig. 4-3, which match the experimental data well, see table 4.2. This validates the model, and also shows that, for a regime where the broad circuit behaviour is dominant, the FE model delivers macroscopic values consistent with a simple circuit model [41, 100]. However, fig. 4-3 also shows that the model predicts a small remnant magnetisation for each coil. This phenomenon is not captured by any lumped-circuit or circuit-grid models [41], as it requires a model which can describe both azimuthal and axial current distributions in the coil.

Table 4.2 also shows the quoted values from the original work [100] extracted using eq. 4.14. As we see these values differ from those extracted using eq. 4.13 from the same experimental date. This discrepancy has no bearing on the validity of the FE model. Essentially, the results in table 4.2 only show that the model replicates

Parameter	N20	N40	N60
Inductance L (μH)	50.9	195.5	427.6
R_c (eq. 4.13) ($\mu\Omega$)	323.8	458.7	615.8
Time constants τ (ms)			
Experiment eq. 4.13	157.1	426.3	694.4
Model	153.6	419.3	683.5
Experiment eq. 4.14	277	552	810

Table 4.2: Extracted coil parameters, showing comparison of time constants extracted using the semi-log definition eq. 4.13 from both the original experimental data in [100], and numerically simulated data produced from the FE model. The naively evaluated, eq. 4.14, values for the experimental τ are also included.

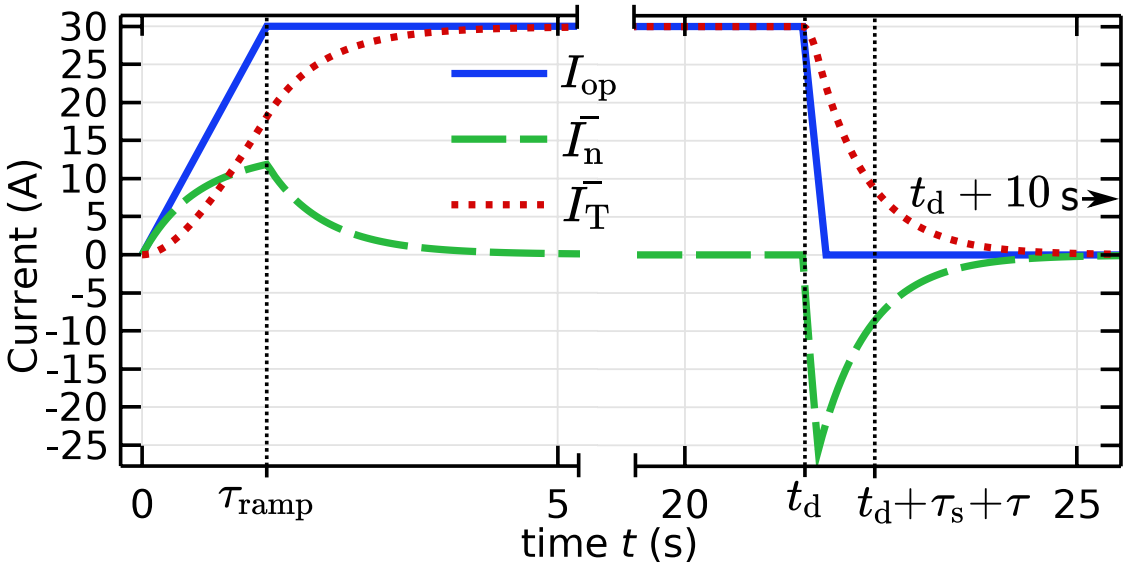

Figure 4-4: Time evolution, in the 60-turn NI coil, of the average turn-to-turn current $\bar{I}'_n$ (both averaged across the full cross-section of the coil) and the spiral current $\bar{I}'_T$. The applied current I_{op} is also shown.

macroscopic behaviours as a lumped circuit model would, not that the coils should produce a given time constant. This is because the FE model employs a value of R_c derived from eq. 4.13. Models run on values of R_c taken as quoted in the original work [100], do not give the same discharge curves as shown in fig. 4-3. This does have a direct impact on the results quoted in [100], and implies that the 3 coils do not exhibit the same contact resistivity as claimed.

4.4 Model interrogation

The real strength of numerical models is the ability to interrogate the implied dynamics of a system beyond what can be easily observed experimentally. This establishes new expectations for future work, and deeper understanding of complicated devices.

4.4.1 Area-average current evolution

Figure 4-4 shows the evolution of the area-average currents in the 60 turn coil FE model:

$$\bar{I}'_{\mathrm{n}} = \frac{w}{A}\int_{R_{\mathrm{in}}}^{R_{\mathrm{out}}} dr I'_{\mathrm{n}}(r) = \frac{2\pi}{A}\int_{R_{\mathrm{in}}}^{R_{\mathrm{out}}} dr \int_{-w/2}^{w/2} dz J'_{\mathrm{n}}(z,r), \tag{4.15}$$

and:

$$\bar{I}'_{\mathrm{T}} = \frac{w}{A}\int_{R_{\mathrm{in}}}^{R_{\mathrm{out}}} dr I'_{\mathrm{T}}(r) = \frac{d}{A}\int_{R_{\mathrm{in}}}^{R_{\mathrm{out}}} dr \int_{-w/2}^{w/2} dz J'_{\mathrm{T}}(z,r), \tag{4.16}$$

where A is the cross sectional area of the coil. These two currents capture the essence of the NI coil as interpreted in a lumped circuit model; the average turn-to-turn bypass current $\bar{I}'_{\mathrm{n}}$, and the current that provides field $\bar{I}'_{\mathrm{T}}$. Both currents are the result of the applied current I_{op}, which is applied as a standard linear ramp over a time period τ_{ramp}, the currents are then given time to settle before a sudden discharge is simulated over τ_{s}.

As expected, fig. 4-4 shows that ramping the applied current I_{op}, induces a spiral current $\bar{I}'_{\mathrm{T}}$ but with an inductive lag. The bypass turn-to-turn current $\bar{I}'_{\mathrm{n}}$ also flows which initially accounts for all of the applied current flow. However this then decreases as a percentage of I_{op}. Once the applied current ramp stops at $t = \tau_{\mathrm{ramp}}$, $\bar{I}'_{\mathrm{n}}$ decays exponentially as current adopts the resistance-free spiral pathway. Some time later, I_{op} is switched off and falls to zero over a switching time τ_{s}. This causes a rapid increase in $\bar{I}'_{\mathrm{n}}$ which is now required to return the radial component of the spiral current. It is noteworthy that $\bar{I}_{\mathrm{n}}$ reaches its peak before the modelled switch is fully open. After this point the average currents then proceed to decay as expected.

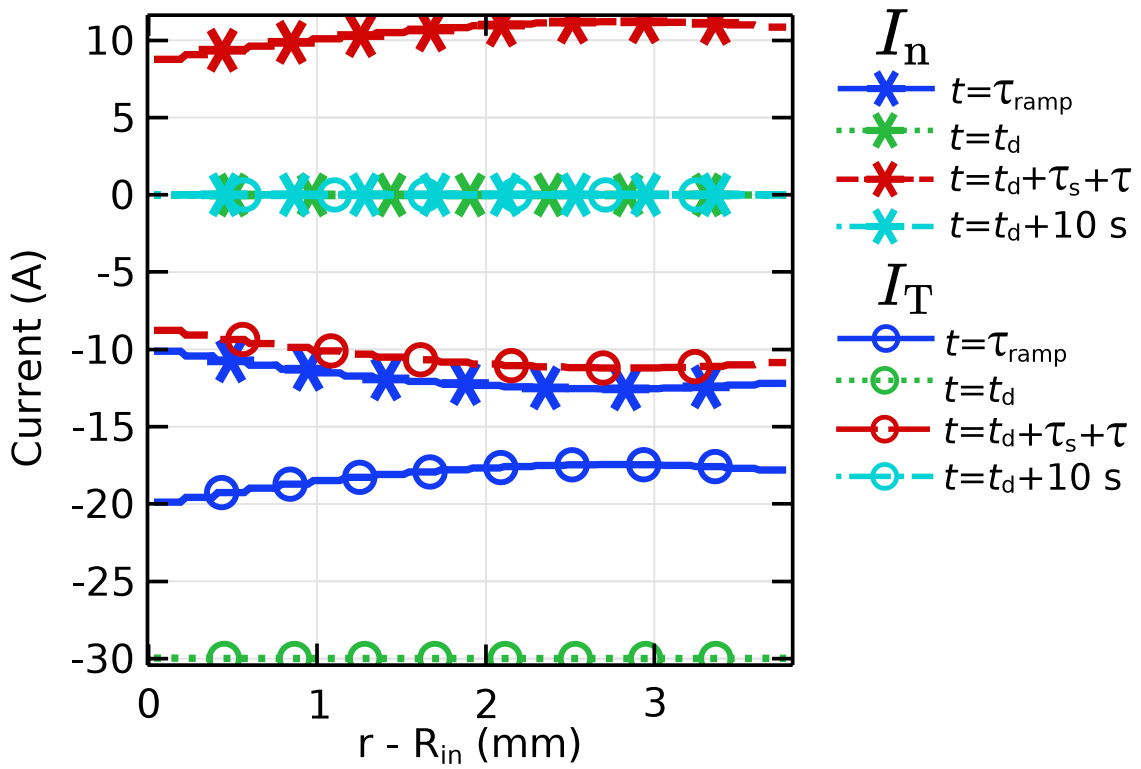

Figure 4-5: Radial profile across the 60-turn coil of the spiral current in the HTS tape I'_{T} and the turn-to-turn current I'_{n} plotted for each of the four key times highlighted in fig. 4-4

4.4.2 Current flow vs radius

Exploring deeper, fig. 4-5 shows the spiral current in the HTS tape I'_{T}, and the total current flowing between each turn I'_{n}, plotted as a function of radial position across the coil at 4 times indicated in fig. 4-4 (see eq. 4.15 and eq. 4.16). We see that the normal and spiral currents always sum to a uniform value over the coil, namely I_{op}. However, both I'_{T} and I'_{n} vary with radial position, r. This is because both the local resistivity and inductance of individual turns change across the coil. For example, at $t = t_{\mathrm{d}} + \tau_{\mathrm{s}} + \tau$ both currents are smallest at the inner diameter of the coil, due to the lower $J_{\mathrm{c}}(B, \theta)$ and lower mutual inductance of the turns at this point. These features are broadly similar to those produced from circuit grid models [41].

4.4.3 Current densities and field aberration

The most direct data from the model comes from directly interrogating the calculated current densities. Figure 4-6(a-d) show the azimuthal current densities J_ϕ for the same moments illustrated in fig. 4-4. Figure 4-6(a) shows that at the conclusion of the applied current ramp, azimuthal current J_ϕ flows at the top and bottom edges of the coil, and is approximately zero in the central regions. An effect of the anisotropic J_{c} suppression on the inner turns of the coil can be seen in the small asymmetry between the top and bottom left hand corners of fig. 4-6(a). Given enough time, J_ϕ current relaxes, into the distribution shown in fig. 4-6(b). Note that $I_{\mathrm{op}} < I_{\mathrm{c,coil}}$ which can be seen as the current has not fully penetrated the coil.

Figure 4-6(c) shows the distribution of J_ϕ at a time equal to one time constant after sudden discharge of the coil. Here we see that the total azimuthal current decays through creating new shielding currents of opposite polarity at the top and bottom edge (not by reducing the current density in the interior). This behaviour is reminiscent of the Bean model-like distributions commonly seen in AC loss scenarios [72,87]. These azimuthal shielding currents are themselves driven by the tendency of the superconductor to resist changes in magnetic flux. As the opposing azimuthal currents can recirculate in the axial direction, they follow a current path which avoids resistive

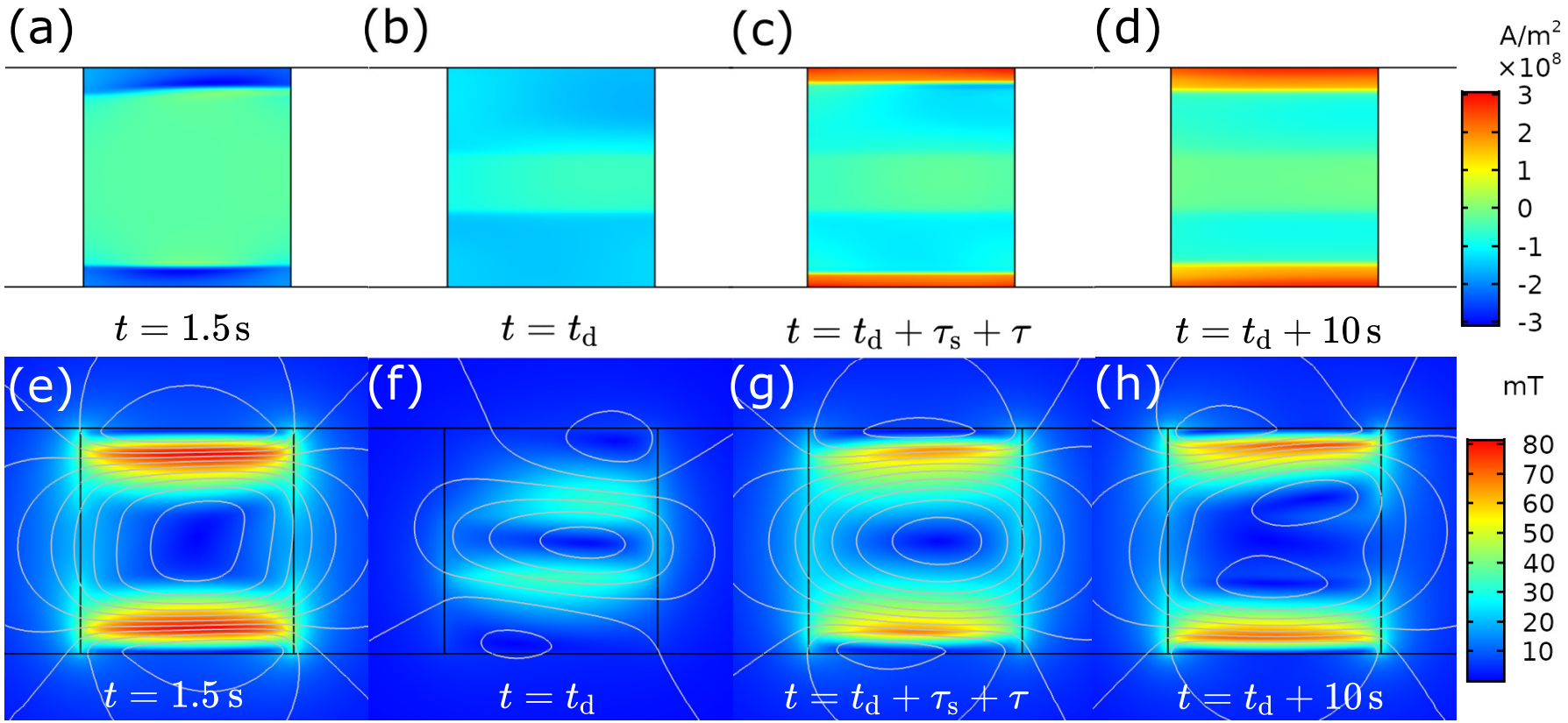

Figure 4-6: Coil cross-sections showing azimuthal current density J_ϕ [(a)-(d)] and magnetic field aberration ΔB [(e)-(h)] at key moments highlighted in fig. 4-4. (a) and (e) show the conclusion of the applied current ramp at $t = 1.5$ s. (b) and (f) show the moment immediately before the discharge test at $t = t_\mathrm{d}$. (c) and (g) show the moment after the switch is fully open, $t = t_\mathrm{d} + \tau_\mathrm{s} + \tau$, at which point the turn-to-turn current achieves its peak value. (d) and (h) show the fully discharged coil at $t = t_\mathrm{d} + 10$s, where the net currents are zero .

turn-to-turn transfer. Eventually the total azimuthal current decays to approximately zero whilst leaving the final remnant currents shown in fig. 4-6(d).

In cases where field homogeneity is critical, the effect of these recirculating shielding currents must be understood and addressed. Figure 4-6(e-h) depict the resulting magnetic field aberration for this NI coil, calculated as:

$$\Delta B = |\vec{B} - \vec{B_{\text{uni}}}|, \tag{4.17}$$

where $\vec{B_{\text{uni}}}$ is the magnetic field for an identical coil wherein the same net azimuthal current I_ϕ is uniformly distributed throughout. ΔB thus captures the difference between a typical 'first-cut' magnet design study, $\vec{B_{\text{uni}}}$, (where current is assumed to be uniform through the conductor) and the real situation where non-uniform current distributions occur $\vec{B}$. Interestingly, we see the largest aberration occurs at the end of the applied current ramp, fig. 4-6(e), before the currents have had time to relax fig. 4-6(f). Even after relaxation, fig. 4-6(f) shows that once the coil is in steady-state operation we still observe non-zero ΔB, due to the incomplete current penetration. During sudden discharge (fig. 4-6(g-h)), aberrations are primarily at the top and bottom edges of the coil, and ultimately equal the remnant magnetisation, $\Delta B = B$, in fig. 4-6(h). For all the results shown in fig. 4-6 the small asymmetry between the top and bottom of the coil is caused by the anisotropy in $J_{\text{c}}(B, \theta)$.

4.5 Current overdrive regime

Driving NI coils at currents above their critical current $I_{\text{c,coil}}$ is an interesting way of maximising coil performance [106]. Normally INS HTS coils are limited once some portion of the coil reaches its local $I_{\text{c}}(B, \theta)$. However, in an NI coil the applied current can radially bypass such regions and hence continue to be increased. This FE model is uniquely capable of tackling this problem, by solving the current bypass and $J_{\text{c}}(B, \theta)$ behaviours simultaneously.

Figure 4-7 shows the effect of driving the 60-turn NI coil well past its critical

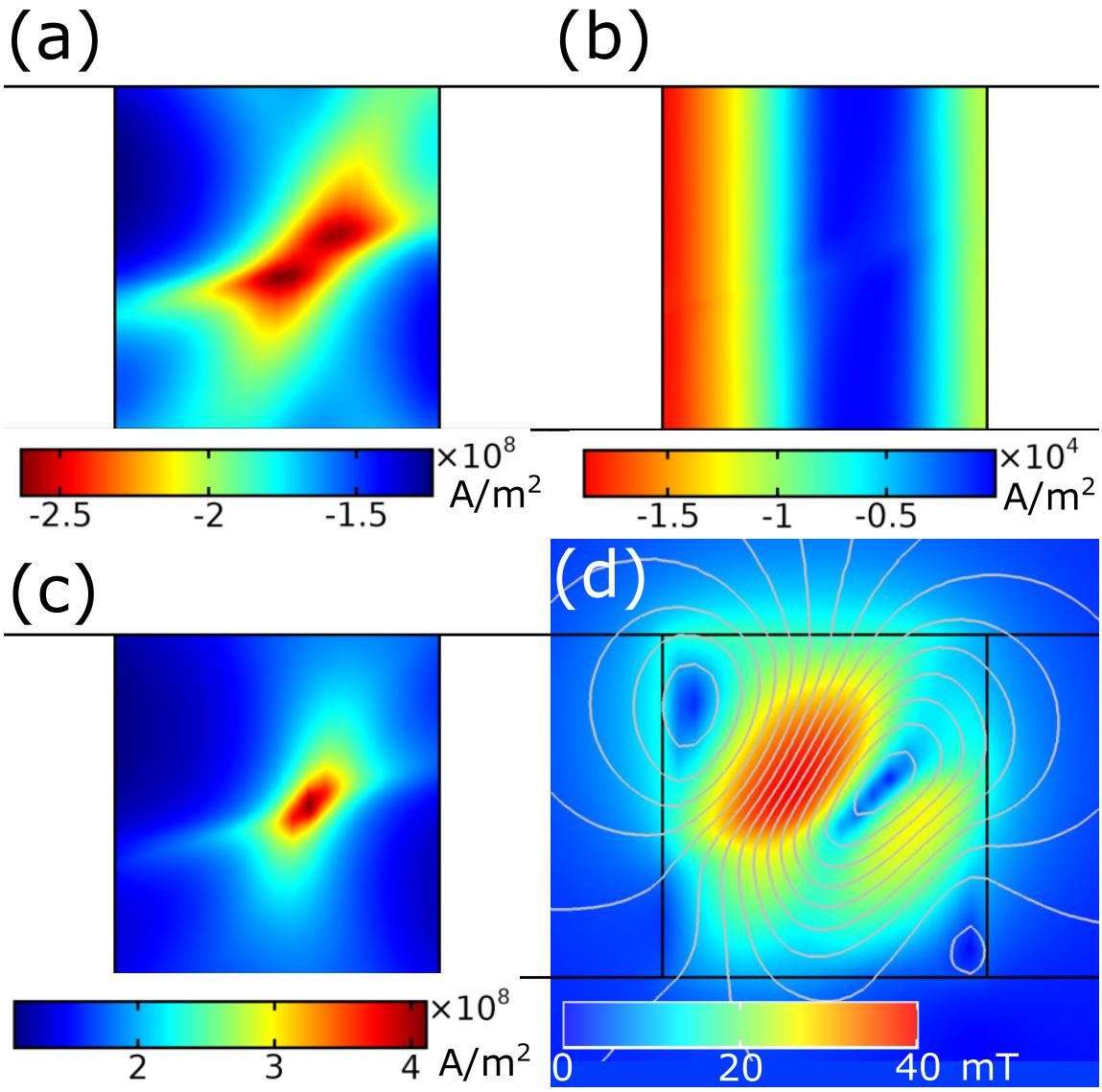

Figure 4-7: Current densities and field aberration for coil overdrive $I_{\mathrm{op}} = 50$ A $> \mathrm{I_c} =$ 43 A. (a) The azimuthal current density. (b) The turn-to-turn bypass current J_{n}. (c) The critical current density J_{c}. (d) The magnetic field aberration ΔB caused by the nonuniform distribution of current in the coil.

current to $I_{\rm op} = 1.16 \times I_{\rm c,coil}$ [100]. As shown in fig. 4-7(a), the distribution of J_ϕ becomes highly non-trivial. Even at 50 A above $I_{\rm c,coil}$, the coil does not appear to be completely saturated, as evidenced by the absence of radial bypass current in the interior region of the coil windings, see fig. 4-7(b). This is reinforced by the fact that $J_\phi < J_{\rm c}$ in much of that region of the coil (compare fig. 4-7 (a) and (c)). Finally, ΔB is shown in fig. 4-7(d) where we see that the aberration is of a similar magnitude to that observed in the under-driven coil in steady-state operation (fig. 4-6(f)). However, in the over-driven case the spatial distribution of ΔB becomes highly asymmetric, and oriented in a different direction. Again we should attribute this behaviour to the anisotropy in $J_{\rm c}$.

4.6 Summary

The simulation of shielding currents, field inhomogeneities and remnant fields are integral to the development and design of future NI coils. This chapter has presented the derivation, and demonstration, of a computationally and conceptually simple H-formulation FE model which captures and predicts the full electromagnetic behaviour of an NI coil. This model correctly replicates experimental 'sudden-discharge' data reported in literature [100], and delivers macroscopic values which correspond to lumped equivalent-circuit models. The model also reproduces the interchange between the turn-to-turn current and spiral current across the width of the coil, as seen in circuit grid models [41]. However, the power of this FE model lies in its ability to predict the evolution of fields and current at each point within the full coil cross-section. Interrogation of these results reveal the evolution of currents within the cross-section of the NI coil during current ramping, steady-state operation and sudden discharge — with full radial and axial fidelity. Finally, we have also interrogated the current and field distribution within a model coil operated in an 'over-driven' regime, $I_{\rm op} > I_{\rm c,coil}$, revealing the highly nontrivial azimuthal current densities.

This is all achieved within a single, cohesive finite-element model which requires no inter-model coupling. Indeed, no *a priori* azimuthal current constraints are ever

imposed on the coil to produce the delivered results. As a result this approach could be readily incorporated into other coupled physics problems such as thermal and stress simulation and offer an easy extension to 3D and coupled physics problems.

Chapter 5

The origin of the open circuit dc voltage from a high-T_{C} superconducting dynamo

Foreword

The following 2 chapters include previously published material, which are reproduced here with permission. The focus and results of this chapter are reproduced from: Origin of the DC output voltage from a high-T_c superconducting dynamo, *Appl. Phys. Lett.* 114, 162601 (2019) [107], with the permission of AIP Publishing. Introductory theory is also reproduced from: Mechanism of the High-T_c Superconducting Dynamo: Models and Experiment, *Phys. Rev. Applied* 14, 024012 (2020) [108], with the permission of APS Publishing. The text has also been altered to flow with the overall thesis, including pulling the supplementary materials into the body of the text.

5.1 Introduction

Despite extensive experimental study [67–71, 74, 109–115], the underlying physical origin of the dc output obtained from an HTS dynamo has not been well understood. The central point of confusion has been that the HTS dynamo develops a dc

open-circuit output from a rotating ac magnetic field, in apparent contravention of Faraday's law [74, 116]. Several different explanations had previously been proposed to reconcile this issue [62, 66–68, 70, 74, 112, 117], but quantitative predictive calculations which matched experimental data proved elusive. As proposed in [74] the addition of a non-linear resistivity of the HTS should be the only additional physics necessary for the dynamo. Using similar numerical methods to those deployed in ch. 4, a model incorporating the non-linear resistivity of the HTS material should be possible. The following is an exploration of such a model, from which we can then expand a phenomenological explanation of the device. The models show that the open-circuit output voltage is well explained using classical electromagnetic theory, without invoking either exotic quantum flux-coupling mechanisms [67, 117], nor consideration of flux-trapping within an extended closed superconducting loop [62, 112]. Rather, the dc output arises from a local rectification effect within the HTS stator tape [68, 70, 74]. This is caused by overcritical eddy currents which flow within the HTS film during the high field part of the rotor cycle, and which encounter a non-linear local resistivity.

5.1.1 Chapter overview

To understand the correspondence between experimentally measured quantities, and their computationally calculated counterparts, we must explore the nature of the measurements in some depth (secs. 5.2.1 and 5.2.2). The key difficulty is to relate the field based solutions generated by FEM to the scalar values recorded by a voltmeter (sec. 5.2.3). The treatment developed here not only gives a strong basis for understanding the dc voltage effect, but also shows why such an effect is clearly permissible in the classical electromagnetic theory. With a sensible foundation to relate the two types of data (experimental and numerical) to each other the specific modelling method is outlined, sec. 5.2.4, and the specific experimental arrangement is stated, sec. 5.2.5.

The results lay out an explicit hypothesis for the generation mechanism, sec. 5.2.6, before presenting a comparison between measured and modelled voltage results, sec. 5.3.1 which clearly confirms the model's validity. From there the model

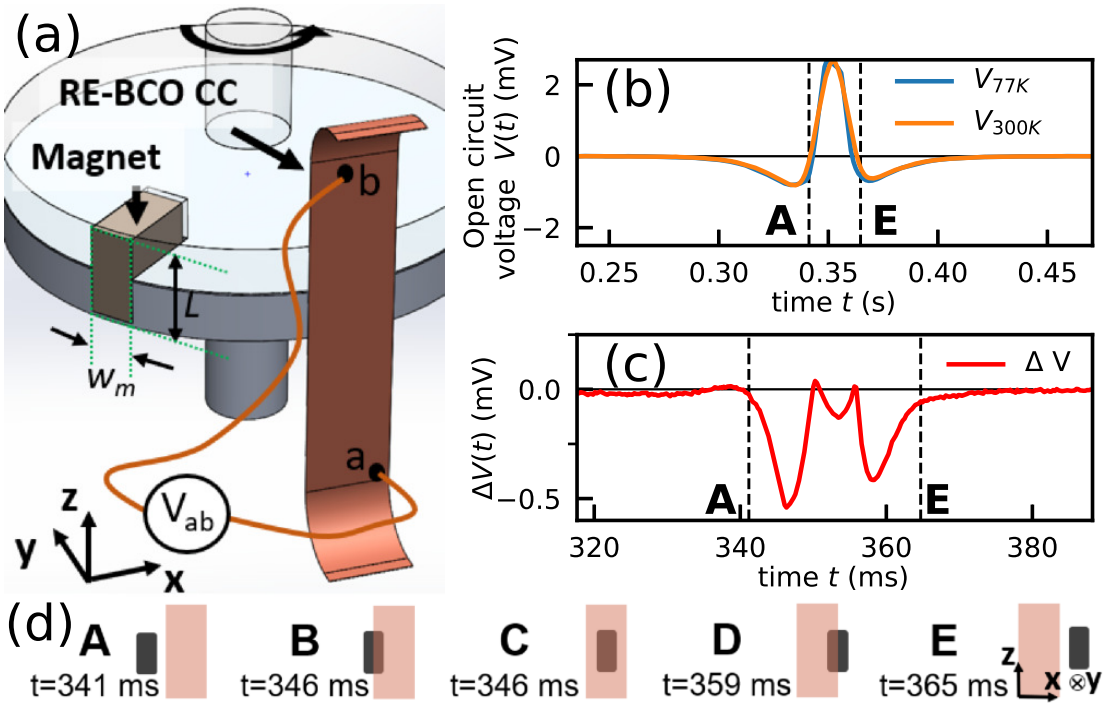

Figure 5-1: (a) Schematic of the experimental HTS dynamo studied in this chapter. (b) Experimental open-circuit voltage waveforms measured in the superconducting ($V_{77\mathrm{K}}$) and normal-conducting ($V_{300\mathrm{K}}$) states.(c) $\Delta V(t)$ waveform during the high field part of the cycle. (d) Key positions of the rotor magnet as it traverses the HTS stator tape.

current distributions are interrogated directly, sec. 5.3.2, to confirm and expand the phenomenology proposed. Lastly in sec. 5.3.3, the core hypothesis that conductor non-linearity is at the root of the dc voltage effect is tested by varying $n-$value down to equal 1, where the device reverts to the normal conducting case.

5.2 Methods

5.2.1 Measuring and interpreting voltages

The open-circuit output obtained from this device is similar to those previously reported in [74]. Figure 5-1(b) shows the open-circuit voltage waveform measured in both the normal-conducting state at 300 K ($V_{300\mathrm{K}}$), and in the superconducting state at 77 K ($V_{77\mathrm{K}}$). The large positive peak at position **C** corresponds to the moment at

which the rotor magnet is centred directly above the stator tape. Subtle differences between the normal and superconducting waveforms are apparent during this part of the cycle. These are highlighted in fig. 5-1(c) which plots the difference:

$$\Delta V(t) = V_{77\mathrm{K}}(t) - V_{300\mathrm{K}}(t). \tag{5.1}$$

Voltage taps are positioned on the stator tape such that small variations in position do not alter the measured dc output from the device [74]. However, small displacements of the voltage tap leads will always change the inductive-*emf* pick up of the total loop. By taking measurements of the device at both room temperature, $V_{300\mathrm{K}}$, and in liquid nitrogen, $V_{77\mathrm{K}}$, the behaviour of the normal conducting and superconducting states can be differentiated and the influence of the arbitrary *emf* pick up from the voltage tap leads can be removed.

Provided the applied magnetic field is much higher than any internal field produced by induced eddy currents in the HTS tape, $V_{300\mathrm{K}}$ can be considered a measurement of the *emf* induced by the magnet in the closed loop formed by the stator tape and tap leads to the voltmeter. This motivates the definition of the difference between the induced *emf* and the actual measured voltage across the stator tape as in (5.1).

For clarity I shall reserve the symbol Δ for measurement differences between 77 K and 300 K.

5.2.2 Time-averaged voltages

While eq. 5.1 allows us to examine the transient dynamics of the device during operation, the useful output of the device is its time-averaged dc voltage:

$$V_{\mathrm{dc}} = f \int_0^{\frac{1}{f}} V_{77\mathrm{K}}(t)dt = f \int_0^{\frac{1}{f}} \Delta V(t)dt, \tag{5.2}$$

where f is the cycle frequency of the dynamo. The RHS of eq. 5.2 holds, because in the normal-conducting case at 300 K, $V_{\mathrm{dc}} = 0$. This is expected as the dynamo

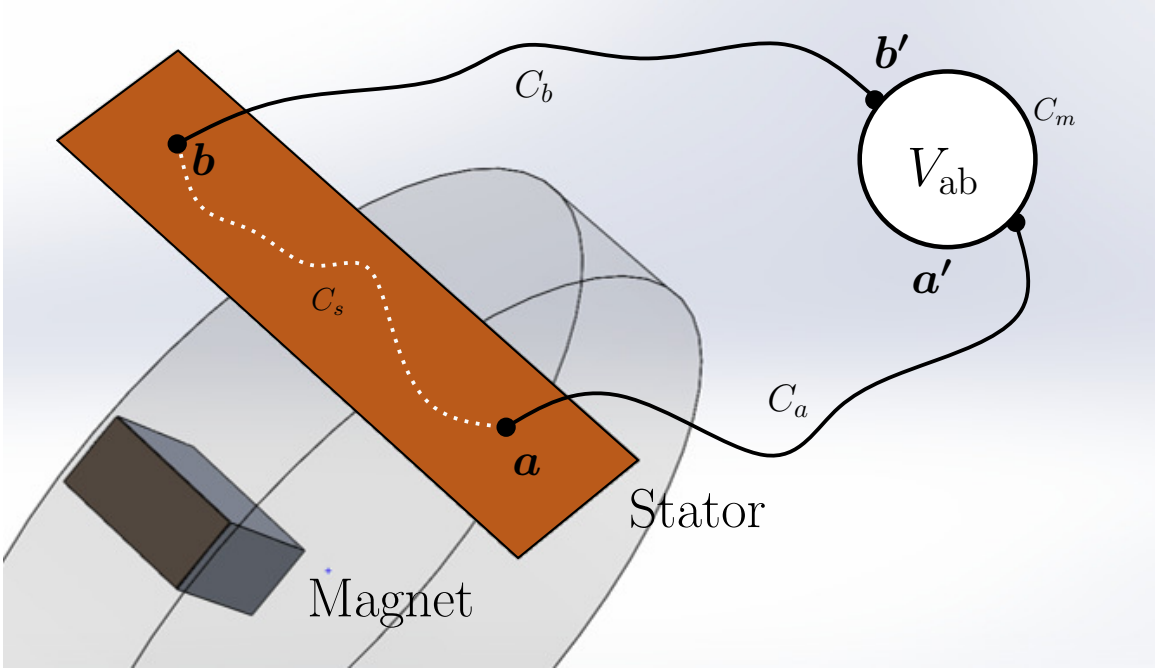

Figure 5-2: The HTS stator and the attached voltage leads, forming the 4 sections of the Amperian loop C; through the sample C_s, through the two leads C_a, and C_b, as well as through the meter C_m.

geometry is that of a simple ac alternator [74]. However, it is clear from fig. 5-1(c) that in the superconducting state at 77 K, $V_{\mathrm{dc}} \neq 0$. As a result, if a superconducting coil is connected in series with the dynamo, the non-zero dc output voltage will drive a dc current to flow through the coil [3, 71, 73].

It should be noted that a dc output voltage cannot arise from magnetisation effects within the HTS tape. This is because $\vec{B}$, must always be periodic over 1 cycle at all points in space, such that:

$$\int_0^{1/f} \left(\nabla \times \vec{E}\right) dt = -\int_0^{1/f} \frac{d\vec{B}}{dt} dt = 0. \tag{5.3}$$

5.2.3 Modelling, measurement, and theory

In order to investigate the experimentally measured voltages using computational modelling we must clearly establish the relationship between the measured values and the physical fields which underlie them. However, unlike in ch. 4, the analysis requires

careful consideration of how voltages, as they appear on a electrostatic voltmeter, relate to the underlying fields (electric and magnetic). The following is a formal description of how the calculated fields are related to their counterparts measured scalar voltages.

We start with the gauge invariant form of the electric field:

$$\vec{E} = -\vec{\nabla}\psi - \partial_{\mathrm{t}}\vec{A}, \tag{5.4}$$

where $\vec{\nabla}\psi$ is the gradient of the scalar potential, and $\vec{A}$ is the magnetic vector potential. As explained well by Clem [78, 118], any measured voltage V_{ab}, such as $V_{300\mathrm{K}}$ or $V_{77\mathrm{K}}$, is given by the electric field in the meter itself. In the case of an ideal voltmeter, the active component is taken to be arbitrarily small such that $\partial_{\mathrm{t}}\vec{A}$ is negligible, and the meter is only affected by the electrostatic potential $\vec{\nabla}\psi$ (see fig. 5-2). Therefore the value of $\vec{E}$ in the meter can be found by solving for $\vec{\nabla}\psi$. As an integral of $\vec{\nabla}\psi$ between $\boldsymbol{a'}$ and $\boldsymbol{b'}$ is path independent, it must be equivalent to the integral along the nearly-closed loop made by the sample and the measurement leads, between the same points $\boldsymbol{a'}$ and $\boldsymbol{b'}$. Denoting the path through the leads as $C_l = C_a + C_b$, the path through the sample as C_s, and assuming $\vec{E} = 0$ in the leads, we can define a measured voltage V_{ab} as:

$$\begin{aligned} V_{\mathrm{ab}} &= \int_{C_m} \vec{\nabla}\psi \cdot d\vec{l} = \int_{C_s} \vec{\nabla}\psi \cdot d\vec{l} + \int_{C_l} \vec{\nabla}\psi \cdot d\vec{l} \\ &= -\int_{C_s} \vec{E} \cdot d\vec{l} - \int_{C_l + C_s} \partial_{\mathrm{t}}\vec{A} \cdot d\vec{l} \\ &= -\int_{C_s} \vec{E} \cdot d\vec{l} - d_t \iint_S \vec{B} \cdot d\vec{s}, \end{aligned} \tag{5.5}$$

where we note that while the integral through $C_l + C_s$ is not closed (missing the contribution through the meter C_m), as the length of C_m tends to zero, this term fully captures the rate of change of the captured magnetic flux through the surface S.

Re-examining the experimental logic behind eq. 5.1, that $V_{300\mathrm{K}}$ is a measure of the *emf*, we can frame the approximation as a condition on the magnetic flux through

the loop:

$$\partial_t \iint_S \vec{B}_{77\mathrm{K}} \cdot d\vec{a} = \partial_t \iint_S \vec{B}_{300\mathrm{K}} \cdot d\vec{a}. \tag{5.6}$$

With the approximation well defined, we may express ΔV, eq. 5.1, from eq. 5.5:

$$\Delta V = -\int_{C_s} \left(\vec{E}_{77\mathrm{K}} - \vec{E}_{300\mathrm{K}}\right) \cdot d\vec{l}. \tag{5.7}$$

Focusing our analysis on the symmetric plane bisecting the dynamo, we can capture the necessary physics, without considering the nature of the integral paths. In the symmetric x, y plane only currents into and out of the plane J_z need to be considered; this of course limits $\vec{E}$ to E_z as well. Furthermore, it can be shown that assuming reflectional symmetry along the plane forces $\vec{\nabla}\psi$ to be constant over the plane, up to a choice of gauge. Therefore, the spatial variations in E_z can be attributed entirely to the changing vector potential $d_\mathrm{t}A_\mathrm{z}$. Hence, in the symmetric plane, $\vec{\nabla}\psi$ can be thought of as:

$$\vec{\nabla}\psi(x,y,z,t)|_{z=0} = \partial_\mathrm{z}\psi(t) = -E_\mathrm{z}(x,y,t) - d_\mathrm{t}A_\mathrm{z}(x,y,t), \tag{5.8}$$

which leads to the fact that only the spatially averaged components of both E_z and $d_\mathrm{t}A_\mathrm{z}$ contribute to $\partial_\mathrm{z}\psi$:

$$\begin{aligned}
\partial_\mathrm{z}\psi(t) &= \frac{1}{A}\int_\Omega \partial_\mathrm{z}\psi(t)da \\
&= \frac{1}{A}\int_\Omega E_\mathrm{z}(x,y,t) - d_\mathrm{t}A_\mathrm{z}(x,y,t)da \\
&= -E_\mathrm{ave} - d_\mathrm{t}A_\mathrm{ave}.
\end{aligned} \tag{5.9}$$

From eq. 5.9 we can examine Faraday's alternator, where for a homogeneous normal conductor, $E = \rho J$ implies $E_\mathrm{ave} = \rho J_\mathrm{ave}$, i.e., Ohm's law. Then the ac alternator has a dc component proportional to the dc current flowing through the stator, and if that dc current is zero, then there is no dc output voltage. However, in

the case of the superconductor $E = \rho(J)J$ does not imply $E_{\rm ave} = \rho(J_{\rm ave})J_{\rm ave}$, rather:

$$E_{\rm ave} \neq \rho(J_{\rm ave})J_{\rm ave}. \tag{5.10}$$

This should immediately dispel any remaining suspicion that the HTS dynamo violates some deep principle in electromagnetism. Rather, the traditional argument for the zero dc voltage of the ac alternator is rooted in the application of Ohm's law, which can no longer be applied. This realisation alone is not a theory of the dc voltage in the dynamo by itself, instead it is a simple check that a dc voltage is not forbidden at some basic level.

Looking back at eq. 5.1 and eq. 5.7 and using the same assumptions, we can use eq. 5.9 to define a similar state comparison (super- vs normal-conducting) for $\partial_{\rm z}\psi$:

$$\begin{aligned} \Delta\partial_{\rm z}\psi(t) &= \partial_{\rm z}\psi_{\rm 77K}(t) - \partial_{\rm z}\psi_{\rm 300K}(0,t) \\ &= -E_{\rm ave,77K}(t), \end{aligned} \tag{5.11}$$

where again, the spatially averaged electric field at zero net current and room temperature $E_{\rm ave,300K} = 0$ V/m and the A vector is the same at both RT and 77 K $d_{\rm t}A_{\rm ave,77K} = d_{\rm t}A_{\rm ave,300K}$, which is true in the context of the full measurement loop, regardless of gauge as long as we assume eq. 5.6.

If we make the simple approximation that the 3D system is translationally symmetric under the length of the magnet L, then the solution in plane can be extrapolated, and related to measurement:

$$\begin{aligned} \Delta V(t) &= \int_{-L/2}^{L/2} \Delta\partial_{\rm z}\psi(t)dz \\ \Delta V(t) &= -L \times E_{\rm ave,77K}(t), \end{aligned} \tag{5.12}$$

where the *lhs* is measurable and the *rhs* can be calculated. For brevity, I will refer to $E_{\rm ave,77K}$ as simply $E_{\rm ave}$ from this point on.

5.2.4 Modelling methodology

To calculate the RHS of eq. 5.12 we can again use H-formulation. Similar to the NI coil, a constitutive relation is also needed, in order to link E and J. In this case I take the simple case of the power-law E-J relation eq. 2.3. While we could assume that the conductivity of the HTS layer dominates, the model includes a 20 μm copper layer with resistivity $\rho_{\mathrm{Cu}} = 0.19$ $\mu\Omega$ cm regardless.

Figure 5-1 shows a 3D schematic of the device, including a transparent cross section highlighting the bisecting plane to be modelled. Again, it is computationally advantageous, if not necessary, to reduce the model to two dimensions shown in fig. 3-4[1]. The model is split into 3 separate domains, the rotor domain Ω_{R}, the air domain Ω_{A}, and the HTS domain Ω_{T}. Unlike the NI coil model, the geometry has reflectional symmetry in Cartesian coordinates, and hence x and y are taken in plane and z out of plane.

In order to reduce computation time, the HTS domain is modelled as a 100 μm thick film (rather than the true 1.7 μm). This approximation is standard practice [87, 103], and in this case its accuracy was confirmed through comparison with a limited number of simulations performed using a much thinner tape domain of $\sim$ 10 μm.

In this chapter I shall focus on the open circuit voltage of this device, and hence set the net transport current:

$$I_{\mathrm{T}} = \int_{\Omega_{\mathrm{T}}} J_{\mathrm{z}} da = 0, \tag{5.13}$$

which, much like the current shell J_{s}, is imposed using a weak contribution to the finite element model. Finally, each numerical simulation was run for 10 full cycles to ensure periodicity, and all computed values were fully periodic after the first cycle. Reported results are all from the second cycle of the simulation.

[1] While 2D remains the fastest method for modelling these devices, significant improvements have since enabled several 3D models, which will be covered in ch. 9

5.2.5 Parameters of the Badcock 2017 dynamo

The dynamo topology modelled in this chapter is similar to that examined experimentally in previous work [96], and is depicted in fig. 5-1(a). It consists of a rotor which houses a Nd-Fe-B magnet with an edge length, L, of 12.7 mm, and width, w_{m}, of 6 mm. The magnet has a manufacturer's grade of N42, and is assumed to have a remnant flux density of 1.25 T. The magnet's outer face is positioned 35 mm from the axis of rotation, with its pole facing outwards. A section of 12 mm wide REBCO tape (Superpower SF12050CF) is oriented parallel to the axis of rotation, with its planar surface facing the rotor. The flux gap, g, between the superconducting tape and the rotor magnet was set to 3.7 mm. A rotational frequency of 4.25 Hz was employed, with the rotor magnet traversing the tape once during each cycle. Illustrative locations of the magnet's transit across the tape are illustrated in fig. 5-1 (d). Thin copper wires were mechanically fixed in place and attached as voltage taps at either end of the REBCO tape. The entire arrangement was then placed in a liquid nitrogen cryostat. The output voltage waveform and time-averaged dc voltage were measured at both room temperature and 77 K.

5.2.6 The mechanism that produces the dc voltage

Figure 5-3(a), depicts the circulating eddy currents flowing in the dynamo stator when the rotor magnet is at position B. Figure 5-3(b) shows a hypothetical J_{z} profile along the line $z = 0$ across the tape, for both the superconducting and normal-conducting cases. In the superconductor two distinct regions are observed, where eddy currents with $|J| \geq J_{\mathrm{c}}$, flow in either the forward or reverse direction. Forward currents flow in the region directly under the magnet. Here, flux penetrates and moves through the superconductor, such that charge carriers experience a Lorentz force which drives $|J_{\mathrm{z}}| > J_{\mathrm{c}}$. It is clear from fig. 5-1(c) that circulating currents $> J_{\mathrm{c}}$ must flow at this time, as ΔV reaches a peak value of -500 μV at position B. If we assume this is solely due to circulating currents beneath the 12 mm long magnet, this implies an average value of $\rho J_{\mathrm{z}} >$400 μV cm^{-1}, which is well within the flux-flow region of the HTS tape.

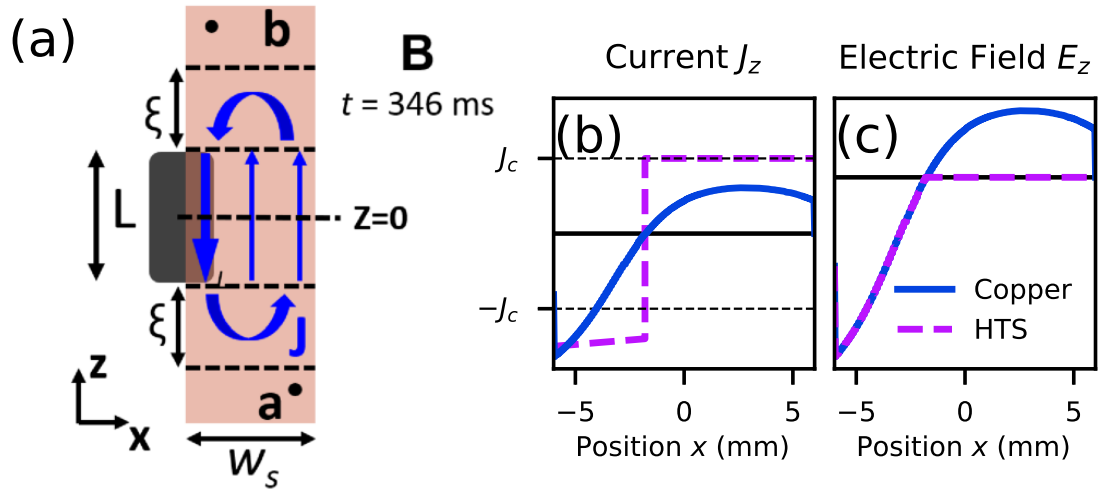

Figure 5-3: (a) Schematic depiction of the circulating currents flowing in HTS tape when the rotor magnet is at position **B**. Bold arrows indicate over-critical current densities. (b) J_z profiles along the line $z = 0$ flowing in either copper or HTS stators. (c) $E_z = \rho J_z$ profiles corresponding to currents depicted in (b).

Figure 5-3(c) shows the resulting hypothetical local internal electric field profile, $E_z = \rho J_z$ across the tape. The *forward-current region* where $|J_z| > J_c$ incurs a non-zero E_z that opposes the local $\partial_t \vec{A}$. However, in the *reverse-current region* outside the magnet, $|J_z| \leq J_c$ (due to eq. 5.13), and hence $E_z \approx 0$. As a result, the average field across the full width of the tape is non-zero at this point in the cycle. This situation differs markedly from the normal (linear) conductor, where E_z is always directly proportional to J_z at all points, such that the average value of E_z across the tape must always equal zero (from eq. 5.13). As a result, ΔV for a linearly resistive conductor is zero at all times. By contrast ΔV is non-zero for the superconductor, with its value determined by the relative distribution of forward and reverse eddy currents within the tape. Furthermore, if the magnet width is less than half the tape width, the reverse current region may always be wider than the forward current region. This means that E_z will always be high in the *forward-current region*, and zero in the *reverse-current region*. As a result, the full-cycle integral, V_{dc} will also be non-zero and have the opposite polarity to the emf caused by the magnet traversing the tape.

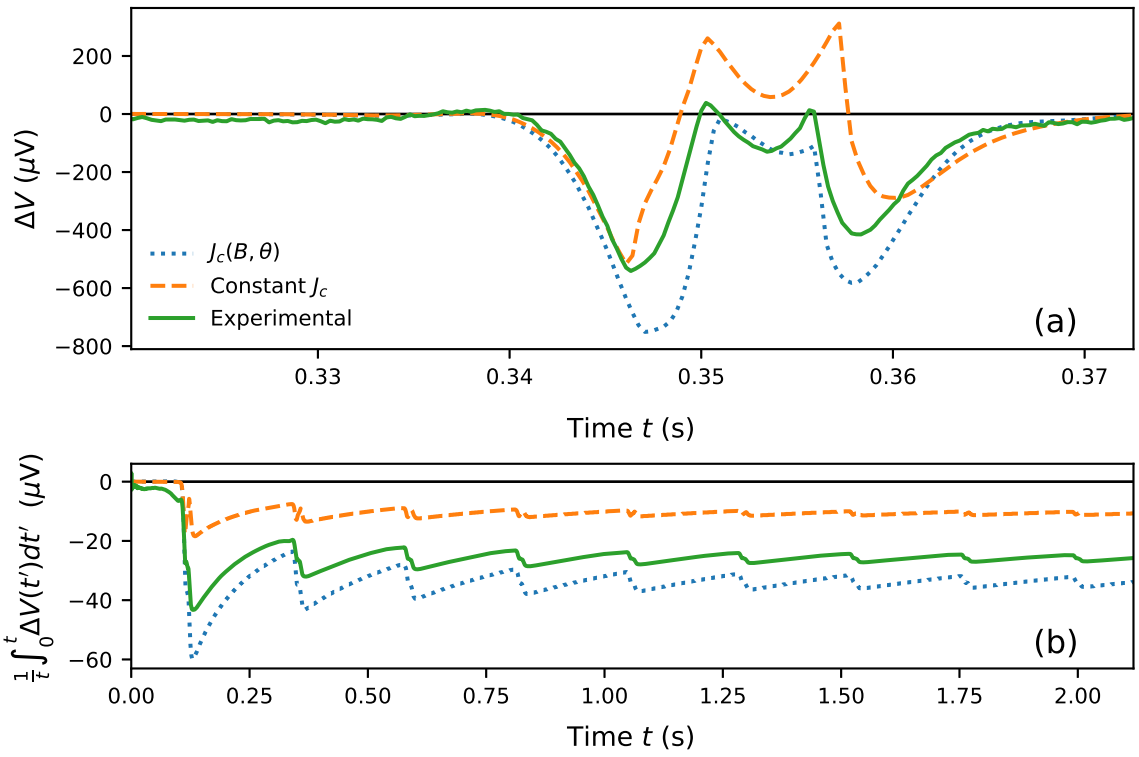

Figure 5-4: (a) Plot showing comparison of experimentally-measured ΔV alongside numerically calculated waveforms (following $\Delta V = -E_{\text{ave}} \times L$ convention). Data shown for numerical calculations using either $J_{\text{c}} = const.$, or the experimentally determined $J_{\text{c}}(B,\theta)$ function. (b) Cumulative time average, $\frac{1}{t}\int_0^t \Delta V dt$, for each waveform shown above. As $t \to \infty$ these converge to V_{dc} in each case.

5.3 Results

5.3.1 Voltage modelling

To probe this effect in more detail numerically simulated current flows in the stator tape of the dynamo are shown in fig. 5-1 (a). Two versions of the numerical model were calculated, using different functions to describe the HTS resistivity (eq. 2.3). In the first case, J_c was assumed to be constant and equal to 23.6 A mm^{-2}. This is the self-field value measured at the 1 μV criteria for the stator tape used in experiments. In the second case, values for $J_c(B, \theta)$ are interpolated from the data set shown in fig. 3-8. In both cases $n = 20$ is assumed.

Figure 5-4 shows a comparison between values calculated from the numerical model and experiment. Figure 5-4(a) shows good qualitative agreement in ΔV, for both J_c models. In each case the distinctive sequence of quadruple peaks is observed in the ΔV waveform, which coincide with rotor positions A to E (fig. 5-1). There is a noticeable left-to-right asymmetry in all of the experimental and calculated ΔV waveforms, with the leading negative peak having a larger amplitude than the trailing peak in each case. This occurs because the internal field in the tape includes a contribution from the circulating currents within the superconductor. These currents switch direction as the magnet passes across the centre of the wire, causing the internal magnetic field within the tape to differ between points A and E. Similar left-to-right asymmetry also occurs in normal-conducting stator sheets carrying very large eddy currents [119]. However, it must be noted that this is a magnetisation effect which cannot give rise to a non-zero V_{dc} (due to eq. 5.3).

More detailed comparison is possible if we consider the cumulative time-averaged voltage shown in fig. 5-4(b). This value converges to V_{dc} as $t \to \infty$ (experimentally measured to be -24.3 μV). Figure 5-4(b) shows that both numerical models output a non-zero dc voltage of the correct polarity. However, whilst the $J_c = const.$ model certainly produces a non-zero negative value for V_{dc}, this is significantly smaller than the experimental value (-10.7 μV). By contrast the field-dependent $J_c(B, \theta)$ resistivity

yields a value (-33.9 μV), which is comparable to experiment[2].

These observations indicate that the constant J_c model possesses all of the essential dynamics necessary to deliver a dc voltage. This is because the constant J_c model possesses a non-linear resistivity described by eq. 2.3, which is all that is required for eq. 5.9 to develop a non-zero dc voltage component. However it is also clear that consideration of J_c suppression with applied field $\vec{B}$ increases the calculated value of V_{dc}, and is needed for good agreement with experiment.

5.3.2 Current distributions

Further insight can be obtained by inspecting the currents flowing in the HTS tape. It is important to recognise that circulating currents flow within the dynamo stator wire at all times during the dynamo cycle. This is because remnant magnetisation of the tape persists, even when the rotor magnet is at the furthest point away from the stator tape. These remnant currents exhibit $|J| \leq J_c$, and hence do not contribute to ΔV. Figure 5-4, clearly shows that $\Delta V = 0$ for all times when the rotor magnet is away from the tape. However, as the rotor magnet approaches and traverses the tape, more complex dynamics occur.

Figures 5-5 and 5-6 show the current distributions and internal field profiles at key rotor positions, with the rotor magnet moving from left to right over time. Figure 5-5 shows data for the $J_c = const.$ case, where as Figure 5-6 shows the $J_c(B, \theta)$ case. Focusing on fig. 5-5, at position A, inductively-driven eddy currents with $|J_z| \geq J_c$ are present at the left edge of the tape (closest to the magnet), whilst remnant currents from the previous rotor cycle remain at the right-hand edge of the tape (with $|J| \leq J_c$). As a result the over-critical currents incur a small local internal field at the left hand side of the tape, which denotes the start of the first negative peak in ΔV (see fig. 5-5(c)). At position B, eddy currents flow counter-clockwise through the tape, and the situation is similar to that discussed for fig. 5-3. This corresponds to the first negative peak in ΔV. At position C, the rotor magnet is centred above the HTS tape

[2]Note that the values quoted in the text of [107] differ slightly from the ones given here, this is a minor error in the original paper.

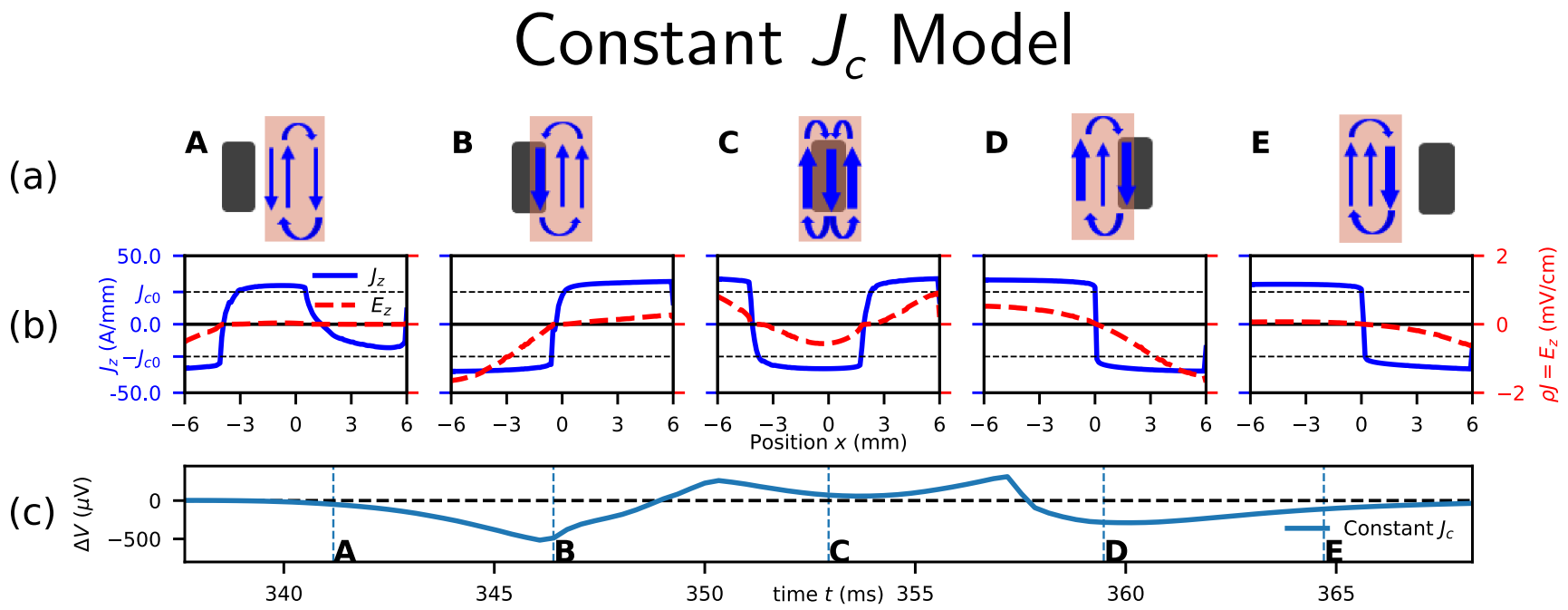

Figure 5-5: (a) Schematic denoting key magnet positions A-E and the eddy currents flowing in the stator tape at each moment. (b) Calculated profiles of J_z and $E_z = \rho J_z$ across the tape at each magnet position for the J_c= const. model (b) Calculated ΔV waveform for the constant J_c model showing points corresponding to each profile depicted in (b) above.

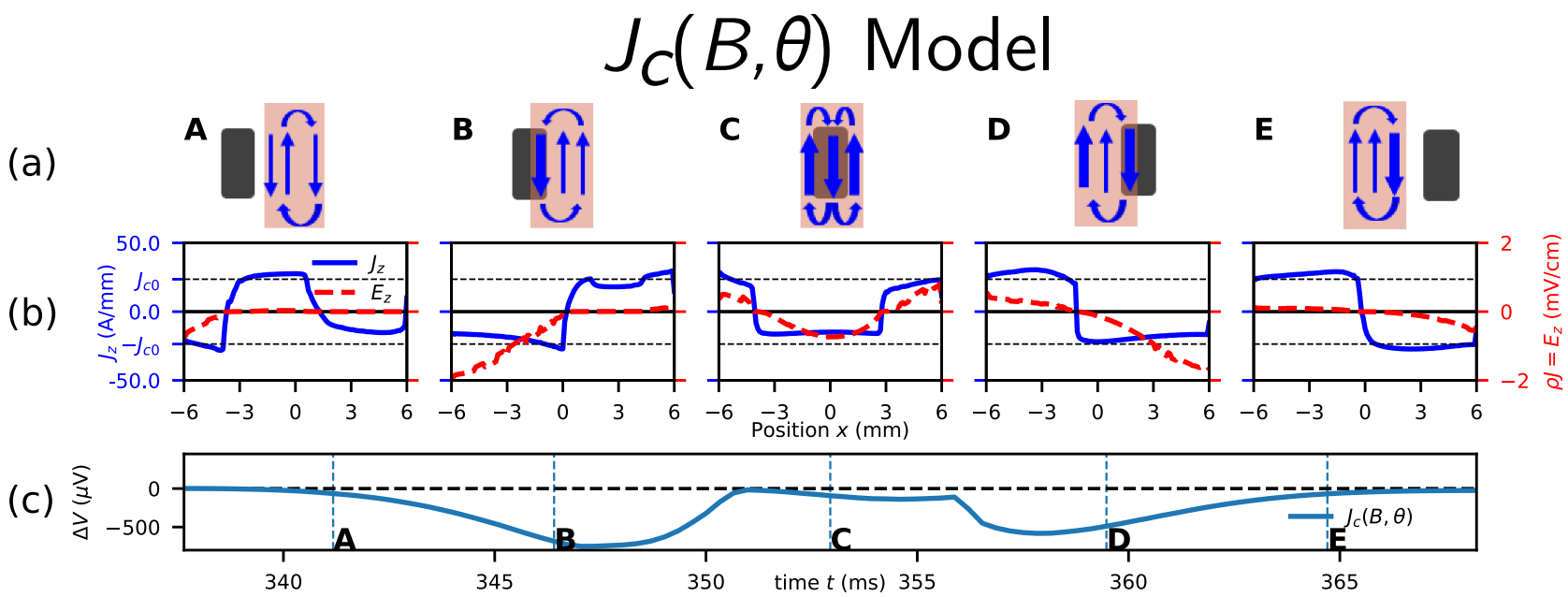

Figure 5-6: (a) Schematic denoting key magnet positions A-E and the eddy currents flowing in the stator tape at each moment. (b) Calculated profiles of J_z and $E_z = \rho J_z$ across the tape at each magnet position for the $J_c(B,\theta)$. model (b) Calculated ΔV waveform for the constant J_c model showing points corresponding to each profile depicted in (b) above.

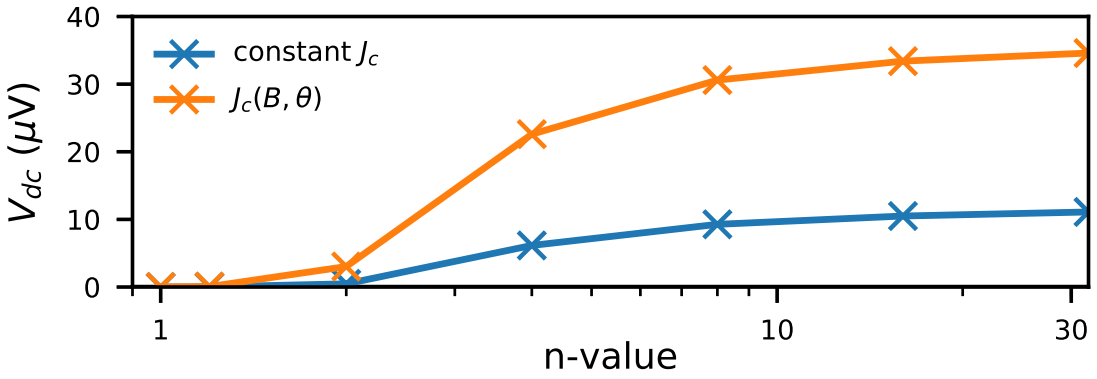

Figure 5-7: Plots of V_{dc} vs n, obtained from calculations using each of the different functions for the HTS resistivity ($J_{\mathrm{c}} = const.$ or $J_{\mathrm{c}}(B,\theta)$).

and the forward- and reverse-current regions are approximately equal in width. As a result, $|J_{\mathrm{z}}| > J_{\mathrm{c}}$ across the full width of the tape. At this position forward and reverse components of the internal field approximately cancel, such that $\Delta V \approx 0$. Position C also denotes the point at which eddy currents within the stator switch from counter clockwise to clockwise, with points D and E representing the reverse situations for B and A respectively, with eddy currents now flowing in counter-rotation. Figure 5-5 (c), illustrates that the ΔV (or E_{ave}) waveform, emerges from the evolving average internal electric field across the tape (fig. 5-5(b)). Similar current profiles are obtained for the $J_{\mathrm{c}}(B,\theta)$ case in fig. 5-6. However, in this case, J_{c} is depressed in the high-field region beneath the magnet, meaning that less current needs to flow for the same level of electric field, and hence less current needs to return, when compared to the $J_{\mathrm{c}} = const.$ case.

5.3.3 Influence of n-value

Figure 5-7 shows further evidence that non-linear resistivity is the only necessary condition to obtain a non-zero V_{dc} from the dynamo. This plots calculated values of V_{dc} as a function of $n-$value for both the $J_{\mathrm{c}} = const.$, and $J_{\mathrm{c}}(B,\theta)$ models. Higher values of n denote greater non-linearity in resistivity and it is clear that this leads to greater V_{dc} in both cases. Importantly we also see that when $n = 1$ then V_{dc}=0 in both cases. This means that a linear resistivity which is magnetic field dependent, is not

sufficient by itself to deliver a partial rectification effect. This contradicts previously proposed explanations of dynamo operation based on magneto-resistance, which was proposed by Giaver [77].[3]

While not investigated here, an extension of this model to LTS dynamos could be achieved by appropriate treatment of n-value. While $n(B, \theta)$ data from HTS tapes did not produce a meaningful impact in this model, and was hence not explored further, this is not true of LTS. The production of a normal spot could be captured in by $n(B, \theta) \to 1$ as $B \to B_c$.

5.4 Summary

These results show that the time-averaged dc output voltage obtained from an HTS dynamo arises naturally from a local rectification effect caused by overcritical eddy currents flowing in the HTS stator sheet. This is a classical electromagnetic effect, and eq. 5.9 implies that any dynamo for which the stator comprises a material with non-linear resistivity should output a non-zero dc voltage - although the very small eddy currents expected in any non-superconducting stator would make the effect rather difficult to measure[4].

Furthermore, a significant increase in V_{dc} can be achieved through the use of an HTS stator wire which exhibits a strong decrease in J_{c} under a perpendicular magnetic field. Fortuitously, such behaviour is commonly observed in thin film REBCO coated conductors [95,120], although modern commercial REBCO wires increasingly include artificial pinning centers to counteract this effect. These 'advanced pinning' wires are unlikely to represent the optimal material for HTS dynamo construction.

[3]The method here of decreasing n potentially yields an extremely conductive material in the $n = 1$ limit. Other normalisations of the E-J law, where J_c is scaled down along with n could be considered, such that $\rho_{sc} = \rho_{cu}$ as $n \to 1$

[4]We will come back to this point in ch. 8.

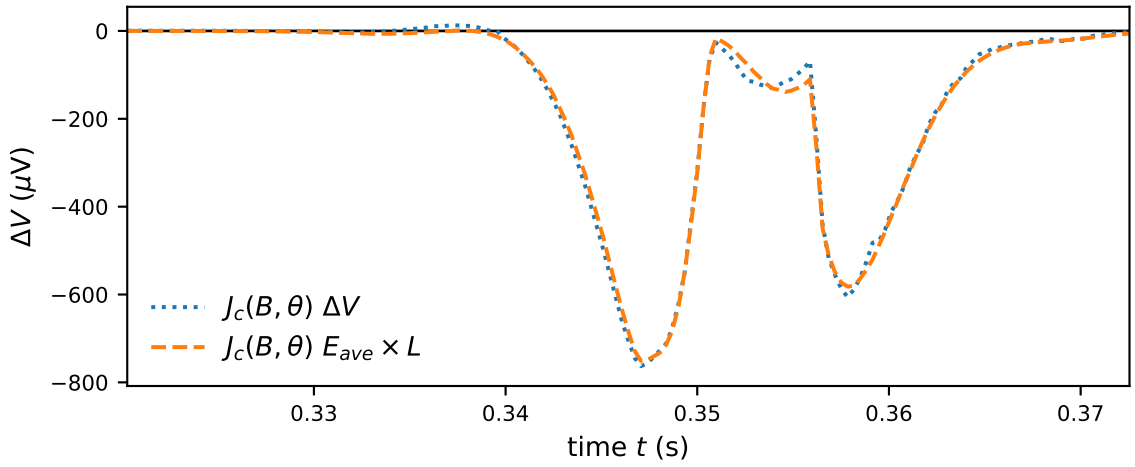

Figure 5-8: ΔV as calculated in [107] vs $\Delta V = E_{\text{ave}} \times L$ as described in this work.

5.5 Afterword: E_{ave} vs ΔV

In the original paper [107] the equivalent figure to fig. 5-5 showed the result of a more convoluted expression for ΔV that actually involved modelling both the normal conducting situation and the superconducting situation. Essentially, the solution of the H-formulation model was then fed into an A-vector formulation model so that A_{z} and V could be solved for explicitly. The situation then called for subtracting the two models from each other, in a similar procedure to the experimental analysis. In the course of that work, it became apparent that this was unnecessary, and that E_{ave} did, in its own right, directly correspond to the value of ΔV. This was initially a numerical observation that required additional thought, which is now captured in eq. 5.6. To close this issue permanently fig. 5-8 shows the result reported in fig. 5-4 vs the result originally reported in [107] for $J_{\text{c}}(B,\theta)$.

Chapter 6

Characteristics and behaviour of the HTS dynamo

Foreword

The following chapter is largely reproduced from [108], with the permission of APS Publishing. All content included is from the final accepted manuscript. Changes have been made largely to match the overall structure of this thesis, including much the introductory material and theory being moved to ch. 5. I would also like to thank and acknowledge Dr. Andres (*Olly*) Pantoja for his experimental work on these devices; experimental results presented in this chapter were undertaken by Dr. Pantoja.

6.1 Introduction

Before the work presented in ch. 5, all engineering improvements to the HTS dynamo had been made empirically through intuition, empirical scaling, and old fashioned trial and error. But without a predictive numerical model other, more exotic, explanations continued to abound. These explanations would then also affect how one thinks about improving the performance and characteristics of the devices. Furthermore, there was a growing amount of experimental data within the Robinson laboratory that was going unpublished, without a predictive theory in which to contextualise such data.

Here, I now describe an expansion of the HTS dynamo model introduced in [107], and presented in ch. 5, to provide a detailed explanation of how the non-linear resistivity changes the electromagnetic physics of the HTS dynamo, and hence gives rise to the dc voltage component over its full range of operation.

In ch. 5, FE modelling was used to show that the open-circuit voltage output arises due to the presence large over-critical eddy currents which flow in the HTS stator for a short period of each rotor cycle, and act to 'partially rectify' the induced *emf*. In this chapter this is extended to model the *closed-circuit* case, thus enabling current and voltage outputs to be fully calculated for the full range of operating conditions of the device. I show that this simple 2D model captures all of the essential electrical behaviour which has been observed by experiment [71, 74, 96].

6.1.1 Chapter overview

The following chapter first introduces specific experimental details in sec. 6.2, as they differ and expand on those presented in ch. 5. In a similar fashion sec. 6.3 outlines extension of the model to produce the results presented here.

A large number of results are presented in sec. 6.4, beginning with dc characterisations in sec. 6.4.1, including linear dc I-V characteristics, linear frequency dependencies of both internal resistance and output voltages. This is then extended to transient characterisation in sec. 6.4.2, which also examines the instantaneous resistance of the dynamo. With a feel for examining transient behaviour, additional, spatially-resolved, magnetic field data is compared from the models and experiments in sec. 6.4.3, which confirm the existence of large over-critical currents in the HTS stator. Such currents are then interrogated directly in the model in sec. 6.4.4.

All of these results form the basis of discussion in sec. 6.5 where five main points are examined. First, sec. 6.5.1 expands on the core question of the dc voltage origin, expanded in light of the presented models. Secondly, the nature of the dc voltage and the internal resistance is discussed in sec. 6.5.2 as they relate to each other. Third, sec. 6.5.3 argues that the short circuit current of the HTS dynamo is an emergent — non fundamental — quantity determined by the dynamics of the internal resistance

and dc output voltage. Fourth, sec. 6.5.4 presents a motivated discussion of how the dynamic resistance evolves with transport current in the HTS dynamo and asserts that such resistance can be reduced by increasing stator width. Finally, the fifth major observation of a "partially penetrated" regime is discussed and contextualised in sec. 6.5.5. A summary is then presented in sec. 6.6.

6.2 Experimental methods

Data was collected using an experimental HTS dynamo similar to that presented in ch. 5 and used in [96] and is depicted in fig. 6-1(a). The dynamo stator was made from 12 mm wide SCS12050 AP SuperPower Inc HTS coated-conductor tape, rather than the SuperPower CF tape used in ch. 5. The transport critical current, I_c, of the stator tape used here was measured and found to be 293 A at 77 K (using the 1 μV/cm criterion). A 12.7 mm long, 12.7 mm deep and 3.2 mm wide Nd-Fe-B permanent magnet, magnetised through its depth, is mounted within an aluminium rotor such that the outer face of the magnet is rotated about a radius of 35 mm. The remnant magnetisation of the Nd-Fe-B Magnet is taken as 1.3 T[1]. The stator tape is positioned perpendicular to the plane of rotation such that the vector normal to the tape surface faces in toward the rotor axis, with a flux gap g of 3.7 mm between the stator tape and the rotor circumference. The ends of the stator tape are then soldered onto copper current leads that connect to an external electronic current supply. The combination of the leads and the external current supply act as an electronic load for the output of the HTS dynamo [68, 110], see fig. 6-1(c).

An example open-circuit waveform for one rotor cycle is shown in fig. 6-2(b). An issue arises when seeking to measure the $\Delta V(t)$ waveforms in the presence of a net transport current $|I_T| > 0$, as $V_{300K}(t, I_T)$ is not available due to the inability to transport large currents through the stator in the normal conducting state at 300 K.

[1]Note that this is slightly larger than the value used in ch. 5.

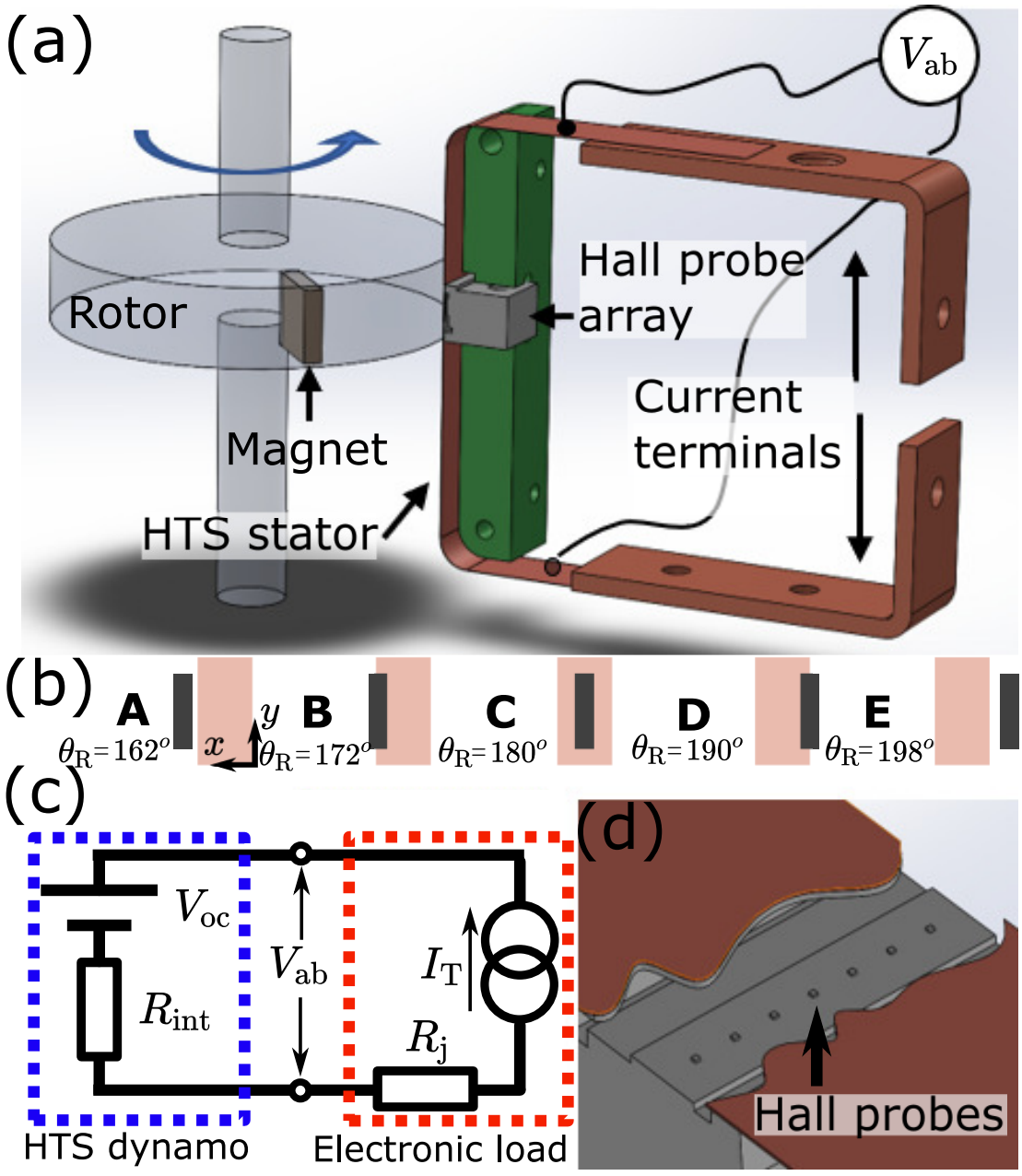

Figure 6-1: (a) Schematic of the HTS dynamo, including the rotor magnet, rotor housing, HTS stator, voltage leads, Hall probe array, and the current terminations. (b) Illustrated key rotor positions θ_R, as viewed from the Hall probe array rotor. (c) Circuit diagram showing the dynamo as a voltage V_{oc} and internal resistance R_{int}, and the current source, current leads, termination blocks, and joints combined into a single electronic load R_j. (d) Cutaway from the rotor side of the stator showing the Hall probes in the array.

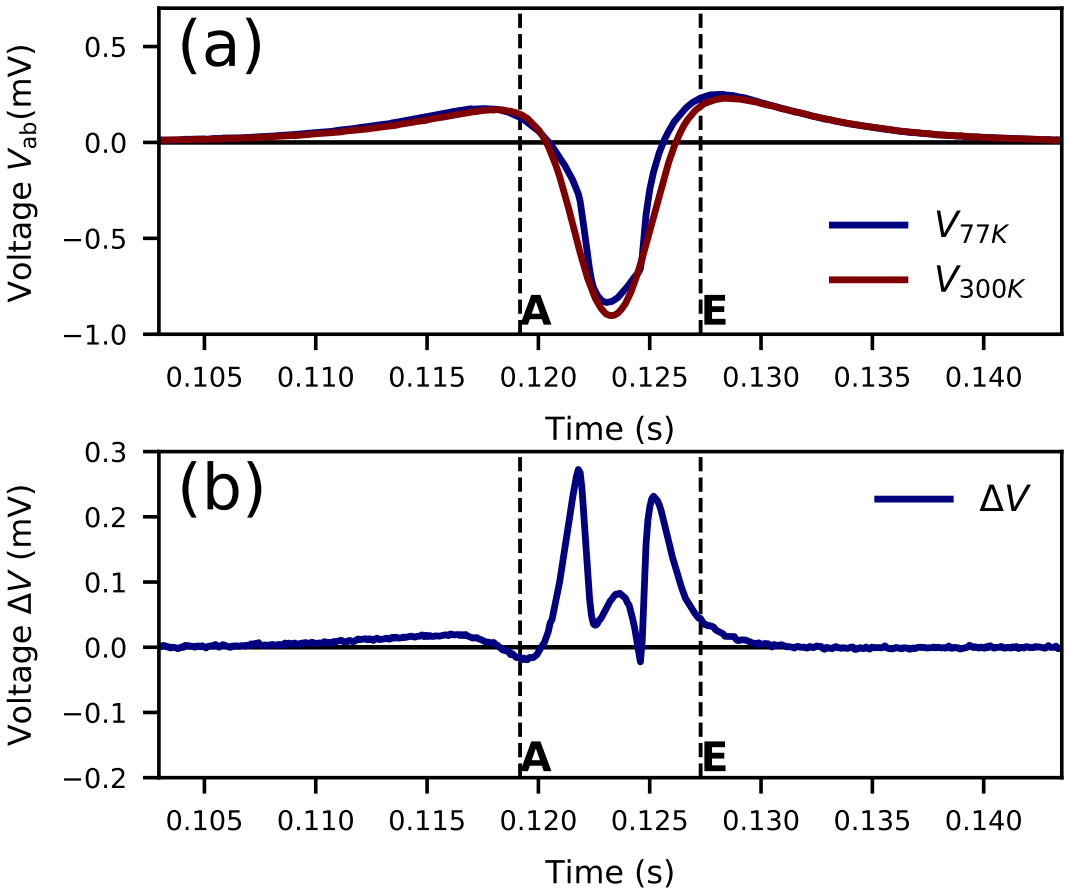

Figure 6-2: (a) Comparison between 77 K and 300 K voltage pulse measurements for the dynamo operating at 12.33 Hz as the magnet transits the stator. (b) Voltage difference ΔV, as defined in eq. 5.1, showing a clear dc bias in the 77 K waveform.

Hence more generally, we define:

$$\Delta V(I_{\mathrm{T}}, t) = V_{77\mathrm{K}}(I_{\mathrm{T}}, t) - V_{300\mathrm{K}}(0, t). \tag{6.1}$$

where, $V_{300\mathrm{K}}(0, t)$ still captures the *emf* contribution assuming a static and/or uniform transport current.

Underneath the HTS stator tape, an array of 7 Arepoc cryogenic Hall probes were mounted approximately 0.5 mm away from the tape surface, measuring the component of the magnetic field perpendicular to the tape, B_{y}. Again, measurements of the magnetic field were taken at 77 K, $B_{77\mathrm{K}}$, and 300 K, $B_{300\mathrm{K}}$. As the Nd-Fe-B magnet exhibits approximately the same magnetisation at these two temperatures, any difference between the measured magnetic fields must be caused by currents flowing in the HTS tape:

$$\Delta B(x, t) = B_{77\mathrm{K}}(x, t) - B_{300\mathrm{K}}(x, t) = \mu_0 H_{\mathrm{y}}(x, t), \tag{6.2}$$

where H_{y} is the perpendicular auxiliary field due to the free currents in the conductor.

A major restriction in the experimental data presented is that hall probe zero-field offsets are temperature dependant, but also susceptible to drift over the course of a day. The method used experimentally was to record a zero field offset before each measurement. While the magnet can be moved reasonably far from the tape, unfortunately remnant magnetisation makes recording a zero field offset impossible once the tape has been exposed to the magnet. This means that magnetic field data recorded too far into a day, where a re-measurement of the offset would be necessary, cannot be used due to the drift of the signal voltage. The experimental data set presented in this chapter happens to fulfil the criteria that the very first offset measurement was enough to cover the entire data set.

The rotor and stator assembly of the device was placed in a bath cryostat, with 77 K measurements made following submersion in liquid nitrogen. Mechanical power to the rotor was provided through a G10 composite shaft connected to an external servo motor at room temperature. The servo motor control enables a selection of

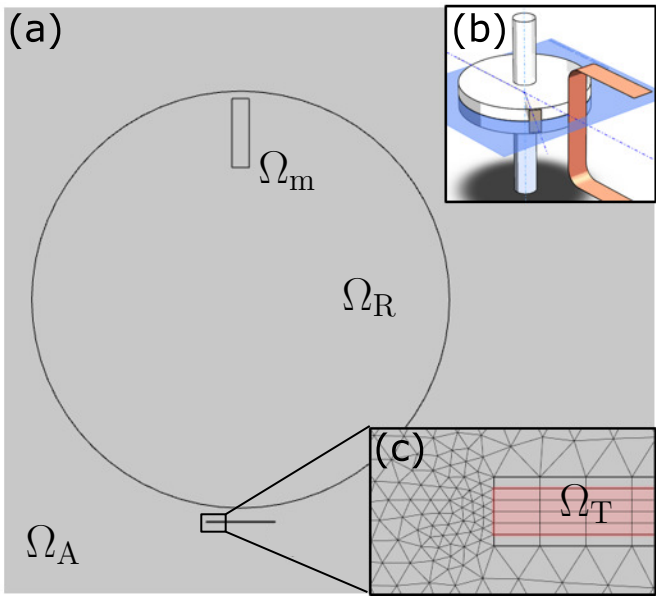

Figure 6-3: (a) 2D model of the bisecting plane, with the Air Ω_A, rotor Ω_R, tape Ω_T, and magnet Ω_m domains. (b) Inset showing a 3D schematic of the dynamo stator and rotor, and the modelled bisecting plane. (c) Magnified view of the Tape domain Ω_T and FE model mesh.

rotational frequencies, 178, 255, 365, 520, 740, 1051, and 1490 RPM. Measurements were taken using a single magnet in the rotor assembly, such that there was a 1:1 relation between motor speed and applied magnetic field frequency f at the stator tape. At each rotor speed the full I-V curve was examined by adjusting the net current flowing through the stator tape, using the Agilent 6680A #J04 current supply to step in 2 A increments.

6.3 Model construction

As in ch. 5, to calculate $E_{\text{ave}}(t)$ we must calculate the full solution for $E_z(x, y, t)$ in the modelled plane. As argued previously, I take advantage of the device's reflectional symmetry to reduce the problem to the 2D plane bisecting the stator and rotor. In this arrangement, shown in fig. 6-3(a), the x axis is defined to be oriented along the width of the tape, the y axis along its thickness, and z axis as out of plane.

The 12 mm wide superconducting layer is modelled as a 100 μm thick domain. As in ch. 5, this avoids the logarithmic singularity solutions for 2D conductors [121],

and therefore improves convergence times [87, 103]. The copper stabiliser of the tape is modelled as two 25 μm domains on the top and bottom surfaces of the superconducting domains. The resistivity of copper is assumed to be electrical grade, $\rho_{\mathrm{Cu}} = 0.19\ \mu\Omega$cm.

In this chapter results are presented exclusively for an FE model employing eq. 2.3 for the resistivity of the HTS wire. We take $J_{\mathrm{c}}(B, \theta)$ as measured experimentally in the SuperCurrent facility at Robinson Research Institute [16,95]. The specific data for the SuperPower AP tape used is shown in fig. 3-9 (note the differences to fig. 3-8) and then normalised by the self-field critical current of the stator $I_{\mathrm{c}} = 293$ A.

To account for a net transport current I_{T} the external power supply is considered to be an ideal current source. Therefore the currents in the tape are restricted to obey:

$$I_{\mathrm{T}} = \int_{\Omega_{\mathrm{T}}} \vec{J} \cdot d\vec{a} = \oint_{\partial\Omega_{\mathrm{T}}} \vec{H} \cdot d\vec{l}, \tag{6.3}$$

where I_{T} is giving externally to the problem. Finally, the whole model is bounded on $\partial\Omega_{\mathrm{A}}$, taken 300 mm away from the center, where $\hat{n} \times \vec{B} = 0$.

Each model is run for a total of 3 cycles (learning from ch. 5). During the first cycle, the transport current is arbitrarily[2] distributed but despite this, on the second and third cycle the system is found to be periodic, and hence no further cycles are necessary. To capture the effect of frequency and transport current, the models were run with different rotational speeds of the rotor shell current J_{s}, and different values for I_{T}.

6.4 Results

In this section, measured dc values are presented, in sec. 6.4.1, which highlights that the model agrees with experiment over a large range of parameters, but does not test the local dynamics of the model directly. Next, transient electrical waveforms are presented, in sec. 6.4.2, which confirms that the model replicates the dynamics of

[2]For the first instant of the model, the solution is nearly singular with all current concentrated in one corner element of the model.

the system. Then, locally collected magnetic field data is shown, in sec. 6.4.3, that confirms dynamic spatial agreement between the model and the experiment. This finally justifies presenting modelled current distributions, in sec. 6.4.4, which give deeper insight into the dynamo's operation.

6.4.1 DC characterisation

The HTS dynamo can be characterised as a simple voltage source, as shown in fig. 6-1(b), with an open-circuit voltage V_{oc}, an internal resistance R_{int}, and a short-circuit current I_{sc}. Figure 6-4 presents dc (time averaged) values from the electrical characterisation of the experimental device and the FE model. I-V characteristics from the model, fig. 6-4(a), and experiment, fig. 6-4(b), are presented. From these I-V characteristics, the key idealised parameters V_{oc}, V_{oc}/f, I_{sc}, and R_{int} can be extracted, as shown in fig. 6-4(c) - (e) respectively. Broadly speaking the model reproduces the I-V behaviour observed in experiment. At every frequency, the slope of the curves in fig. 6-4(a) and (b) is essentially linear, implying a constant internal resistance R_{int}. The magnitude of the values is clearly similar.

While the modelled V_{oc} includes a factor, L, from the extrapolation, see eq. 5.12, the short-circuit current I_{sc} should not. That is, as we extrapolate the model from the 2D plane the amount of current flowing through the plane is unaffected. Hence, fig. 6-4(c) provides the most stringent test of the model's accuracy. From this we see that the model reproduces the behaviour extraordinarily well, with only a 5% deviation from the experimental I_{sc} values at frequencies > 5 Hz. The factor L, which is the only geometric degree of freedom, was determined by fitting V_{oc} for the 5 matching frequencies from fig. 6-4(c). This gives a fitted value $L' = 10.2$ mm which is strictly smaller than the geometric length $L = 12.7$ mm. Note that $L' < L$ is expected given the divergence of the field in 3D. Figures 6-4(d-f) present both the the results from the raw model and the scaled values.

One of the most widely accepted behaviours of the HTS dynamo is the linear dependence of output voltage on frequency. This behaviour is borne out in the models. Figure 6-4(d) compares the measured V_{oc} with the values extrapolated from the model,

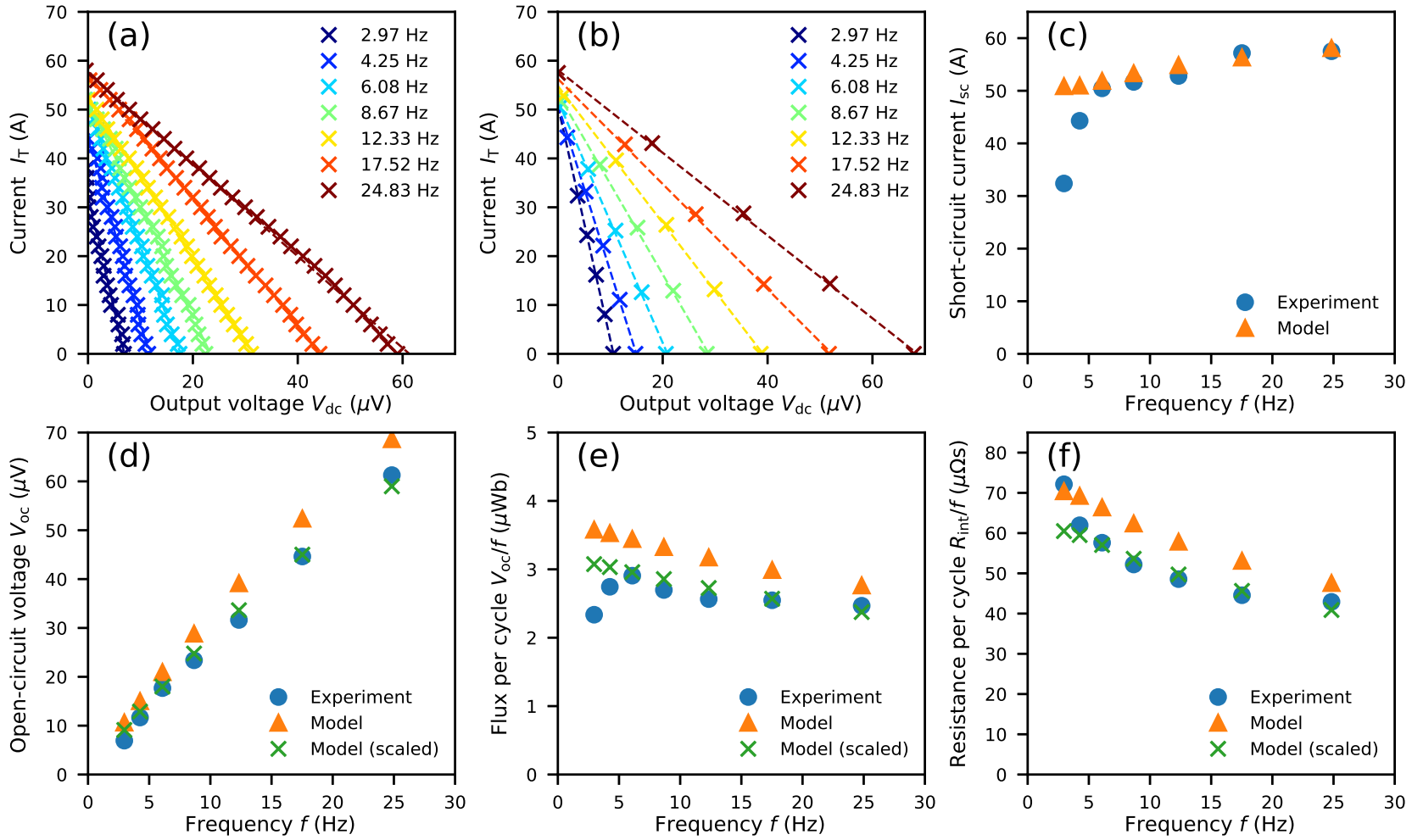

Figure 6-4: Comparison of the dc electrical characterisation of the HTS dynamo for experimental and modelled values. (a) Modelled, and (b) experimental I-V characteristics for various frequencies. (c) modelled and measured short-circuit current I_{sc} vs frequency. (d) Comparison of measured, modelled, and scaled open-circuit voltages V_{oc} vs frequency f. (e) Frequency normalised open-circuit voltage (flux per cycle) vs frequency. (f) Frequency normalised internal resistance R_{int} vs frequency.

showing that while the unscaled model overestimates the output, the linearity is indeed reproduced. To examine the behaviour more closely, fig. 6-4(e) normalises the output voltages by the rotational frequency, exaggerating the deviations from the linear behaviour. We can see that the experimental data shows a small scatter around what could be assumed to be a constant value, and hence an assumption of linearity is justified. This scatter is not present in the modelled data, showing a clear non-linear component.

A central question of the device is the nature of the internal resistance, and whether it can be appropriately described in the context of dynamic resistance effects reported elsewhere [72, 105]. The scaled model and experimental data show tight agreement for the internal resistance of the device, including the downward trend in resistance per cycle for increasing frequency.

The interplay between V_{oc}, R_{int}, and I_{sc} highlights that the dynamo cannot be simply explained via flux transfer across the stator tape. For example, the simplest flux transfer models would predict a constant flux per cycle. This is even more interesting when considering that the internal resistance per cycle of the device not only drops — but drops faster than the flux transferred per cycle, as evidenced by the increasing I_{sc} with frequency.

6.4.2 Transient characterisation

The HTS dynamo is not a dc device, and its transient behaviour can be measured to test the model. Figure 6-5 shows several of the key ΔV waveforms from the scaled models and experiment. All the qualitative features are replicated in the transient behaviour of the models. Furthermore, quantitative agreement is again achieved by using the scaled value for L', further implying that no qualitatively important physical effects have been left out of the model.

Figures 6-5(a) and (b) show that, when normalised by frequency and plotted vs rotor position θ_{R}, the open-circuit ΔV falls onto the same curve for all frequencies measured or modelled. The small deviations from linear scaling can be attributed to specific moments in the cycle. This indicates that while frequency has an effect, as

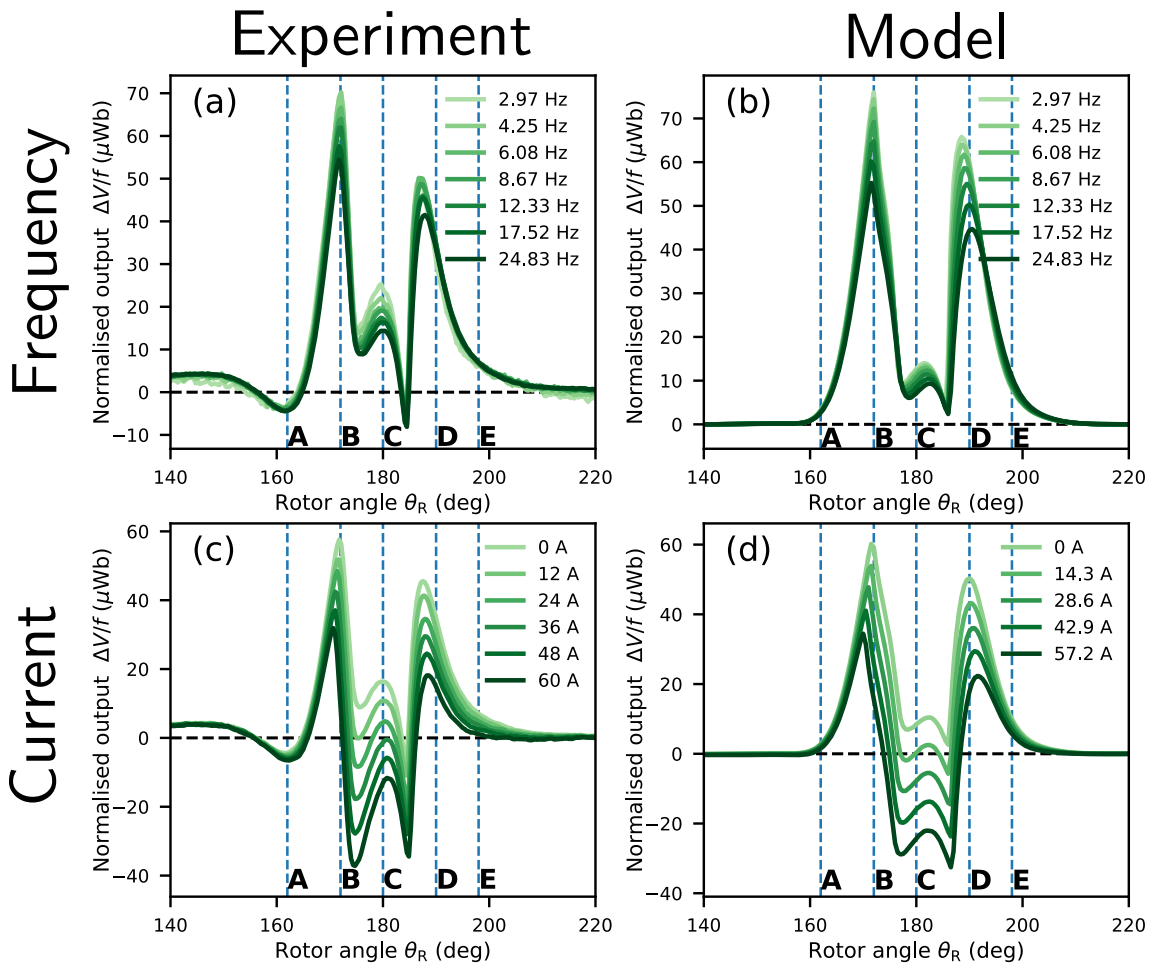

Figure 6-5: Transient ΔV waveforms measured, left column, and modelled (scaled), right column. The points marked **A** to **E** match those defined in fig. 6-1(b). (a) and (b) show open-circuit frequency normalised ΔV vs rotor angle at several different frequencies. (c) and (d) show $\Delta V(I)$ waveforms for increasing transport current for 17.5 Hz.

shown in fig. 6-4, the effects are only small but systematic adjustments to a broadly similar behaviour. Figures 6-5(a) and (b) show the key qualitative features of the HTS dynamo 'rectification', i.e., that it occurs primarily as the magnet enters $\mathbf{A} \rightarrow \mathbf{B}$, and exits $\mathbf{D} \rightarrow \mathbf{E}$. This is seen in the two dominant peaks. Figures 6-5(a) and (b) also show some important qualitative differences; fig. 6-5(a) has a clear lift as the magnet approaches and $\theta_{\mathrm{R}} < 155^{o}$, this lift, and subsequent dip, are not present in the modelled value. This is the clearest example of how our approximation in eq. 5.6 breaks down. However, the break down in the approximation does not obscure our ability to identify the dominant behaviours.

The appearance of the internal resistance can be seen in figs. 6-5(c) and (d), which show how each ΔV waveform changes with the increasing current through the stator. From these curves we can see that the dynamic resistance appears as a reduction in the output voltage waveform. Not only is this reduction localised to the voltage generating portion of the cycle, where the magnet is over the stator, but also seems to peel the waveforms away from each other at around point **B**. This peeling indicates that there is a portion of the cycle that does not experience the internal resistance, and that this portion reduces with increasing current. Furthermore, changes in the middle of the wave forms between $\mathbf{B} \rightarrow \mathbf{D}$ clearly indicate that the initially (open-circuit) low output during these times is not due to a lack of dynamics, but rather coincidental to the lack of transport current.

A further question regarding the internal resistance is its apparent constant value for any fixed frequency. This could simply be a coincidence, hidden by the dc time average used in fig. 6-4. To avoid this we can consider the instantaneous resistance:

$$R_{\mathrm{inst}} = \frac{V_{77\mathrm{K}}(I_{\mathrm{T}}, t) - V_{77\mathrm{K}}(0, t)}{I_{\mathrm{T}}} \tag{6.4}$$

$$= L' \frac{E_{\mathrm{ave}}(I_{\mathrm{T}}, t) - E_{\mathrm{ave}}(0, t)}{I_{\mathrm{T}}}. \tag{6.5}$$

Figure 6-6 shows (a) the measured and (b) modelled values of R_{inst} vs magnet position during each cycle. All curves follow the same non trivial shape, just as the frequency-scaled open-circuit voltages in fig. 6-5(a) collapsed onto each other. While we see some

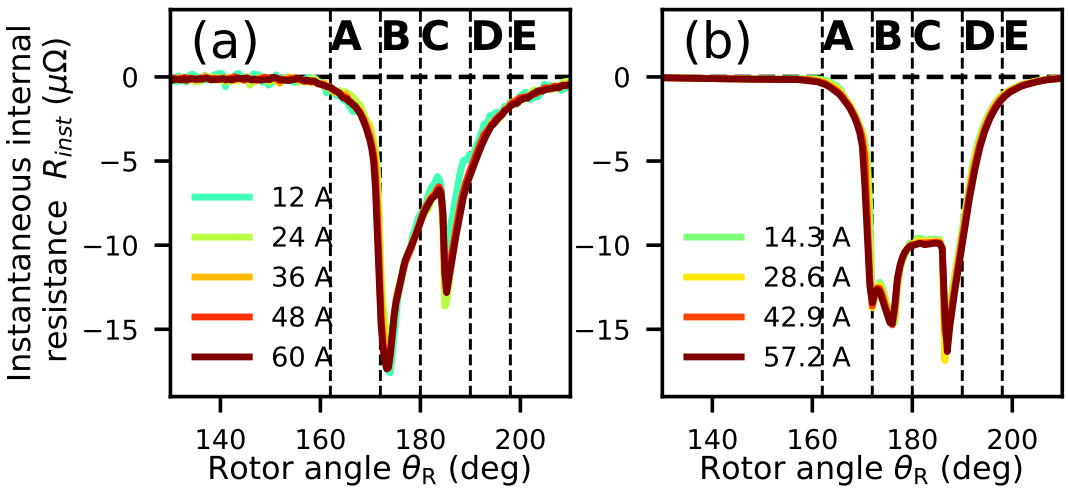

Figure 6-6: Instantaneous resistance R_{inst} values vs rotor angle θ_{R} for the transport currents reported in fig. 6-5 for (a) measured data, and (b) scaled models.

deviations between the model and experiment, again I attribute this to a breakdown in our approximation eq. 5.6, and note that the amount of diamagnetically shielded flux must therefore be highly systematic.

6.4.3 Magnetic field

While dc values are critical for operational predictions, and transient behaviours allow us to confirm the behaviour without the dc time average, all the results presented so far are obscured by the spatial averaging effect of comparing ΔV with E_{ave}, see eq. 5.9. Ultimately, E_{ave} is the result of the spatial dynamics of the over-currents flowing inside the stator. Therefore, if claims are to be made as to the effects of the spatial distributions of these currents, then the model's spatial degrees of freedom need to also be tested against experiment.

Figure 6-7 compares experimental and modelled values for the magnetic field difference ΔB, defined in eq. 6.2, for f =17.52 Hz (clockwise rotation). This is perpendicular to the stator's surface and taken along a line across the width of the stator and 0.5 mm behind it, as shown in Figure 5-2. In the case of the experimental data, the contour plots linearly interpolate the values in between the 7 sensors of the array. For the model itself, the data is taken along a line, 0.5 mm from the tape's back edge,

and is plotted at spatial intervals corresponding to the model mesh density which is sufficiently higher than the experimental data density. The x axis of the contours corresponds to the x position along the width of the tape, whereas the y axis is used to denote the angle of the rotor θ_{R}. Figure 6-7 shows the full cycle of the dynamo, which is dominated by the remnant magnetisation, where the magnet is far from the tape and over-currents relax under flux creep. Here we see the largest disagreement between the model and experiment, with the remnant magnetisation profiles being strikingly different. However, the aim of the model is not to reproduce the flux creep effects in these devices. Note that the n-index was set at 20 as models appeared insensitive to its value, with respect to values of the output voltage, see fig. 5-7. This discrepancy may provide further evidence that a more sophisticated E-J model maybe required, such as the eta-beta model proposed by Riva *et. al.* [122].

Figure 6-8 presents ΔB for the 17.52 Hz data, zooming in to focus on the induced magnetic field during the magnet's transit across the tape, for several different values of the net transport current I_{T}. We see excellent agreement between the model and the experiment during the dynamics of the magnet's transit over the tape. Inspecting fig. 6-8 further, we can identify several features during the transit. We can see the magnet enter from the right hand side of the plot, as the induced current precedes the applied magnetic field. As the magnet travels across the conductor, these shielding currents erase the remnant magnetisation in the conductor. As the magnet leaves, this remnant magnetisation reasserts itself, with a characteristic jump in intensity between **D** and **E**, as the magnetic field suppression of $J_{\mathrm{c}}(B,\theta)$ subsides. Finally, with the magnet clear of the conductor, we see a slow decay of these currents into the final remnant magnetisation.

Looking at fig. 6-8, notice that the response is almost unchanged with the addition of transport current. The easiest way to identify that there is a change at all is to focus on the center of the remnant magnetisation as it shifts to the left. Spanning the I-V characteristic of the device, from $I_{\mathrm{T}} = 0$ to $I_{\mathrm{T}} = I_{\mathrm{sc}}$, we see essentially no change in the shielding behaviour of the device. And yet, the ΔV waveforms in figs. 6-8(c) and (f) clearly capture the reduction in output voltage.

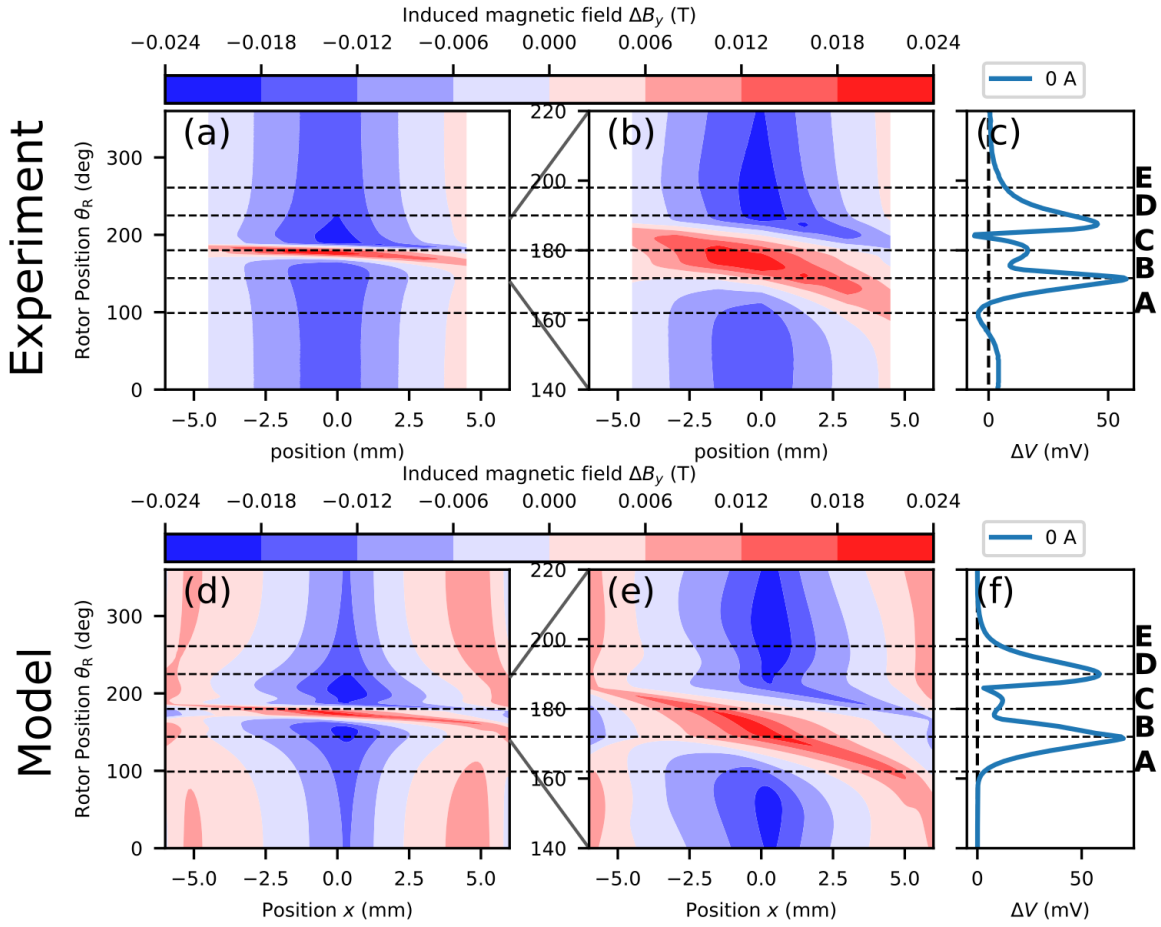

Figure 6-7: Induced magnetic field ΔB across the width of the tape (x-axis) vs rotor angle θ_{R} (y-axis) at 17.52 Hz clockwise rotation (right to left). (a) Measured values from 7 Hall probes at 0.5 mm from the stator. (b) Zoomed view of (a). (c) Measured ΔV for (b). (d) modelled data from full width of tape, at the same distance from the tape. (e) Zoomed view of (d). (f) Scaled ΔV for (e).

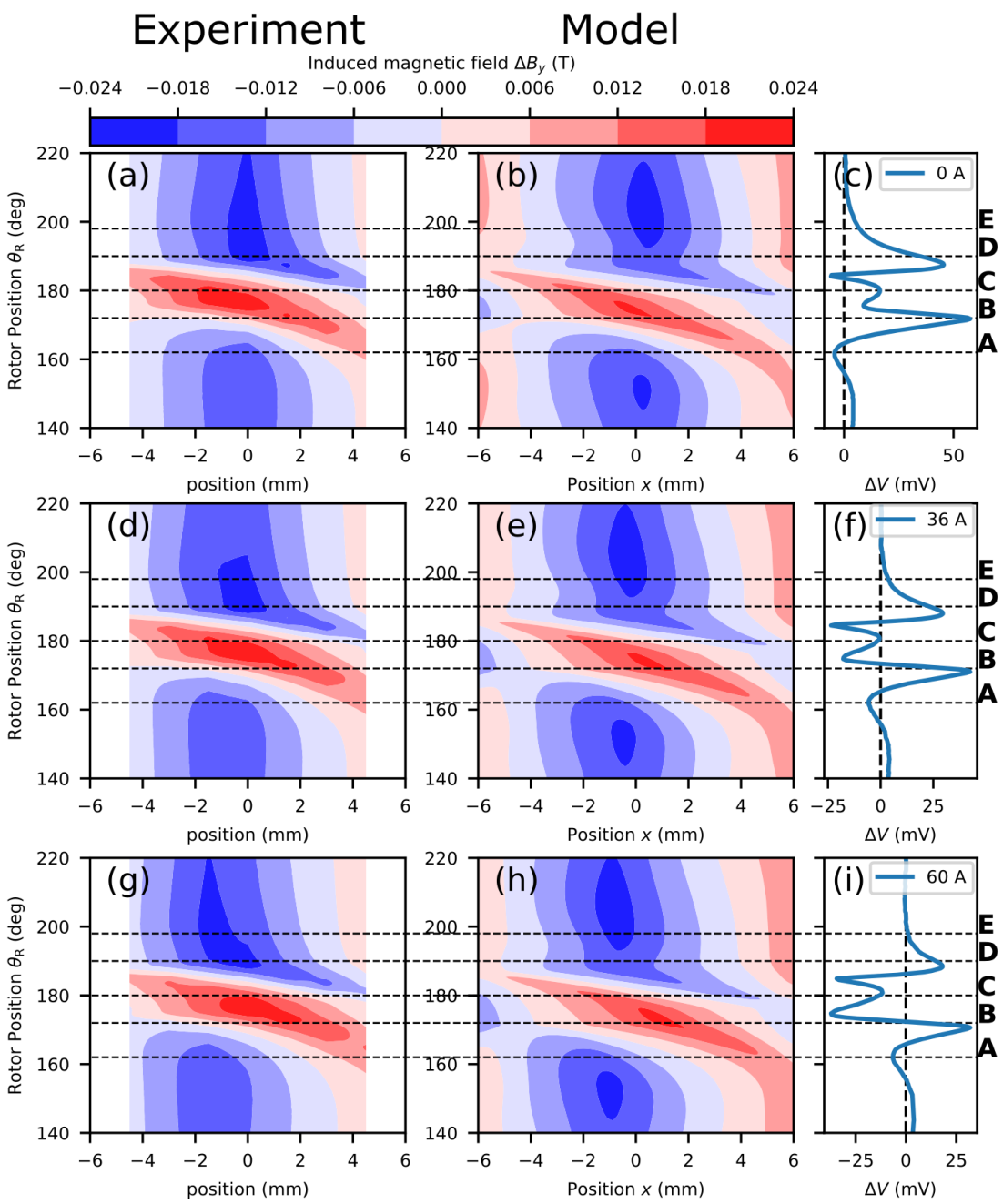

Figure 6-8: Induced magnetic field ΔB position along tape width x and rotor angle θ_R contour plots for measured and modelled values at several net transport currents for 17.52 Hz clockwise rotation (right to left). (a), (b) Measured and modelled ΔB respectively at $I_T = 0$. (c) Measured ΔV at $I_T = 0$. (d), (e) Measured and modelled ΔB respectively at $I_T \approx 0.5 I_{sc}$. (f) Measured ΔV at $I_T \approx 0.5 I_{sc}$. (g), (h) Measured and modelled ΔB respectively at $I_T \approx I_{sc}$. (i) Measured ΔV at $I_T \approx I_{sc}$

6.4.4 Current maps

Ultimately it is our goal to reconstruct the dynamics of the device, which are determined by the dynamics of the underlying current flows $\vec{J}$. As ΔB is the induced magnetic field from those currents, we can make the desired conclusions from the calculated current density $\vec{J}$ with some certainty given a correspondence between the measured and modelled values of ΔB.

Figure 6-9 shows several contour plots (constructed similarly to fig. 6-7) of the current densities flowing through the tape at each part of the cycle for both HTS and copper stators. Note that the current density shown here is the sheet current density defined by:

$$K_{\mathrm{z}} = \int_h J_{\mathrm{z}} dy, \tag{6.6}$$

where, h is the thickness of the tape. During the transit of the magnet, the current density in the HTS is significantly higher than the critical current of the tape, $J_{\mathrm{z}} > 1.5 J_{\mathrm{c}}$. This correlates with the fact that the measured voltages imply that the stator has been driven considerably far into the flux flow regime. It also implies that the real device has a significantly different current distribution to any prediction that could be obtained using Bean's critical state model which would limit $J_{\mathrm{z}} \leq J_{\mathrm{c}}$. In contrast, the current distribution in the copper, figs. 6-9(e) and (f), is simply a scaled multiple of the local *emf* fig. 6-9(g). Given the similarity between the *emf* in the HTS (fig. 6-9(c)) and copper (fig. 6-9(g)), we can also conclude that the stator dynamics are dominated by the applied magnetic field for the majority of the magnet's transit. As the conductor is primarily in the flux flow regime, the shape of the electric field is essentially set by the rate of change of the applied magnetic field, via Faraday's law (as the applied field is much larger than the HTS shielding field).

The source of the small difference between the *emf* in the copper and the HTS (fig. 6-9(c) and (g) respectively) can be seen by examining the current densities figs. 6-9(b) and (f). From this we see why it is that the HTS dynamo is capable of generating a non-trivial E_{ave}. That is, at every moment of the cycle, the current densities across the tape must sum to the total transport current, in this case $I_{\mathrm{T}} = 0$. However, that

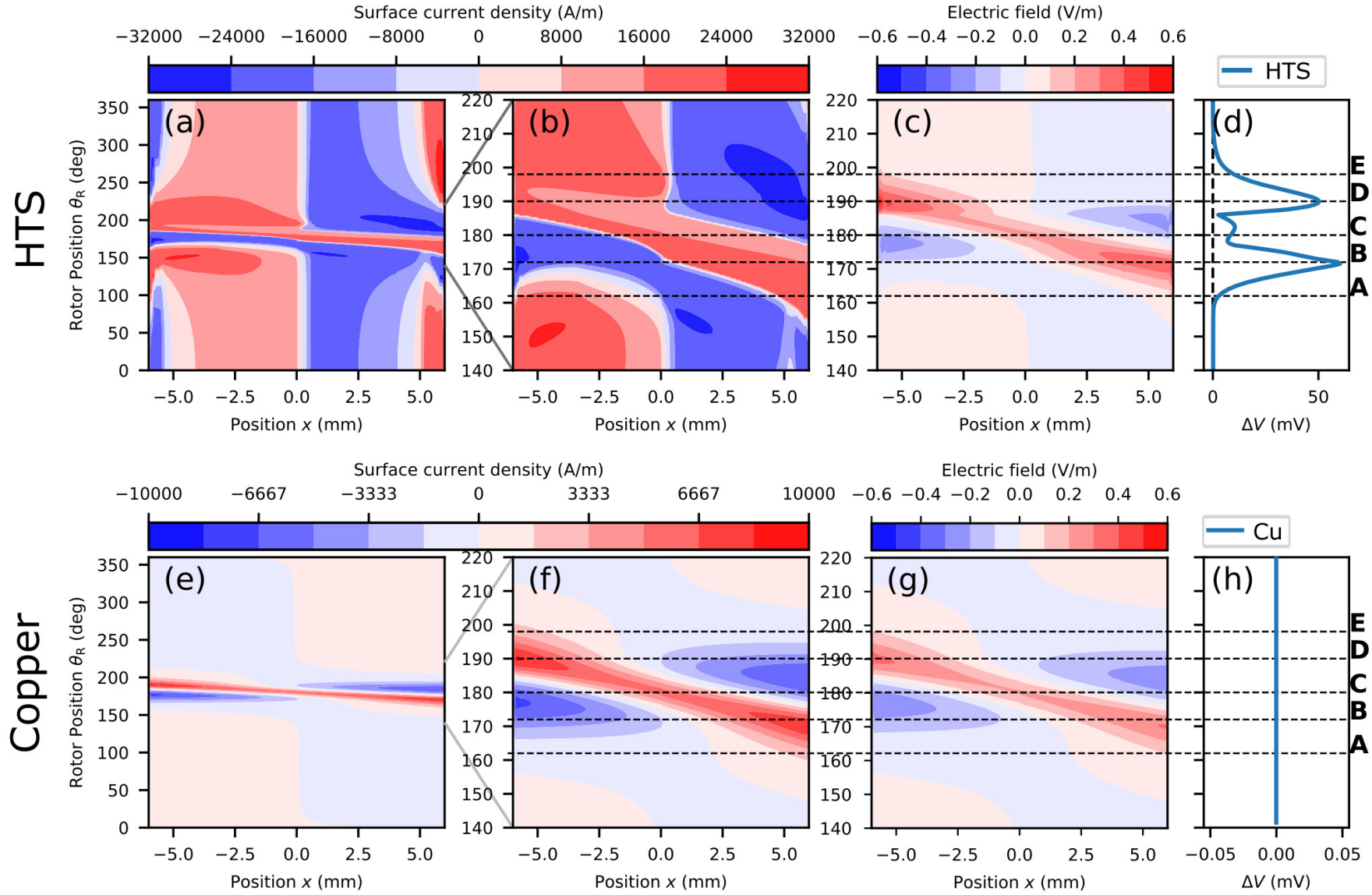

Figure 6-9: modelled sheet current densities, electric field in the superconducting (a)-(d) and normal (e)-(h) stators vs position across the width of the tape x and rotor angle θ_R for 17.52 Hz clockwise rotation (right to left) in open-circuit. (a), (e) Sheet current density for full cycle. (b), (f) Zoomed view of the sheet current density for the magnet's transit. (c), (g) Zoomed view of the local electric field E_z in the sheet. (d), (h) corresponding plot of modelled ΔV equal to zero for copper. Dashed lines highlight key magnet positions.

same constraint is not, by default, applicable to the electric field. In the case of the copper, Ohms' law translates the restriction of net current to a restriction on the average electric field $E_{\text{ave}} \propto I_{\text{T}}$. For the HTS, there is no direct translation between E_{ave} and I_{T}. In both cases the overall distribution of the electric field $E_{\text{z}}(x)$ is quite similar, with the difference being largely captured by the E_{ave} term.

Locally speaking, the output voltage of the dynamo, as a source of electrical energy for a connected load, must be associated with the eddy current underneath the magnet (the red forward current that transitions from right to left), as it has the correct polarity. We can also note that the device is also fundamentally dissipative: no currents ever experience a negative power i.e. $E \cdot J > 0$. Note that the output of the device naturally drives current in the backward direction.

Further inspection of fig. 6-9(c) shows that the magnet continues to provide the desired *emf* (a peak of the electric field distribution, seen as red in fig. 6-9(c)) for the entire transit, as one would have predicted from a normal spot/flux transfer model in the LTS case. However, unlike the the LTS dynamo, the current under the magnet as it transits is considerably larger, and must return in order to maintain the current constraint. It is this return current that both reduces the output between **B** and **D**, but also becomes the driven current I_{T}.

Figure 6-10 shows a snapshot of the current and electric field distributions across the width of the tape, for copper and HTS, at position **C** in the cycle for varying net transport currents. For copper, fig. 6-10(a), we see the expected curves, where the positive peak electric field is under the magnet, and the current densities are simply scaled versions of the electric field profile. For increasing currents, the current distributions in copper shift uniformly downward, resulting in the expected resistive E_{ave}. For HTS we observe that the shape of E_{z} is broadly similar for each current, (as well as to copper), again reinforcing that the shape of the electric field is predominantly determined by the applied magnetic field via Faraday's law. Unlike copper, increasing net currents I_{T} are achieved by shifting the turning points of the current distribution J_{z} inward. However, the effect of changing the position of the current turning points, combined with the observation that the shape of E_{z} is broadly similar

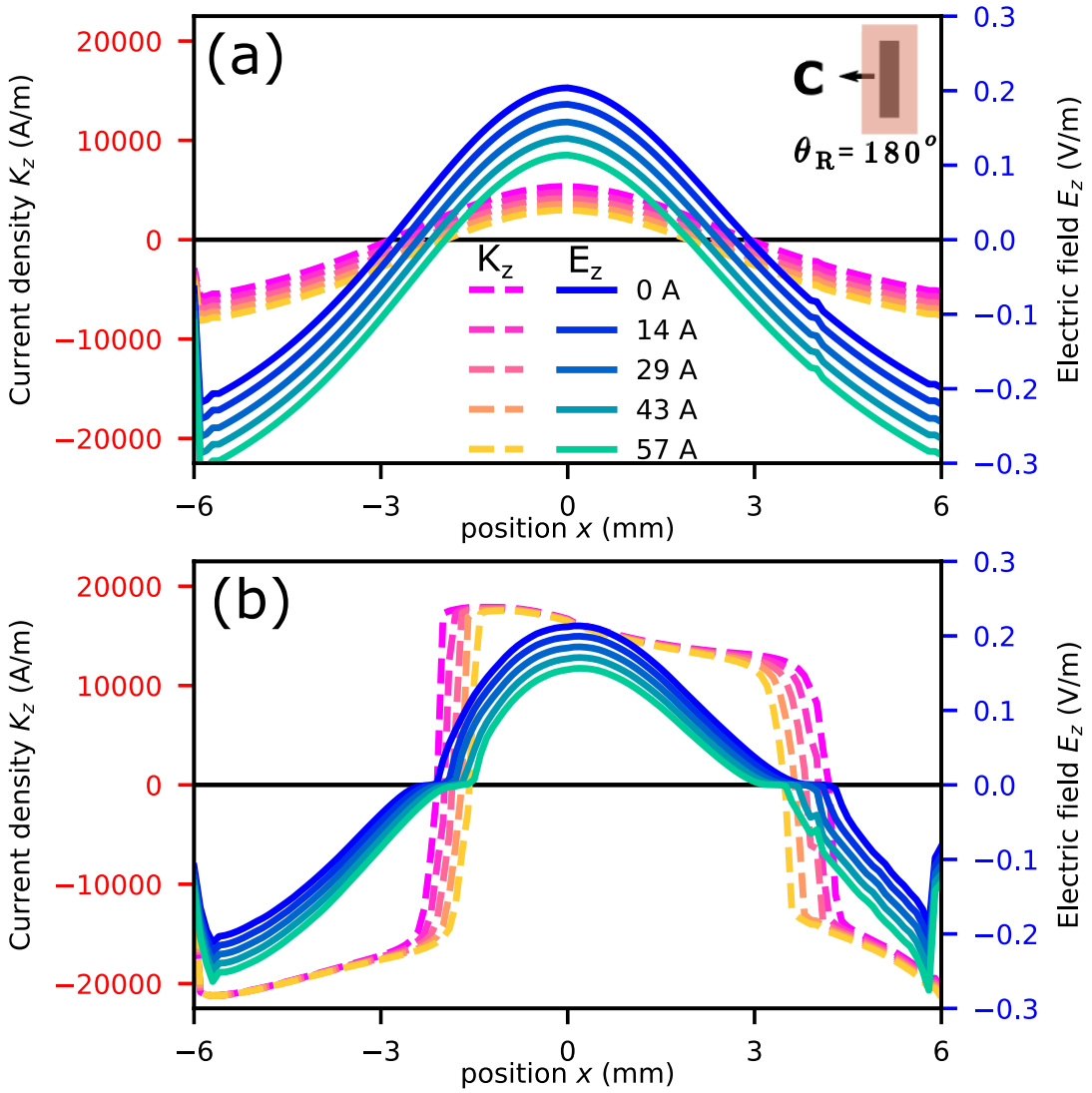

Figure 6-10: Current (dashed lines) and local electric field (solid lines), from $I_T = 0$ (dark shades) to $I_T = I_{sc}$ (light shades) vs position across the width of the tape x, for copper (a) and HTS (b) at rotor position **C**. Data presented for 17.52 Hz. Magnet position is illustrated as viewed from the Hall array.

each time, leads to the simple conclusion that the average electric field is whatever it needs to be in order to satisfy the current constraint on the system.

The shape of $E_z(x)$ is determined by the local-*emf*, i.e. the *emf* that is closed off in the stator tape or equivalently the local curl of the electric field, $\partial_x E_z$. However, the overall level of E_z, i.e. E_{ave}, is governed by the interplay of the current constraint and the shape of E_z itself. Even so, if we consider the HTS dynamo to be a generative device, then the source of E_{ave} must essentially be the local *emf*, as opposed to being externally determined/driven. In this view, E_{ave} is an allocation of the local-*emf* from one polarity or another. Furthermore, the internal resistance of the HTS dynamo corresponds to a reallocation of the applied local-*emf* from the the driving direction (forward eddy current under the magnet) to the output direction (return eddy currents around the magnet), as the current through the device changes.

Figures 6-11(a), (b), and (c) show how the eddy currents redistribute in order to accommodate the transport current I_T at three different positions along the I-V characteristic, matching the ΔB plots presented in fig. 6-8. Here it is useful to distinguish between eddy currents driven by the magnet, and the remnant magnetisation currents that these eddy currents relax into after position **E**. If we focus on rotor positions before the magnet's transit, the transport current is asymmetric with respect to the forward and backward remnant currents, which is similar to the case of the dynamic resistance. As the magnet enters at **A**, the remnant current, including the transport current, is pushed to the right of the conductor, and we see the forward eddy current under the conductor makes its way across the width. The fact that there is no location in the conductor where the current does not at some point flow in the backward direction distinguishes this situation from simple dynamic resistance.

Increased transport current displaces the forward remnant current shown in red. Because this system is cyclical, and the output current is kept constant, the competition (loss) between the transport current and remnant current is not apparent at the start of the cycle. Secondly, we see that the backward eddy current underneath the magnet decreases in size (as a fraction of conductor width) as the transport current is increased, which can also be seen in fig. 6-10. This decrease in size reduces the

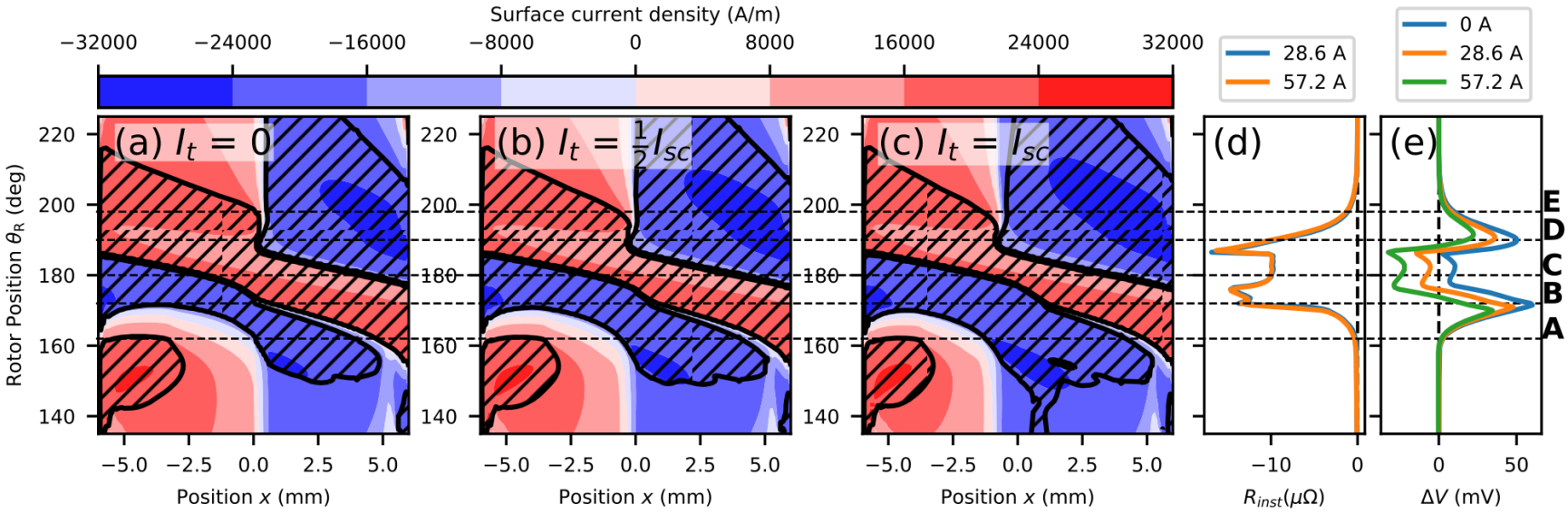

Figure 6-11: modelled current contours vs R_{inst} and ΔV for several currents at 17.52 Hz, cross-hashed regions identify $J > J_{\text{c}}$. (a) $I_{\text{T}} = 0$. (b) $I_{\text{T}} = 1/2 I_{\text{sc}}$. (c) $I_{\text{T}} = I_{\text{sc}}$. (d) R_{inst}. (e) ΔV.

amount of the applied *emf* that is captured in the driving direction, and instead we see it picked up in the backward direction as transport dissipation or $R_{\text{int}} \times I_{\text{T}}$.

As was previously noted from fig. 6-5, the internal resistance does not appear uniformly across the cycle. Instead, we can see parts of the cycle that experience very little dynamic resistance. This can be inspected by following the dashed line for **B** through all the plots in fig. 6-11, where we see that the sharp increase in the dynamic resistance corresponds to the elimination of sub-critical currents in the stator. Once the stator is full with over-critical currents, the competitive effect between the forward and backward eddy currents leads to the internal resistance. This leads to the conclusion that there must be some other smaller mechanism to the internal resistance that is in play before **B**.

To examine this, fig. 6-12 shows the sheet current and electric field, for both copper and HTS, when the rotor is halfway between positions **A** and **B**, denoted $\mathbf{A}^{+}$, across the whole *I-V* curve. For copper, fig. 6-12(a), we see the effect of the magnet entering from the right and currents returning on the left, with a uniform shift up the y-axis for increasing I_{T}. In complete contrast fig. 6-12(b) shows that, the current distribution in the HTS accommodates the additional I_{T} by broadening in the x-axis direction, thus 'filling' in the sub-critical region on the left hand side of the stator. This leaves the local *emf* from the applied magnetic field unchanged with current. It is clear from fig. 6-11(d) that there should be some small internal resistance at this position, which can be identified with the smaller electric field lobe (identified by the blue arrow in fig. 6-12(b)) in the center of the tape. This smaller lobe of the electric field corresponds to the remnant magnetisation being forced out of the tape, and constitutes a completely different resistive mechanism to the one seen between positions **B** and **D**.

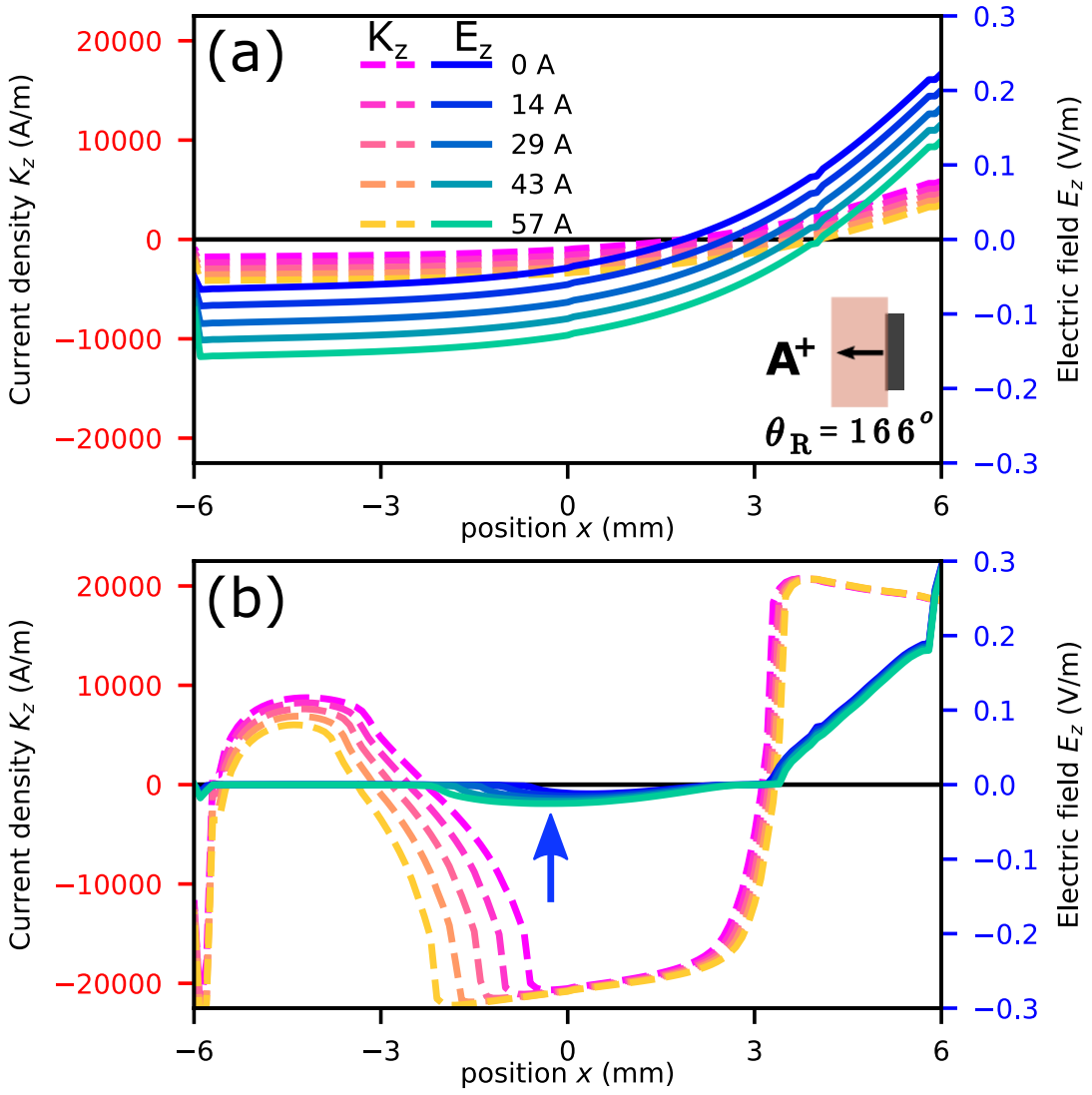

Figure 6-12: Sheet current density K_z (dashed lines) and local electric field E_z (solid lines), along the 17.5 Hz I-V curve from $I_T = 0$ (dark shades) to $I_T = I_{sc}$ (light shades) vs position across the width of the tape x, taken for the rotor position $\mathbf{A}^+$, halfway between positions $\mathbf{A}$ and $\mathbf{B}$, $\theta_R = 166^o$. Data presented for 17.52 Hz. Magnet position is illustrated as viewed from the Hall array.

6.5 Discussion

6.5.1 Origin of the dc voltage V_{oc}

The arguments presented here revolve around 3 equations eq. 2.10, eq. 2.3, and eq. 6.3, and how they interact to give E_{ave}. While it is absolutely true that the A-vector must be cyclical in these conditions, the currents that flow in response to the local electric field can give rise to non trivial solutions for $\vec{\nabla}\psi$. By examining fig. 6-10 we can see that the shape of the local electric field is essentially the same across the tape regardless of transport current, only shifting up and down to match the current constraint. This phenomenon is fundamentally different to the equivalent conventional dynamo, where the current constraint also maintains zero voltage. However, this story doesn't hold when there are still sub-critical regions of the tape. When there is still room for transport current to displace sub-critical currents, the penetrated magnetic field only contributes to the driving direction (forward current under the magnet). This situation is likely much more similar to the normal spot operation seen in the LTS dynamos [63], where the penetrated flux can migrate within penetrated normal zones.

The mechanism here should have some bearing on the mechanism of other flux pumps. For the HTS rectifier-type flux pumps Geng et. al. [123] give an explanation in terms of flux linkage and the movement of the electric central line. As the HTS rectifier is based on a dynamic resistance switch to rectify an applied ac *emf*, the movement of the electric field central line is very much akin to the movement of the electric field distributions in fig. 6-10. The situation in the dynamo is of course complicated by the fact that the applied *emf* and the rectifying *emf* are one and the same. What does not have an analogue in the model by Geng et. al. is the secondary resistive or generative mechanism highlighted in fig. 6-12. In the rectifier, the only way to link the applied flux into the load is to create the kind of current competition we see between positions **B** and **D**.

There is no evidence that the results presented here require any new exotic physics, such as the magnetic flux coupling propoesd by Wang et. al. [67]. Two major points

support this: (A) The work in Wang et. al. is in a rotationally symmetric system where an azimuthal voltage cannot be defined, let alone adapted to results for the dynamo. (B) The results presented in Wang et. al. do not use a $J_c(B,\theta)$ function and so the equations solved cannot be affected by the dc offset of the magnetic field as claimed by the authors. Even if this was disputed, results in [107], presented in ch. 5, clearly show that the dc voltage can also be achieved by a system with zero dc magnetic field sensitivity.

6.5.2 Output voltage vs current, R_{int} vs V_{oc}

The internal resistance in the HTS dynamo can be conceptualised as a dc dynamic resistance [71], akin to what is seen with dc transport currents in purely oscillatory magnetic fields [72]. To explain the rest of the I-V curves, given the gradient of the curve $R_{\text{int}} = R_{\text{dyn}}$, there are two options for the additional physics required, either to fix I_{sc} as some fundamental property of the system, or relate V_{oc} to R_{int} via some underlying mechanism.

As argued in sec. 6.4.4, the internal resistance is generated by competition between the transport current and the driven eddy currents. Figure 6-10 shows that the shape of electric field is largely unchanged by I_{T}. Rather it appears that $\partial_z\psi$ is determined at any given time to be the shift of E_z that solves eq. 6.3. Therefore, we must conclude that the correct interpretation is that V_{oc} and R_{int} must be understood with respect to the same underlying mechanism that generates E_{ave} in general. Although, this is not true before position **B**, as seen in fig. 6-12, where the resistive mechanism is related to the movement of remnant magnetisation rather than a reallocation of the applied local-*emf*. This secondary smaller mechanism is again similar to that described by Mawardi [124] in the LTS dynamos.

6.5.3 Short-circuit current I_{sc}

Given the relationship between R_{int} and V_{oc}, we see that I_{sc} is not a fundamental parameter of the system. In fact this behaviour makes sense with respect to the

definition of I_{sc} used here, where it is a dc property of an otherwise dynamic device. Nothing particularly special happens at any given moment of the cycle when I_{sc} is flowing through the tape. Rather I_{sc} simply happens to be the current where the time average of the output voltage happens to be zero. If one considers a dynamic definition of I_{sc}, using a voltage rather than current control, one then naturally asks what the relationship between this dynamic and the dc short-circuit currents would be.

While this point is left for future work, it does highlight that we might expect the load reactance to play some role in the rectification effect. This also explains the experimental results presented in fig. 6-4 for the two lowest frequencies 2.97 and 4.25 Hz, where the experimental electronic load has an insufficient inductance to oppose the small changes in net current driven by the magnet as it passes the stator at a relatively slow speed. I also take the view that in fig. 6-4(c) the trend must approach zero at zero frequency, as the plot will invert to the opposite polarity as the rotational direction is inverted, a behaviour the experimental data here seems to bear out. This does provide some motivation for a model with an inductive boundary condition, rather than the infinite reactance used here. Ultimately, essentially all practical magnets will have an inductance suitably high to appear essentially infinite to the dynamo (i.e. greater than a few μH).

6.5.4 Resistivity vs current

One of the primary observations of reported HTS dynamo devices is their linear I-V characteristic. In complex systems, something can be linear for two reasons: (A) The underlying mechanism is linear, and superposition maintains the linearity in the emergent behaviour; or (B) the effect in question is only interrogated over a small part of its full range, in which it appears linear. In the case of the HTS dynamo, it appears safe to say the underlying behaviour is not linear, and therefore case A can be rejected.

We must conclude that the dynamos built so far only explore a small portion of some underlying behaviour. It is shown here, for example, that the internal resistance

not only has a steady dc value, but also when expressed instantaneously at every moment of the cycle, with varying transport current. However, the difference in the behaviour of the device between open-circuit and closed circuit is very small. In fact, the qualitative behaviour of the device is the same for all currents. If we focus on fig. 6-10 we can see that the shape of the electric field across the width of the conductor is unaffected by the introduction of transport current. Consider how this curve moves, upward or downward, which corresponds to a change in the output voltage $\partial_z \psi(t)$. We can see that it is the gradient of the applied magnetic field, at the turning points of the current, that determines the change in voltage for a given change in current.

Figure 6-11 shows that the turning points of the sheet current K_z do not change all that drastically over the I-V curve of the device. That is to say, the dynamo only explores a small section of the applied local-*emf*, when deciding its turning points. Hence, while the overall output of the device is a function of the total applied local-*emf*, the behaviour when changing the current only samples the applied local-*emf* at the locations of the turning points. Therefore, when changing the current, only a small section of the local-*emf* is explored, over which it must appear linear.

To further test this, I proposed experiments using far wider stators than those explored so far, or to use parallel stators to create multiple return paths. Wider stators or stator networks can carry more current over all, broadening the space over which the turning points in the current can be pushed. For sufficiently large/high-current stators, we would expect a non-linear I-V characteristic, as the local-*emf* is probed at different current constraints. An intermediate set of experiments using a squirrel cage arrangement of narrow stators connected in parallel was completed by Hamilton and myself [125] which confirms the appearance of a non-linear I-V characteristic. This effect is explicitly confirmed in the next chapter, ch. 7, where models of varying stator width are presented.

6.5.5 Partial magnetic field penetration

The second observation that prompts us to suggest using wider stators is that for some part of the cycle the internal resistance is an order of magnitude lower even

while generating rectified output. This can be seen in fig. 6-5, and by inspecting the instantaneous resistance in fig. 6-6 between $\mathbf{A} \rightarrow \mathbf{B}$. First, we observe the fact that the applied magnetic field fully penetrates the whole tape for most of the magnet's transit. However, this is a geometric effect; a sufficiently wide stator would always have some region that was in the shielded regime. Alternatively parallel stators could act as return paths when not under a magnet. We see that the internal resistance effect when displacing remnant magnetisation is quite different to that when the transport current is competing with the driven eddy currents. While the output E_{ave} at the start of the transit is unaffected by increasing transport current, the loss associated with the competition between magnetisation currents and transport current is likely seen in the tail of the internal resistance past **E**, see fig. 6-6. That is, as the driven eddy currents relax into the remnant magnetisation, the presence of transport current reduces the output. If this mechanism results in a significantly lower drop in ΔV, then wide stators should have significantly improved short-circuit currents for a given magnet geometry.

6.6 Summary

This chapter has presented an expanded, powerful, and predictive model of the HTS dynamo, and validated it against experiments. The agreement between the model and the experimental data clearly indicates that inclusion of the non-linear E-J characteristics of the HTS film has a profound effect. This non-linearity gives rise to the dc voltage, as it breaks the oft overlooked symmetry in eddy current effects which is imparted by Ohm's law. The effects of this are seen at several levels of the analysis: scalar agreement in dc quantities, temporal agreement in transient voltage waveforms, and spatial-temporal agreement in locally induced magnetic field distributions.

The model's dynamics can be interrogated to provide insights into the device's driving principles. Here I have outlined how the local applied magnetic field across the HTS stator is rectified by the non-linear E-J characteristic of the HTS material in the flux flow regime. Furthermore, the link between this rectified output and the

transport current through the stator is shown to be predominantly caused by the competition between the transport current and the driven eddy current caused by the magnet's transit.

Finally, a partially-critical regime is identified where the stator is only partially penetrated by the applied magnetic field. While a small resistance is attributed to the competition between the transport current and magnetisation currents in this regime, this resistive mechanism is much smaller than when the stator is fully penetrated by the applied magnetic field. Logically, it is concluded that much lower internal resistances can be achieved by increasing the stator width sufficiently that the stator is never fully penetrated during the cycle of the device.

Chapter 7

A less resistive dynamo

Foreword

While working on: Mechanism of the High-T_c Superconducting Dynamo: Models and Experiment, *Phys. Rev. Applied* 14, 024012 (2020) [108] it became clear that over-currents were competing for space inside the HTS tape. That paper, [108], took nearly a year and a half to write and was increasingly complicated to edit. Hence, I set out to "quickly test" the effect of changing the stator width in the dynamo model. This 'stator width effects' work is a concise illustration of a new design rule for HTS dynamos, and was published in: Modeling of Stator Versus Magnet Width Effects in High-T_c Superconducting Dynamos, *IEEE Trans. on Appl. Supercond.*, vol. 30, no. 4, June 2020, Art no. 5204406. The following chapter is largely drawn from this work. Some changes have been made to make the text consistent with the flow of this thesis.

7.1 Introduction

In the previous two chapters we saw how large over-critical currents flow in the HTS stator of a simple dynamo. In ch. 5 I gave an explanation of how these over-currents break the standard expectation that the dc output voltage of a simple dynamo should be zero. Further to that, ch. 6 then explored how these over-currents evolved with

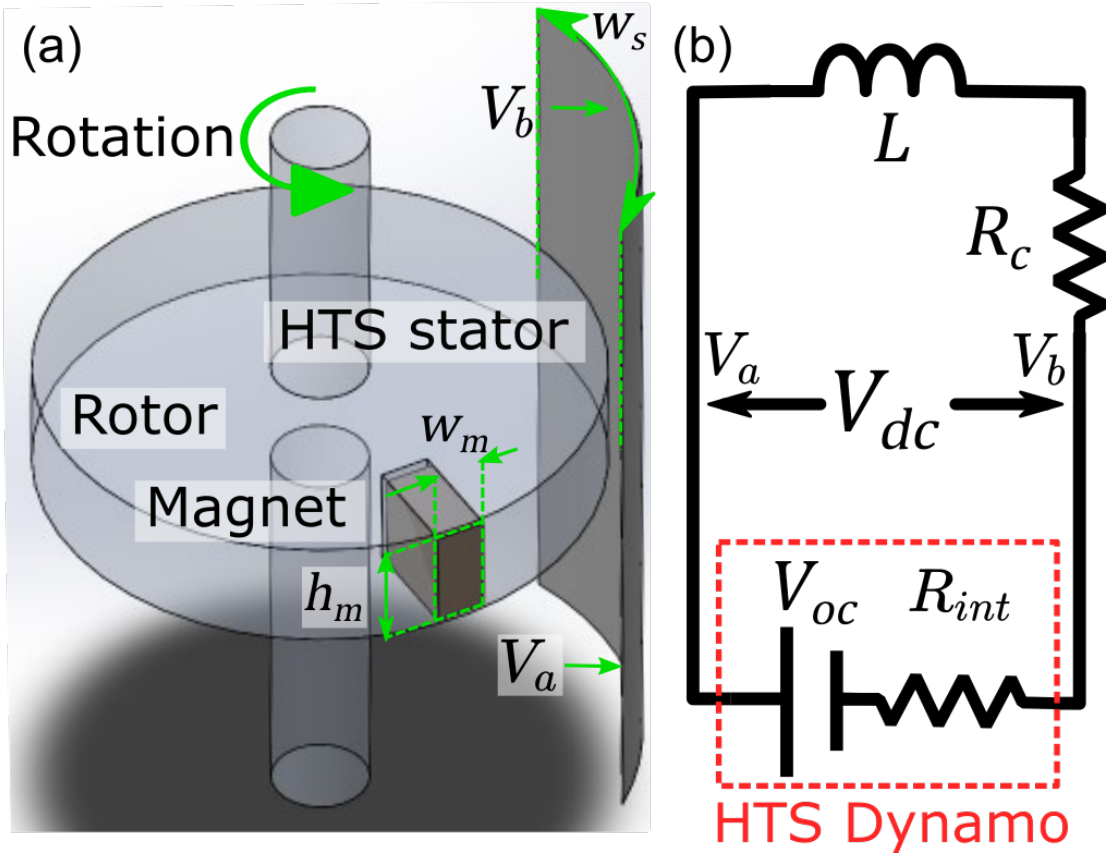

Figure 7-1: (a) Schematic of the HTS dynamo modelled in this work, with a stator width of 46 mm. (b) Equivalent circuit defining the dc characterisation of the device in (a), where R_c is the joint resistance to the HTS coil L.

changing transport current I_{T}. The most striking result is that there are portions of the cycle that generate $\Delta V > 0$[1], but show no internal resistance as I_{T} increases. This implies that as long as the forward over-critical current has ample space to be returned over the remaining width of the stator, no dynamic-resistance-like effect would be seen. The following chapter expands on this concept by varying the width of the HTS tape, thus altering the extra space available to return current.

First, we must consider a new geometry of device. Figure 7-1 (a) shows a schematic of an HTS dynamo device similar to that modelled in the previous two chapters [107]. However the model has been modified to accommodate a larger stator width, w. As before, in ch. 6, the output of the HTS dynamo can be analysed in terms of simple equivalent circuit parameters, as shown in fig. 7-1 (b). The 'equivalent circuit' describes the dynamo as a simple voltage source with an internal resistance R_{int}, and open-circuit voltage V_{oc}. In experiments, the magnetic field of the load coil can be measured to discern the net current, I_{T} flowing through the device [97]. Alternatively, a current controlled electronic power supply can be used as an artificial load admitting a defined current [70, 110]. This along with measurements of the voltage, can be presented as the output I-V characteristic of the device, which allows V_{oc}, $R_{\mathrm{int}} = V_{\mathrm{dc}}/I_{\mathrm{T}}$, and the short-circuit current $I_{\mathrm{sc}} = I_{\mathrm{T}}(V_{\mathrm{dc}} = 0)$ to each be defined.

In ch. 6, the FE model shows that large over-critical currents, $J >> J_c$ are present during the transit of the magnet across the stator wire, which are associated with the large locally-induced electric fields. However, ch. 6 only considered stator wires of 12 mm width, a 'similar' width to the 3 mm rotor magnet's applied field width[2]. In this case the stator is saturated with over-critical currents (in both the forward and backward directions) for most of the magnets transit time over the stator tape. This leads to the natural question: *'Can the HTS stator be made large enough to support both the induced eddy currents from the magnet's transit, as well as the dc transport current that is accumulated in the circuit?'*. There is clear experimental evidence that increasing the stator width has a marked effect on dynamo output [97]. Furthermore,

[1]This is our sign convention in treating the dynamo as a source rather than a sink of electrical energy.

[2]given the larger flux gap

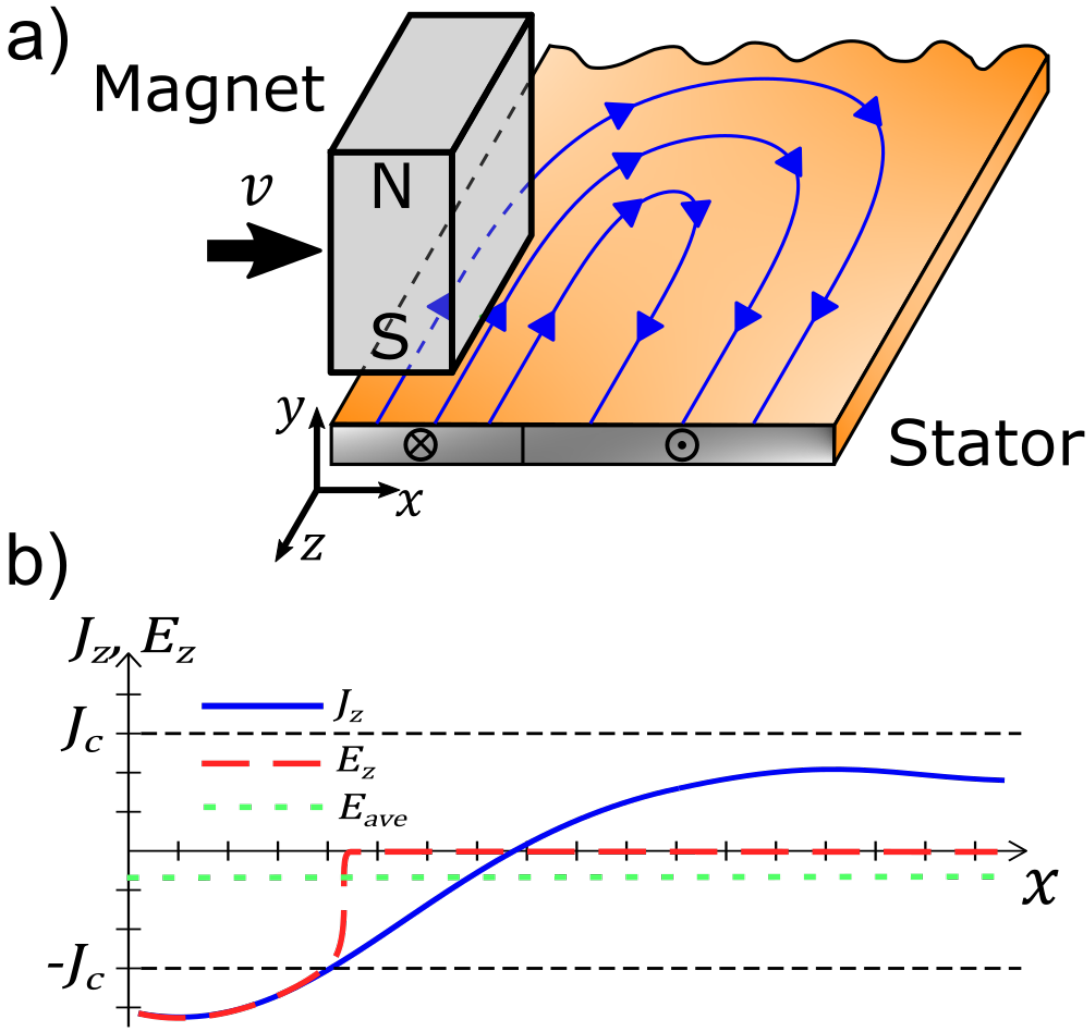

Figure 7-2: (a) Illustration of the eddy currents driven by a magnet moving with velocity, v, across a conductive stator, current flow is shown in blue in the $x-z$ plane. (b) Illustration of the eddy current flows, J_z in open circuit through the cross section of the conductor. Only over-currents where $J_z > J_c$, experience a resistivity giving E_z, leading to a bias in the electric field E_{ave}.

fig. 7-2 shows the situation observed in ch. 6, where the driven eddy current has ample room to return without inducing an electric field in the backward direction. In this chapter, an FE model of a simple HTS dynamo is used to explore the effect of this parameter on the dc output of the device, and on the internal eddy current distributions flowing within the wire.

7.1.1 Chapter overview

in this chapter, sec. 7.2 gives a brief description of how the model has been changed, in this case to account for a wider HTS stator. The results, which are entirely modelling based, are presented in sec. 7.3. The first result — non-linear I-V curves — are presented in sec. 7.3.1. To understand, the now non-linear, I-V curves, sec. 7.3.2, parameterises the curves so that the effect of HTS stator width can be clearly seen. Section 7.3.3 tests and proves the hypothesis proposed in ch. 6 that wider stators can support large critical currents without driving the whole tape above I_c.

The results presented here have the most bearing on the performance of the squirrel cage and drum dynamos, discussed in sec. 7.4.1 and sec. 7.4.2 respectively. The overall consequences of increasing stator width are then summarised in sec. 7.5

7.2 Methods

The model used here, see fig. 7-3, is expanded from ch. 5 and ch. 6 but differs in four key respects. $J_c(B,\theta)$ is interpolated from measured in-field critical current $I_c(B,\theta)$ parameters acquired from AMSC 46 mm, see fig. 3-10, superconducting wire to match the wire used in Pantoja [97]. $I_c(B,\theta)$ data was collected from a small sample of material using the Super-Current facility at Robinson Research Institute [16, 95]. The $J_c(B,\theta)$ was obtained by normalising I_c by the cross section of the modelled tape. Secondly, several values of the stator tape width w, 6, 12, 15, 18, 24, 30, 36, 46, and 60 mm are modelled. Third, for all the tape widths studied, a smaller flux gap $g = 2$ mm is used, which is selected to match B_{peak} in the model here with the device presented in [97] with the same width magnet, $w_m = 6$ mm. And fourth, the tape

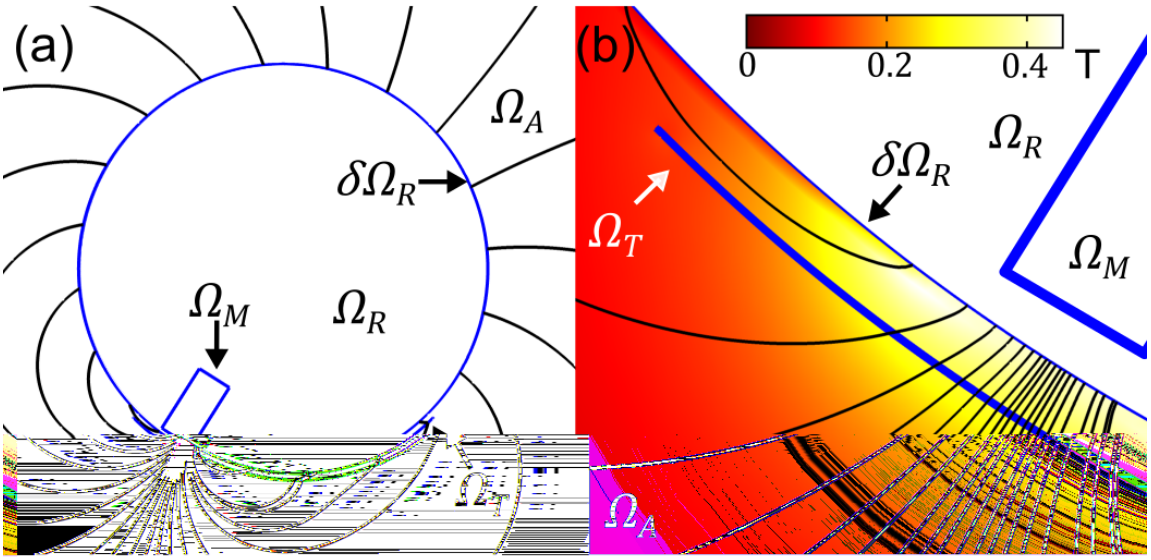

Figure 7-3: Schematic illustration of the basic geometry for the 2D H-formulation model used in this chapter, showing the modelled cross-section of the device with a 60 mm wide stator tape. The field in the rotor domain Ω_R is not shown as it lies outside the boundary conditions of the model. (a) View of the model domains, showing magnet, rotor and tape domains (Ω_M,Ω_R, Ω_A and Ω_T respectively). (b) Magnified view of the cross section of part of the HTS stator tape Ω_T as the rotor magnet traverses the stator. Brightness corresponds with field intensity.

cross section is conformed to be concentric with the rotor, with a radius of curvature $\tau = g + r_{\text{rotor}} = 38$ mm, which keeps the flux gap constant across the full width of the stator tape. As a result, θ is defined as the direction of the magnetic field with respect to the normal $\hat{n}$ of the curved conductor. The models are run at a relatively low rotational frequency $f = 38.25$ Hz, to enable comparison with the experimentally similar device [97].

7.3 Results

7.3.1 I-V curves

Figure 7-4 shows the modelled dc output from the dynamo in the form of output I-V curves for a range of different stator widths. This data was obtained by calculating the dc output obtained for a series of net transport current through the stator wire. In this way, the simulations produce the full I-V curve, from V_{oc} to I_{sc}. This differs from the experimental data presented in Pantoja [97], where the maximum measured current was constrained by the I_{c} of a series-connected load coil. A key observation shown by fig. 7-4 is that at higher current levels, the I-V curves of the wider tapes become highly non-linear. This non-linearity has not previously been experimentally observed as it only becomes noticeable at currents above 200A - which is well above the limiting current of the load coil used in [97]. It is perhaps not surprising that as the total transport current approaches the critical current of the stator wire, the intrinsically non-linear conductivity of the HTS stator causes an internal resistance within the stator wire which is no longer constant across its full operating range. Notwithstanding the above, it should also be noted (Figure 7-4(b)) that for narrower stator widths $\leq$18 mm the I-V curves remain approximately linear, which is consistent with experimental result from devices using 12 mm wide coated conductor wire [71, 73, 115].

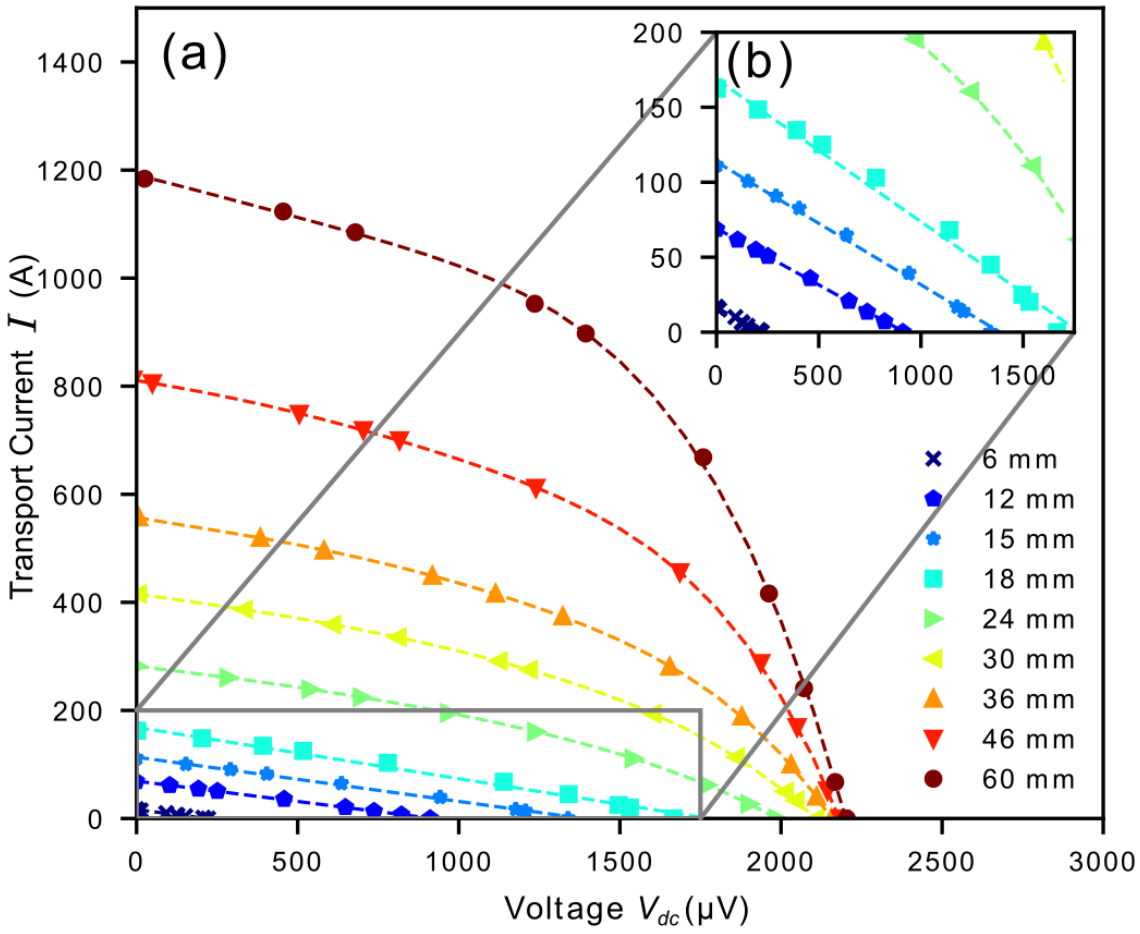

Figure 7-4: I-V curves for varying stator tape widths at 38.25 Hz. (a) Full I-V curves. (b) Magnified inset for 6 mm to 18 mm curves. Symbols indicate modelled values; dashed lines are a polynomial fit to modelled data.

7.3.2 Derived parameters

Further insight into the evolution of these I-V curves with stator width can be obtained by considering the circuit parameters defined in fig. 7-1 (b), namely, V_{oc}, I_{sc} and the internal resistance of the dynamo stator, R_{int}. fig. 7-5 (a) shows the evolution of the open circuit voltage V_{oc} with increasing width, which clearly approaches a limiting value V_{lim}. This mirrors the behaviour in [97] for stator widths up to 46 mm; whilst the addition of modelled data at 60 mm makes the limiting behaviour more apparent. One way to interpret this observation is to consider that dynamos employing narrower stators have a restricted ability to efficiently rectify the available *emf*. This is an important finding and implies that an important design rule for dynamo devices is that the width of a stator wire [97], or stator network [113,125,126], should be sufficiently wide to achieve the maximal dc voltage, V_{lim} (in this case $w > 4w_m$).

Figure 7-5 (b) shows how, for wider stators, the short-circuit current I_{sc} of the device increases approximately linearly with stator width. As the stator width increases, the increase in I_{sc} begins to correlate with the increase in stator I_{c}. To further explore this we can consider the capacity factor of the tape, α, which can be defined as:

$$\alpha = \frac{I_{\mathrm{sc}}}{I_{c,min}}, \tag{7.1}$$

where $I_{c,min}$ is the minimum critical current of the tape during the operation of the device. Ultimately, if the device is able to drive short-circuit currents equal to the stator's own critical current, then this implies that all other resistive mechanisms in the stator must have become negligible compared to the unavoidable flux flow resistivity at I_{c}. Figure 7-5 (c) shows that α approaches 1 for the widest tape simulated. This suggest that further increases in stator width should be expected to increase I_{sc} by an amount equal to the additional I_{c} of the wider stator. (Although, because I_{c} is a somewhat arbitrary criteria, it is possible that α could slightly exceed 1 for very wide stators in which $E_0 > 1\mu\mathrm{V/cm}$).

As the curves in fig. 7-4 are non-linear, we must consider the differential internal

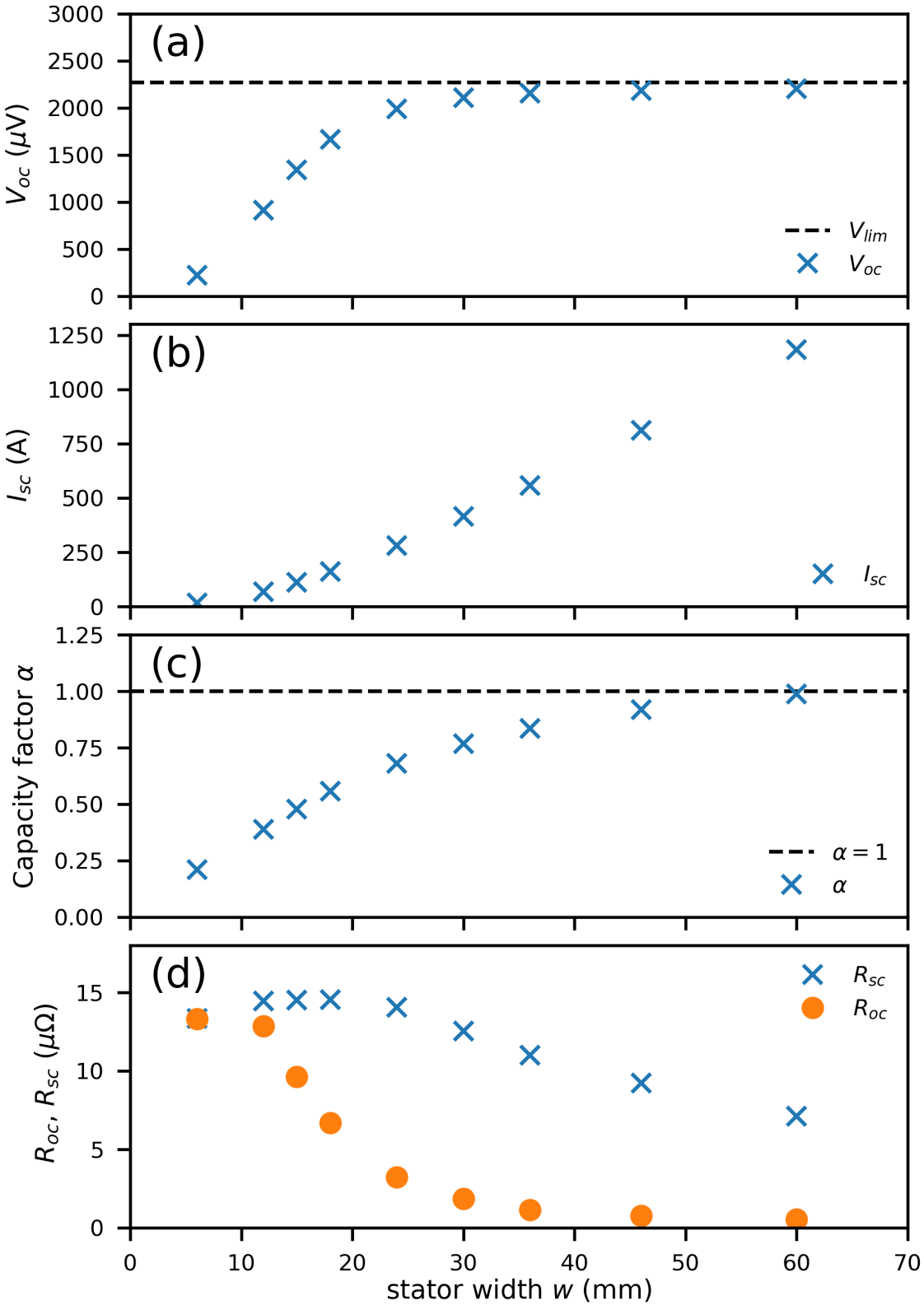

Figure 7-5: Circuit parameters for varying stator width. (a) V_{oc}. (b) I_{sc}. (c) Capacity factor $\alpha = I_{\mathrm{sc}}/I_{\mathrm{c,min}}$.(d) Differential resistance at open, R_{oc}, and short R_{sc} circuit.

resistance:

$$R'(I) = -\frac{\partial V(I)}{\partial I}, \tag{7.2}$$

where the minus sign ensures that the resistance is positive under the polarity convention used here. Different values of the differential resistance are obtained either at open circuit, $R_{oc} = R'(0A)$, or short-circuit, $R_{sc} = R'(I_{\rm sc})$, and these are shown in fig. 7-5 (d). The behaviour of R_{oc} shows the most dramatic effect with stator width, where it drops from 13.3 $\mu\Omega$ for a 6 mm wide stator, to 0.53 $\mu\Omega$ at 60 mm width. This transition occurs sharply between $w = 12$ mm and $w = 24$ mm, such that the majority of the resistance has vanished for greater values of w. This massive reduction in R_{oc}, coupled with the relative stability of R_{sc}, suggests that some resistive mechanism in the HTS stator can be eliminated for low dc currents, but reemerges for high currents.

7.3.3 Current distributions

The internal resistance of the stator wire arises due to the spatial restriction of the transport current, by the eddy currents which also flow around the magnet region, see ch. 6 and [108]. When this transport current does not have enough space to flow, local currents are forced to exceed the critical current $J_z > J_c$, generating a local resistive electric field in the stator. Furthermore, the backward eddy current (in the direction of the transport current) competes for available conductor width with the forward eddy current induced under the magnet. The resistance experienced in the forward eddy current region is responsible for generating the dc voltage, so a reduction in the size of this region also reduces the dc voltage output.

Figure 7-6 (a) shows a snapshot of the modelled currents flowing in the 12 mm wide stator tape at open-circuit when $\theta_R = 187^o$, when the rotor magnet is positioned at the right hand edge of the stator tape. The plot displays the sheet currents K_z and critical sheet current $\pm K_c$, at each position across the tape. These sheet currents are defined according to

$$K_z(\phi) = \int_{\tau-b}^{\tau+b} J_z(r,\phi)dr, \tag{7.3}$$

and

$$K_c(\phi) = \int_{\tau-b}^{\tau+b} J_{\mathrm{c}}(B, \theta, r, \phi) dr, \tag{7.4}$$

where ϕ is the angular coordinate, b is the half thickness of the modelled tape, and current densities J_{z} and J_{c} are expressed with respect to the arc of the stator wire.

We can define a function u to express whether overcritical current is flowing at a given position across the stator tape:

$$u(K_z, K_c) = \begin{cases} 1 & \text{if } |K_z| \geq K_c \\ 0 & \text{otherwise.} \end{cases} \tag{7.5}$$

From this, we can then define a geometric fill factor η to denote the fraction of the conductor width that contains a sheet current K_z greater than the sheet critical current K_c,:

$$\eta = \frac{1}{w_s} \int_{-w_s/2\tau}^{w_s/2\tau} u(\theta) d\theta. \tag{7.6}$$

Figure 7-6(b) shows the fill factor η of the stator wire as a function of rotor angle θ_R for the 12 mm stator. Modelled data is shown for a full rotation of the magnet for three different transport currents which span the full I-V curve, namely $I_{\mathrm{T}} = 0$ (open-circuit), $I_{\mathrm{T}} = I_{\mathrm{sc}}$ (short-circuit) and $I = I_{\mathrm{sc}}/2$. We see that for every transport current, the fill factor of the 12 mm tape is essentially $\eta = 1$ (neglecting the small current reversal zone) during the transit of the magnet across the stator wire (blue shaded region). Figure 7-6(c) shows a similar situation pertains for the 60 mm stator at I_{sc}. However, the same is not true for the 60mm stator at $I = 0A$ and $I_{\mathrm{T}} = 1/2 I_{\mathrm{sc}}$. In both these cases η never rises above 75%, indicating that there is still ample room in the conductor width for additional transport current to flow around the eddy current region.

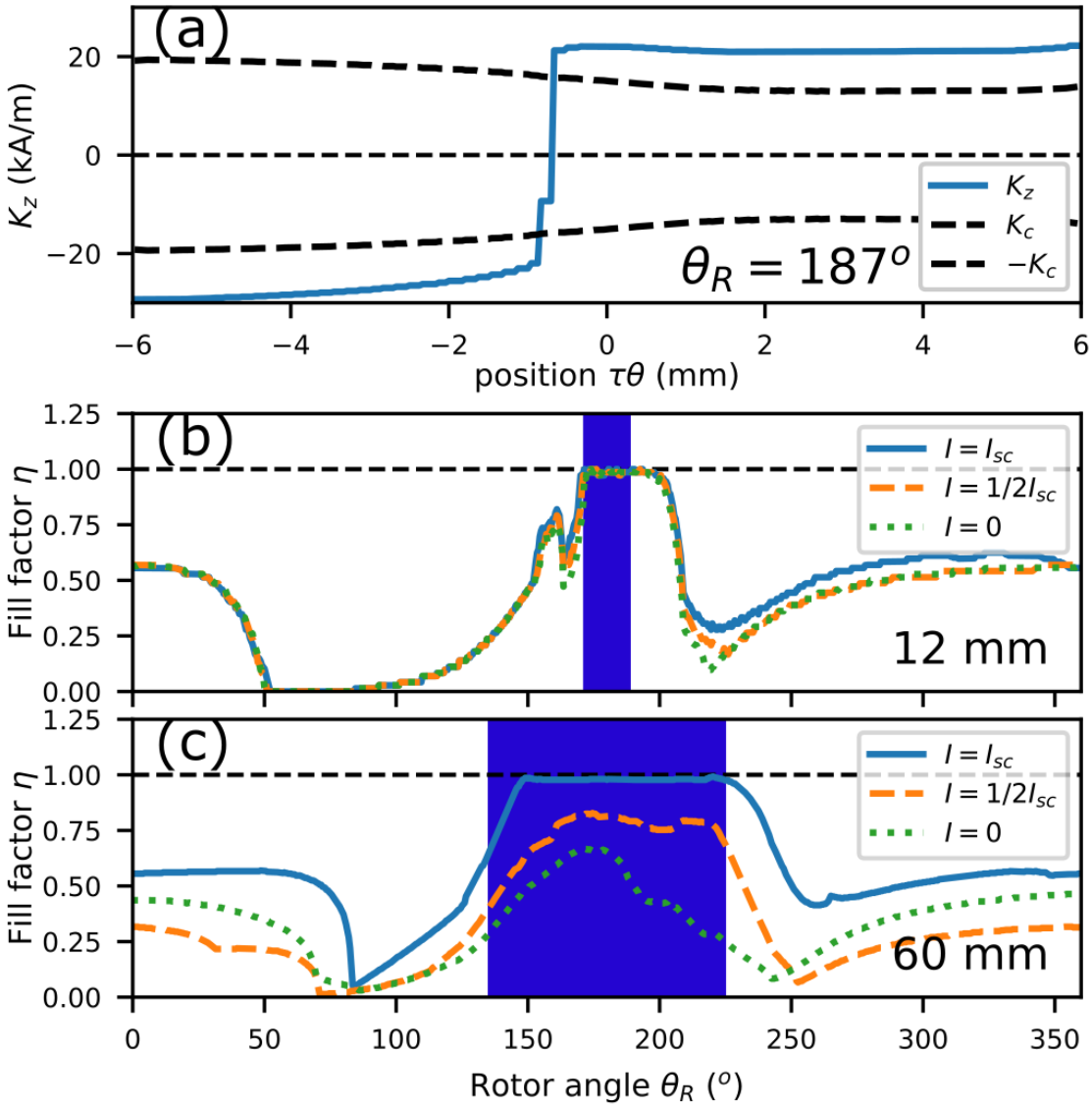

Figure 7-6: (a) The sheet current density K_z and sheet critical current $\pm K_c$ for $\omega_R = 187^o$. (b) Fill factor η for a 12 mm stator across the I-V curve. (c) Fill factor η for a 60 mm stator across the I-V curve. Dark blue region denotes the location of the stator tape in (b) and (c)

7.4 Discussion

7.4.1 The squirrel cage dynamos

This current redistribution effect also helps us understand the operation of 'squirrel cage' dynamos [113, 125, 126], see fig. 7-7. In such a dynamo many stators, which would be considered narrow ($w = 12$ mm), are connected in parallel using a superconducting bus at each end. In measurements of the efficiency of such devices, Hamilton [125] discovered similarly non-linear I-V curves. The increased performance characteristics, including increased output voltage $V_{\rm oc}$ of experimental squirrel cage dynamos again indicated that ample current recirculation is advantageous. This effect was hard to understand by considering each stator as an individual simple dynamo acting as a parallel voltage sources. However, by analysing the squirrel cage system in the light of the model presented here, it is clear that the additional circulating current pathways give the same advantages as increased stator width and dramatically reduce the incurred dynamic resistance.

The drawback with the squirrel cage geometry is caused by the resistive solder joints used to connect each stator to the shared superconducting bus. In the model presented in this chapter recirculating currents only incur losses if they are above $J_{\rm c}$. In the squirrel cage however, recirculating currents that travel from one stator to another will incur a linear loss due to the resistivity of the joints. While it is somewhat obvious that such joints must contribute to the internal resistance $R_{\rm int}$, it is not perhaps so obvious that they will also reduce the magnitude of $V_{\rm oc}$. However, if we consider the available "local" *emf*, the *emf* that circulates in the closed loops of the dynamo stator or stator network, generation of dc voltage is seen where that local *emf* is completely dropped over the forward current. If some of the local *emf* is instead dropped over the joint resistance, we would again see a reduction of $V_{\rm oc}$. That is, electric field generated in the joints by currents flowing from one stator to another, must come from the local emf, but come in equal parts forwards and backwards when compared to the load. This reduces the net *emf* that can be biased in the output direction. Furthermore, this effect may become more or less pronounced over the

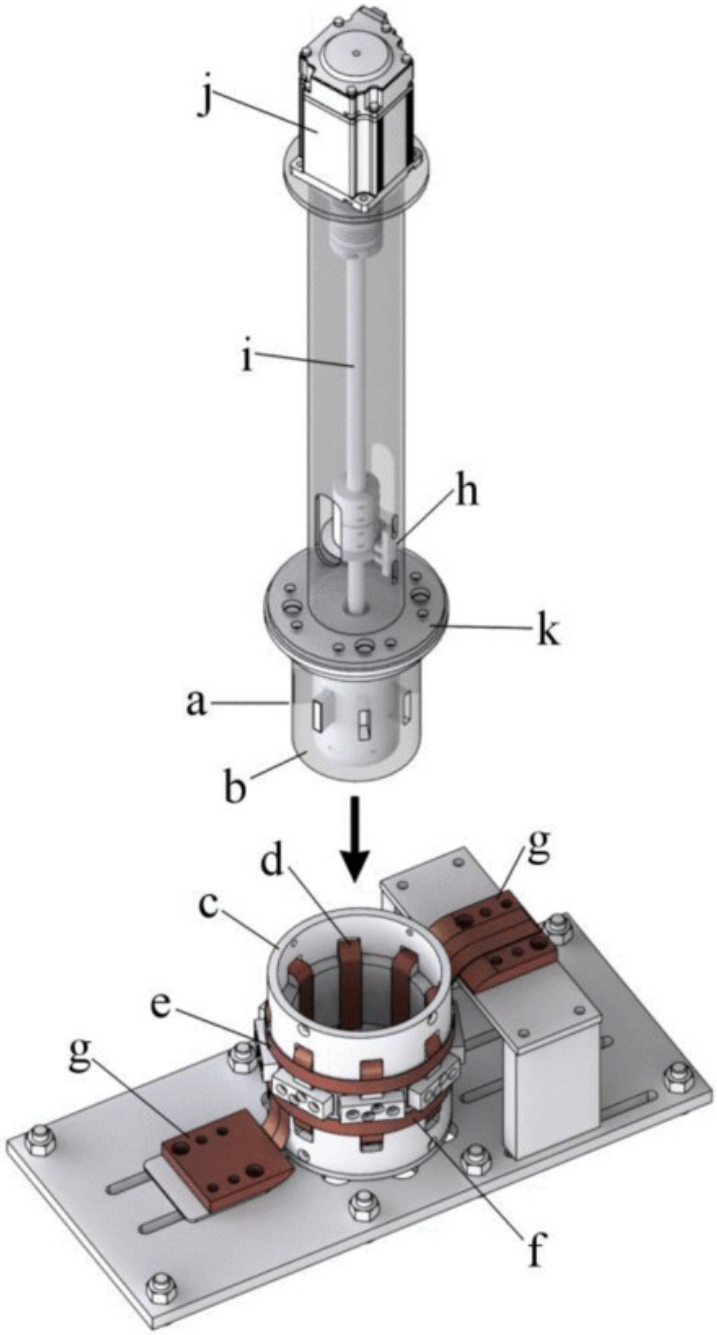

Figure 7-7: Illustration of disassembled test hardware showing (a) Rotor with magnets attached, (b) Aluminium magnet retaining collar, (c) Stator barrel, (d) Superconducting stator tapes, (e) Positive superconducting bus-ring, (f) Negative superconducting bus-ring, (g) Copper terminal lugs, (h) Optical interrupt, (i) Composite driveshaft, (j) Drive motor. For clarity, the magnet retaining collar and stainless steel motor mounting tube are displayed as semi-transparent. When assembled the iron stator end cap (k) bolts to the stator barrel, closing the magnetic circuit between the barrel and the rotor. (reproduced from [113])

range of different transport currents I_{T}, and hence have non-trivial effects on R_{oc} and R_{sc}.

7.4.2 The drum dynamo

The only drum type dynamo in literature is an LTS dynamo constructed by Mawardi [124], see fig. 2-11. This dynamo increased the effective width of the dynamo to its maximum, encircling the superconducting stator. The model here provides clear motivation for such a device. Indeed, experimental motivation can also be found in [97]. However, a counter point raised here would be that stators need only be sufficiently wide. Attempts to build a drum dynamo, fig. 7-8, at Robinson Research Institute (RRI), which are yet to be published, utilise the same 46 mm AMSC tape [97] to construct such a barrel type device. Unfortunately, the RRI drum is constructed by wrapping the tape length wise around the drum, and hence the length of the superconducting drum is only 46 mm. This is problematic as it probably doesn't allow enough space for recirculating currents away from the magnet to drop below J_{c}.[3] The conclusion from this chapter would imply that the 46 mm width of the tape is close enough to ideal to be used as the width, allowing the drum to be extend lengthwise, and connected into parallel sections.

For the purpose of engineering margin, it would be advantageous to have superconducting tapes of sufficient width ~ 60 mm to produce dynamos with $V_{\mathrm{oc}} \sim V_{lim}$, although this not generally avaliable from HTS tape manufacturers. Unfortunately for those of us building dynamos, the major demand for HTS wire comes from the magnet community, which for reasons highlighted in ch. 4, much prefer narrower tapes. As dynamo designers, we are forced to optimise the parameters that we can control. Hence a study of the effect of flux gap and the interplay with stator and magnet width, is a logical next step. Ideally, a reduction in flux gap would result in allowing the use of narrower magnets, which would reduce the required width of the HTS stator tape.

[3] No experimental investigations have been made to test this effect explicitly. However, 3D models now exist which could be used for this purpose.

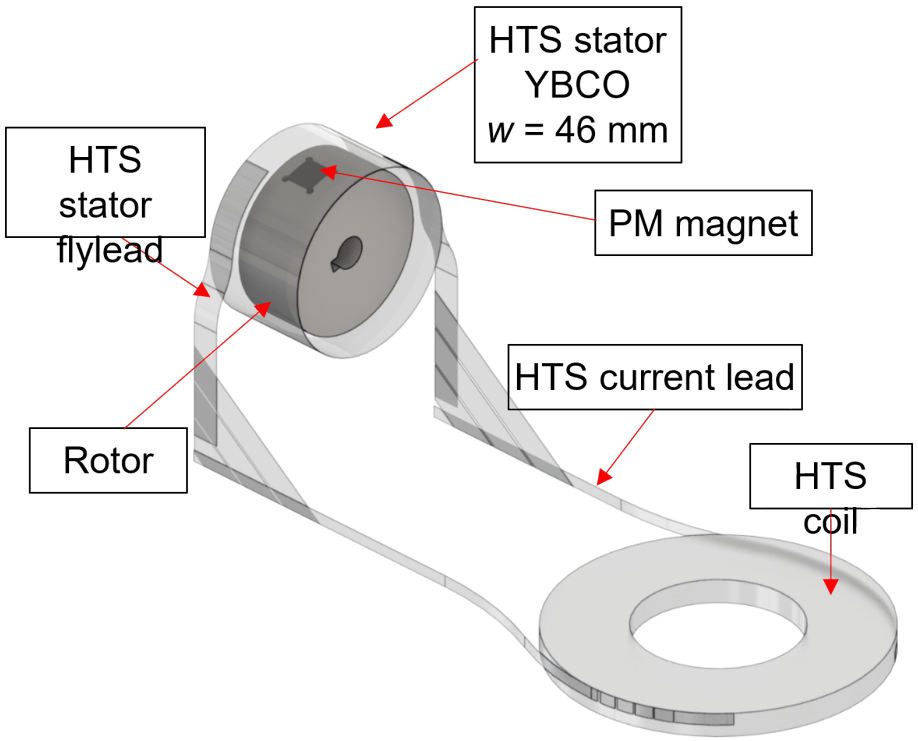

Figure 7-8: Schematic of the drum dynamo built at Robinson Research institute. The experiment served two purposes, one to investigate the drum topology, and secondly to operate a conduction cooled HTS dynamo.

7.5 Summary

The optimised design of HTS dynamo devices requires a deeper understating of their operating mechanism. In this chapter, I have presented the effect of increasing stator width on the key dc output parameters of the HTS dynamo. The first and most striking observation is the appearance of a non-linear I-V characteristic with increasing stator width, with the non-linear aspect most apparent at high output currents. We also observed that both $V_{\rm oc}$ and $I_{\rm sc}$ increase significantly with increasing stator width. This is attributed to a very significant (order of magnitude) reduction in the open-circuit internal resistance of the device R_{oc} which occurs between $w = 12$ mm and $w = 24$ mm. Once the stator width exceeds approximately four times the magnet width the $V_{\rm oc}$ of the device approaches a limiting maximum value V_{lim} whilst the short-circuit current $I_{\rm sc}$ of the dynamo starts to approach the in-field critical current of the stator $I_{c,min}$.

The sharp reduction in R_{oc} above $w = 24$ mm, marks a distinct change in the operating mechanism of the device. Previously, in ch. 5 and ch. 6 (which studied narrow stator dynamos), I described the HTS dynamo in the context of large over-currents, $J >> J_c$, fully occupying the superconducting stator at all times during the magnet transit. However, the FE models used here show that, given enough space, the induced eddy currents around the moving rotor magnet can co-exist with the transport current without driving the entire stator into the flux flow regime. However, at large transport currents approaching $I_{\rm sc}$, the transport and eddy currents do still compete for available space within the conductor during at least some parts of of the cycle (fig. 7-6). As a result the differential resistance increases rapidly as $I \rightarrow I_{\rm sc}$.

These findings suggest that high current HTS dynamos are quite possible, and could in fact produce larger voltages at their operating current than implied from previous linear I-V models. Furthermore it suggests that optimal dynamo designs will involve stators, or stator networks, of sufficient width to efficiently rectify the *emf* of the applied field $V_{\rm oc} \rightarrow V_{lim}$.

Chapter 8

A semiconducting dynamo

Foreword

Unlike other chapters, this chapter concerns unpublished results that were only completed in the last part of my studies. As such, the results themselves and discussion around them is shorter, and less resolved than previous chapters. The following chapter should not be read as authoritative, but rather an exploration of the mechanism, that we have attributed to the HTS dynamo, analysed through a new hypothetical lens. Given its brevity, a chapter overview is omitted.

8.1 Introduction

If the HTS dynamo is based on the nonlinear conductivity of the HTS material, do we expect to see similar behaviour in other non-linear systems? This idea, raised in ch. 5 and originally in the conclusion of [107], has been a curiosity of mine ever since. Originally, all the people involved in this work came to the idea independently, but I still remember Dr Ainslie raising the point, "What if we had a semi-conducting material [for the stator]?". Our initial point of view was that such a device would not support large enough currents for us to see a similar effect.

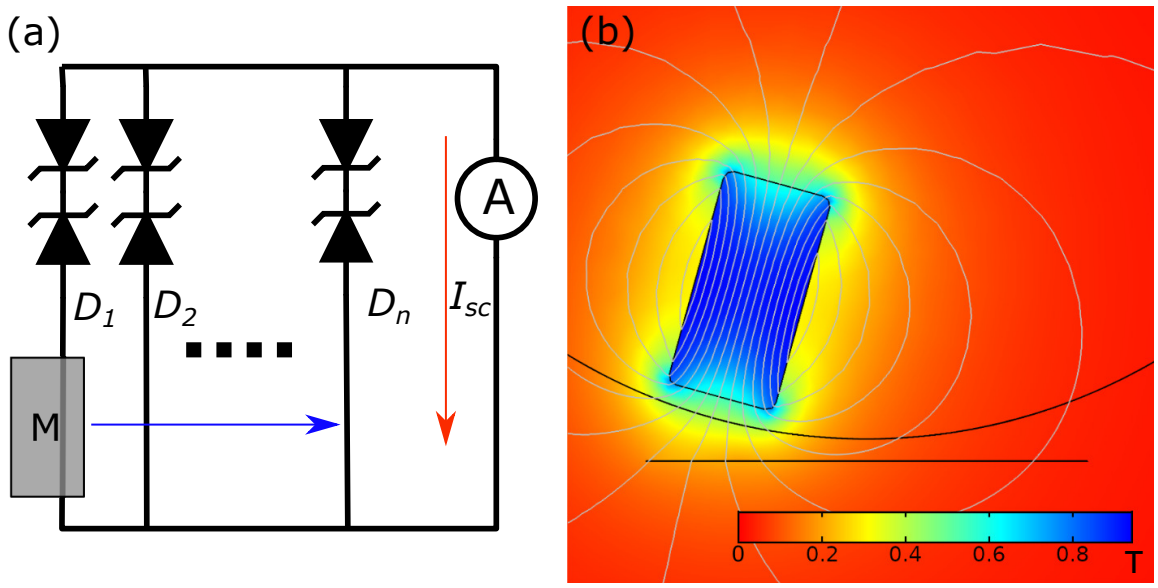

Figure 8-1: (a) Circuit schematic of the Semiconducting dynamo with parallel back to back Zener diodes providing non-linear conductivity, (loop inductances omitted), where the blue arrow indicates the velocity of the magnet. (b) A-vector formulation implementation of the semiconducting dynamo taken as the magnet begins its transit from left to right. Note that we can see the magnet itself as rotation is implemented natively in the A-vector model.

8.2 Theory

It is only now, at the end of this PhD, where I can present the leap of logic required for a "*semiconducting dynamo*". As we have ventured through this thesis one of the major selling points for the HTS dynamo is that it is an ultra low impedance power supply, up to some maximum current, for dc superconducting circuits. However, the semiconducting dynamo represents the opposite behaviour, being arbitrarily high impedance up to some voltage.

This high impedance mirrors the modern power electronics used today, based again on semiconducting components. Recall that the advantage of a low impedance power supply is that it does not interfere with the current in the circuit when in the "off" or non-driven state. That is, when an HTS dynamo is turned off, current will continue to flow, and decay naturally against what ever nominal resistances are present in the joints of the circuits. The first thing we can say for sure about a semiconducting dynamo is that current will only flow while the dynamo is running.

A semiconducting dynamo would instead be *useful*[1] in applications where steady currents are not expected, but steady voltages are expected. Consider that an HTS dynamo drives magnetic flux into a load loop, hence adding energy to that part of the system in the form of flux and current flow. The semiconducting dynamo would, in principle, drive charge into the load and store energy in the charge differential and voltage. Hence, if connected to a capacitor, such a dynamo would have the advantage of not allowing discharge currents to flow through the stator when the dynamo is not operating; in the exact same way as the HTS dynamo does not allow flux to leave an inductive load when not operating[2]. And also consider that an HTS dynamo would be of no merit in charging a capacitor bank for similar reasons.

This thesis is a culmination of 3 years of my work, and one of the things that I have learned in this time is that it is often better to quickly pursue an idea to a satisfactory conclusion than let it linger, consuming mental space. Hence, it is my pleasure to briefly present a functional model of a semiconducting dynamo.

8.3 Model

Briefly, this model is based on the notion of back-to-back Zener diodes which give a nonlinear V-I response but no asymmetry. Simply, for voltage applied in any direction one of the two diodes must be in reverse bias. This gives two quantities, a nominal current density J_0 taken as 1 Am^{-2} and a threshold electric field E_c. These are used to define a nonlinear conductivity similar to the E-J power law eq. 2.3:

$$\sigma_{\mathrm{semi}}(\vec{E}) = \frac{J_0}{E_\mathrm{c}} \left(\frac{|\vec{E}|}{E_\mathrm{c}} \right)^n , \tag{8.1}$$

where n is again some exponent defining the nonlinearity, and is set equal to 20 in the following model[3]. These back-to-back Zener diodes are arranged in parallel as

[1] I suspect that this device is entirely un-useful, but is presented here as a test of the underlying theory we have proposed for the HTS dynamo

[2] assume perfect joints.

[3] This is obviously not quite the right expression for how a Zener diode would behave, however it is non-linear and monotonic, so it possesses all the required properties

depicted in fig. 8-1 (a). This replicates the topology of the HTS dynamo and permits a similar 2D model shown in fig. 8-1 (b). The model is run using a final conductivity that includes a series contribution from hypothetical copper wires, σ_{Cu}:

$$\sigma_{\mathrm{semi}} = \frac{1}{\frac{1}{\sigma_{\mathrm{semi}}} + \frac{1}{\sigma_{\mathrm{Cu}}}}. \tag{8.2}$$

The semiconducting dynamo is modelled as a flat sheet with a width w_{t} of 24 mm and a thickness of 25 μm. A flux gap g of 2.4 mm is chosen along with a magnet width w_{m} of 6 mm. E_{c} is based on the breakdown voltage, $V_{\mathrm{b}} = 3$ V, of an arbitrary 'planarsed' Zener diode, normalised over some length scale, $L = 0.3$ m:

$$E_{\mathrm{c}} = \frac{V_{\mathrm{b}}}{L} = 10 \text{ Vm}^{-1}, \tag{8.3}$$

where L can be considered the length of a copper stator winding exposed to the rotating magnet.

Finally, the model is constructed in A-formulation rather than H-formulation. This again reflects the duality between the low and high impedance behaviour of the devices respectively. The nonlinear conductivity of the semiconducting dynamo could cause convergence issues in an H-formulation model just as the HTS dynamo doesn't converge in A-formulation.

8.4 Results

If we consider an HTS dynamo to deliver flux into a load and observe that, at least experimentally, they seem to deliver a constant flux per cycle ϕ, then we would expect the semiconducting version to deliver a constant amount of charge per cycle. To probe this a parametric sweep of the model is taken running at different rotational frequencies f, with the results shown in fig. 8-2. The results show that this is not the case for *small* frequencies, where the amount of charge delivered per cycle (defined as the integral of the current during a cycle) obeys a suppressive power-law down to low

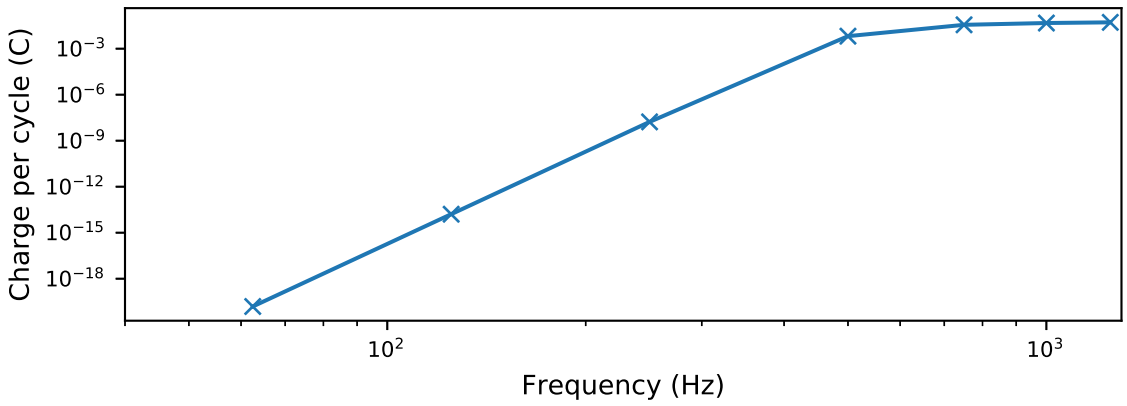

Figure 8-2: Charge per cycle delivered by the semiconducting dynamo vs frequency.

frequencies, but seems to plateau once the frequency is high enough[4]. The exponent of the observed power-law suppression, $N_{\mathrm{em}} = 19.52$, is also suspiciously close to the input exponent to eq. 8.1, $n = 20$.

For the HTS dynamo we have a notion of penetration field B_{pen}, below which we do not deliver flux into the load. In the case of the semiconducting dynamo the requirement instead is that the local *emf* be sufficiently higher than E_{c}. However, *emf* is proportional to velocity, and hence we expect the same notion of "penetration" to be convoluted with frequency, in a way that we would not for the HTS device. In the same sense that the semiconducting dynamo would need to run sufficiently fast to generate charge, an HTS dynamo with an applied magnetic field under B_{pen} could still deliver flux if run slow enough that flux creep would allow flux transfer[5].

This dynamo is potentially useful to consider as it seems more obvious that it should generate a dc biased current and deliver charge to a load. However, it is also fair, therefore, to ask if the device is in fact trivial. Does the arrangement of parallel current/voltage paths give rise to a nontrivial result when compared to the single branch device. Figure 8-3 compares the output *emf* (in this case equal to $E_{\mathrm{ave}}(\theta)$) to the current produced in the model $I_{\mathrm{sc}}(\theta)$, and to the current that would flow in a single branch device with the same nonlinear conductivity $I_{\mathrm{single}}(\theta)$. Figure 8-3(a)

[4]This is the highest frequency that the model continued to run, higher frequencies maybe left to future work.

[5]Sounds crazy? consider Ghabeli's models of increasing flux gap [127], see reproduction in fig. 9-8.

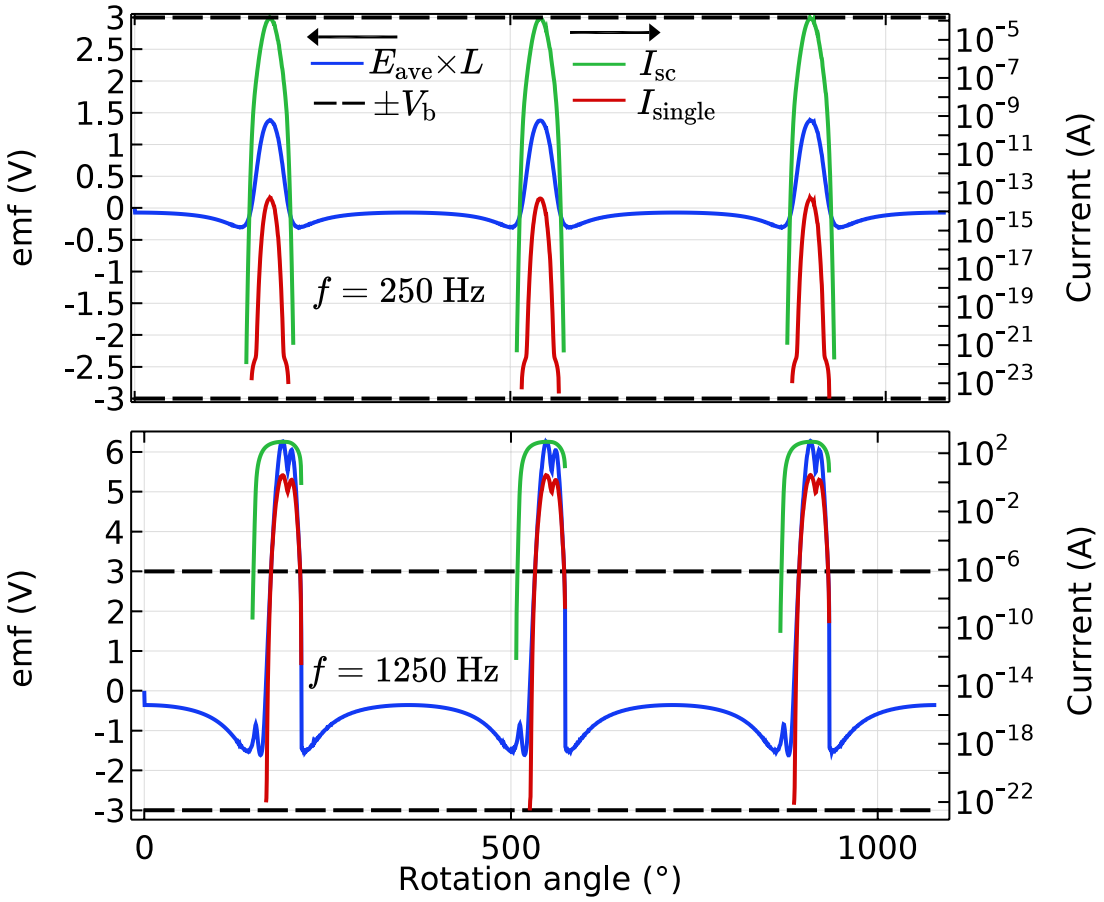

Figure 8-3: Induced voltage E_{ave}, net short circuit current I_{sc}, and single path equivalent current I_{single} vs rotor angle for (a) 250 Hz and (b) 1250 Hz.

shows these quantities for the relatively slow rotation speed of 250 Hz, where two facts are apparent; one, the short circuit current is indeed higher, by several orders of magnitude, to the equivalent single path device, and two, the device generates current even when the average *emf* is significantly below the breakdown voltage V_b.

8.5 Summary

This model could easily require the same level of investigation as its HTS counter part in order to understand; which is not the purpose of this work. Rather this device has been introduced to provide and insightful analogous system to the HTS dynamo. The similarities, differences, and analogies between the two systems allow as to question what it is exactly about HTS materials, and their non-linear resistivity, that gives us the open circuit dc voltage. Here we have seen that such a semiconducting dynamo produces a closed-circuit dc current where none would have been expected by textbook logic. By simple interrogation this current is confirmed to be non-trivial as it can exist even when the average *emf* is below the breakdown voltage of the modelled diodes.

This semiconducting dynamo stands as the end of a line of logic trying to understand the HTS dynamos themselves. Starting from the experimental work showing the HTS dc effect itself by Hoffmann [3], continuing to, what would be, the correct physical insight made by Bumby [74], carried out and examined here, and in [107], by myself. The core premise presented for the HTS dynamo is that non-linear resistivity can, without any other intrinsic asymmetry give rise to such dc biases. Here, in this last step, I have shown that this logic can be continued to predict and model a new and altogether different system and effect.

Chapter 9

Review of ensuing literature

Foreword

The following chapter provides a literature review of papers that have been published after the work presented in this thesis. Overall, the aim is to provide literature context for the work contained in this thesis. It is also an opportunity to reexamine the results of this thesis in the light of work done by the larger community. While I am a coauthor on some of the results presented in this chapter, any results conveyed here should be attributed to the other authors to whom the results primarily or entirely belong. Once this context has been provided, fully informed conclusions are drawn in the final chapter. All figures are reproduced under fair use or with permission.

9.1 Introduction

Since the publication of the results presented in this thesis a large number of works have referenced or built upon that same material. The tools for modelling NI coils, presented in ch. 4, are slowly gaining recognition in the NI coil modelling community. Even so, my coauthors and I are confident that the impact of that model will be large as researchers integrate the technique into more complicated analyses. In the case of the HTS dynamo, pent-up demand for a model and mechanism for the device resulted in a flurry of results following [107], presented in ch. 5. This new work covered a

large range of topics, including speculations on how the dynamo can be modelled, how such models contribute to the wider HTS modelling community, the expanded modelling of dynamo performance, measurements of the dynamo efficiency, and its application in integrated HTS machines.

9.1.1 Section overview

This chapter will first cover the early impact of the NI coil modelling in sec. 9.2. The following sections concern developments surrounding the HTS dynamo, starting with Archie Campbell's circuit model, sec. 9.3. Next, the modelling community's work and use of the "HTS dynamo modelling benchmark" is introduced in sec. 9.4. With a large number of research groups and models available to work on the HTS dynamo, work on characterising the various operational parameters of the dynamo is presented in sec. 9.5. Some of these parameters are not reproduced accurately with 2D models, inspiring the introduction of 3D HTS dynamo models, as presented in sec. 9.6. Finally, ongoing work to understand the integration of HTS dynamos into full superconducting machines is summarised in sec. 9.7.

9.2 Developments in the anisotropic modelling of the NI coil

A major conclusion of ch. 4 is that the anisotropic modelling technique is simple enough that it can easily be incorporated with other physics such as thermal or mechanical effects. Work by Duan et. al. [128] does exactly this, by combining the the anisotropic coil model with a thermal model of NI coil.

Including thermal effects not only allows modellers to validate coil operating parameters internally in the coils structure, but also leads to more accurate current distribution dynamics. In the case of coils close to their critical current, local increases in temperature lead to a reduction in local critical current. While this seems to have an effect in Duan's work, the ability of the NI coil to continue to reallocate

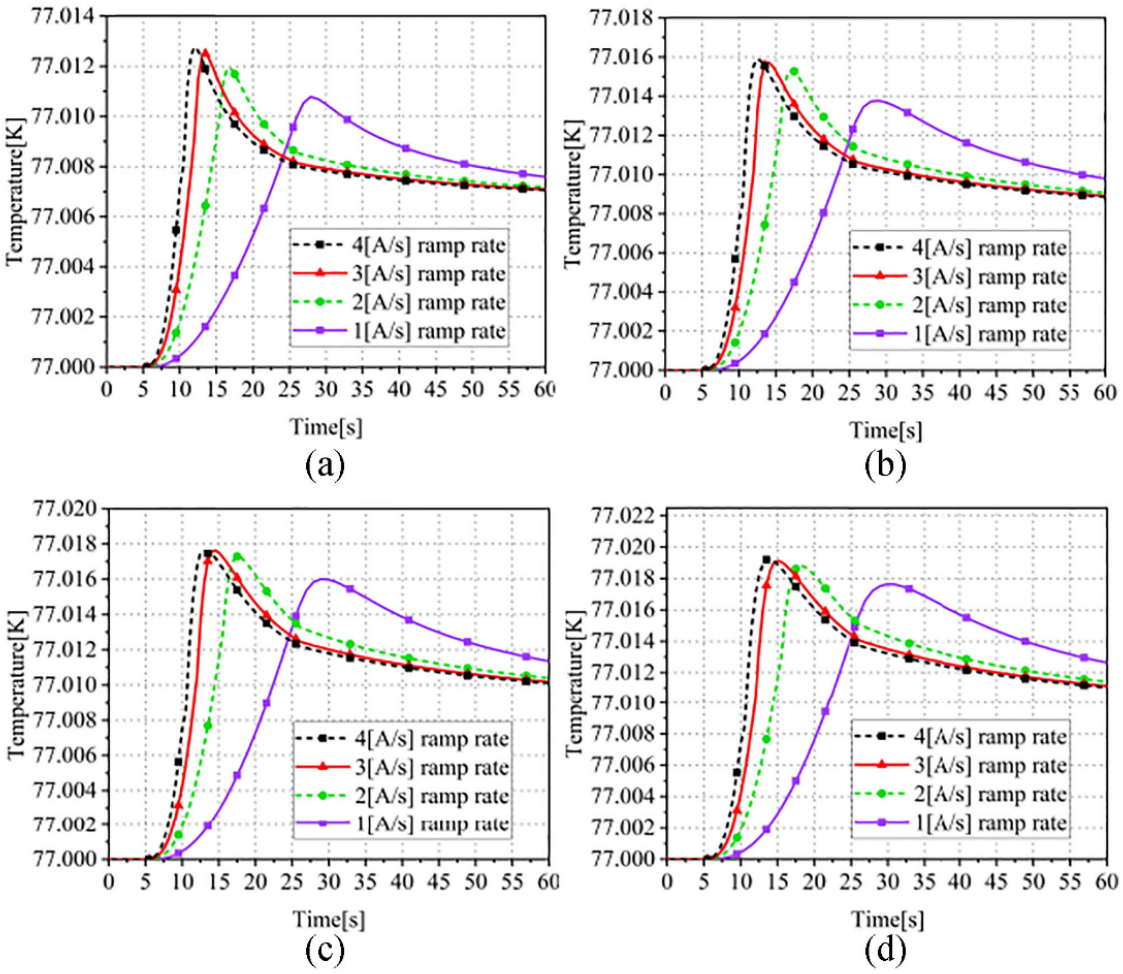

Figure 9-1: Temperature curves for modelled coil ramping in 77K background for: (a) 40, (b) 60, (c) 80, and (d) 100 turns. Reproduced from [128].

current — even as $J_c(B, \theta, T)$ drops due to temperature rise — means that macroscopic coil performance is not largely affected. The effects of coil ramp rate and associated heating are reproduced in fig. 9-1.

Further to analysing NI coils under operational stress, the thermal model allows designers to place operational bounds on coil ramp rate. That is, higher ramp rates lead to larger bypass currents, which give resistive loss and thus heating. This leads to coil temperature rise during ramping that is also proportional to ramp rate. The obvious conclusion is that there is a maximum ramp rate where temperature increases can run away leading to a magnet quench. A potentially not so obvious conclusion, that could be expanded from Duan's model, is that current ramp heating could be used to temporarily suppress J_c, leading to a more uniform distribution of current, before allowing the coil to cool back down to an operational stable, $I_{op} < I_c$, level.

New effects aside, the most valuable aspect of a thermally integrated model is the ability to test the effect of different cooling designs on coil performance. Given the large cost of building an integrated magnet system, and the even higher difficulty of building one that can implement many different cooling techniques, the ability to model different cooling strategies on a numerically repeatable HTS NI coil will lead to better design choices. In view of my first research question, this work not only shows that finite element techniques can be expanded for the NI coils, but that expansion has far to go, yielding new insights, better design choices, and more dependable technologies.

9.3 Archie Campbell's circuit model

The first citation that my paper, [107], ever received was from a paper by Professor Archie Campbell. I had the pleasure of meeting Archie at the start of my PhD when I was doing the original work now presented in ch. 5. While my motivating research question was focused on finite element techniques Archie maintained that circuit analysis should yield an explanation of the HTS dynamo dc voltage effect. While I beat Archie to the punch, he subsequently published such an analysis based

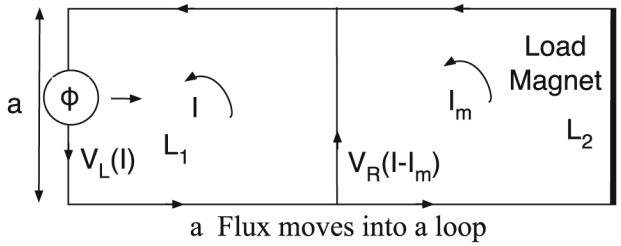

a Flux moves into a loop

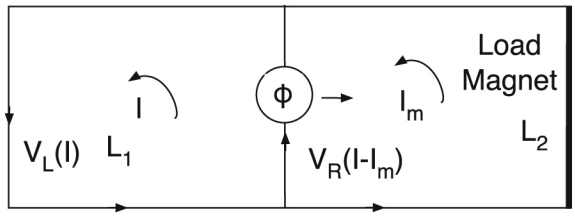

b The flux moves from the loop to the load circuit.

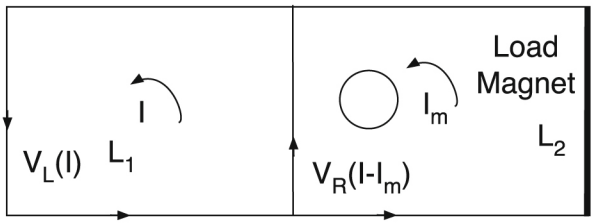

c The flux is turned off

Figure 9-2: A step by step illustration of Campbell's circuit dynamo model. (a) Flux moves into a loop. (b) The flux moves from the loop to the load circuit. (c) The flux is turned off. (a)–(c) A flux ϕ moves into a square loop of side a and of inductance L1 which puts current into a load magnet of inductance L2. Figure and caption reproduced from [129].

on treating the dynamo stator as a pair of non-linear conductors [129].

Archie's work is a direct challenge to the underlying strategy behind my first research question. Finite element methods are useful because they provide a more direct translation of field theory concepts to numerical methods. However, Archie correctly maintained that circuit theory, was a perfectly applicable pathway for getting to the same answers. The logic of his model can be seen in fig. 9-2. While the circuit model of the HTS dynamo does not yield the same quantitative agreement seen in ch. 5 and ch. 6, it yields a similar insight into the role of non-linear resistivity in providing a rectification effect. Sadly, Professor Campbell passed away before he could expand

on his work, which deserves further consideration. Archie's core motivation was that electrical engineers understand their systems through the lens of circuit theory and that an explanation was possible in that context. This remains true, and in conveying the results presented in ch. 5 I have found a distinct weakness in matching the described phenomenology with circuit concepts. Rather than an intellectual inconvenience, this stumbling block encapsulates a deeper issue in reconciling the HTS dynamos with the HTS transformer rectifiers.

Archie's work motivates and justifies the notion that a singular explanation of the HTS dynamos and the HTS rectifiers should be possible. In line with my first research question, finite element models have now been extended as far as possible in this regard, and yet progress on this issue will likely come from improved and articulated circuit models of the HTS dynamo. I am of the view that such a description is possible and has the potential to be more elegant than the existing phenomenology laid out in this thesis.

9.4 The HTS dynamo modelling benchmark

Once my model of the HTS dynamo was finished and my time visiting at the University of Cambridge was coming to an end, discussions with Dr Ainslie looked at what would come next. Dr. Ainslie is one of the preeminent modellers in the field of HTS machines, and noted that the dynamo problem had now been solved very concisely. A simple system, easy to describe, with clear non-trivial effects, Dr. Ainslie suggested the creation of a modelling benchmark based on the HTS dynamo.

The HTS dynamo benchmark, published with contributions from nearly every major HTS modelling research group in the world [130], is a simple test that cross validates different numerical techniques against the same physical problem. Effectively, modellers want to know that their various techniques are all capturing the same underlying physics. Benchmarks not only validate this, alleviating the need to run multiple different numerical methods for each problem, but also give insight into the relative suitability of different techniques to different problems.

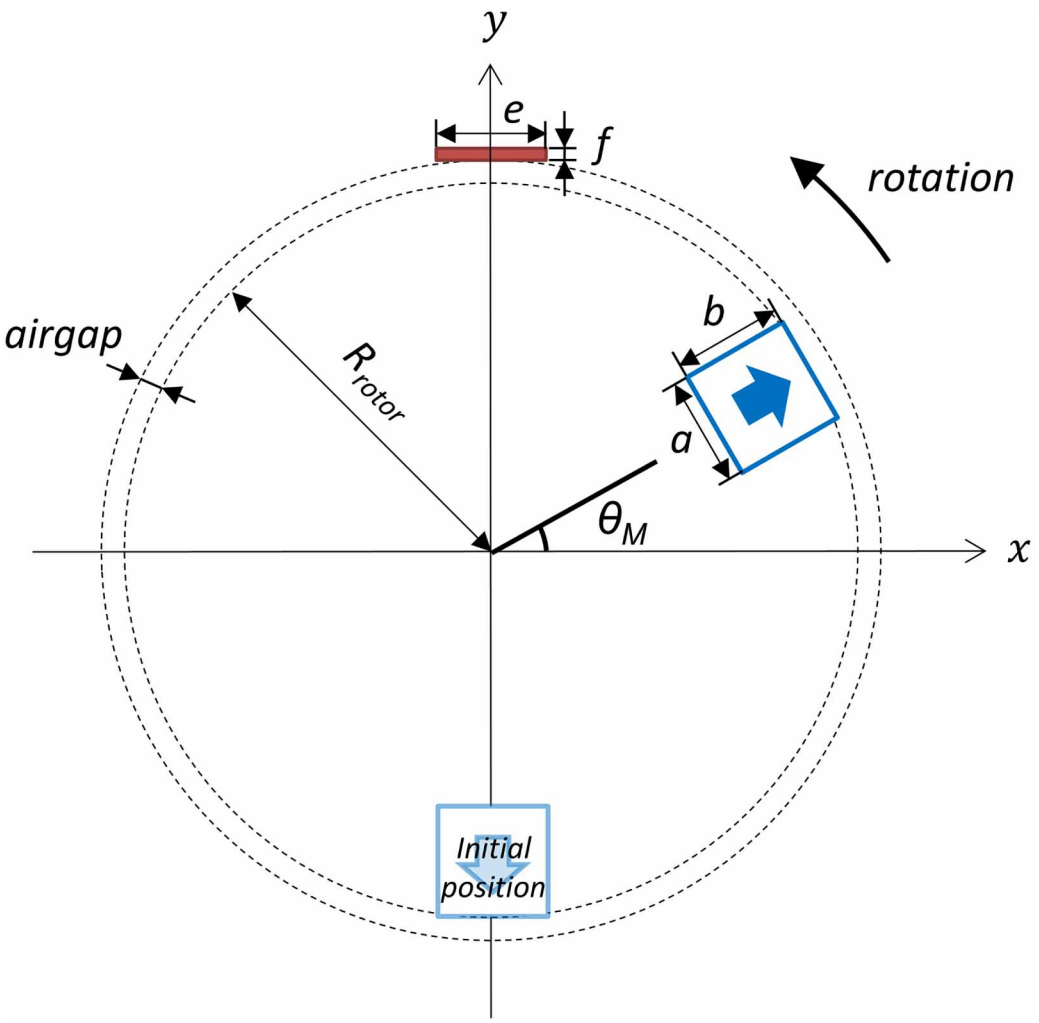

Figure 9-3: Schematic of the HTS dynamo benchmark problem, similar to fig. 5-1. Reproduced from [130].

The benchmark itself was essentially a repeat of the constant J_c model presented in ch. 5, that avoids potential ambiguities of the $J_c(B, \theta)$ implementation. The specific geometry is pictured in fig. 9-3. Overall 10 different numerical methods were compared with each other, including several variations based on H-formulation and finite elements more generally. Of the 10 models, 7 were based on finite element techniques and 3 on integral methods. All the techniques were capable of capturing the 2D cross sectional geometry of the overall dynamo system, with some techniques changing the dimensionality of the HTS stator cross section between 2D and 1D. Of these models, 3 were variations of the H-formulation and 4 were variations of the T-A formulation models. Where the formulations or modelling techniques permitted some freedom of choice in its construction, such choices were left to the modellers in charge. In effect, those small choices that did remain were shown not to have discernible effects on the modelling outcomes. Figure 9-4 shows the agreement in transient ΔV waveforms between the different models. This was an important validation of some of the many kinds of approximations physicists and engineers commonly make in this field.

Another critical factor is that the modelling benchmark captures the developmental nature of modelling. While individual modellers dedicate time to making their own techniques faster, more efficient, and more accurate, the modelling community itself increases the computational efficiency by spreading the problem across different methods of computation. The fastest method, provided by Dr. Enric Pardo's group, is the Minimum electromagnetic entropy production (MEMEP) and while computationally faster, it is slower to design and iterate with. This may simply be due to the fact that MEMEP methods are run on bespoke software, rather than a dedicated programme such as COMSOL Multiphysics. In the long run it may be advantageous to wrap the MEMEP method in a professional development suite so that models can be made easily, iterated on and shared. While slower, the H-formulation method was the basis of the first solution to the dynamo problem in large part because of its ease of use and numerical robustness.

Again, it is a great boon that my first modelling question can be answered so

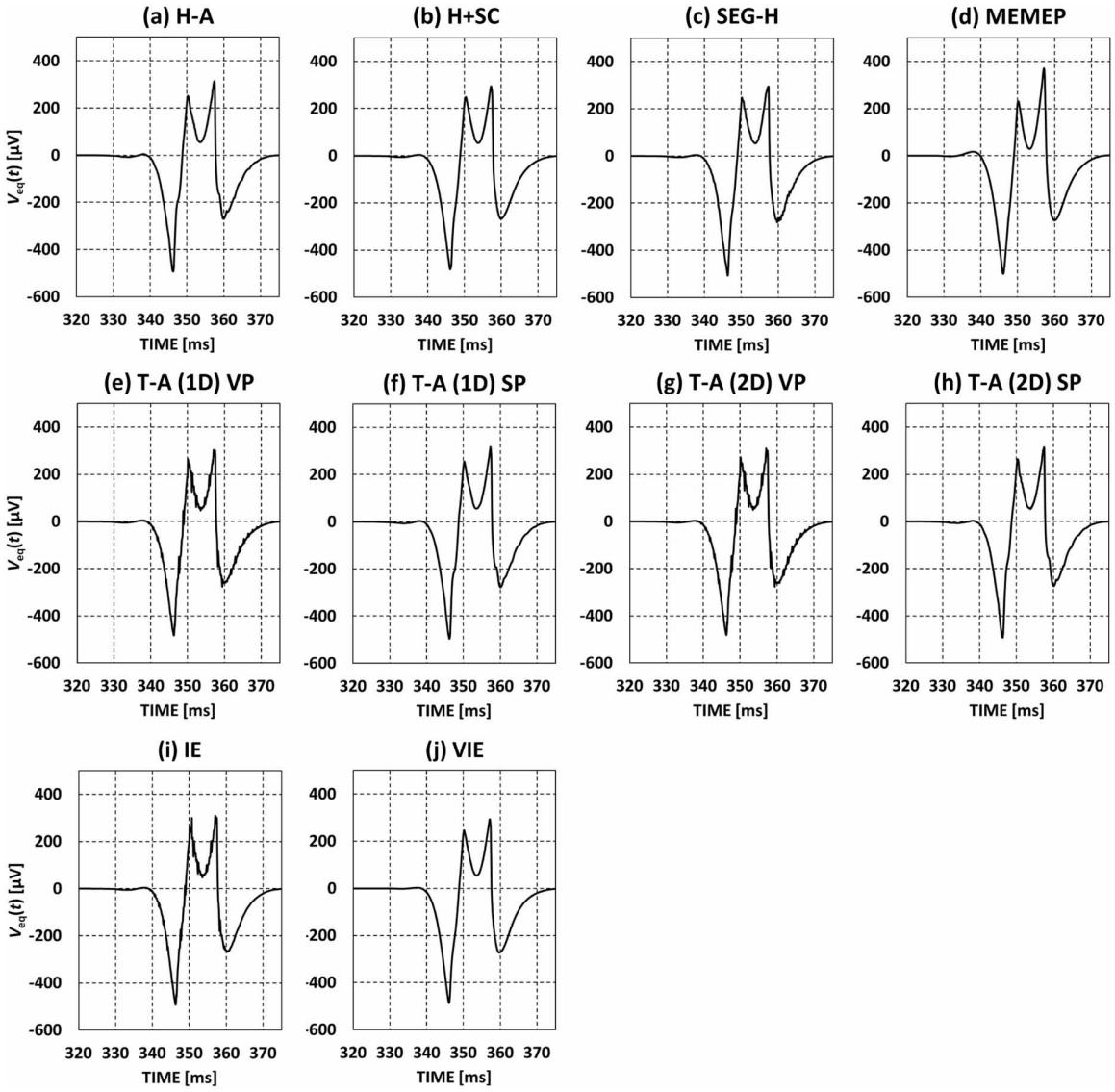

Figure 9-4: (a-j) Transient waveforms of ΔV as produced from the various benchmark models. Reproduced from [130].

thoroughly. While Professor Campbell's work, see sec. 9.3, is an alternative to my first research question, the modelling benchmark is its ultimate extension. Not only does this 'benchmark paper' capture the essence of solving the HTS dynamo problem across numerous numerical methods, it also lays a clearer challenge for all remaining methods to do the same.

9.4.1 The faster model

The value of the modelling benchmark was quickly confirmed with the publication of Prigozhin *et.al.* [131], which utilised a, very specialised, Chebyshev polynomial technique to model the supercurrents in the dynamo. Unlike finite element techniques, that use polynomial approximation within the discretized sub elements of a given domain, Chebyshev polynomials can be used to express the current in the whole superconducting strip as a sum of a single set of such polynomials. That is, Chebyshev polynomials form an orthonormal basis, that can express current densities, over the whole width of the superconducting stator. While a simple discrete Fourier series could do the same, Chebyshev polynomials avoid the numerical singularities that would be seen in a Fourier expression of the step-like current distributions common in superconductors.

By expressing the current density in the basis of Chebyshev polynomials, the overall problem can be reduced to a series of ordinary differential equations that can be solved by integration from a set of initial conditions. This is one of the most straightforward numerical solving techniques and hence solves the HTS dynamo benchmark problem extremely quickly. The fastest computation using polynomials to degree 100 (referred to as mesh nodes) calculates a single cycle of the HTS dynamo in 1.2 s with relative error of 2.3%. This is significantly faster than MEMEP, which can use 100 mesh elements to solve a single cycle in 11.5 s where the relative error of MEMEP is lower at 0.85%. This comparison is obviously somewhat skewed as the notion of mesh element/node is different between the two methods. A clear comparison shows that at 200 mesh nodes the Chebyshev method solves in 4.8 s with a relative error of 0.67% which is strictly faster and more accurate than the MEMEP

method.

As these methods become faster they also become more esoteric. While faster than MEMEP, Chebyshev polynomials are also significantly less obvious as a technique to employ. The HTS dynamo Benchmark will continue to help span comparisons of this trade off between ease of model formulation and model performance, hopefully to the benefit of the entire modelling community. In the case where these models move from being tools for physical inquiry, toward being models for engineering optimisation, speed of computation directly translates to the range of parameters that can be optimised and the complexity of systems that can be modelled whole.

9.5 Modelling the performance parameters of the HTS dynamo

Chapter 6 explored my second research question, by expanding the dynamo model of characterise the performance of the HTS dynamo. That work was not itself exhaustive, only capturing the performance space for one configuration of the device. But with a large number of research groups working on the HTS dynamo problem the effects of varying the configuration and operational parameters of the HTS dynamo have been modelled at great pace.

9.5.1 Coil charging and AC loss

Back in ch. 6, fig. 6-4 (c) showed that at very low frequencies the experimentally measured short-circuit current and the open-circuit flux-per-cycle dropped away from linear trends and away from the model result. Speculation as to the cause of this drop-off led us to consider the differences between the model and experiment. While all models have assumptions, the biggest that might give non-trivial results over different frequency ranges is the inductance of the load. Chapter 6 presented experimental results that used an electronic power supply as an electronic load. Such power supplies have non-uniform frequency response, and the power supply used did not quote its

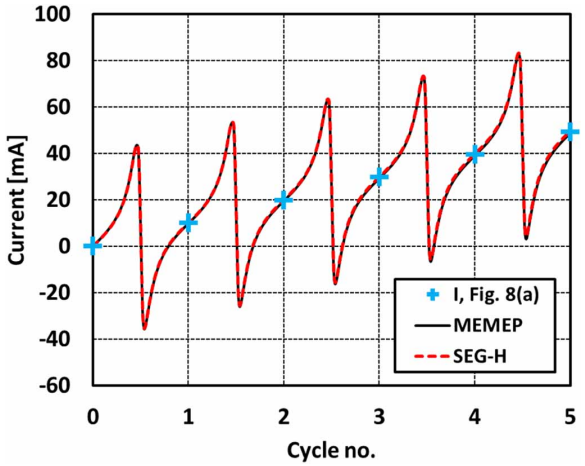

Figure 9-5: "Dynamic charging current curve of the modelled coil over the first five cycles for the two studied models. The cross symbol refers to the extracted data points at the end of each cycle used for plotting figure 8. The case belongs to 3.7 mm airgap and 25 Hz frequency." Figure and caption reproduced from [132]

frequency behaviour at such low levels. The potential interaction between the load and the dynamo is not accounted for in any of the models in this thesis, and was a major reason for my own contribution to [132].

Ghabeli et. al. [132] establishes two different models that incorporate the effect of load inductance into the model of the HTS dynamo. There are two motivations for this, one is that some load reactance should be necessary for establishing a voltage. Or rather, that we would expect a zero inductance load to develop no voltage, and hence receive no flux from the HTS dynamo. The second motivation is that the output waveform of the HTS dynamo is not uniform and has a large ac component. This ac voltage, when applied to superconducting circuits or loads can lead to ac loss.

To some extent the level of loss does not seem concerning, as it has been shown that HTS dynamos can drive HTS coils up to and past their I_c. However, in real engineering scenarios, the cryogenic cooling budget for a given system is a major determiner of both feasibility and cost. Here Ghabeli et. al. presents the AC loss in the HTS stator for the first time. The level of loss is not terrible, peaking at 1.5 W instantaneously or 135.7 mW continuous (at 25 Hz). While relatively low, even this level of loss may be a consideration for systems running at 4 K or in space applications.

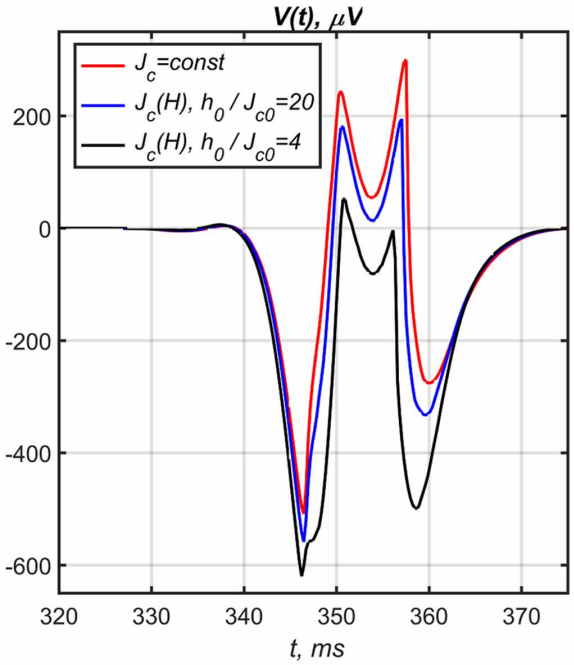

Figure 9-6: Transient ΔV waveforms calculated for varying Kim model field sensitivities h_0. Figure reproduced from [131].

9.5.2 Effects of $J_c(B, \theta)$

Chapter 5 introduced explicit evidence that $J_c(B, \theta)$ plays an important role in the quantitative dc voltage output of the HTS dynamos. While this is attributed to $J_c(B, \theta)$ suppression as the magnet transits, a deeper explanation as to why this affects the voltage output has not been fully explored in this thesis. Two studies have explored this effect further, one that I presented at the AMN9 conference, and a second performed by Prigozhin [131]. Briefly, the work I presented at AMN9 simply substituted many different $I_c(B, \theta)$ profiles, measured at Robinson, into the HTS dynamo model to determine the optimal HTS material. While interesting, my study was limited to making simplistic engineering choices. Primarily, that more field sensitive conductors make better dynamos, inline with expectation.

Prigozhin et.al. introduce the use of a Kim model [133] to explore the effect of $J_c(B, \theta)$ on the dynamo output. The Kim model presents an empirical model for the anisotropy of $J_c(B, \theta)$:

$$J_c = \frac{J_{c,0}}{1 + h_0^{-1}\sqrt{\kappa H_y^2 + H_z^2}}, \tag{9.1}$$

where $J_{c,0}$, h_0, and κ are fitting parameters. The Kim model parameterizes the absolute effect of magnetic field via h_0, and the effect of anisotropy through κ. Prigozhin focuses on the simpler effect of h_0 vs $J_{c,0}$, as reproduced in fig. 9-6, keeping $\kappa = .5$. As h_0 approaches infinity $J_{c,0}$ approaches the constant J_c model. This systematically captures the effect of field suppression on the HTS dynamo mechanism.

A further and expanded Kim model study is more than justified. While Prigozhin touches on the effect, expanding to analyse anisotropy, κ, will be deeply insightful for the study of such devices. Furthermore, the relationship between field suppression, anisotropy, applied field, and field penetration could be combined into a unified study.

9.5.3 High frequency behaviour and thermal effects

This thesis has focused on the phenomenology of the HTS dynamo for a frequency range where the dc voltage is found to be linear. With respect to the output I-V characteristic, discussed in ch. 6, the reasons for linearity are not actually fundamental instead they come from probing a small range of the underlying behaviour. Previous experimental work by Pantoja et.al. [134] explored higher frequency ranges and found that the linearity with frequency eventually breaks down.

The explanations put forward by Pantoja et.al. focused on potential thermal effects creating a feedback between increasing frequency, loss, heating, and therefore a decrease in $J_c(B, \theta)$. Instabilities seen at high frequencies also seemed reminiscent of unstable cooling and nucleate boiling of the liquid nitrogen. Ultimately, these explanations were only offered as speculation, and experimental tests to investigate the hypothesis were not undertaken.

However, the electromagnetic model of the HTS dynamo can be coupled with a thermal model that accounts for the heating caused by EM dissipation and its effects on $J_c(B, \theta)$. This coupled approach was undertaken by Ainslie et.al [135] who found that accounting for heating over the appropriate frequency range does not account for the larger reduction in frequency normalised output voltage. These results can be surmised from fig. 9-7 . Instead, the model shows that accounting for current flowing in the copper stabiliser, that surrounds the HTS and substrate of the tape,

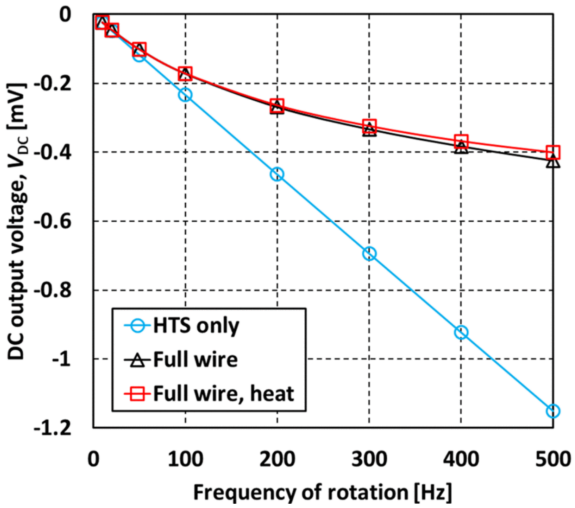

Figure 9-7: Open-circuit DC output voltage of the HTS dynamo, as given by [135, (4)], for the three models. For the "HTS only" and "Full wire" models, these values are calculated after 10 cycles of rotation; for the "Full wire, heat" model, the number of cycles varies with frequency, ranging from 10 cycles up to 50 cycles to ensure thermal equilibrium is reached (see [135, Fig. 5]) and the DC output voltage is stable. Figure and caption reproduced from [135]

can account for a large reduction in frequency normalised output voltage.

Effectively, as frequency increases, the available *emf* becomes sufficient to drive appreciable currents in the copper stabiliser. Among other effects, the increased current flowing in the stabiliser acts to shield the penetrating field seen by the superconducting layer. This is essentially a skin effect and increases the effective penetration field of the tape overall. With less magnetic field penetrating the HTS, the output of the dynamo decreases. Critically, this puts some upper limits, or at least implies trade-offs, associated with increasing HTS dynamo design output by simply 'running them faster'.

9.5.4 2D models of flux gap

Other than increasing frequency, the other major reason an HTS dynamo might see a lower applied field would be an increase in the flux gap g between the stator and the magnet. Increasing g reduces the applied field magnitude as well as broadening the applied field profile.

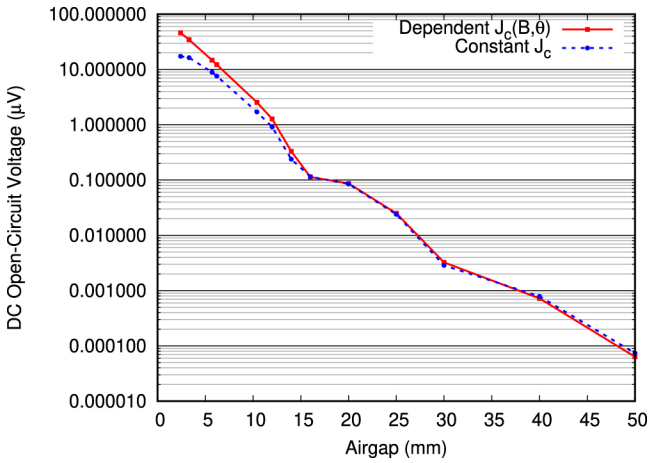

Figure 9-8: Although the DC open-circuit voltage in the flux pump decreases with the airgap, it never vanishes. Calculated voltage for the cases of constant J_c and magnetic-field dependent $J_c(B,\theta)$ for airgaps in the range of 2.4-50 mm. Figure and caption reproduced from [127].

These behaviours were first modelled, systematically, by Ghabeli et.al. [127]. Broadly there are three things to take from this work. One, that increasing flux gap has all the effects that one would expect given the mechanism of the device. Two, that the dependence on g is not accurately portrayed for distances where $g \approx w$, where w is the width of the magnet. Third, and most surprising, is that while the output voltage decreases with flux gap, it never reaches zero, as reproduced in fig. 9-8. While surprising, recall the similar feature of the semiconducting dynamo presented in ch. 8 and fig. 8-2. This may also represent a novel probe into the limiting behaviour of HTS materials and the applicability of the E-J power law.

9.6 3D models of the HTS dynamo

As different numerical methods were bought to bear on the HTS dynamo problem, the computational advantage of particular models became clear. But with new computing power, comes the ability to model aspects of the HTS dynamo that were previously handled by assumption. The biggest of these is the shift from 2D to true 3D simulation of the device. Two groups have now expanded their models to 3D to capture the full current distributions of these devices.

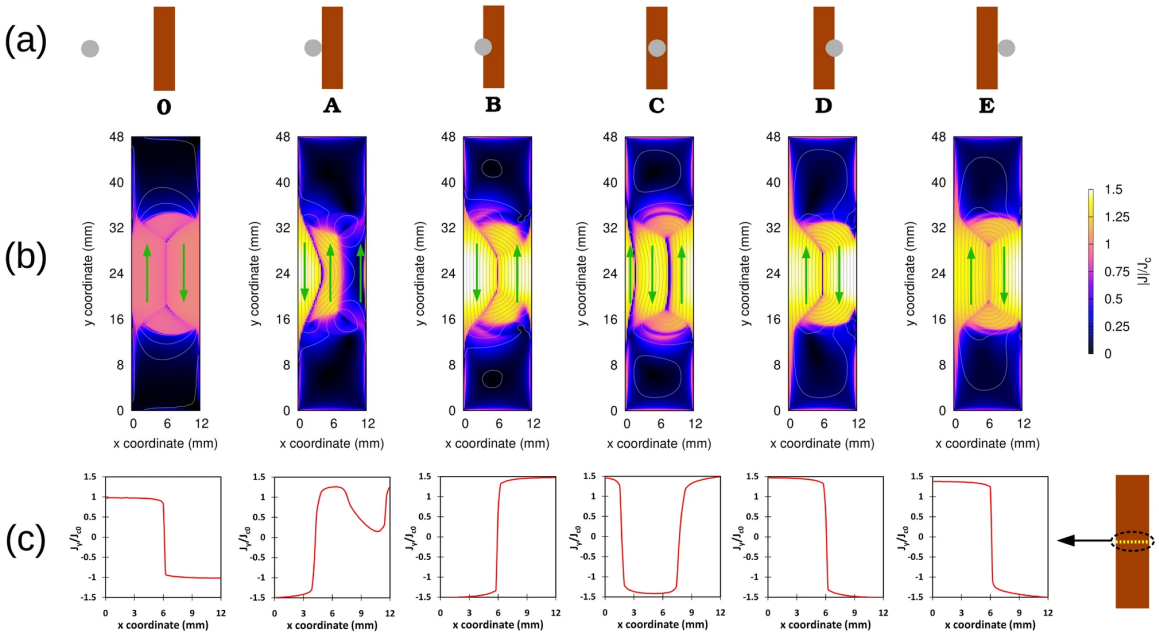

Figure 9-9: Current modeling results for airgap 3.3 mm and constant J_c: (a) Key magnet positions including step 0, when magnet is very far from the tape, (b) Current modulus maps and current lines regarding the key magnet positions, (c) Current profiles of J_c-normalized J_y regarding the key magnet positions in the mid-plane of the tape (y=24 mm). y_x vanishes due to symmerty at the mid-plane. Figure and caption reproduced from [136].

Naturally, the two fastest (model speed) groups have produced 3D models. First, (by one week), was Ghabeli et.al. [136] who applied their MEMEP method to the 3D case. Second, but entirely independently, Prigozhin et.al. [137] presented two methods for solving the HTS dynamo problem in 3D. Fascinatingly, the two methods proposed by Prigozhin are not based directly on their 2D method from [131]. Rather, they propose a mixed finite element based on their much older work [138] as well as a Fast Fourier Transform (FFT) method originally introduced by Brandt [139].

Based on the previous section, sec. 9.5.4, the major advantage of 3D models would be the evaluation of the proper flux gap dependence. However, this is only explored in [136]. Indeed, it is found that a 3D model gives more accurate predictions of the flux gap dependence at larger gaps.

Both papers report full 2D current distributions as they flow in the plane of the tape. While this increased detail has some effect on the predicted dc voltage, they

are actually much better visual evidence for another design parameter that has not yet been widely discussed. That is, the stator tape must be sufficiently long to accommodate the circulating currents as they extend beyond the applied magnetic field. Figure 9-9 shows that as these currents recirculate they begin dropping down below J_c.

If the current does not have enough tape length to accommodate this drop off, the currents recirculating in the x direction, across the tape width, will remain above J_c and dissipate local *emf* in the wrong direction, resulting in a drop in V_{oc}. This design consideration has already impacted devices built at Robinson Research, namely the drum dynamo discussed in sec. 7.4.2, where it is evident that the experimental drum's length is insufficient to provide current turn around.

9.7 Dynamo efficiency

One of my original research questions, which was subsumed in the broader definition of question 3, was related to the efficiency of HTS dynamos. That is, while such devices can be used to avoid thermal leak caused by current leads, the HTS dynamo itself does indeed generate heat. A study of HTS dynamo efficiency was carried out by Hamilton et.al. [125] and established the design relationships associated with using HTS dynamos over copper current leads.

Figure 9-10 shows the relationship between dynamo efficiency and dynamo output current while also comparing different operational speeds. The key result is that the HTS dynamo's efficiency is a function of the delivered operational power, whereas current leads deliver a constant heat load proportional to their design current. This opens a magnet design space that is accessible to the dynamos but not to current leads i.e. magnets operating at high current, and low inductance/voltage. This design space remains to be fully explored.

While [125] is not deeply informed by my work in [107], its is worth discussing here in the context of future work. Of all the papers that have been generated from the work in this thesis, as well as this thesis itself, very little mention of efficiency is

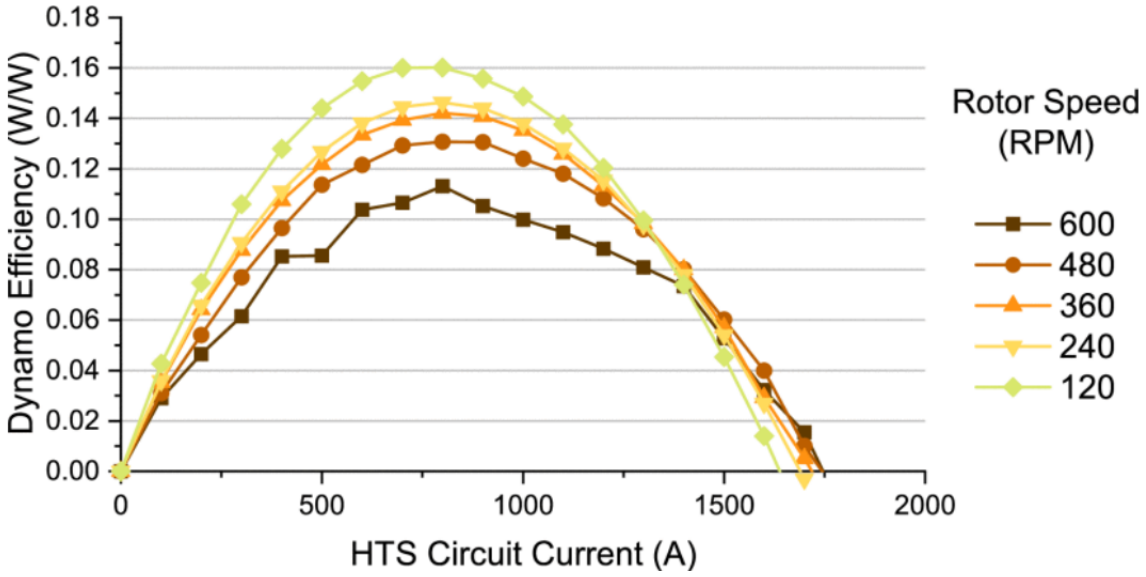

Figure 9-10: Measured dynamo efficiency, delivered power divided by dissipation, characteristics at selected rotational speeds. Figure and caption reproduced from [125].

made. This is not due to a lack of modelling power, in fact all such electromagnetic models can explicitly calculate the losses in the HTS dynamo. Rather, the efficiency of the HTS dynamo is an important enough topic to warrant explict treatment in the literature.

Essentially, every one of the parameters explored in sec. 9.5 may have an effect on the efficiency of the device. Efficiency studies are significantly more difficult to complete experimentally, and the work undertaken by Hamilton et.al. was a specific measurement campaign undertaken for this purpose. However, all the authors of the previously mentioned work give little space to discuss these efficiency issues. This is essentially because there is no bedrock paper explicitly discussing the efficiency of these devices from a modelling perspective. Now that models exist that can span these various parameters, it maybe worth considering a piece of specific work that lays out the efficiency ramifications of several of these design choices.

Chapter 10

Conclusion

Highlights

- NI Coils and HTS dynamos can be modelled using reduced dimension FEA and thus expanded multi physics models are possible at low computational overhead.
- The mechanism of the HTS dynamo can be derived from classical electrodynamics as a consequence of the macroscopic constitutive behaviour of HTS materials.
- The phenomenology of the mechanism can be observed in a numerical model that corresponds with experiment over all available observational and operational parameters.
- The phenomenology predicts improved operational designs for the device through wider stators. Such designs lead to higher output currents and voltages which are born out in expanded modelling. These models also reveal a new and yet unexplored resistive effect.
- Non-linearity should also lead to similar effects in systems based on other materials such as semiconductors, where it should be possible to build a electromagnetically "dual" device with a similar emergent mechanism as the HTS dynamo.

- The work herein has spurred a large amount of work by other groups whose contributions have dramatically expanded — and largely completed — an operational understanding of the HTS dynamos as they exist today.

10.1 Overview

At the start of this thesis I introduced two innovations in HTS technology, the NI coil and the HTS dynamo. These two technologies, in their own ways, had serious open questions regarding their design, application, and in the case of the HTS dynamo a physical mechanism. Hopefully, this thesis has taken you through a journey in understanding these two innovations and how our maturing understating of them will affect the future.

Open questions are always interesting and the NI coils, for the first time in decades, posed new problems and opportunities in high field magnets. And while the NI coils resisted finite element analysis for nearly a decade, the physics was quickly and essentially understood. In the case of the NI coils, progress was only limited by lagging numerical techniques.

In the case of the HTS dynamo, the issue extended beyond numerical limitations and into the underlying physics of the device. In the absence of simple models, speculation on the physical mechanism of the HTS dynamo's dc voltage abounded. Not only was a new model needed, but it needed to be numerically accurately enough to leave no gap for speculation on the mechanism. Without such a mechanism, how was the research community to plead the case for such devices in application? How were they to develop the certainty needed to integrate them into as complex a machine as a modern aircraft?

This thesis does not present material in the order it was completed. The first thing that I did was solve the HTS dynamo problem. Indeed at the time I was not yet aware of the NI coils or their potential impact. Nevertheless, the material has been presented here in an order to best serve clarity and understanding. Hence, the research questions established an order to understanding the material presented.

First in our ability to model such devices, second in our ability to interrogate them for physical insight, and third to test if such insights would lead to improvements.

10.1.1 The NI Coil

Chapter 4 practically explored how to use an H-formulation technique, and the concept of rotated anisotropic resistivity, to build and validate a simple finite element model the NI Coil. It was shown that such a model is possible, that the model matches existing experiments, and furthermore resolves the complicated supercurrent profiles with both radial and axial fidelity. The ability to capture such supercurrent distributions in 2D axisymmetry opens a large new space for understanding, validating, and optimising the designs of such magnets. Furthermore, being based on a simple commercial finite element software the method lends itself specifically to being coupled with other physical models of the NI coil, or associate systems like the dynamo or target systems such magnetic yokes or plasma. As we have now seen in ch. 9, a coupled electromagnetic-thermal model of the NI coil has already been achieved and published [128]. We may see in the future years a variety of models coupling thermal, mechanical, ferromagnetic, radiological effects, and more into the analysis of such coils.

10.1.2 Origin of the dc voltage in an HTS dynamo

Chapter 5 applied similar H-formulation techniques to the problem of the HTS dynamo. There we saw that the primary issue did not lie in some simple mathematical trick, but rather in establishing what key input physics would be sufficient to model the device. Again, the challenge was not so much in building a model, but navigating the interplay between modelling logic and physical implications. Ultimately, to untangle 10 years of speculation, quantitative agreement was required to provide the necessary clarity. Chapter 5 outlined that all the phenomena in question emerged, as long as the necessary physics was included, namely the geometry, rotation, electromagnetism, and the constitutive behaviour of the HTS wire. This experimental

agreement was provided by the $J_c(B, \theta)$ model of the device, providing the necessary clarity. And further still, the qualitative phenomena was also seen in a constant J_c model, drilling down into the deeper origin of the mechanism.

With a quantitatively accurate model in hand, and a qualitatively identical, yet simpler, model also available the phenomenology of the dc voltage effect was interrogated from detailed model outputs. An expansion on the work by Bumby et.al. [74], the mechanism of the dc effect was observed to be the large over current driven underneath the magnet as it transited the HTS stator. The uni-polar nature of this over-current, and the sub-criticality of the return current, gives rise to a dc biased output voltage, whilst the interplay of the forward current and the return current was seen to give rise to a dynamic resistance effect as observed by [71].

To further test the input logic, ch. 5 leveraged the power of FE modelling to explore logic that is inaccessible experimentally, namely to vary the n-value of the dynamo material, showing that non-linearity is the critical behaviour for achieving a dc output as $V_{dc} \to 0$ as $n \to 1$. This provided the final proof point needed to cement the physics and mechanism of the dc voltage of the HTS dynamo as a solved issue.

10.1.3 Characteristics and behaviour of the HTS dynamo

With the mechanism of the HTS dynamo explained, and on a strong physical foundation, the FE model was expanded to analyse a much larger range of experimental observables. Chapter 6 explored the ability of the model to replicate full I-V characteristics of an HTS dynamo. From there, the transient electrical correspondence was examined where agreement with experiment continued to be observed. Transient electrical analysis across the whole I-V curve also identified that dynamic resistance is not always present during the magnet's transient across the stator, indicating that dynamic resistance may not be essential to the mechanism itself.

To further test the proposed mechanism, comparisons of magnetic field observations across the width of the HTS stator were made against model data. This again showed agreement between models and experiment during the magnet transit. This correspondence is taken as proof of the validity of the supercurrent distributions,

determined within the model. These were then interrogated directly. This led to several expansions of the HTS dynamo phenomenology: one, that additional current only slightly changes overall current distributions; two, that during the beginning of the magnet transit ample space is available for the return current to remain sub-critical; and three, as additional transport current is added, this sub critical regime remained, but reduced in duration as remnant magnetisation currents were displaced. The interaction of transport current and remnant magnetisation, during the sub-critical regime, results in a small resistive effect qualitatively different to traditional dynamic resistance. Hence by the end of ch. 6 the phenomenology was sufficiently advanced to make a clear prediction, that wider stators should produce higher output voltages and current, as return currents are allowed to remain sub-critical.

10.1.4 A less resistive dynamo

If the purpose of ch. 5 was to investigate V_{oc}, and the purpose of ch. 6 was to investigate how V_{oc} and R_{int} interact to give the I-V behaviour, then ch. 7 is an investigation of what causes the internal resistance of an HTS dynamo in the first place. Previous work had established that the internal resistance of the HTS dynamo obeyed the empirical rules of a dynamic resistance [71], however, ch. 6 identified that this was not true for all moments of the dynamo's operation. Hence, ch. 7 is motivated because one of the best ways to understand an effect is to see if it can be eliminated.

Chapter 7 presented models of wider stator dynamos where the width of the HTS stator was allowed to be significantly larger than the width of the rotating magnet, $w_s > 4w_m$. As hypothesised, this gives ample space for return currents to recirculate without forcing them above J_{c}. For low transport currents this eliminates the 'dynamic resistance' effect and gives a very small value for the differential resistance at zero current R_{oc}, and a very steep I-V curve about V_{oc}.

Without overcritical return currents, the local *emf* from the traversing magnet can be dropped over the forward current, and therefore the forward polarity, almost entirely. This effectively eliminates the dynamic resistance and provides a much clearer

view of the generation mechanism of the HTS dynamo. Critically, the generative effect of the HTS dynamo is not caused by a type of dynamic resistance, and nor is the effect of dynamic resistance isolated to being an internal resistance. In fact, the dynamic resistance of the HTS dynamo has a direct effect in decreasing the open-circuit output of the devices, even when no transport current flows. From this view, eliminating dynamic resistance can be seen as a pure engineering advantage involving no trade-offs. What remains is to continue developing experimental and practical HTS dynamos that are based on wider stators, or "effectively wider" stator networks. Such devices will deliver the maximum output for any given engineering constraint, be it heat, power density, or otherwise.

10.1.5 A semiconducting dynamo

This thesis has presented an aggressive theoretical and numerical campaign to understand the mechanism of the HTS dynamo. We have started with no mechanism, a genuine physical mystery, and can now apply our validated phenomenology to predict optimal performance designs. This progress, means that future opportunities to continue testing these theories are becoming increasingly about engineering accuracy. However, there is one final, and obvious question raised from the conclusion of ch. 5, "would we expect this effect in semiconducting devices?".

Chapter 8 presents very preliminary results from a hypothetical semiconducting dynamo. Such a device tests the underlying phenomenology that was established for the HTS dynamo in a completely new system. Semiconductors, being high impedance by default, represent, in many ways, the electromagnetic "dual" of superconductors. Hence, it was observed that the semiconducting dynamo model produces a dc short circuit current I_{sc}, where paradoxically one should not exist.

With the semiconducting dynamo in mind, the HTS dynamo can be viewed as a low impedance dc source, ideal for charging superconducting inductive loads. The semiconducting dynamo is more similar to existing power electronics, being capable of delivering large voltages, but with high internal impedance and lower currents.

While I do not propose that the semiconducting dynamo will be a useful device,

given that semiconducting power electronics is extremely mature, I do think that experiments could be built. Clear example systems, that look like the HTS dynamo, but are different, would allow researchers a contrasted and decoupled view of the dynamics and mechanism of the HTS system itself. And perhaps, it will be a bridge for those familiar with semiconducting systems, to understand the HTS dynamo in a more reasonable light.

10.1.6 Broad Impact

I have been privileged to watch my tools and models have meaningful impact on the modelling community. From the NI coil models being integrated into multiphysics models, all the way to the nascent experimental work on dynamo efficiency, I look forward to what this community can do next. These models, mine and the community's, represent a full maturation of the study of HTS dynamos.

We now have 3D models of the dynamo that confirm current recirculation dynamics in the HTS stators, with more experiments forthcoming from the Robinson Research group. We have deeper insights into the effect of $J_c(B, \theta)$, which will hopefully lay the ground work for not just specific material selection, but also real material science to be done. There are now an enormous number of research groups capable of modelling, testing, expanding, and probing the science of the HTS dynamo. And all of us equipped to tackle the remaining big questions around HTS dynamo efficiency and power/current density.

Finally, it is my pleasure to say that I feel my time working specifically on these devices has come to an end. While I remain deeply opinionated, I am confident that this subject can now be pushed forward by a large number of brilliant people and groups. With, what has been achieved so far, I have faith that the HTS dynamo is on a pathway to be incorporated in all the devices that we have speculated, hybrid electric aircraft, research magnets, field effect thrusters for satellites, etc. And as I leave this topic for now, I would finish with a taste of what I think the future of this research looks like.

10.2 Future work

10.2.1 The NI coils

It is clear that the NI coil models can now be readily and rapidly integrated with additional design analysis. The most valuable of these will be:

- coupled temperature analysis for quench propagation,
- coupled strain analysis for high field magnets: $J_c(B, T, \varepsilon)$,
- coupled neutron loading for fusion magnet failure modes.

While versions of the above should be possible now, it is fair to conjecture that such models will need to be applied to non-axisymmetric geometries. Hence, an extension to 3D is sorely needed. While ch. 4 lays out the advantages of using the rotated anisotropic resistivity model to solve NI coils in axisymmetric geometries, the method is completely general. In the 3D case, the advantage of homogenising the turns remains, and NI coil models of large complicated magnets should remain possible. Such an effort may also be combined with similarly homogenised models of HTS cables, used in such magnets.

And finally, as modelling power increases, opportunities to test and validate such models must also keep pace. A small, relatively cheap, NI coil experiment is needed that gives a richer variety of experimental observables on which models and assumptions can be verified. Such an experiment would form the basis of an NI coil modelling benchmark, against which all models could be compared.

10.2.2 HTS dynamos

If the performance of the HTS dynamos is now understood, where should the community go next? First, it should be recognised that the entire field of HTS power supplies is based on reducing the thermal load, and increasing power density, of supercondcuting magnet systems. However, what has not yet been covered in any full detail is the efficiency of such HTS flux pumps, the dynamo included. This situation is somewhat

odd, in that the existing models, all of them, have the ability to define and calculate the modelled dynamo efficiency. However, as experimental measurements are few and far between, each individual piece of work on HTS dynamo modelling has not had clear reason to delve into as complicated a topic as the dynamo efficiency. Regardless, tackling the efficiency is the next major task for the modelling community.

The issue of efficiency takes on three parts: one, how do we appropriately calculate the efficiency of a given dynamo for a given purpose; two, what parameters effect the efficiency of a dynamo the most; and three, given all the parameters and design choices, what does the 'efficient frontier' of HTS dynamo design look like?

Finally, throughout my work on these devices, I have consistently witnessed a great chasm between those who think in terms of circuits and those who think in terms of fields. And I would not be surprised if you the reader had some very different mental models to myself, when you were making your way through this thesis. While having specific effects on how we talk about the dynamo physics, this issue is much larger, and can be seen in the broader discourse around electromagnetic theory. All of which leads me to one question: " Can the circuit and field theory models of the HTS dynamos be unified or translated to each other?" I have no doubt that such a unification would help improve the communities grasp of such devices and is a very worthy goal.

10.2.3 A new set of questions

Along the same theme of this thesis, a new set of research questions can be proposed that continue the spirit of this work.

1. Can a set of simple, repeatable, relevant, experimental measurements be established for an NI coil benchmark problem that models can be verified against?

2. Can a unified circuit / field-theory explanation of the dynamos be articulated, and in so doing, can the HTS dynamo be reduced to a travelling wave type rectifier?

3. How does efficiency affect the design of the HTS dynamos, given all of the possible design choices/parameters, and does this lead to a well defined notion of optimal design?

10.3 The end.

I hope that what you have found here has been as interesting to read as it was to research. It was a privilege, and one becoming more rare, to work on a novel problem with such an open field to make progress. The HTS dynamo was an amazing opportunity to rapidly fill in physical understanding, with a large amount of preexisting experimental development and a clear industrial application. Broadly, HTS power supplies, dynamo or otherwise, combined with NI coil technology, represent a huge push in the maturity, deployablity and scalablity of HTS systems. It is my hope that the progress that I have outlined here, will lay the foundation for measurable progress in application, to address many of the issues that the world faces over the next decades. Further, I hope that others can take up the curiosities that remain unaddressed. While this thesis represents a body of work that has bloomed and closed back in, covering many of the obvious questions, I suspect that there are a huge number of interesting questions and challenges left to be addressed, and that the ones I have highlighted here are only a small sample, due to a lack of imagination and time. Again I hope that you have found this useful, and I hope that some of you reading this take up the challenges here, explict, implied or otherwise.

Hei konā mai,

Ratu Craig Te Ahurangi Mataira-Cole

Bibliography

[1] H Kamerlingh Onnes. Further experiments with liquid helium. c. on the change of electric resistance of pure metals at very low temperatures etc. iv. the resistance of pure mercury at helium temperatures. 01 1991.

[2] S. Hahn, D. K. Park, J. Bascunan, and Y. Iwasa. HTS Pancake Coils Without Turn-to-Turn Insulation. *IEEE Trans. Appl. Supercond.*, 21(3):1592–1595, June 2011.

[3] C. Hoffmann, D. Pooke, and A. D. Caplin. Flux pump for HTS magnets. *IEEE Trans. Appl. Supercond.*, 21(3):1628–1631, June 2011.

[4] S. Hahn, K. Kim, K. Kim, X. Hu, Thomas Painter, Iain Dixon, S. Kim, K. R. Bhattarai, So Noguchi, Jan Jaroszynski, and David C. Larbalestier. 45.5-tesla direct-current magnetic field generated with a high-temperature superconducting magnet. *Nature*, 570(7762):496–499, June 2019.

[5] R.P. Huebener, R.T. Kampwirth, and V.A. Rowe. High resolution magneto-optical studies of the intermediate state in thin film superconductors. *Cryogenics*, 12(2):100 – 108, 1972.

[6] U. Essmann and H. Träuble. The direct observation of individual flux lines in type II superconductors. *Physics Letters A*, 24(10):526 – 527, 1967.

[7] Michael Tinkham. *Introduction to Superconductivity*. Dover Publications, 2 edition, June 2004.

[8] Yukikazu Iwasa. *Superconducting Magnet Technology*, page 1–25. Springer, 2009.

[9] John Bardeen and M. J. Stephen. Theory of the motion of vortices in superconductors. *Phys. Rev.*, 140:A1197–A1207, Nov 1965.

[10] J. Bardeen. Theory of the meissner effect in superconductors. *Phys. Rev.*, 97:1724–1725, Mar 1955.

[11] Y. B. Kim, C. F. Hempstead, and A. R. Strnad. Flux-flow resistance in type-II superconductors. *Phys. Rev.*, 139:A1163–A1172, Aug 1965.

[12] L P Gorkov and N B Kopnin. Vortex motion and resistivity of type-II superconductors in a magnetic field. *Soviet Physics Uspekhi*, 18(7):496–513, jul 1975.

[13] P. G. DE GENNES and J. MATRICON. Collective modes of vortex lines in superconductors of the second kind. *Rev. Mod. Phys.*, 36:45–49, Jan 1964.

[14] P. W. ANDERSON and Y. B. KIM. Hard superconductivity: Theory of the motion of abrikosov flux lines. *Rev. Mod. Phys.*, 36:39–43, Jan 1964.

[15] E. F. Talantsev and **R. C. Mataira**. Polar projections for big data analysis in applied superconductivity. *AIP Advances*, 8(7):075213, 2018.

[16] Nicholas Strickland, C Hoffmann, and Stuart Wimbush. A 1 kA-class cryogen-free critical current characterization system for superconducting coated conductors. *The Review of scientific instruments*, 85:113907, 11 2014.

[17] Joseph P. Straley and Stephen W. Kenkel. Percolation theory for nonlinear conductors. *Phys. Rev. B*, 29:6299–6305, Jun 1984.

[18] Jakob Rhyner. Magnetic properties and AC-losses of superconductors with power law current—voltage characteristics. *Physica C*, 212(3):292 – 300, 1993.

[19] F. Bitter. *Magnets: The Education of a Physicist*. Anchor science study series. Doubleday, 1959.

[20] J. Béard, J. Billette, N. Ferreira, P. Frings, J. Lagarrigue, F. Lecouturier, and J. Nicolin. Design and tests of the 100-t triple coil at lncmi. *IEEE Transactions on Applied Superconductivity*, 28(3):1–5, April 2018.

[21] J. G. Bednorz and K. A. Müller. Possible high T_c superconductivity in the Ba-La-Cu-O system. *Zeitschrift für Physik B Condensed Matter*, 64(2):189–193, Jun 1986.

[22] M. K. Wu, J. R. Ashburn, C. J. Torng, P. H. Hor, R. L. Meng, L. Gao, Z. J. Huang, Y. Q. Wang, and C. W. Chu. Superconductivity at 93 K in a new mixed-phase y-ba-cu-o compound system at ambient pressure. *Phys. Rev. Lett.*, 58:908–910, Mar 1987.

[23] Chao Yao and Yanwei Ma. Recent breakthrough development in iron-based superconducting wires for practical applications. *Superconductor Science and Technology*, 32(2):023002, jan 2019.

[24] Yeonjoo Park, Myungwhon Lee, Heesung Ann, Yoon Hyuck Choi, and Haigun Lee. A superconducting joint for GdBa2Cu3O7-d-coated conductors. *Npg Asia Materials*, 6:e98 EP –, May 2014.

[25] B.N. Sorbom, J. Ball, T.R. Palmer, F.J. Mangiarotti, J.M. Sierchio, P. Bonoli, C. Kasten, D.A. Sutherland, H.S. Barnard, C.B. Haakonsen, J. Goh, C. Sung, and D.G. Whyte. ARC: A compact, high-field, fusion nuclear science facility and demonstration power plant with demountable magnets. *Fusion Engineering and Design*, 100:378–405, 2015.

[26] Zachary S Hartwig, Rui F Vieira, Brandon N Sorbom, Rodney A Badcock, Marta Bajko, William K Beck, Bernardo Castaldo, Christopher L Craighill, Michael Davies, Jose Estrada, Vincent Fry, Theodore Golfinopoulos, Amanda E Hubbard, James H Irby, Sergey Kuznetsov, Christopher J Lammi, Philip C Michael, Theodore Mouratidis, Richard A Murray, Andrew T Pfeiffer, Samuel Z Pierson, Alexi Radovinsky, Michael D Rowell, Erica E Salazar, Michael Segal,

Peter W Stahle, Makoto Takayasu, Thomas L Toland, and Lihua Zhou. VIPER: an industrially scalable high-current high-temperature superconductor cable. *Superconductor Science and Technology*, 33(11):11LT01, oct 2020.

[27] Peter J. Lee. Engineering critical current density vs. applied field: April 11th 2018. *Critical current comparison charts — scaling spreadsheet — Applied Superconductivity Center*, Apr 2018, https://fs.magnet.fsu.edu/ lee/plot/plot.htm.

[28] *Cooling and Thermal Insulation Systems*, chapter 3, pages 35–58. Wiley-Blackwell, 2011.

[29] S. Hahn, K. Radcliff, K. Kim, S. Kim, X. Hu, K. Kim, Dmytro V Abraimov, and Jan Jaroszynski. 'Defect-irrelevant' behavior of a no-insulation pancake coil wound with REBCO tapes containing multiple defects. *Supercond. Sci. Technol.*, 29(10):105017, October 2016.

[30] Y. Wang, Wan Kan Chan, and Justin Schwartz. Self-protection mechanisms in no-insulation (RE)Ba2Cu3Ox high temperature superconductor pancake coils. *Supercond. Sci. Technol.*, 29(4):045007, March 2016.

[31] Donghui Liu, Weiwei Zhang, Huadong Yong, and Youhe Zhou. Thermal stability and mechanical behavior in no-insulation high-temperature superconducting pancake coils. *Supercond. Sci. Technol.*, 31(8):085010, July 2018.

[32] Y. Iwasa and S. Hahn. First-cut design of an all-superconducting 100-T direct current magnet. *Appl. Phys. Lett.*, 103(25):253507, December 2013.

[33] S. Hahn, Youngjae Kim, Dong Keun Park, K. Kim, John P. Voccio, J. Bascuñán, and Y. Iwasa. No-insulation multi-width winding technique for high temperature superconducting magnet. *Appl. Phys. Lett.*, 103(17):173511, October 2013.

[34] H. W. Weijers, W. D. Markiewicz, A. J. Voran, S. R. Gundlach, W. R. Sheppard, B. Jarvis, Z. L. Johnson, P. D. Noyes, J. Lu, H. Kandel, H. Bai, A. V. Gavrilin,

Y. L. Viouchkov, D. C. Larbalestier, and D. V. Abraimov. Progress in the Development of a Superconducting 32 T Magnet With REBCO High Field Coils. *IEEE Trans. Appl. Supercond.*, 24(3):4301805, June 2014.

[35] Ben Parkinson. Design considerations and experimental results for MRI systems using HTS magnets. *Supercond. Sci. Technol.*, 30(1):014009, November 2016.

[36] K. Kim, K. R Bhattarai, Jae Young Jang, Young Jin Hwang, K. Kim, Sangwon Yoon, SangGap Lee, and S. Hahn. Design and performance estimation of a 35 T 40 mm no-insulation all-REBCO user magnet. *Supercond. Sci. Technol.*, 30(6):065008, June 2017.

[37] Uijong Bong, Soobin An, John Voccio, Jaemin Kim, Jung Tae Lee, Jihoon Lee, Ki Jin Han, Haigun Lee, and S. Hahn. A Design Study on 40 MW Synchronous Motor With No-Insulation HTS Field Winding. *IEEE Trans. Appl. Supercond.*, 29(5):5203706, August 2019.

[38] Sangwon Yoon, Jaemin Kim, Kyekun Cheon, Hunju Lee, S. Hahn, and Seung-Hyun Moon. 26 T 35 mm all-GdBa2Cu3O7–x multi-width no-insulation superconducting magnet. *Supercond. Sci. Technol.*, 29(4):04LT04, March 2016.

[39] Dongliang Wang, Zhan Zhang, Xianping Zhang, Donghui Jiang, Chiheng Dong, He Huang, Wenge Chen, Qingjin Xu, and Yanwei Ma. First performance test of a 30 mm iron-based superconductor single pancake coil under a 24 T background field. *Supercond. Sci. Technol.*, 32(4):04LT01, April 2019.

[40] D X Ma, S Matsumoto, R Teranishi, T Ohmura, T Kiyoshi, A Otsuka, M Hamada, H Maeda, Y Yanagisawa, H Nakagome, and H Suematsu. Degradation analysis of REBCO coils. *Supercond. Sci. Technol.*, 27(8):085014, August 2014.

[41] Y Wang, H Song, D Xu, Z Y Li, Z Jin, and Z Hong. An equivalent circuit grid model for no-insulation HTS pancake coils. *Supercond. Sci. Technol.*, 28(4):045017, April 2015.

[42] Sukjin Choi, Hyun Chul Jo, Young Jin Hwang, S. Hahn, and Tae Kuk Ko. A Study on the No Insulation Winding Method of the HTS Coil. *IEEE Trans. Appl. Supercond.*, 22(3):4904004, June 2012.

[43] Kwang Lok Kim, S. Hahn, Youngjae Kim, Dong Gyu Yang, Jung-Bin Song, J. Bascuñán, Haigun Lee, and Y. Iwasa. Effect of Winding Tension on Electrical Behaviors of a No-Insulation ReBCO Pancake Coil. *IEEE Trans. Appl. Supercond.*, 24(3):4600605, June 2014.

[44] So Noguchi, S. Hahn, Hiroshi Ueda, SeokBeom Kim, and Atsushi Ishiyama. An extended thin approximation method to simulate screening current induced in REBCO coils. *IEEE Trans. Magn.*, 54(3):7201904, March 2018.

[45] K. R Bhattarai, K. Kim, K. Kim, K. Radcliff, X. Hu, Chaemin Im, Thomas Painter, Iain Dixon, David Larbalestier, SangGap Lee, and S. Hahn. Understanding quench in no-insulation (NI) REBCO magnets through experiments and simulations. *Superconductor Science and Technology*, 33(3):035002, jan 2020.

[46] So Noguchi, Katsutoshi Monma, Sadanori Iwai, Hiroshi Miyazaki, Taizo Tosaka, Shunji Nomura, Tsutomu Kurusu, Hiroshi Ueda, Atsushi Ishiyama, Shinichi Urayama, and Hidenao Fukuyama. Experiment and simulation of impregnated no-insulation REBCO pancake coil. *IEEE Trans. Appl. Supercond.*, 26(4):4601305, June 2016.

[47] T Lécrevisse, A Badel, T Benkel, X Chaud, P Fazilleau, and P Tixador. Metal-as-insulation variant of no-insulation HTS winding technique: pancake tests under high background magnetic field and high current at 4.2 K. *Supercond. Sci. Technol.*, 31(5):055008, May 2018.

[48] Tae Sung Lee, Young Jin Hwang, Jiho Lee, Woo Seung Lee, Jinsub Kim, Seung Hyun Song, Min Cheol Ahn, and Tae Kuk Ko. The effects of co-wound Kapton, stainless steel and copper, in comparison with no insulation, on the

time constant and stability of GdBCO pancake coils. *Supercond. Sci. Technol.*, 27(6):065018, June 2014.

[49] Lei Wang, Qiuliang Wang, Jianhua Liu, Hui Wang, Xinning Hu, and Peng Chen. Screening current-induced magnetic field in a noninsulated GdBCO HTS coil for a 24 T all-superconducting magnet. *IEEE Trans. Appl. Supercond.*, 27(4):8200106, June 2017.

[50] Tao Wang, So Noguchi, Xudong Wang, Issei Arakawa, Katsuhiko Minami, Katsutoshi Monma, Atsushi Ishiyama, S. Hahn, and Y. Iwasa. Analyses of transient behaviors of no-insulation REBCO pancake coils during sudden discharging and overcurrent. *IEEE Trans. Appl. Supercond.*, 25(3):4603409, June 2015.

[51] Xudong Wang, Tao Wang, Erika Nakada, Atsushi Ishiyama, Ryusei Itoh, and So Noguchi. Charging behavior in no-insulation REBCO pancake coils. *IEEE Trans. Appl. Supercond.*, 25(3):4601805, June 2015.

[52] So Noguchi and S. Hahn. Torque simulation on NI REBCO pancake coils during quench. *J. Phys.: Conf. Ser.*, 1293:012061, September 2019.

[53] Yi Zhang, Yuejin Tang, Zhong Xia, Li Ren, and Jingdong Li. Investigation on performance of no-insulation coil considering the influence of stress distribution on radial characteristic resistivity. *IEEE Trans. Appl. Supercond.*, 28(4):4604007, June 2018.

[54] Yi Li, Dongkeun Park, Yufan Yan, Yoonhyuck Choi, Jiho Lee, Philip C Michael, Siwei Chen, Timing Qu, Juan Bascuñán, and Yukikazu Iwasa. Magnetization and screening current in an 800 MHz (18.8 T) REBCO nuclear magnetic resonance insert magnet: experimental results and numerical analysis. *Supercond. Sci. Technol.*, 32(10):105007, aug 2019.

[55] D. G. Yang, K. L. Kim, Y. H. Choi, O. J. Kwon, Y. J. Park, and H. G. Lee. Screening current-induced field in non-insulated GdBCO pancake coil. *Supercond. Sci. Technol.*, 26(10):105025, September 2013.

[56] S. Kim, Changhyung Lee, Jeseok Bang, and S. Hahn. Manipulation of screening currents in an (RE)Ba2Cu3O7-x superconducting magnet. *Mater. Res. Express*, 6(2):026004, November 2018.

[57] So Noguchi, Hiroshi Ueda, S. Hahn, Atsushi Ishiyama, and Y. Iwasa. A simple screening current-induced magnetic field estimation method for REBCO pancake coils. *Supercond. Sci. Technol.*, 32(4):045007, April 2019.

[58] S. L. Wipf. The case for flux pumps and their problems. *Proceedings of the 1968 Summer Study On Superconducting Devices and Accelerators*, page 632–653, 1968.

[59] J Van Suchtelen, J Volger, and D Van Houwelingen. The principle and performance of a superconducting dynamo. *Cryogenics*, 5(5):256 – 266, 1965.

[60] H.H.J. ten Kate, P.B. Bunk, R.B. Britton, and L.J.M. van de Klundert. High current and high power superconducting rectifiers. *Cryogenics*, 21(5):291 – 296, 1981.

[61] G.B.J Mulder, O.A Shevchenko, M.A Fedorovsky, and H.H.J ten Kate. NbTi thermally controlled switches for superconducting converters with operation frequency up to 50 Hz. part 2: Theory and analysis. *Cryogenics*, 32:451 – 454, 1992. Proceedings of the Fourteenth International Cryogenic Engineering Conference and International Cryogenic Materials Conference Cryogenic Engineering —& Superconductor Technology.

[62] L.J.M. van de Klundert and H.H.J. ten Kate. Fully superconducting rectifiers and fluxpumps part 1: Realized methods for pumping flux. *Cryogenics*, 21(4):195 – 206, 1981.

[63] J. Volger and P.S. Admiraal. A dynamo for generating a persistent current in a superconducting circuit. *Physics Letters*, 2(5):257 – 259, 1962.

[64] H. Van Beelen, Miss A.J.P.T. Arnold, H.A. Sypkens, J.P. Van Braam Houckgeest, R. De Bruyn Ouboter, J.J.M. Beenakker, and K.W. Taconis. Flux pumps and superconducting solenoids. *Physica*, 31(4):413 – 443, 1965.

[65] O. Mawardi, A. Gattozzi, and H. Chung. Operational characteristics of a flux pump. *IEEE Transactions on Magnetics*, 15(1):828–831, January 1979.

[66] I. Giaever. A dc transformer. *IEEE Spectr.*, 3(9):117–122, Sept 1966.

[67] Wei Wang and Tim Coombs. Macroscopic magnetic coupling effect: The physical origination of a high-temperature superconducting flux pump. *Phys. Rev. Applied*, 9:044022, Apr 2018.

[68] J Geng, K Matsuda, L Fu, J-F Fagnard, H Zhang, X Zhang, B Shen, Q Dong, M Baghdadi, and T A Coombs. Origin of dc voltage in type II superconducting flux pumps: field, field rate of change, and current density dependence of resistivity. *J. Phys. D*, 49(11):11LT01, 2016.

[69] T. A. Coombs, J. F. Fagnard, and K. Matsuda. Magnetization of 2-G coils and artificial bulks. *IEEE Trans. Appl. Supercond.*, 24(5):8201005, Oct 2014.

[70] J. Geng, B. Shen, C. Li, H. Zhang, K. Matsuda, J. Li, X. Zhang, and T. A. Coombs. Voltage-ampere characteristics of YBCO coated conductor under inhomogeneous oscillating magnetic field. *Appl. Phys. Lett.*, 108(26):262601, 2016.

[71] Zhenan Jiang, K. Hamilton, Naoyuki Amemiya, R. A. Badcock, and C. W. Bumby. Dynamic resistance of a high-T_c superconducting flux pump. *Appl. Phys. Lett.*, 105(11):112601, 2014.

[72] V. V. Andrianov, V. B. Zenkevich, V. V. Kurguzov, V. V. Sychev, and F. F. Ternovskiĭ. Effective resistance of an imperfect type II superconductor in an oscillating magnetic field. *Soviet Journal of Experimental and Theoretical Physics*, 31:815, 1970.

[73] Zhenan Jiang, Chris W Bumby, Rodney A Badcock, Hae-Jin Sung, Nicholas J Long, and Naoyuki Amemiya. Impact of flux gap upon dynamic resistance of a rotating HTS flux pump. *Supercond. Sci. Technol.*, 28(11):115008, 2015.

[74] C. W. Bumby, Zhenan Jiang, J. G. Storey, A. E. Pantoja, and R. A. Badcock. Anomalous open-circuit voltage from a high-T_c superconducting dynamo. *Appl. Phys. Lett.*, 108(12):122601, 2016.

[75] W. Wang and T. A. Coombs. Vortex migration caused by travelling magnetic wave in a 2 in. diameter YBa2Cu3O7-δ thin film. *Journal of Applied Physics*, 113(21):213906, 2013.

[76] Wei Wang, Fred Spaven, Min Zhang, Mehdi Baghdadi, and Timothy Coombs. Direct measurement of the vortex migration caused by traveling magnetic wave. *Appl. Phys. Lett.*, 104(3):032602, 2014.

[77] Ivar Giaever. Magnetic coupling between two adjacent type-II superconductors. *Phys. Rev. Lett.*, 15:825–827, Nov 1965.

[78] John R. Clem. Theory of magnetically coupled type-II superconducting films. *Phys. Rev. B*, 9:898, Feb 1974.

[79] A. M. Campbell. An introduction to numerical methods in superconductors. *Journal of Superconductivity and Novel Magnetism*, 24(1):27–33, Jan 2011.

[80] K. Kajikawa, T. Hayashi, R. Yoshida, M. Iwakuma, and K. Funaki. Numerical evaluation of ac losses in HTS wires with 2D FEM formulated by self magnetic field. *IEEE Trans. Appl. Supercond.*, 13(2):3630–3633, June 2003.

[81] Z. Hong, A. M. Campbell, and T. A. Coombs. Numerical solution of critical state in superconductivity by finite element software. *Supercond. Sci. Technol.*, 19(12):1246–1252, 2006.

[82] D. N. Arnold. Periodic table of the finite elements. *SIAM News*, Nov 2013, https://sinews.siam.org/Details-Page/periodic-table-of-the-finite-elements.

[83] Charles M. Elliott and Yohei Kashima. A finite-element analysis of critical-state models for type-II superconductivity in 3D. *IMA Journal of Numerical Analysis*, 27(2):293–331, 04 2007.

[84] Antonio Morandi. 2D electromagnetic modelling of superconductors. *Superconductor Science and Technology*, 25(10):104003, sep 2012.

[85] Julien Dular, Christophe Geuzaine, and Benoît Vanderheyden. Finite-Element Formulations for Systems With High-Temperature Superconductors. *IEEE Transactions on Applied Superconductivity*, 30(3):1–13, April 2020.

[86] Z. Hong and T. A. Coombs. Numerical modelling of ac loss in coated conductors by finite element software using H formulation. *J. Supercond. Nov. Magn.*, 23(8):1551–1562, Dec 2010.

[87] Mark D Ainslie, Chris W Bumby, Zhenan Jiang, Ryuki Toyomoto, and Naoyuki Amemiya. Numerical modelling of dynamic resistance in high-temperature superconducting coated-conductor wires. *Supercond. Sci. Technol.*, 31(7):074003, 2018.

[88] M D Ainslie and H Fujishiro. Modelling of bulk superconductor magnetization. *Supercond. Sci. Technol.*, 28(5):053002, mar 2015.

[89] Ye Hong, Jun Zheng, and Hengpei Liao. Modeling of high-T_c superconducting bulk using different J_c–T relationships over dynamic permanent magnet guideway. *Materials*, 12(18), 2019.

[90] Loïc Quéval, Kun Liu, Wenjiao Yang, Víctor M R Zermeño, and Guangtong Ma. Superconducting magnetic bearings simulation using an h-formulation finite element model. *Supercond. Sci. Technol.*, 31(8):084001, jun 2018.

[91] Boyang Shen, Francesco Grilli, and Tim Coombs. Overview of H-formulation: A versatile tool for modeling electromagnetics in high-temperature superconductor applications. *IEEE Access*, 8:100403–100414, 2020.

[92] Valerii M. Vinokur, Tatyana I. Baturina, Mikhail V. Fistul, Aleksey Yu. Mironov, Mikhail R. Baklanov, and Christoph Strunk. Superinsulator and quantum synchronization. *Nature*, 452(7187):613–615, Apr 2008.

[93] R88M-K[], R88D-KN[]-ECT, I576-E1-05, AC servomotors/servo drives User's Manual, https://www.omron-ap.co.nz/products/family/2644/download/manual.html.

[94] Victor M. R. Zermeño, Krzysztof Habelok, Mariusz Stepień, and Francesco Grilli. A parameter-free method to extract the superconductor's $J_c(B, \theta)$ field-dependence from in-field current–voltage characteristics of high temperature superconductor tapes. *Supercond. Sci. Technol.*, 30(3):034001, 2017.

[95] S. C. Wimbush and N. M. Strickland. A public database of high-temperature superconductor critical current data. *IEEE Trans. Appl. Supercond.*, 27(4):8000105, June 2017.

[96] R. A. Badcock, S. Phang, A. E. Pantoja, Z. Jiang, J. G. Storey, H. Sung, M. Park, and C. W. Bumby. Impact of magnet geometry on output of a dynamo-type HTS flux pump. *IEEE Trans. Appl. Supercond.*, 27(4):5200905, June 2017.

[97] A. E. Pantoja, Z. Jiang, R. A. Badcock, and C. W. Bumby. Impact of stator wire width on output of a dynamo-type HTS flux pump. *IEEE Transactions on Applied Superconductivity*, 26(8):1–8, Dec 2016.

[98] **R C Mataira**, M D Ainslie, R A Badcock, and C W Bumby. Finite-element modelling of no-insulation HTS coils using rotated anisotropic resistivity. *Superconductor Science and Technology*, 33(8):08LT01, jun 2020.

[99] **Ratu Mataira**, Mark D. Ainslie, Rod Badcock, and Chris W. Bumby. Modelling parallel-connected, no-insulation high-T_c superconducting magnets. *IEEE Transactions on Applied Superconductivity*, 31(5):1–5, 2021.

[100] Xudong Wang, S. Hahn, Youngjae Kim, J. Bascuñán, John Voccio, Haigun Lee, and Y. Iwasa. Turn-to-turn contact characteristics for an equivalent cir-

cuit model of no-insulation ReBCO pancake coil. *Supercond. Sci. Technol.*, 26(3):035012, March 2013.

[101] John R Clem, J H Claassen, and Yasunori Mawatari. AC losses in a finite Z stack using an anisotropic homogeneous-medium approximation. *Supercond. Sci. and Technol.*, 20(12):1130–1139, sep 2007.

[102] Leonid Prigozhin and Vladimir Sokolovsky. Computing AC losses in stacks of high-temperature superconducting tapes. *Supercond. Sci. Technol.*, 24(7):075012, may 2011.

[103] Victor M. R. Zermeno, Asger B. Abrahamsen, Nenad Mijatovic, Bogi B. Jensen, and Mads P. Sørensen. Calculation of alternating current losses in stacks and coils made of second generation high temperature superconducting tapes for large scale applications. *J. Appl. Phys.*, 114(17):173901, November 2013.

[104] Enric Pardo. Calculation of AC loss in coated conductor coils with a large number of turns. *Supercond. Sci. Technol.*, 26(10):105017, sep 2013.

[105] J M Brooks, M D Ainslie, Zhenan Jiang, A E Pantoja, R A Badcock, and C W Bumby. The transient voltage response of ReBCO coated conductors exhibiting dynamic resistance. *Supercond. Sci. Technol.*, 33(3):035007, feb 2020.

[106] Greg Brittles, Robert Slade, and Rod Bateman. Testing of Quality Assessment (QA) HTS Magnets at Tokamak Energy. In *Proceedings of MT26 Indico:Tue-Af-Po2.14-12 [11].*

[107] **R. C. Mataira**, M. D. Ainslie, R. A. Badcock, and C. W. Bumby. Origin of the dc output voltage from a high-T_c superconducting dynamo. *Appl. Phys. Lett.*, 114(16):162601, 2019.

[108] **Ratu Mataira**, Mark Ainslie, Andres Pantoja, Rod Badcock, and Chris Bumby. Mechanism of the high-T_c superconducting dynamo: Models and experiment. *Phys. Rev. Applied*, 14:024012, Aug 2020.

[109] R. M. Walsh, R. Slade, D. Pooke, and C. Hoffmann. Characterization of current stability in an HTS NMR system energized by an HTS flux pump. *IEEE Trans. Appl. Supercond.*, 24(3):4600805, June 2014.

[110] Chris W Bumby, Rodney A Badcock, Hae-Jin Sung, Kwang-Min Kim, Zhenan Jiang, Andres E Pantoja, Patrick Bernardo, Minwon Park, and Robert G Buckley. Development of a brushless HTS exciter for a 10 kW HTS synchronous generator. *Supercond. Sci. Technol.*, 29(2):024008, 2016.

[111] S. Lee, W. Kim, Y. Kim, J. Lee, S. Park, J. Lee, G. Hong, S. Kim, J. Han, Y. J. Hwang, and K. Choi. Persistent current mode operation of a 2G HTS coil with a flux pump. *IEEE Trans. Appl. Supercond.*, 26(4):0606104, June 2016.

[112] A M Campbell. A finite element calculation of flux pumping. *Supercond. Sci. Technol.*, 30(12):125015, 2017.

[113] K. Hamilton, A. E. Pantoja, J. G. Storey, Z. Jiang, R. A. Badcock, and C. W. Bumby. Design and performance of a "squirrel-cage" dynamo-type HTS flux pump. *IEEE Trans. Appl. Supercond.*, 28(4):5205705, June 2018.

[114] H. Jeon, J. Lee, S. Han, J. H. Kim, C. J. Hyeon, H. M. Kim, H. Kang, T. K. Ko, and Y. S. Yoon. Pid control of an electromagnet-based rotary HTS flux pump for maintaining constant field in HTS synchronous motors. *IEEE Trans. Appl. Supercond.*, 28(4):5207605, June 2018.

[115] J. Ma, J. Geng, J. Gawith, H. Zhang, C. Li, B. Shen, Q. Dong, J. Yang, J. Chen, Z. Li, and T. A. Coombs. Rotating permanent magnets based flux pump for HTS no-insulation coil. *IEEE Trans. Appl. Supercond.*, page 8663420, 2019.

[116] M. Faraday. V. experimental researches in electricity. *Phil. Trans. R. Soc. Lond*, 122:125–162, 1832.

[117] VK Kaplunenko, SI Moskvin, and VV Schmidt. The nature of voltage produced in superconductors by moving magnetic-flux. *Fizika Nizkikh Temperatur*, 11(8):846–853, 1985.

[118] John R. Clem. Theory of flux-flow noise voltage in superconductors. *Phys. Rev. B*, 1:2140–2155, Mar 1970.

[119] Sándor Bilicz. Approximate and proper electromagnetic modelling in moving conductors. *Period. Polytech. Elec. Eng. Comp. Sci.*, 59(2):43–47, 2015.

[120] L. Civale, B. Maiorov, A. Serquis, J. O. Willis, J. Y. Coulter, H. Wang, Q. X. Jia, P. N. Arendt, J. L. MacManus-Driscoll, M. P. Maley, and S. R. Foltyn. Angular-dependent vortex pinning mechanisms in YBa2Cu3O7 coated conductors and thin films. *Appl. Phys. Lett.*, 84(12):2121–2123, 2004.

[121] Ernst Helmut Brandt and Mikhail Indenbom. Type-II-superconductor strip with current in a perpendicular magnetic field. *Phys. Rev. B*, 48:12893–12906, Nov 1993.

[122] Nicolò Riva, Frederic Sirois, Christian Lacroix, Felix Pellerin, Jael Giguere, Francesco Grilli, and B. Dutoit. The eta-beta model model: an alternative to the power-law model for numerical simulations of REBCO tapes, 2021.

[123] Jianzhao Geng and T A Coombs. Modeling methodology for a HTS flux pump using a 2D H-formulation. *Supercond. Sci. Technol.*, 31(12):125015, 2018.

[124] O. Mawardi and Shangang Xu. Armature reaction in a flux pump. *IEEE Trans. Magn.*, 23(2):587–590, March 1987.

[125] Kent Hamilton, **Ratu Mataira**, Jianzhao Geng, Chris Bumby, Dale Carnegie, and Rod Badcock. Practical estimation of HTS dynamo losses. *IEEE Transactions on Applied Superconductivity*, 30(4):9037084, 2020.

[126] K. Hamilton, A. E. Pantoja, J. G. Storey, Z. Jiang, R. A. Badcock, and C. W. Bumby. Asynchronous magnet–stator topologies in a squirrel-cage superconducting dynamo. *IEEE Transactions on Applied Superconductivity*, 29(5):1–5, Aug 2019.

[127] Asef Ghabeli and Enric Pardo. Modeling of airgap influence on DC voltage generation in a dynamo-type flux pump. *Supercond. Sci. Technol.*, 33(3):035008, feb 2020.

[128] Pu Duan, Li Ren, Xianhao Li, Ying Xu, Jingdong Li, Yuejin Tang, Jing Shi, and Shuqiang Guo. Thermal and electrical analysis of no-insulation magnet during transient process based on 2D finite element method. *IEEE Transactions on Applied Superconductivity*, page 9525296, 2021.

[129] Archie Campbell. A circuit analysis of a flux pump. *Superconductor Science and Technology*, 32(11):115009, oct 2019.

[130] Mark Ainslie, Francesco Grilli, Loïc Quéval, Enric Pardo, Fernando Perez-Mendez, **Ratu Mataira**, Antonio Morandi, Asef Ghabeli, Chris Bumby, and Roberto Brambilla. A new benchmark problem for electromagnetic modelling of superconductors: the high-T_c superconducting dynamo. *Superconductor Science and Technology*, 33(10):105009, sep 2020.

[131] Leonid Prigozhin and Vladimir Sokolovsky. Fast solution of the superconducting dynamo benchmark problem. *Superconductor Science and Technology*, 34(6):065006, may 2021.

[132] Asef Ghabeli, Mark Ainslie, Enric Pardo, Loïc Quéval, and **Ratu Mataira**. Modeling the charging process of a coil by an HTS dynamo-type flux pump. *Superconductor Science and Technology*, 34(8):084002, jul 2021.

[133] Y. B. Kim, C. F. Hempstead, and A. R. Strnad. Critical persistent currents in hard superconductors. *Phys. Rev. Lett.*, 9:306–309, Oct 1962.

[134] Andres E. Pantoja, James G. Storey, Rodney A. Badcock, Zhenan Jiang, Sinhoi Phang, and Chris W. Bumby. Output during continuous frequency ramping of a dynamo-type HTS flux pump. *IEEE Transactions on Applied Superconductivity*, 28(3):8258876, 2018.

[135] Mark D. Ainslie, Loïc Quéval, **Ratu C. Mataira**, and Chris W. Bumby. Modelling the frequency dependence of the open-circuit voltage of a high-T_c superconducting dynamo. *IEEE Transactions on Applied Superconductivity*, 31(5):9350153, 2021.

[136] Asef Ghabeli, Enric Pardo, and Milan Kapolka. 3D modeling of a superconducting dynamo-type flux pump. *Scientific Reports*, 11(1):10296, May 2021.

[137] Leonid Prigozhin and Vladimir Sokolovsky. Two-dimensional model of a high-T superconducting dynamo. *IEEE Transactions on Applied Superconductivity*, 31(3):9340255, 2021.

[138] Leonid Prigozhin. Solution of thin film magnetization problems in type-II superconductivity. *Journal of Computational Physics*, 144(1):180–193, 1998.

[139] Ernst Helmut Brandt. Square and rectangular thin superconductors in a transverse magnetic field. *Phys. Rev. Lett.*, 74:3025–3028, Apr 1995.